Black Scintillators

Exploring Sm2+ as a near-infrared emitting activator for gamma-ray spectroscopy

van Aarle, C.

DOI
10.4233/uuid:37091b0a-1a34-4213-a2f1-4a883d4da721

Publication date
2024

Document Version
Final published version

Citation (APA)
van Aarle, C. (2024). *Black Scintillators: Exploring Sm2+ as a near-infrared emitting activator for gamma-ray spectroscopy*. [Dissertation (TU Delft), Delft University of Technology].
https://doi.org/10.4233/uuid:37091b0a-1a34-4213-a2f1-4a883d4da721

Important note
To cite this publication, please use the final published version (if applicable).
Please check the document version above.

Black Scintillators

Exploring Sm^{2+} as a near-infrared emitting activator for γ-ray spectroscopy

Black Scintillators

Exploring Sm^{2+} as a near-infrared emitting activator for γ-ray spectroscopy

Dissertation

for the purpose of obtaining the degree of doctor
at Delft University of Technology,
by the authority of the Rector Magnificus prof. dr. ir. T.H.J.J. van der Hagen,
chair of the Board of Doctorates,
to be defended publicly on
Thursday 27 June 2024 at 12:30 o' clock.

by

Casper VAN AARLE

Master of Science in Applied Physics,
Delft University of Technology, Delft, the Netherlands,
born in the Hague, the Netherlands.

This dissertation has been approved by the promotors.

Composition of the doctoral committee:

Rector Magnificus,	chairperson
Prof. dr. P. Dorenbos,	Delft University of Technology, promotor
Dr. E. van der Kolk,	Delft University of Technology, promotor

Independent members:

Prof. dr. A.J. Houtepen,	Delft University of Technology
Prof. dr. A. Meijerink,	Utrecht University
Dr. ir. D.R. Schaart,	Delft University of Technology
Dr. P. Schotanus,	Scionix bv, the Netherlands
Prof. dr. L.D.A. Siebbeles,	Delft University of Technology, reserve member

Other member:

Prof. dr. K.W. Krämer,	Bern University, Switzerland

Keywords: Near-infrared scintillators, γ-ray spectroscopy, halides, lanthanide spectroscopy, divalent samarium, single crystals.

Printed by: Ipskamp Printing

Front & Back: An artist's impression of the emissive and electronic properties of black scintillators.

ISBN 978-94-6366-873-6

An electronic version of this dissertation is available at
http://repository.tudelft.nl/.

Contents

1 Introduction

1.1. What is gamma-ray spectroscopy

While ionising radiation is all around us, special techniques are required to convert it to something humans can perceive. Arguably the most famous technology for this is the Geiger-Müller counter, which generates an electronic pulse upon detection of an ionising particle. Often this electronic pulse is converted to the well-known clicking sound that these detectors produce. A Geiger-Müller counter, however, only gives information about the number of ionising particles, but it gives little information about the energy of these particles. For γ-rays, information on the energy can be attained using a measurement technique called γ-ray spectroscopy.

γ-ray spectroscopy relies on a detector material interacting with a γ-ray passing through it. Within this interaction, the γ-ray creates free charge carriers, the number of which is proportional to the amount of energy the γ-ray deposits in the detector material. The aim of the technique is then to determine the amount of deposited energy by measuring how many free charge carriers were created. This is done by either directly or indirectly converting these free charge carriers into an electronic pulse, the intensity of which must then be proportional to the amount of free charge carriers. A histogram of the intensity of many such electronic pulses is called a pulse height spectrum (PHS).

An example of a PHS is shown in Figure 1.1. The γ-ray spectrometer consisted of a $LaBr_3$:Ce^{3+} scintillation crystal optically coupled to a Photonis XP2060B photomultiplier tube (PMT). It measured the 662 keV γ-rays and 32 keV X-rays coming from a ^{137}Cs source. When a γ-ray spectrometer is exposed to a flux of monoenergetic γ-rays with an energy below 1,022 keV, there are two types of interactions possible. The first is photoelectric absorption, where the γ-ray transfers all of its energy to an electron in the detector material. The second is Compton scattering, where only part of the γ-ray energy is transferred to an electron in the detector. Above 1,022 keV there also is the possibility that an electron-positron pair is produced. However, since it is conventional to compare detector performance under excitation with a 662 keV γ-rays from a ^{137}Cs source, this pair production will not be discussed in detail.

The pulse height spectrum in Figure 1.1 contains 3 distinct features: a Compton continuum and two photopeaks at 32 keV and 662 keV. The Compton continuum, running from 0 keV to 477 keV, is caused by 662 keV γ-rays that undergo Compton scattering after

which the lower energy scattered γ-ray escapes the detector material. The probability of this escape decreases with increasing detector size, and therefore the probability that all energy is absorbed within the detector increases. When all energy is absorbed, an event ends up in the photopeak. This is mostly due to photoelectric absorption. The energy resolution of a detector is defined as the full width at half maximum (FWHM) of the photopeak ΔE divided by the energy of the incoming γ-ray E (Equation 1.1) [1]. For the 662 keV photopeak in Figure 1.1, ΔE = 30 keV at E = 662 keV, giving an energy resolution of 4.5 %. The main goal of this work is to find scintillating materials that can yield better energy resolutions than current scintillation detectors.

$$R = \frac{\Delta E}{E} \tag{1.1}$$

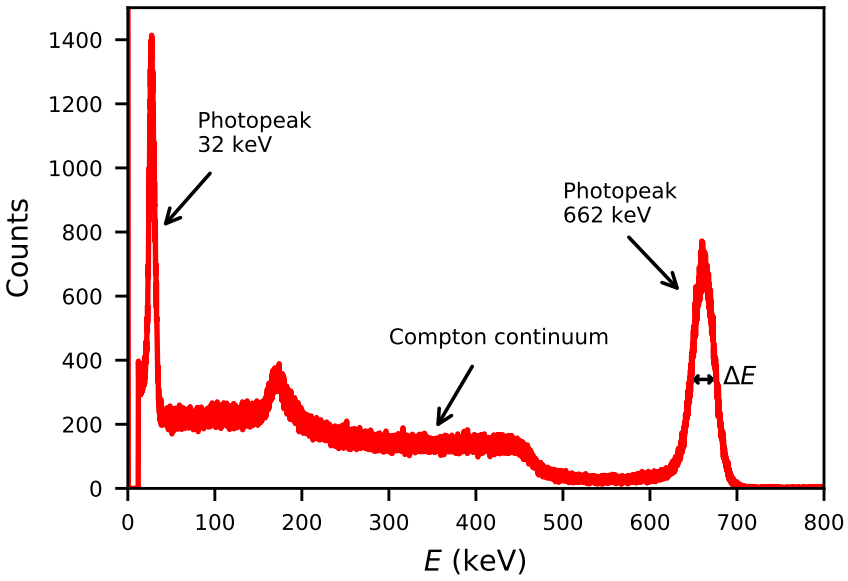

Figure 1.1: Pulse height spectrum of a ^{137}Cs source measured with a γ-ray spectrometer consisting of a $LaBr_3$:Ce^{3+} crystal optically coupled to a Photonis XP2060B PMT.

1.2. Semiconductors and scintillators

Common detectors that are used for γ-ray spectroscopy can be separated in two main categories, semiconductor detectors and scintillation detectors [2]. A semiconductor detector consists of a semiconductor (~1 eV band gap) as detector material to which two electrodes are attached [3]. When a voltage is applied over the electrodes, the electric field separates the free electrons and holes that are created in the depletion layer when a γ-ray interacts with the detector material, generating an electronic pulse. The intensity of this pulse is directly proportional to the amount of free charge carriers, which relates the intensity of a pulse to the amount of energy the γ-ray deposited in the detector.

When the highest achievable energy resolution is required, the detector material of choice is high purity germanium (HPGe). The energy resolution of HPGe detectors can reach an excellent value of 0.3% at 662 keV [4]. It does, however, have several drawbacks. For example, HPGe detectors are expensive and can easily cost over 10 times as much as a NaI:Tl^+ scintillation detector [5,6]. They also need to be kept at cryogenic temperatures at all time [7], making them rely on liquid nitrogen facilities or other often bulky methods of cooling [5]. Lastly, the density of germanium is relatively low compared to that of scintillators, which gives HPGe detectors limited stopping power for high energy γ-rays.

There also exist semiconductor detectors that operate at room temperature, among which are CdTe, CZT and TlBr [8]. These consist of elements with higher atomic number Z than HPGe, resulting in a higher stopping power for γ-rays. An energy resolution of approximately 0.5% has been achieved with a 6 cm^3 CZT detector [9]. While this is worse than HPGe, it is still far better than any scintillation detector. These detectors, however, also come with several large drawbacks. They tend to have a higher concentration of defects than HPGe and consequently they have a significantly lower drift velocity of electrons and holes. As a result, the dead time of large detectors can be as long as 100 µs [9], which severely limits their count rate [10–12]. Therefore, detectors larger than several cm^3 are often impractical. Since the stopping power is lower for high energy γ-rays, the small size of these detectors often limits their use to detection of γ-ray energies below 1 MeV [13]. Exposing these detectors to high energy (MeV) protons, neutrons and electrons causes the creation of defects in the bulk of the detector material, causing further degradation of the charge carrier mobility. Therefore, all these semiconductor detectors are sensitive to radiation damage [8].

Opposed to the semiconductor detectors, scintillation detectors convert the free charge carrier into an electronic pulse indirectly. They consist of a scintillator as detector material, which is coupled to a photodetector. The free charge carriers that are created inside the scintillator are converted into photons near their point of creation. The wavelength of these scintillation photons typically lies in the UV or visible part of the electromagnetic spectrum. The scintillation photons are then detected by the photodetector attached to the outside of the scintillator. The number of photons detected during a scintillation event then becomes a measure for the energy absorbed in the scintillator.

One large benefit of scintillation detectors compared to semiconductor detectors is their stopping power and potential size. The problems in semiconductor detectors arise during the transport of free charge carriers to the electrodes. The transport length increases with increasing detector size. Since, in scintillators, the recombination of free charge carriers happens close to their point of creation, the charge carrier transport is replaced by optical photon transport. As the ideal scintillator is transparent to its own emission, the generated scintillation photons are unobstructed when travelling through the crystal. This means that the light collection efficiency is almost independent of detector size. The main downside of scintillation detectors, however, is that the energy resolution is much worse than that of semiconductor detectors. Commercial NaI:Tl^+ detectors typically have an energy resolution worse than 6% at 662 keV [14]. The more recently developed $LaBr_3$:Ce^{3+},Sr^{2+} detectors can reach significantly better energy resolution of 2.2% [15].

1

1.3. The need for high resolution scintillators

Often it is worth sacrificing some of the energy resolution by using a scintillation detector instead of a semiconductor detector. When an application does not have very high requirements for the energy resolution, their lower cost and ease of use are often the selling points. However, there are scenarios in which using semiconductor detectors is not even feasible. There are many examples reported in literature where scintillation detectors are preferred over semiconductor detectors due to constraints in the spectrometer design. Take for example the nuclear incident at the Fukushima Dai-ichi reactor. In order to construct a decontamination plan, both the inside of the reactor and its surrounding had to be screened for presence and identification of radioactive isotopes. Scintillation detectors have often been the detector of choice for these tasks.

The perimeter around the reactor was screened using γ-ray spectrometers in fixed locations and portable ones carried by backpack, car and helicopter [16]. The aim was to map out the distribution of radioisotopes with both short half-lives, such as ^{131}I, ^{132}Te, and ^{133}I, as well as long half-lives, such as ^{134}Cs and ^{137}Cs [17]. Japanese aerospace law restricts aerial radiation monitoring by manned helicopter to altitudes higher than 150 m, providing limited spatial resolution. It was necessary to perform measurements with better spatial resoltuion to form a decomtamination plan for the area within a radius of several km around the reactor. Therefore, Sanada et al. designed γ-ray spectrometer attached to an unmanned helicopter, which are allowed to fly at altitudes below 150 m [18]. The design was made around existing unmanned helicopter models typically used for agricultural purposes, which have a maximum payload of 10 kg [19]. This introduced a weight limit in the γ-ray spectrometer design. The γ-ray spectrometer also needed a high detection efficiency for accurate measurements in regions with low activity. Additionally, a sufficiently good energy resolution was required to resolve the γ-ray energies of ^{134}Cs (605 keV and 796 keV) and ^{137}Cs (662 keV). These requirements ruled out both HPGe and classical commercial scintillators such as NaI:Tl^{+} [17]. In the end, the γ-ray spectrometer design that fit all the design criteria consisted of 3 $LaBr_3$:Ce^{3+} scintillation crystals of 1.5 inch coupled to a photomultiplier tube [19].

To prevent further spread of radioactive material, the inside of the reactors was flooded for moderation and cooling. Consequently, localisation and identification of fuel debris has to be performed underwater [20] in an environment with a dose rate as high as 10 Sv/h and a large neutron flux. Kaburagi et al. designed a γ-ray spectrometer that can operate in such an environment [8]. In this scenario the main design criteria were small size, low detection efficiency and radiation hardness. Additionally, the energy resolution had to be better than 4.5% at 1,333 keV to resolve the γ-rays coming from ^{154}Eu (1,274 keV) and ^{60}Co (1,333 keV). Semiconductor detectors were ruled out due to their susceptibility to radiation damage from neutrons and specifically the bulky cooling solution of HPGe was deemed problematic. In this case the choice was made for a small 5×5×5 mm^3 $CeBr_3$ scintillation crystal, which can fulfill the requirements in energy resolution and has high radiation hardness.

Another example of where scintillators were preferred over direct detection materials can be found in space exploration. The BepiColombo space mission launched two spacecrafts which will study the origin and evolution of the planet Mercury [21]. One of them, the Mercury Polar Orbiter (MPO), is equipped with a γ-ray spectrometer. Its scien-

tific goal is to determine the elemental composition of Mercury's subsurface [22], information of which is contained in γ-rays escaping into space. These γ-rays have energies up to 10 MeV. The γ-ray spectrometer was designed for an energy range from 100 keV to 9 MeV [23], needed to operate at a low count rate and discriminate between dozens of γ-ray energies. Therefore, the requirements called for the spectrometer to have an energy resolution of 1% at 1 MeV and detection efficiency of 3% around 6 MeV [24]. The use of both a HPGe detector and a $LaBr_3:Ce^{3+}$ scintillation detector was explored.

It proved difficult to construct a spaceborne HPGe detector that complied with the strict weight and power consumption requirements [22]. Additionally, operating multiple years within the inner solar system, the detector would be exposed to a high proton flux produced by solar flares and coronal mass ejections. The expected radiation damage in such an event would degrade the energy resolution so much that it would no longer fit the design requirement of 1% at 1 MeV. Additionally, the detection efficiency would drop so much that the detector would become completely unfit for its mission. While both energy resolution and detection efficiency could be largely recovered by annealing the detector for several months, this would cause a massive loss of valuable measurement time. Especially given that the instruments are designed to operate in orbit around Mercury for only about 2 years [25].

The design of a γ-ray spectrometer using a $LaBr_3:Ce^{3+}$ scintillator would be a large sacrifice in terms of energy resolution. In fact, it could not comply to the energy resolution requirement of 1% at 1 MeV. However, the higher detection efficiency that $LaBr_3:Ce^{3+}$ scintillation detectors can offerl largely compensated for the poorer energy resolution. Because of this, its energy resolution was considered good enough to resolve almost all γ-ray energies of interest [22]. Radiation hardness tests showed that except for activation of the scintillator material, the detectors performance would hardly be affected by the same radiation dose that would render the HPGe detector unusable [26]. Because of this, the choice was initially made to equip the spacecraft with a $LaBr_3:Ce^{3+}$ scintillation detector, which was later replaced for $CeBr_3$ for its lower internal radioactivity [23, 27].

What these three examples have in common is that the inherent drawbacks of semiconductor detectors prevent their use in scenarios where high energy resolution is required, while classical commercial scintillators such as $NaI:Tl^+$ do not fit these energy resolution requirements. The application of γ-ray spectroscopy in all these examples therefore became possible due to the development of the high resolution scintillation materials $LaBr_3:Ce^{3+}$ and $CeBr_3$. $LaBr_3:Ce^{3+}$ and $CeBr_3$ scintillators were not designed with these precise applications in mind, but their discovery and further development automatically made them the most suitable candidates. This shows the value that the development of high resolution scintillators can have. Further improvement of the energy resolution will therefore likely contribute to solving many societal problems that are still hindered by the current state of this technology.

1

1.4. Contributions to the energy resolution

It has become clear that the discovery of $LaBr_3:Ce^{3+}$ has had a large impact on the applicability of scintillators in high resolution γ-ray spectroscopy. Understanding what the next step is in designing even higher resolution scintillation detectors requires some background knowledge on how scintillators work and what their fundamental limitations are. A schematic of the scintillation mechanism is shown in Figure 1.2. When a γ-ray transfers energy to an electron, the electron escapes the ion it was initially bound to and travels with high velocity through the scintillator. This electron then transfers its kinetic energy to other electrons in the scintillator through Coulomb interactions, promoting them into the conduction band and leaving behind holes in the valence and core bands. This process corresponds to arrow A in Figure 1.2. The total number of electron-hole pairs created per MeV of γ-ray energy is given by Equation 1.2 [28]:

$$N_{\text{eh}} = \frac{10^6}{\beta E_g} \tag{1.2}$$

Here, E_g is the band gap energy, and the constant β resembles loss processes from electrons gaining more energy than E_g [29]. These electrons relax to the bottom of the conduction band, creating many phonons in the process. Similarly, holes relax to the top of the valence band. β typically has a value between 2 and 3 [30].

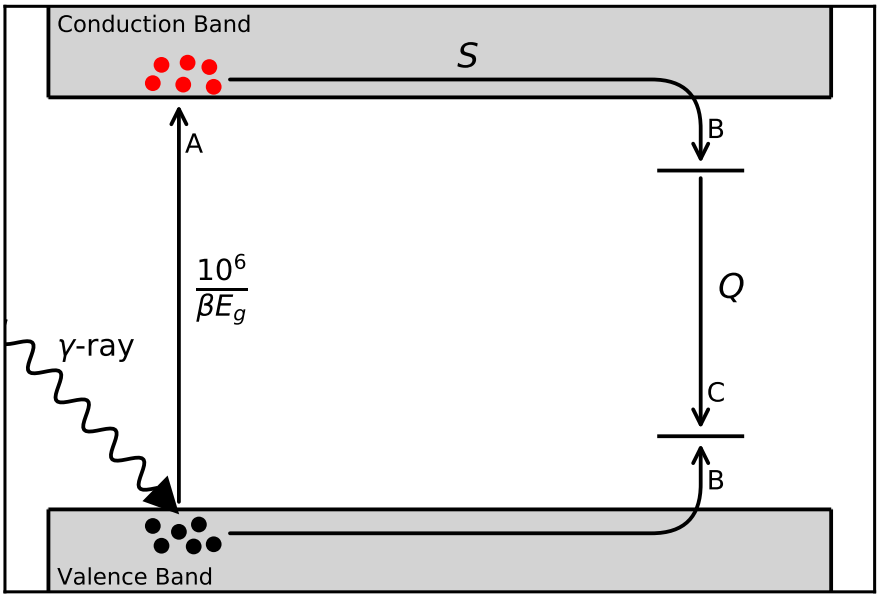

Figure 1.2: Schematic of the scintillation mechanism. A fast electron produced by an incoming γ-ray promotes electrons from the valence band to the conduction band. After this the free charge carriers migrate to the luminescence centers with efficiency S, which emit the scintillation photons with efficiency Q.

After promotion of electrons to the conduction band, the free charge carriers migrate to the luminescence centers indicated by Arrow B. Along the way, some charge carriers might get lost due to deep traps or nonradiative recombination processes. The migration process therefore happens with a certain transfer efficiency S. This is equal to the fraction of generated electron hole pairs that result in excitation of the luminescence centers. Once excited, luminescence will occur with quantum efficiency Q (Arrow C). The final light yield Y in units of photon per MeV of γ-ray energy (ph/MeV) can then be expressed by Equation 1.3 [30]. When $S = Q = 1$, the light yield is equal to the number of generated electron-hole pairs, which is the theorical maximum light yield Y_{max} for a scintillator.

$$Y = \frac{10^6}{\beta E_g} SQ \tag{1.3}$$

The importance of light yield in the development of high energy resolution scintillators can be understood from Equation 7.1 [31]. This equation is often used to describe the multiple components that contribute to the energy resolution R.

$$R^2 = \frac{2.35^2}{N_{\text{dp}}} + R_{\text{np}}^2 + R_{\text{det}}^2 \tag{1.4}$$

The first term contains the contribution of Poisson statistics in the number of detected photons N_{dp}, which is the product of the number of photons generated in a scintillation event and their probability of being detected. The second term, R_{np}, relates to the degree of nonproportionality of the scintillators response to different γ-ray energies. The third term, R_{det}, contains all other contributions. Among these are the inhomogeneity in the crystal and detector surface and variation in the light collection efficiency depending on the point of γ-ray interaction. Minimising R_{det} is typically an engineering problem which involves optimising crystal growth and using detectors and electronics that generate little electronic noise. However, some material properties of a scintillator can also influence R_{det}. An important example of this is that a scintillator should be transparent to its own emission, i.e., the scintillator should be free of self-absorption.

Self-absorption occurs when the absorption spectrum of the scintillator overlaps with its emission spectrum. Almost all lanthanide doped scintillators emit through the dipole allowed $4f^{n-1}5d \rightarrow 4f^n$ transition of their dopants. This emission fundamentally always has some spectral overlap with the $4f^n \rightarrow 4f^{n-1}5d$ transition of that dopant, meaning some self-absorption is always present. The probability of a photon being reabsorbed scales with the distance the photon has to travel through the scintillation crystal before it reaches the detector. This creates variations in N_{dp} depending on the point where the γ-ray deposits its energy inside the scintillator, thereby worsening the energy resolution. This is one of the reasons why the best energy resolutions are typically measured in small crystals of only a few mm in size. Self-absorption is especially strong in Eu^{2+}-doped scintillators, making it difficult to scale them up for application.

1

1.5. Current limitations of scintillator materials

The nonproportional response of a scintillator has the largest contribution to the energy resolution for many scintillator-detector combinations, even for $LaBr_3$:Ce^{3+} coupled to a PMT [32]. Engineering scintillator materials to make their response more proportional can therefore be an effective way of improving the energy resolution. This strategy has led to the invention of $LaBr_3$:Ce^{3+},Sr^{2+}, in which the co-doping with Sr^{2+} greatly reduced R_{np} [31]. This improvement resulted in the record energy resolution of 2.04% at 662 keV, which was attained by coupling a small $LaBr_3$:Ce^{3+},Sr^{2+} crystal to a Hamamatsu R6231-100 super bialkali PMT. It was assessed that R_{np} became so small that the largest contribution to the energy resolution now became N_{dp}. This means that making further significant improvements of the energy resolution beyond 2.04% requires the number of detected photons to increase.

There are two ways to increase N_{dp}. The first is to develop scintillators with a light yield higher than $LaBr_3$:Ce^{3+},Sr^{2+}. Using Equation 1.3 for $LaBr_3$ with a band gap of 5.7 eV [33] and light yield of 78,000 ph/MeV [32], and assuming $S = Q = 1$, it is found that $\beta = 2.3$. As this value is on the lower side of what is expected, it can be concluded that the light yield of $LaBr_3$:Ce^{3+} is already close to the theoretical maximum. Therefore significant improvements can only be expected when using compounds with a smaller band gap. Unfortunately, it does not seem possible to find lanthanide doped halide scintillators with a band gap much smaller than 4 eV [15], meaning the light yield is limited to about 100,000 ph/MeV. Two scintillator materials that get close to this maximum achievable light yield are SrI_2:Eu^{2+} and $CsBa_2I_5$:Eu^{2+}. Their light yields are reported to be around this 100,000 ph/MeV [34–36] and respective energy resolutions of 2.6% [37] and 2.3% [38] have been achieved with these scintillators. However, as this increase in light yield is limited, solely focussing on the development brighter scintillator materials is expected to yield only limited improvements in energy resolution.

The other way to increase N_{dp} is to increase the detection efficiency of the scintillation photons. Scintillators have primarily been developed for readout with PMTs. The main reason is that PMTs are detectors with high signal gain and low noise. They have also been around since the discovery of some of the most used scintillator materials. PMTs typically have maximum quantum efficiency (QE) in the ultraviolet and blue part of the spectrum. As an example, the QE of a Hamamatsu R1791 PMT is shown in Figure 1.3a. It has a maximum between 300 nm and 450 nm. Because the efficiency of PMTs is highest in this wavelength range, most scintillators are developed to emit light between 300 nm and 450 nm. As a result, the most used lanthanide dopants for scintillation are Ce^{3+}, Pr^{3+} and Eu^{2+}. The maximum QE of the PMT shown in figure 1.3a is only about 35%. Even when the scintillator is optically coupled to the PMT and is surrounded by reflective material, the total detection efficiency hardly ever exceed 50% [31, 39]. This means that at least 50% of photons are still not detected and recovering these losses would be a requirement for further improving the energy resolution.

1.6. How to surpass the existing limitations

Silicon based photodetectors are an alternative photodetector with higher photon detection efficiency than the conventionally used PMT. The two silicon based photodetectors of importance to this work are the avalanche photodiode (APD) and silicon photomultiplier (SiPM). An APD consist out of a p-n junction with a high reverse-bias voltage. When a photon creates an electron-hole pair in the p-n junction, the high reverse-bias accelerates the electron and hole in opposite directions giving them enough energy to create an avalanche effect with large gain. This turns the absorption of a single photon into a sizeable electronic signal that is easily detected, similar to the workings of a PMT. The total charge collected on the electrodes scales linearly with the number of detected photons. An SiPM is an array of many tiny APDs with a reverse-bias larger than the breakdown voltage. These APDs are often referred to as single photon avalanche photodiodes (SPAD), as their signal saturates upon detection of a single photon, i.e., it is either on or off. Each time a SPAD triggers, it generates a charge pulse of about 10^6 electrons, thus the entire array generates a total amount of charge proportional to the number of detected photons.

Silicon based photodetectors can detect photons with an energy larger than the 1.12 eV band gap of Si, which corresponds to roughly 1,100 nm [40]. This makes it possible to detect photons of much longer wavelength than with PMTs. This is illustrated by the QE curve of the Advanced Photonix 630-70-72-510 APD shown in Figure 1.3a. Silicon based photodetectors are often optimised for a specific wavelength that lies between 400 nm and 800 nm. At wavelengths shorter than 400 nm, the absorption strength of silicon becomes so strong that most photons are absorbed within 100 nm under the detector surface [41]. In this region, surface states and a higher impurity concentration reduce the charge carrier lifetime. This creates unrecoverable losses in the detection efficiency and is responsible for the drop in QE at wavelengths shorter than 400 nm [42]. At wavelengths longer than 800 nm, the absorption strength of silicon becomes too weak. In this case, some photons remain undetected as they are transmitted through the detector.

When using an APD to detect scintillation photons with a wavelength between 400 nm and 800 nm, the detection efficiency of photons hitting the detector surface can reach values higher than 80%. Virtually all photons that remain undetected are reflected off the detector surface. These photons are not necessarily lost as they can be recovered by wrapping the scintillator and detector combination in reflective material such as PTFE. Almost all photons that were initially undetected and reflected off the detector surface will finally reach the detector surface again and have a second chance of being detected. This allows APDs to reach an effective detection efficiency close to 100% between 400 nm and 800 nm [39]. This does not work for SiPMs, as opposed to APDs they do not have a continuous sensitive area. The SPADs at the detector surface have space between them and photons that fall between the SPADs will not be detected. The maximum detection efficiency of an SiPM is therefore necessarily lower than that of an APD. However, with photon detection efficiencies of over 60% [45, 46], they can still outperform a PMT. Furthermore, the field of silicon based photodetectors is rapidly evolving and further improvements are to be expected in the near future [47], making them increasingly competitive with PMTs.

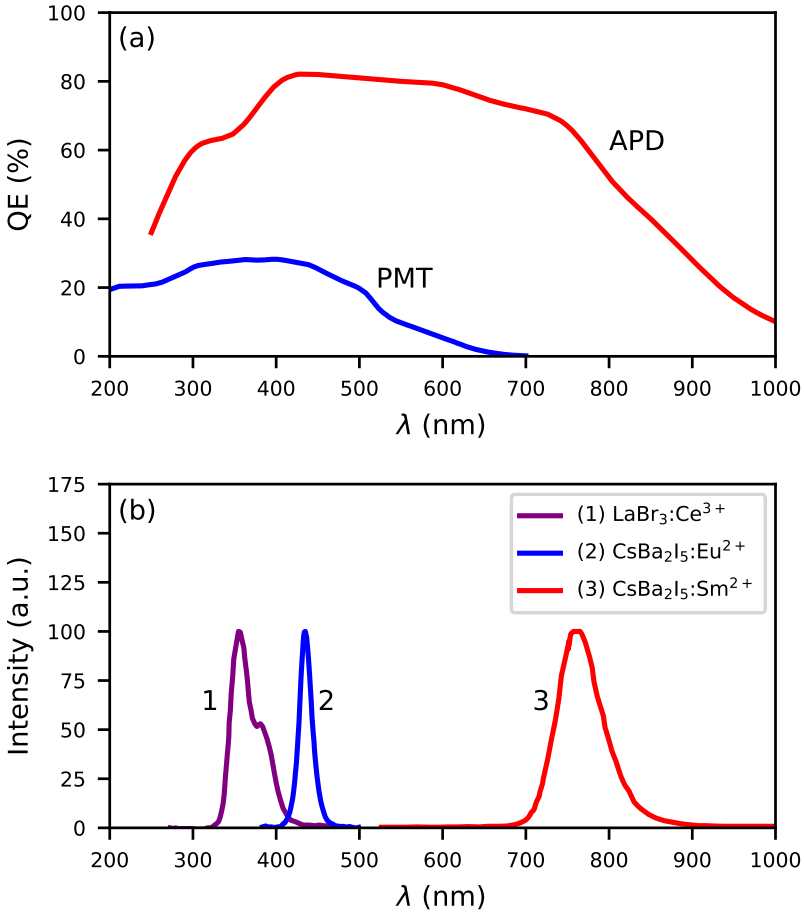

Figure 1.3: a) the quantum effiiciency curves of 1) an Advanced Photonix 630-70-72-510 APD and 2) a Hamamatsu R1791 PMT. b) X-ray excited emission spectra of 1) $LaBr_3:Ce^{3+}$ [43], 2) $CsBa_2I_5:Eu^{2+}$ [38], and 3) $CsBa_2I_5:Sm^{2+}$ [44].

The emission spectra of $LaBr_3:Ce^{3+}$ [43], $CsBa_2I_5:Eu^{2+}$ [38] and $CsBa_2I_5:Sm^{2+}$ [44] are shown in Figure 1.3b. $LaBr_3:Ce^{3+},Sr^{2+}$ emits at shorter wavelength than 400 nm and detection losses cannot be entirely avoided when coupling it to silicon based photodetectors. This is the case for many other Ce^{3+}-doped scintillators as well. The emission spectrum of $CsBa_2I_5:Eu^{2+}$ lies almost entirely at wavelengths longer than 400 nm. However, just like almost all other Eu^{2+}-doped halide scintillators, it suffer from a high probability of self-absorption [38, 48–52]. $CsBa_2I_5:Sm^{2+}$ emits almost entirely beyond 700 nm, making it incompatible with a PMT as photodetector. However, its emission spectrum still largely falls within the optimal wavelength range for detection with an APD. The use of APDs as photodetector therefore makes Sm^{2+} interesting an activator for scintillator applications.

An energy level diagram of Sm^{2+} in $CsBa_2I_5$ is shown in Figure 1.4a. Its first 7 energy levels belong to the $4f^6[^7F_J]$ multiplet (J = 0-6), of which $4f^6[^7F_0]$ is the ground state. In compounds where the $4f^55d$ level lies below the $4f^6[^5D_0]$ level, exclusively $4f^55d \rightarrow 4f^6$ broad band emission is observed [53]. There are several benefits to using Sm^{2+} as an activator. For example, the $4f^55d \rightarrow 4f^6$ emission can have any of the $4f^6[^7F_J]$ states as final state [15]. The transitions to the $4f^6[^7F_{1-6}]$ states lie at longer wavelength than the transition to the $4f^6[^7F_0]$ state, which effectively shifts part of the emission spectrum away from the Sm^{2+} $4f^6[^7F_0] \rightarrow 4f^55d$ absorption bands. This is different than the situation in Eu^{2+} (Figure 1.4b), where the $4f^65d \rightarrow 4f^7$ emission always leaves Eu^{2+} in the ground state. This causes significant overlap between the emission and absorption bands of Eu^{2+}. The result is that Sm^{2+}-doped scintillator suffer less from self-absorption than their Eu^{2+}-doped counterparts [54,55]. As both Sm^{2+} and Eu^{2+} have the same charge and similar ionic radius, it is easy to replace Eu^{2+} for Sm^{2+} in the same host material. Because of this, the vast knowledge attained during the development of Eu^{2+}-doped scintillators over the past decade can directly be applied to the development of their Sm^{2+}-doped counterparts.

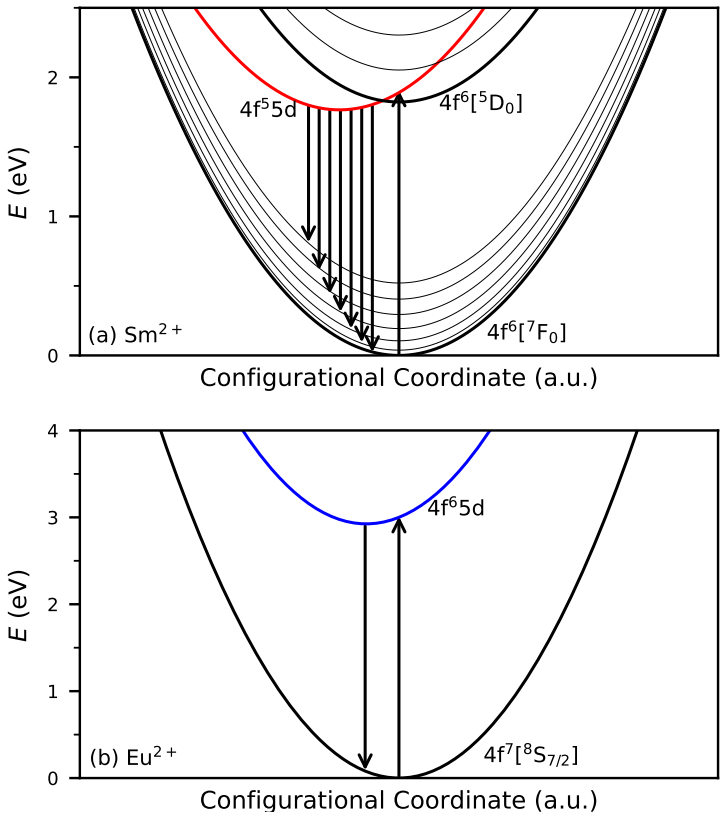

Figure 1.4: Configurational coordinate diagrams of a) Sm^{2+} and b) Eu^{2+} in $CsBa_2I_5$. Note the different energy scales.

Sm^{2+} shows strong absorption bands across the entire optical spectrum. This means that it can be efficiently sensitised by other dopants in the lattice. Co-doping an Eu^{2+}-doped scintillator with a few atomic % of Sm^{2+} replaces almost all the Eu^{2+} emission by that of Sm^{2+} [44, 55]. When a Eu^{2+}-doped scintillator has high light yield, it is known that energy transfer from the host to Eu^{2+} is an efficient process. Since Eu^{2+} excitation can be transferred efficiently to Sm^{2+}, knowledge of high light yield Eu^{2+}-doped scintillators can be used to rapidly develop high light yield Sm^{2+}-doped near-infrared emitting scintillators. With this approach, the self-absorption problem that the Eu^{2+}-doped scintillators face can be solved as well. The opposite strategy can also be applied. When a Sm^{2+}-doped scintillator shows low light yield due to inefficient energy transfer from the host to Sm^{2+}, the scintillator can be co-doped with a sensitiser in an attempt to increase its light yield.

1.7. Research objective and dissertation outline

The development of high resolution Sm^{2+}-doped near-infrared emitting scintillators is a topic that is largely unexplored. Firstly, energy needs to be transferred efficiently from the host compounds to Sm^{2+}. Co-doping Sm^{2+} with Eu^{2+} as sensitiser has already been shown to be a promising strategy, but using two dopants greatly increases the amount of possible concentrations and complicates the optimisation process. This work therefore aims to formulate guidelines in selecting the proper sensitiser and their concentrations. Chapter 2 and 3 cover the use of Yb^{2+} as sensitiser, explain why Yb^{2+} is only suitable as a sensitiser when present in sufficiently high concentration. In Chapter 4, the effects of sensitiser to sensitiser energy transfer are covered and the low self-absorption probability of Sm^{2+} is demonstrated. Chapter 5 explores whether the trivalent lanthanides Ce^{3+} and Pr^{3+} can be used as sensitiser for Sm^{2+} and explains their effects on the thermal quenching temperature of the Sm^{2+} emission.

Next, Sm^{2+} needs to have the desired emission properties, such as emission wavelength and decay time. Chapter 6 aims to formulate what these desired emission properties are and in what compounds they are found. If it can be predicted in what compounds Sm^{2+} does not have the desired properties for scintillator applications, these can be excluded from future attempts in searching for the ideal near-infrared scintillator. Lastly, Chapter 7 formulates the fundamental light yield limits of Sm^{2+}-doped scintillators and compares it to that of Eu^{2+} and Ce^{3+}-doped scintillators, and intrinsically activated scintillators. From this is determined what improvements to the energy resolution can be made with Sm^{2+} and under what circumstances further development of Sm^{2+} is worthwhile.

References

[1] G. F. Knoll, Radiation Detection and Measurement, third ed., Wiley, New York, 2000.

[2] R. Devanathan, L. R. Corrales, F. Gao, W. J. Weber, Nucl. Instrum. Meth. A 565 (2006) 637.

[3] P. N. Luke, M. Amman, C. Tindall, J. S. Lee, J. Radioanal. Nucl. Ch. 264 (2005) 145.

[4] Alan Owens, Nucl. Instrum. Meth. A 238 (1985) 473.

[5] James H. Ely, Edward R. Siciliano, Richard T. Kouzes, IEEE Nucl. Sci. Conf. R. (2004) 1584.

[6] David C. Stromswold, Edward R. Siciliano, John E. Schweppe, James H. Ely, Brian D. Milbrath, Richard T. Kouzes, Bruce D. Geelhood, IEEE Nucl. Sci. Conf. R. (2004) 1065.

[7] G. A. Armantrout, IEEE T. Nucl. Sci. 19 (1972) 289.

[8] Masaaki Kaburagi, Kenji Shimazoe, Yutaka Otaka, Mizuki Uenomachi, Kei Kamada, Kyoung Jin Kim, Masao Yoshino, Ysuhiro Shoji, Akira Yoshikawa, Hiroyuki Takahashi, Yatsuo Torii, Nucl. Instrum. Meth. A 971 (2020) 164118.

[9] Feng Zhang, Cedric Herman, Zhong He, Gianluigi De Geronimo, Emerson Vernon, Jack Fried, IEEE. Trans. Nucl. Sci. 59 (2012) 236.

[10] Kuen Lee, J.W. Martin, A. B. Garson III, M. Beilicke, Q. Guo, Q. Li, G. De Geronimo, M. Groza, A. Burger, H. Krawczynski, Proc. SPIE 7664 (2023) 755423-1.

[11] M. Nakhostin, K. Hitomi, Nucl. Instrum. Meth. A 675 (2012) 47.

[12] Keitaro Hitomi, Toshiyuki Onodera, Tadayoshi Shijo, Nucl. Instrum. Meth. A 579 (2007) 153.

[13] O. Limousin, Nucl. Instrum. Meth. A 504 (2003) 24.

[14] Giulia Hull, Woon-Seng Choong, William W. Moses, Gregory Bizarri, John. D. Valentine, Stephen A. Payne, Nerine J. Cherepy, Bryan W. Reutter, IEEE. T. Nucl. Sci. 56 (2009) 331.

[15] Pieter Dorenbos, Opt. Mater. X. 1 (2019) 100021.

[16] Yukihisa Sanada, Mutsushi Ishida, Kazuya Yoshimura, Satoshi Mikami, J. Radiat. Prot. Res. 46 (2021) 184.

[17] Yukiyasu Nishizawa, Mami Yoshida, Yukihisa Sanada, Tatsuo Torii, J. Nucl. Sci. Technol. 53 (2016) 468.

[18] Yokihisa Sanada, Tadashi Orita, Tatsuo Torii, Appl. Radiat. Isot. 118 (2016) 308.

[19] Yukihisa Sanada, Atsuya Kondo, Takeshi Sugita, Yukiyasu Nishizawa, Youichi Yuuki, Kazutaka Ikeda, Yasunori Shoji, Tatsuo Torii, Explor. Geophys. 45 (2014) 3.

[20] M. Nancekievill, A. R. Jones, M. J. Joyce, B. Lennox, S. Watson, J. Katakura, K. Okumura, S. Kamada, M. Katoh, K. Nishimura, IEEE. T. Nucl. Sci. 65 (2018) 2565.

[21] Johannes Benkhoff, Jan van Casteren, Hajime Hayakawa, Masaki Fujimoto, Harri Laakso, Mauro Novara, Paolo Ferri, Helen R. Middleton, Ruth Ziethe, Planet. Space. Sci. 58 (2010) 2.

[22] I. G. Mitrofanov, A. S. Kozyrev, A. Konovalov, M. L. Litvak, A. A. Malakhov, M. I. Mokrousov, A. B. Sanin, V. I. Tret'ykov, A. V. Vostrukhin, Yu. I. Bobrovnitskij, T. M. Tomilina, L. Gurvits, A. Owens, Planet. Space Sci. 58 (2010) 116.

[23] A. Kozyrev, I. Mitrofanov, A. Owens, F. Quarati, J. Benkhoff, B. Bakhtin, F. Fedosov, D. Golovin, M. Litvak, A. Malakhob, M. Mokrousov, I. Nuzhdin, A. Sanin, V. Tretyakov, A. Vostrukin, G. Timoshenko, V. Shvetsov, C. Granja, T. Slavicek, S. Pospisil, Rev. Sci. Instrum. 87 (2016) 085112.

[24] Stefan Kraft, Erik Maddox, Ernst-Jan Buis, Alan Owens, Francesco G. A. Quarati, Pieter Dorenbos, Winicjusz Drozdowski, Adrie J. J. Bos, J. T. M. de Haas, H. Brouwer, Corinne Dathy, Vladimir Ouspenski, Sytze Brandenburg, Reint Ostendorf, IEEE T. Nucl. Sci. 54 (2007) 873.

[25] F. Quarati, S. Brandenburg, E. J. Buis, P. Dressler, S. Kraft, M. O. Lampert, R. W. Ostendorf, Alan Owens, A. Peacock, P. Quirin, D. Quirion, Nucl. Instr. Meth. A 610 (2009) 354.

[26] W. Drozdowski, P. Dorenbos, A. J. J. Bos, J. T. M. de Haas, S. Kraft, E. Maddox, A. Owens, F. G. A. Quarati, C. Dathy, V. Ouspenski, IEEE. T. Nucl. Sci. 54 (2007) 736.

[27] I. G. Mitrofanov, A. S. Kozyrev, D. I. Lisov, M. L. Litvak, A. A. Malakhov, M. I. Mokrousov, J. Benkhoff, A. Owens, R. Schulz, F. Quarati, Space Sci. Rev. 217 (2021) 67.

[28] A. Lempicki, A. J. Wojtowicz, E. Berman, Nucl. Instrum. Meth. A 333 (1993) 304.

[29] D. J. Robbins, J. Electrochem. Soc. 127 (1980) 2694.

[30] M. J. Weber, Nucl. Instrum. Meth. A 527 (2004) 9.

[31] M. S. Alekhin, J. T. M. de Haas, I. V. Khodyuk, K. W. Krämer, P. R. Menge, V. Ouspenski, P. Dorenbos, Appl. Phys. Lett. 102 (2013) 151915.

[32] Mikhail S. Alekhin, Daniel A. Biner, Karl W. Krämer, Pieter Dorenbos, J. Appl. Phys. 113 (2013) 224904.

[33] E. V. D. van Loef, P. Dorenbos, C. W. E. van Eijk, K. W. Krämer, H. U. Güdel, Phys. Rev. B 68 (2003) 045108.

[34] Yuntao Wu, Qi Li, Daniel J. Rutstrom, Ian Greeley, Luis Stand, Matthew Loyd, Merry Koschan, Charles L. Melcher, Nucl. Instrum. Meth. A 954 (2020) 161242.

[35] E. D. Bourret-Courchesne, G. Bizarri, R. Borade, Z. Yan, S. M. Hanrahan, G. Gundiah, A. Chaudhry, A. Canning, S. E. Derenzo, Nucl. Instrum. Meth. A 612 (2009) 138.

[36] U. Shirwadkar, R. Hawrami, J. Glodo, E. V. D. van Loef, K. S. Shah, IEEE T. Nucl. Sci. 60 (2013) 1011.

[37] L. A. Boatner, J. O. Ramey, J. A. Kolopus, R. Hawrami, W. M. Higgins, E. van Loef, J. Glodo, K. S. Shah, Emmanuel Rowe, Pijush Bhattacharya, Eugene Tupitsyn, Michael Groza, Arnold Burger, N. J. Cherepy, S. A. Payne, J. Cryst. Growth 312 (2010) 1213.

[38] Mikhail S. Alekhin, Daniel A. Biner, Karl W. Krämer, Pieter Dorenbos, J. Lumin. 145 (2014) 723.

[39] Johan T. M. de Haas, Pieter Dorenbos, IEEE T. Nucl. Sci. 55 (2008) 1086.

[40] W. Bludau, A. Onton, W. Heinke, J. Appl. Phys. 45 (1974) 1846.

[41] R. Korde, L.R. Canfield, B. Wallis, Proc. SPIE 0932 (1988) 153.

[42] A. M. Saad, Can. J. Phys. 80 (2002) 1601.

[43] M. D. Birowosuto, P. Dorenbos, K. W. Krämer, H. U. Güdel, J. Appl. Phys. 103 (2008) 103517.

[44] Weronika Wolszczak, Karl W. Krämer, Pieter Dorenbos, Phys. Status Solidi R. 13 (2019) 1900158.

[45] G. Zappalà, F. Acerbi, A. Ferri, A. Gola, G. Paternoster, N. Zorzi, C. Piemonte, J. Instrum. 11 (2016) P08014.

[46] Fabio Acerbi, Stefan Gundacker, Nucl. Instrum. Meth. A 926 (2019) 16.

[47] S. Vinogradov, Nucl. Instrum. Meth. A 1045 (2023) 167596.

[48] Mikhail S. Alekhin, Johan T. M. de Haas, Karl W. Krämer, Pieter Dorenbos, IEEE T. Nucl. Sci. 58 (2011) 2519.

[49] Mikhail S. Alekhin, Karl W. Krämer, Pieter Dorenbos, Nucl. Instrum. Meth. A 714 (2013) 13.

[50] Daniel Rutstrom, Luis Stand, Merry Koschan, Charles L. Melcher, Mariya Zhuravleva, J. Lumin. 216 (2019) 116740.

[51] L. Stand, M. Zhuravleva, G. Camarda, A. Lindsey, J. Johnson, C. Hobbs, C. L. Melcher, J. Cryst. Growth 439 (2016) 93.

[52] Kan Yang, Mariya Zhuravleva, Charles L. Melcher, Phys. Status Solidi R 5 (2011) 43.

[53] P. Dorenbos, J. Phys. Condens. Mat. 15 (2003) 575.

[54] Mikhail S. Alekhin, Roy H. P. Awater, Daniel A. Biner, Karl W. Krämer, Johan T. M. de Haas, Pieter Dorenbos, J. Lumin. 167 (2015) 347.

[55] R. H. P. Awater, M. S. Alekhin, D. A. Biner, K. W. Krämer, P. Dorenbos, J. Lumin. 212 (2019) 1.

2

The role of Yb^{2+} as a scintillation sensitiser in the near-infrared scintillator $CsBa_2I_5:Sm^{2+}$

The feasiblity of using Yb^{2+} as a scintillation sensitiser for $CsBa_2I_5:Sm^{2+}$ near-infrared scintillators has been assessed. $CsBa_2I_5$ samples with concentrations ranging from 0.3% to 2% Yb^{2+} and 0 to 1% Sm^{2+} have been studied. The scintillation properties have been determined and the dynamics of the scintillation mechanism have been studied through photoluminescence measurements. Radiationless energy transfer between Yb^{2+} ions plays a key role in increasing the ratio between the spin-forbidden and spin-allowed emission with increasing Yb^{2+} concentration in samples where Yb^{2+} is the only dopant. In samples co-doped with Sm^{2+}, the Yb^{2+} $4f^{13}[^2F_{7/2}]5d_1$ [LS] and $4f^{13}[^2F_{7/2}]5d_1$ [HS] states both serve as donor states for radiationless energy transfer to Sm^{2+} with a rate of energy transfer that is inversely proportional to the luminescence lifetime the respective donor states. At a Sm^{2+} concentration of 1%, 85% of the Yb^{2+} excitations are transferred to Sm^{2+} through radiationless energy transfer. Almost all of the remaining Yb^{2+} emission is reabsorbed by Sm^{2+}, resulting in nearly complete energy transfer.

The content of this chapter is based on the following publication:
Casper van Aarle, Karl W. Krämer, Pieter Dorenbos, J. Lumin. 238 (2021) 118257.

2.1. Introduction

In the past two decades, extensive scintillation research has been performed on Ce^{3+} and Eu^{2+}-doped halides [1]. The best energy resolution that has been measured to date is 2.0% and was achieved by Alekhin et al. with $LaBr_3$:Ce^{3+},Sr^{2+}. The energy resolution of $LaBr_3$:Ce^{3+},Sr^{2+} is almost entirely determined by Poisson statistics in the number of detected photons [2]. Attaining an energy resolution below 2% thus requires a scintillator with a light yield superior to that of $LaBr_3$:Ce^{3+} (60,000 ph/MeV [3]) paired with a detector with high quantum efficiency. Additionally, the scintillator needs to have a proportional response to different γ-ray energies.

The light yield and proportionality requirements are satisfied by some Eu^{2+}-doped halide scintillators, such as $CsBa_2I_5$:Eu^{2+} and SrI_2:Eu^{2+}. $CsBa_2I_5$:Eu^{2+} shows an energy resolution of 2.3% [4] with a light yield of 100,000 ph/MeV [5] and SrI_2:Eu^{2+} shows an energy resolution of 2.7% with a light yield of 115,000 ph/MeV [6]. After absorption of a 1 MeV photon, approximately 100,000 electron hole pairs are created in these scintillators [7], indicating that the probability of the creation of an electron hole pair resulting in an excitation of Eu^{2+} is near unity. Despite this great performance, Eu^{2+}-doped scintillators often suffer from self-absorption, making them less suitable in applications where large crystals are required [8–11].

The problem of self-absorption in Eu^{2+} can be circumvented by co-doping these scintillators with Sm^{2+}. Eu^{2+} is then used as a scintillation sensitiser. Excitation energy of Eu^{2+} is transferred to Sm^{2+}, after which Sm^{2+} emission is observed from any of the $4f^5 5d \rightarrow 4f^6[^7F_J]$ transitions. As absorption only happens from the $4f^6[^7F_0]$ ground state, emissive transitions to the $4f^6[^7F_{1-6}]$ states reduce the probability of self-absorption [1, 12]. If excitations from Eu^{2+} are transferred with high efficiency to Sm^{2+}, the characteristic high light yield of Eu^{2+} doped scintillators is retained. The resulting near-infrared emission from Sm^{2+} can be detected by an avalanche photodiode (APD) with an almost 100% quantum efficiency [13]. Using this approach, Wolszczak et al. measured an energy resolution of 3.2% with $CsBa_2I_5$:2%Eu^{2+},1%Sm^{2+} [14].

In this new class of sensitised scintillators, energy transfer is added as an additional step to the scintillation mechanism. Energy transfer can be separated into two distinct mechanisms, radiative energy transfer and radiationless energy transfer. Radiationless energy transfer is described by Förster-Dexter theory. The probability of energy transfer from a sensitiser's donor state to an acceptor state through dipole-dipole interactions can be described by equation 2.1 [15]:

$$P_{da}(dd) = \frac{3\hbar^4 c^4 Q_a}{4\pi R^6 n^4 \tau_d} \int \frac{f_d(E) F_a(E)}{E^4} dE \tag{2.1}$$

Here, $\hbar$ is the reduced Planck constant, c is the speed of light in vacuum, n is the host compounds refractive index and E denotes energy. R is the distance between the sensitiser and acceptor ions. $f_d(E)$ is the spectral shape of the donor state's emission band and $F_a(E)$ is the spectral shape of the acceptor state's absorption band. The integral is only non-zero if part of the donor state's emission band overlaps with the acceptor state's absorption band. Q_a is the integral over energy of the absorption cross section of the acceptor's absorption band and τ_d is the luminescence decay time of the donor state.

The criterium for radiationless energy transfer is the presence of overlap between the sensitiser's emission spectrum and the acceptor's excitation spectrum. When this criterium is met, radiationless energy transfer from the sensitiser to the acceptor competes with luminescence from the sensitiser's donor state. As the probability of radiationless energy transfer scales with R^{-6}, sensitiser ions close to acceptor ions return to the ground state at a higher rate than those further away [16]. This causes the donor decay time profile to become non-exponential, with faster decay at the beginning and gradually converging to the intrinsic luminescence decay time of the donor [17–19].

When the sensitiser's emission spectrum and the acceptor's excitation spectrum overlap, emission from the sensitiser can also be reabsorbed by the acceptor. This is radiative energy transfer. Sm^{2+} doped in $CsBa_2I_5$ strongly absorbs across the entire optical spectrum, making millimeter-sized crystals of $CsBa_2I_5$:2%Eu^{2+},1%Sm^{2+} already completely opaque [14]. Eu^{2+} emission originating from deep inside the sample will be completely reabsorbed by Sm^{2+}. Only Eu^{2+} emission that originates near the edge of the sample can escape it. Radiative energy transfer thus further increases the fraction of excitations that are transferred from Eu^{2+} to Sm^{2+}. $CsBa_2I_5$:2%Eu^{2+},1%Sm^{2+} is transparent in the near-infrared, so the Sm^{2+} emission is able to exit the sample without being reabsorbed.

Recently, Yb^{2+} has gained in interest as an alternative to Eu^{2+}. Yb^{2+} has a higher atomic number and smaller ionic radius than Eu^{2+} [20], which increases the scintillator's stopping power of γ-rays when introduced in high concentrations. Scintillation properties have been reported for Yb^{2+}-doped $CsBa_2I_5$ [21], SrI_2 [21, 22], $SrCl_2$ [23], Cs_4CaI_6 and Cs_4SrI_6 [24]. All of these have light yields reported between 40,000 and 60,000 ph/MeV. The best energy resolution of 3.5% has been achieved with Cs_4CaI_6:1%Yb^{2+}.

Owing to its full $4f^{14}$ subshell, Yb^{2+} does not have any 4f-4f transitions. When exciting an electron to the 5d subshell, the spin-orbit interaction of the remaining $4f^{13}$ core causes a splitting of the $4f^{13}5d$ energy level into $4f^{13}[^2F_{7/2}]5d$ and $4f^{13}[^2F_{5/2}]5d$, referred to as the LS-splitting. The $^2F_{5/2}$ level lies at approximately 10,000 cm^{-1} higher energy than the $^2F_{7/2}$ level [25]. Due to the crystal field interaction with the 5d electron, the $4f^{13}[^2F_{7/2}]5d$ and $4f^{13}[^2F_{5/2}]5d$ levels each split into 5 new energy levels, which we label $5d_n$ with $n = 1-5$. The size and pattern of the crystal field splitting depends on the coordination number, site symmetry and distance to the surrounding ligands [26]. The total crystal field splitting is defined as the energy difference between the $4f^{13}[^2F_J]5d_1$ and the $4f^{13}[^2F_J]5d_5$ levels. The $4f^{13}$ core and 5d electron both have a spin S=1/2, creating an additional splitting into S=1 (high spin [HS]) and S=0 (low spin [LS]) states, which is named the exchange splitting. Each $4f^{13}[^2F_{7/2}]5d_n$[LS] state lies at approximately 2,000 cm^{-1} higher energy than the corresponding $4f^{13}[^2F_{7/2}]5d_n$[HS] state [25].

Yb^{2+} emission has been observed from the $4f^{13}[^2F_{7/2}]5d_1$[LS] $\rightarrow$ $4f^{14}$ and $4f^{13}[^2F_{7/2}]5d_1$[HS] $\rightarrow$ $4f^{14}$ transitions, which are referred to as the spin-allowed and spin-forbidden emission, respectively. Room temperature decay times reported for the spin-allowed emission lie typically between 0.1 µs and 1 µs. The spin-forbidden emission is several orders of magnitude slower and reported room temperature decay times lie typically between 100 µs and 1000 µs [22, 27, 28]. These long decay times cause most of the light to be emitted outside the time window of light collection used in γ-ray spectroscopy, thus making it too slow for scintillator applications. Additionally, the ratio between spin-allowed to spin-forbidden emission is found to decrease with increasing

Yb^{2+} concentration in $SrCl_2$ [23], Cs_4CaI_6 and Cs_4SrI_6 [24]. This likely prevents the use of dopant concentrations as high as has often found to be optimal for Eu^{2+} doped halides.

It is often observed that with increase of temperature, the intensity of the spin-allowed emission decreases while simultaneously the intensity of the spin-forbidden increases. This has been attributed to multiphonon relaxation from the $4f^{13}[^2F_{7/2}]5d_1$[LS] state to the $4f^{13}[^2F_{7/2}]5d_1$[HS] state [28]. The temperature at which this thermal relaxation process becomes competitive with the spin-allowed emission strongly depends on the type of anion, being approximately 50 K for fluorides, 200 K for chlorides and 400 K for iodides [29].

Figure 2.1 shows the vacuum referred binding energy (VRBE) diagram of $CsBa_2I_5$. The arrows indicate the energy of the transitions that have been reported, from left to right: band gap excitation [10], Sm^{2+} $4f^6 \rightarrow 4f^5$5d excitation, Sm^{2+} $4f^5$5d $\rightarrow 4f^6$ emission [14], Eu^{2+} $4f^7 \rightarrow 4f^6$5d excitation, Eu^{2+} $4f^6$5d $\rightarrow 4f^7$ emission [10], Yb^{2+} spin-allowed excitation band (this work) and Yb^{2+} spin-allowed emission band [21].

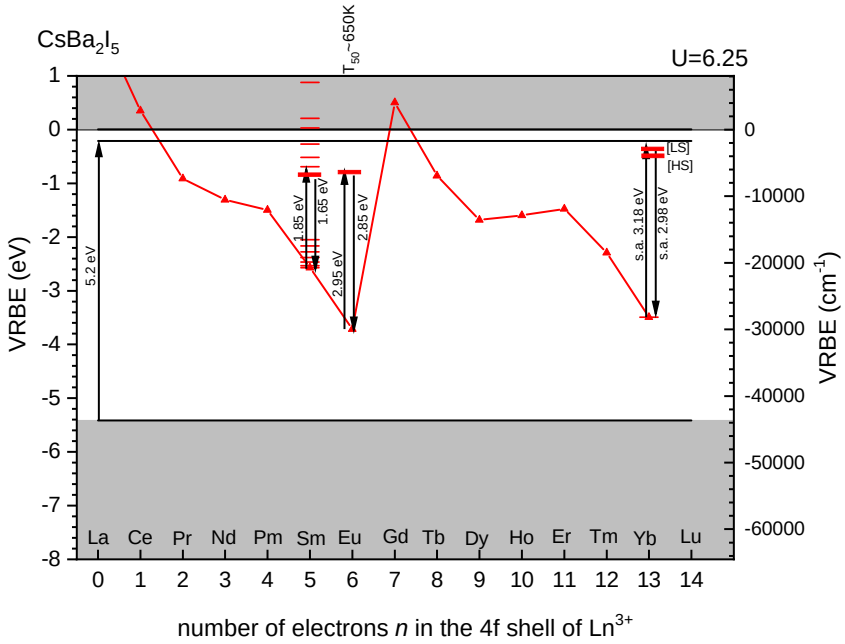

Figure 2.1: VRBE diagram of $CsBa_2I_5$, constructed by the method described in [35]. The parameters used for constructing this diagram are U = 6.25 eV, E_{ex} = 5.2 eV, E_{CT} = 1.7 eV, $\alpha(2+)$ = 0.095, $\beta(2+, A)$ = 0.906 [35]. The U value has been estimated from other iodide compounds [36]. Values for E_{ex}, the Sm^{2+} and Yb^{2+} transitions are presented in this work. The Eu^{2+} transitions have been observed by Alekhin et al. [10].

In this work the feasibility of using Yb^{2+} as a scintillation sensitiser for $CsBa_2I_5:Sm^{2+}$ scintillators is assessed. The goal is to develop a bright near-infrared scintillator with good energy resolution and reduced self-absorption. For this, samples of $CsBa_2I_5$ with Yb^{2+} concentrations from 0.3% to 5% and Sm^{2+} concentrations from 0% to 1% have been studied for temperatures ranging from 10 K to 550 K. X-ray excited emission spectra have been made to confirm whether most emission comes from Sm^{2+}. The light yield and energy resolution have been determined with ^{137}Cs pulse height spectra. The dynamics of the energy transfer process are studied through spectroscopy and photoluminescence decay time profiles of both Yb^{2+} and Sm^{2+} emission. Additionally, the processes affecting the ratio between Yb^{2+} spin-allowed to spin-forbidden emission are further elaborated on.

2.2. Experimental Techniques

$CsBa_2I_5:Yb^{2+},Sm^{2+}$ crystals were grown by the vertical Bridgman technique. CsI (5N, Alfa) was dried in vacuum at 450 °C. BaI_2 was prepared from $BaCO_3$ (4N7, Alfa), HI acid (57% p.a., Merck KGaA) and NH_4I (3N, Alfa) following the ammonium halide synthetic route. The ternary product was decomposed at 470 °C in vacuum. The obtained BaI_2 was purified by melting at 820 °C and crystallization in a glassy carbon ampoule. YbI_2 and SmI_2 were synthesized from the elements (Yb 4N, Metall Rare Earth Ltd.; Sm 3N, Alfa; I_2 p.a., Merck KGaA). YbI_2 was prepared from stoichiometric amounts of the elements in a silica ampoule sealed under vacuum. The ampoule was slowly heated to 750 °C in a tube furnace with one end protruding out of the furnace to avoid excessive iodine pressure. YbI_2 was purified by melting at 790 °C and crystallization in a silica ampoule. SmI_3 was prepared from stoichiometric amounts of the elements in a silica ampoule sealed under vacuum. The mixture was heated to 500 °C in a tube furnace, as discussed for YbI_2 above. SmI_3 was purified by sublimation in a silica ampoule at 800 °C under vacuum. SmI_2 was synthesized from SmI_3 and Sm in a tantalum ampoule sealed under vacuum which was heated to 900 °C for one day and 660 °C for three days.

For crystal growth stoichiometric quantities of CsI, BaI_2, YbI_2 and SmI_2 were sealed in a silica ampoule under vacuum and heated to 625 °C, above the congruent melting point of $CsBa_2I_5$ at 610 °C. Crystals were grown by slow cooling with 0.1 mm/min. during about ten days. Irregularly shaped crystals of approximately 5 mm in size were cleaved from the boules for spectroscopic investigations. The denoted doping represents the percentage of YbI_2 or SmI_2 replacing BaI_2 in the melt. Since starting materials and products are hygroscopic and sensitive to oxidation, all handling was done under strictly dry and oxygen-free conditions (H_2O and $O_2 < 0.1$ ppm) in glove boxes and sealed sample containers.

Pulse height spectra of $CsBa_2I_5:0.3\%Yb^{2+}$ and $CsBa_2I_5:2\%Yb^{2+}$ were measured using a Hamamatsu R6231-100 PMT operated at a voltage of -600 V. The signal from the PMT is amplified by an integrating pre-amplifier followed by an Ortec 672 spectroscopic amplifier, after which the signal is processed by an Ortec 926 analogue to digital converter. The sample was placed on the entrance window of the PMT without optical coupling grease. The scintillator and entrance window were covered with PTFE tape.

Pulse height spectra of $CsBa_2I_5$:2%Yb^{2+},1%Sm^{2+} were measured with an Advanced Photonix APD (type 630-70-72-510) operated at a voltage of 1575 V and at 260 K. The signal from the APD was amplified by a Cremat CR-112 pre-amplifier. The rest of the electronics are the same as used in the PMT set-up described above. The sample was hovering 1 mm above the APD using the pressed powder method described in [13]. The APD was used without a protective entrance window. For light yield measurements, the location of the photopeak was compared with the peak from direct detection of 17.8 keV X-rays of ^{241}Am.

Photoluminescence emission and excitation spectra were measured using a 450 W Xenon lamp and Horiba Gemini 180 monochromator as excitation source. The emission from the sample passed through an optical filter and Princeton Instruments SpectraPro-SP2358 monochromator before being detected by a Hamamatsu R7600U-20 PMT. The spectra have been corrected for the lamp intensity and the quantum efficiency of the monochromator and PMT.

Photoluminescence decay time profiles have been measured using an EKSPLA NT230 OPO laser as excitation source, with a pulse width of 6 ns and repetition rate of 100 Hz. The emission from the sample passed through an optical filter and Princeton Instruments SpectraPro-SP2358 monochromator before being detected by a Hamamatsu R7600U-20 PMT. The PMT signal was processed using a CAEN DT5730 digitizer.

For all photoluminescence measurements, single crystals of the studied materials were crushed to powder. The hygroscopic material was sealed in gas-tight sample holders with a quartz window. For temperature dependent measurements, the sample holders were mounted on the cold finger of a closed cycle helium cryostat operated at a pressure below 10^{-4} mbar.

X-ray excited emission spectra were measured using an X-ray tube with tungsten anode operated at 80 kV and 1 mm thick copper filter. The emission from the sample passed through a ARC VM504 monochromator before being detected by a Hamamatsu R493-02 PMT. The samples were mounted directly onto the cold finger of a Janis cryostat, which was kept under 10^{-4} mbar during operation.

2.3. Results

2.3.1. X-ray excited luminescence and scintillation properties

Figure 2.2 shows the X-ray excited emission spectra of (a) $CsBa_2I_5$:0.3%Yb^{2+} and (b) $CsBa_2I_5$:2%Yb^{2+} at 300 K. Both samples show broad asymmetric emission between 20,000 cm^{-1} and 25,000 cm^{-1} (curve 1). This emission has been fitted with two Gaussian functions (dashed curves), revealing two emission bands centered around 22,500 cm^{-1} and 24,000 cm^{-1}. Based on comparison with the $4f^6 5d_1 \rightarrow 4f^7$ emission of $CsBa_2I_5$:Eu^{2+} (23,000 cm^{-1}) [10,30], the emission bands in Figure 2.2 are assigned to the spin-allowed $4f^{13}[^2F_{7/2}]5d_1$[LS] $\rightarrow 4f^{14}$ and spin-forbidden $4f^{13}[^2F_{7/2}]5d_1$[HS] $\rightarrow 4f^{14}$ emission. The fit to the spin-allowed emission is narrower than the fit to the spin-forbidden emission. This could in part be due to self-absorption of the spin-allowed emission. Self-absorption makes the spin-allowed emission band narrower and non-Gaussian, but due to the strong overlap between the spin-allowed and spin-forbidden emission bands it is not possible to study their shape in such detail. Despite the difficulty in separating

the emission bands, it can be seen that the ratio between the spin-allowed and spin-forbidden emission is higher in $CsBa_2I_5$:0.3%Yb^{2+} than in $CsBa_2I_5$:2%Yb^{2+}. Figures 2.2c and 2.2d show the X-ray excited emission spectra between 300 K and 450 K. As temperature is increased to 450 K, the intensity of the spin-allowed emission decreases until only spin-forbidden emission is left in both samples.

The X-ray excited emission spectra of $CsBa_2I_5$:2%Yb^{2+},0.5%Sm^{2+}, $CsBa_2I_5$:2%Yb^{2+},1%Sm^{2+} and $CsBa_2I_5$:5%Yb^{2+},1%Sm^{2+} at room temperature are shown in Figure 2.3. All the co-doped samples show almost exclusively near-infrared Sm^{2+} emission between 11,000 cm^{-1} and 15,000 cm^{-1}. The same emission was found by Wolszczak et al. in $CsBa_2I_5$:2%Eu^{2+},1%Sm^{2+} and is assigned to the Sm^{2+} $4f^55d \rightarrow 4f^6$ transition [14]. The low signal to noise ratio and asymmetry of the emission band is caused by its proximity to the low energy sensitivity edge of the PMT. The emission spectra show no 4f-4f emission lines, which was also observed for $CsBa_2I_5$:2%Eu^{2+},1%Sm^{2+} [14]. The inset shows that a small amount of Yb^{2+} emission can still be detected between 20,000 cm^{-1} and 26,000 cm^{-1}, but no distinction can be made between the spin-allowed and spin-forbidden emission.

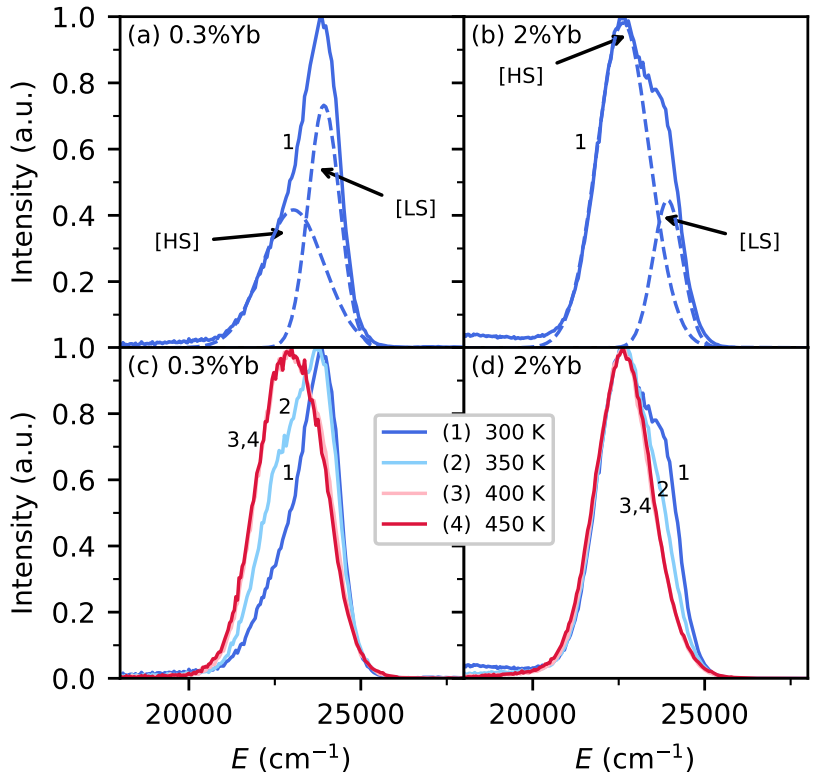

Figure 2.2: X-ray excited emission spectra of (a and c) $CsBa_2I_5$:0.3%Yb^{2+} and (b and d) $CsBa_2I_5$:2%Yb^{2+} at 300 K (a and b) and from 300 K to 450 K (c and d).

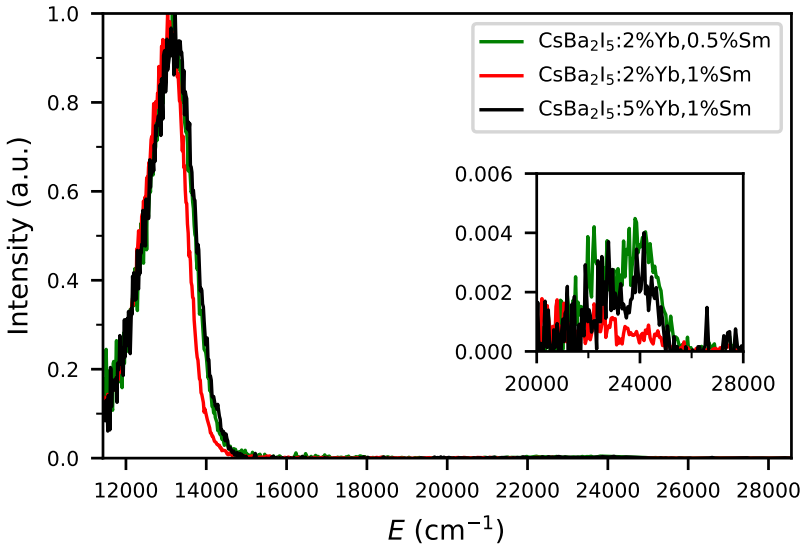

Figure 2.3: X-ray excited emission spectra of $CsBa_2I_5$:2%Yb^{2+},0.5%Sm^{2+}, $CsBa_2I_5$:2%Yb^{2+},1%Sm^{2+} and $CsBa_2I_5$:5%Yb^{2+},1%Sm^{2+}. The inset shows an enlarged view of the spectrum between 20,000 cm^{-1} and 28,000 cm^{-1}.

Figure 2.4a shows the ^{137}Cs pulse height spectrum of $CsBa_2I_5$:0.3%Yb^{2+}. It was measured with a PMT and a shaping time of 10 µs. The light yield has been estimated at 58,000 ph/MeV and an energy resolution of 17.5% was attained. The same PMT and 10 µs shaping time have been used with $CsBa_2I_5$:2%Yb^{2+}, giving a light yield of 39,000 ph/MeV and an energy resolution of 7.2%. About 30% of the light yield is lost when increasing the Yb^{2+} concentration from 0.3% to 2%, although the energy resolution is significantly better.

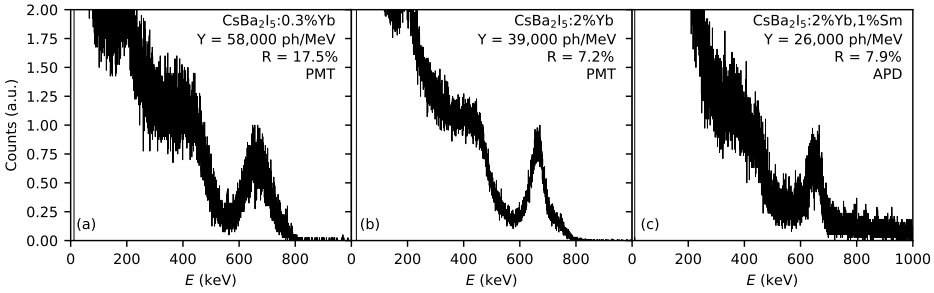

Figure 2.4: Pulse height spectra using a ^{137}Cs γ-source. The light yield Y and energy resolution R of each spectrum are shown as inset. (a) $CsBa_2I_5$:0.3%Yb^{2+} using a PMT as detector, (b) $CsBa_2I_5$:2%Yb^{2+} using a PMT as detector, (c) $CsBa_2I_5$:2%Yb^{2+},1%Sm^{2+} using an APD as detector.

The pulse height spectrum of $CsBa_2I_5$:2%Yb^{2+},1%Sm^{2+} has been measured using an APD and a shaping time of 10 µs. The light yield has been estimated at 26,000 ph/MeV and an energy resolution of 7,9% was attained. A similar decrease in light yield when co-doping with Sm^{2+} was observed for $CsBa_2I_5$:2%Eu^{2+},1%Sm^{2+} [14]. In attempts to create pulse height spectra with $CsBa_2I_5$:2%Yb^{2+},0.5%Sm^{2+} and $CsBa_2I_5$:5%Yb^{2+},1%Sm^{2+}, no clear photopeak could be observed.

2.3.2. Spectroscopy

Figure 2.5 shows photoluminescence excitation and emission spectra of $CsBa_2I_5$:2%Yb^{2+} at 10 K. The emission spectrum (curve 1) shows the spin-forbidden and spin-allowed emission as two bands of approximately equal intensity at 22,200 cm^{-1} and 24,000 cm^{-1}, respectively. The spin-forbidden and spin-allowed emission bands are well resolved at 10 K. Both emissions show the same excitation bands between 25,000 cm^{-1} and 45,000 cm^{-1} (curves 2 and 3). The excitation spectrum of the spin-forbidden emission (curve 3) shows an additional band at 23,800 cm^{-1}, which is therefore assigned to the spin-forbidden $4f^{14} \rightarrow 4f^{13}[^2F_{7/2}]5d_1$[HS] transition.

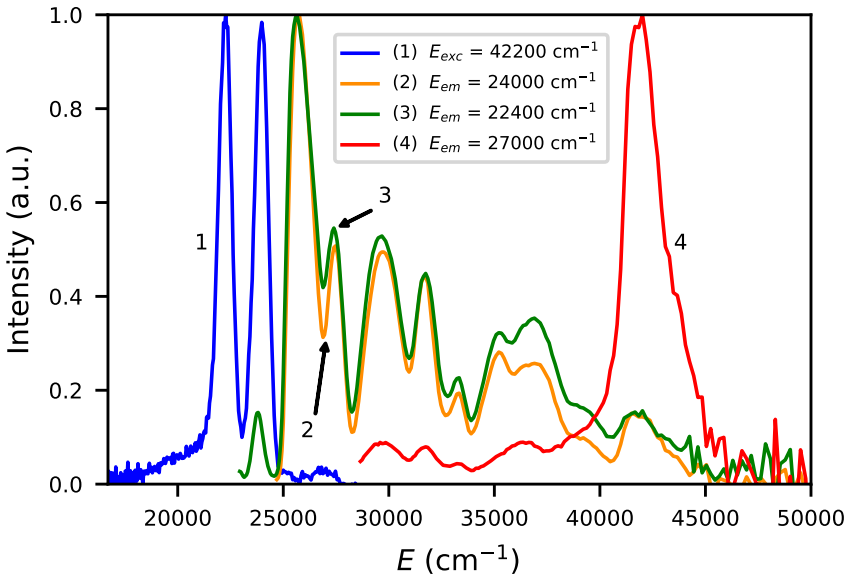

Figure 2.5: Photoluminescence excitation and emission spectra of $CsBa_2I_5$:2%Yb^{2+} at 10 K.

The broad emission band between 17,000 cm^{-1} and 21,000 cm^{-1} (curve 1), the emission band at 27,000 cm^{-1} (curve 1) and excitation band at 42,000 cm^{-1} (curve 4) have all been observed in undoped $CsBa_2I_5$. The emission between 17,000 cm^{-1} and 21,000 cm^{-1} was assigned to near-defect exciton emission, the emission band at 27,000 cm^{-1} was ascribed to self-trapped excitons and the excitation band at 42,000 cm^{-1} corresponds to host exciton creation [10]. The latter has been used for constructing the VRBE diagram in Figure 2.1.

In Figure 2.6, the excitation spectra of the Yb^{2+} spin-allowed and spin-forbidden emission from Figure 2.5 are shown together with an Yb^{2+} energy level scheme created from the data. The values for the LS-splitting, crystal field splitting and exchange splitting can be found on the top side of the figure. The energy and transition assignments of the excitation bands are summarised in table 2.1.

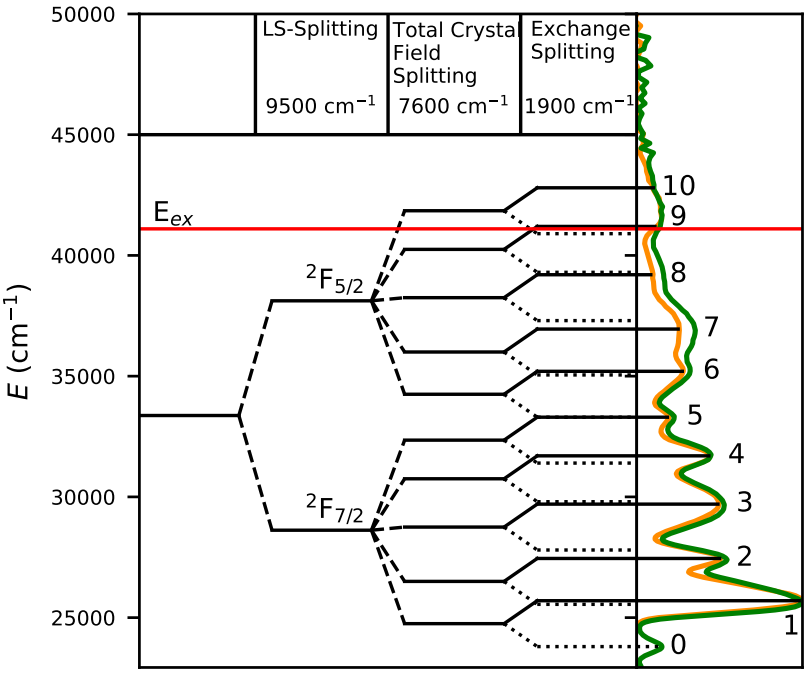

Figure 2.6: Energy level scheme of Yb^{2+} in $CsBa_2I_5$ compared to its photoluminescence excitation spectra at 10 K. The leftmost horizontal line corresponds to the value of the $4f^{13}5d$ absorption bands centroid. It is then split up by the LS-splitting into $4f^{13}[^2F_{7/2}]5d$ and $4f^{13}[^2F_{5/2}]5d$ states. These in turn branch out into 5 different states due to the crystal field splitting of the 5d orbitals. Lastly, the scheme is split up by the exchange splitting. The horizontal lines of the energy level scheme are extended to the corresponding peaks in the absorption spectrum. The energy values of the absorption band peaks are listed in table 2.1.

Band 0 and 1 are assigned to the spin-forbidden $4f^{14} \rightarrow 4f^{13}[^2F_{7/2}]5d_1$[HS] and spin-allowed $4f^{14} \rightarrow 4f^{13}[^2F_{7/2}]5d_1$[LS] transitions, respectively. From this, the value for the exchange splitting of 1,900 cm^{-1} is derived, which is in accordance with the typical value of 2,000 cm^{-1} for iodide compounds [30, 31].

Bands 2 to 5 are assigned to the $4f^{14} \rightarrow 4f^{13}[^2F_{7/2}]5d_{2-5}$[LS] transitions. The transitions to their corresponding [HS] states are not visible in the spectrum due to their lower oscillator strength. The value of the crystal field splitting ϵ_{cfs} is determined by the difference in energy between band 1 and 5, giving a value of 7,600 cm^{-1}. Suta et al. found values of 11,830 cm^{-1} and 10,910 cm^{-1} [31] in $CsCaI_3$:Yb and $CsSrI_3$:Yb, respectively. The approximately equal spacing between bands 1 to 5 suggests that Yb^{2+} is located on a Ba^{2+} site with low symmetry, as a highly symmetric site such as the octahedral coordinated sites in $CsCaI_3$:Yb and $CsSrI_3$:Yb causes the bands to split into two groups, e_g and t_{2g}. Due to the low symmetry of the Ba^{2+} site, the higher coordination number and the larger ionic radius of Ba^{2+} compared to Ca^{2+} and Sr^{2+} [20], the lower value of 7,600 cm^{-1} measured here is expected [26].

Band 6 is assigned to the $4f^{14} \rightarrow 4f^{13}[^2F_{5/2}]5d_1$[LS] transition. The size of the LS-Splitting is determined by the difference between band 1 and band 6, resulting in a value of 9,500 cm^{-1}. This is reasonably close to the 10,000 cm^{-1} LS-splitting of the $4f^{13}$ electrons [31, 32]. In Figure 2.6, the energy of bands 7 to 10 in the energy level scheme are determined by assuming similar crystal field splitting and exchange splitting as observed for the $4f^{13}[^2F_{7/2}]5d_1$ states. This causes accurate alignment with the peaks of bands 7 and 8 in the excitation spectra. Bands 9 and 10 are obscured by the peak corresponding to host exciton creation.

Table 2.1: Energies of the Yb^{2+} excitation bands in $CsBa_2I_5$ measured at 10 K. The numbering of the excitation bands is the same as used in Figure 2.6.

#	Transition	Energy (cm^{-1})
0	$4f^{14} \rightarrow 4f^{13}[^2F_{7/2}]5d_1$[HS]	23,800
1	$4f^{14} \rightarrow 4f^{13}[^2F_{7/2}]5d_1$[LS]	25,700
2	$4f^{14} \rightarrow 4f^{13}[^2F_{7/2}]5d_2$[LS]	27,450
3	$4f^{14} \rightarrow 4f^{13}[^2F_{7/2}]5d_3$[LS]	29,700
4	$4f^{14} \rightarrow 4f^{13}[^2F_{7/2}]5d_4$[LS]	31,700
5	$4f^{14} \rightarrow 4f^{13}[^2F_{7/2}]5d_5$[LS]	33,300
6	$4f^{14} \rightarrow 4f^{13}[^2F_{5/2}]5d_1$[LS]	35,200
7	$4f^{14} \rightarrow 4f^{13}[^2F_{5/2}]5d_2$[LS]	36,950
8	$4f^{14} \rightarrow 4f^{13}[^2F_{5/2}]5d_3$[LS]	39,200
9	$4f^{14} \rightarrow 4f^{13}[^2F_{5/2}]5d_4$[LS]	41,200
10	$4f^{14} \rightarrow 4f^{13}[^2F_{5/2}]5d_5$[LS]	42,800

So far, spectroscopic results are given for samples with only Yb^{2+} doping. In samples containing Sm^{2+}, energy transfer is demonstrated when the Yb^{2+} excitation bands appear in the excitation spectrum of Sm^{2+}. Figure 2.7 shows photoluminescence excitation and emission spectra of $CsBa_2I_5$:2%Yb^{2+},1%Sm^{2+} at 10 K. Curve 1 shows the emission spectrum at 25,700 cm^{-1} excitation, corresponding to the Yb^{2+} spin-allowed $4f^{14} \rightarrow 4f^{13}[^2F_{7/2}]5d_1$[LS] transition. The emission between 12,000 cm^{-1} and 14,000 cm^{-1} is from the Sm^{2+} $4f^5 5d \rightarrow 4f^6$ transition, as was also observed under X-ray excitation (Figure 2.3). Some additional sharp 4f-4f lines are visible at 10 K, but are no longer present at room temperature [33]. The inset shows an enlarged view of the emission between 20,000 cm^{-1} and 25,000 cm^{-1}. The Yb^{2+} spin-forbidden and spin-allowed emission bands can still be observed.

Curve 3 shows the excitation spectrum of the Yb^{2+} emission. The excitation bands are the same as in Figure 2.5, indicating that the chemical environment of Yb^{2+} is the same in the Sm^{2+} co-doped sample as in the sample without Sm^{2+}. Curve 2 is the excitation spectrum of the Sm^{2+} emission. It spans across the entire optical spectrum. Between 25,000 cm^{-1} and 40,000 cm^{-1}, the excitation bands of Yb^{2+} are visible in the excitation spectrum, indicating that energy transfer takes place.

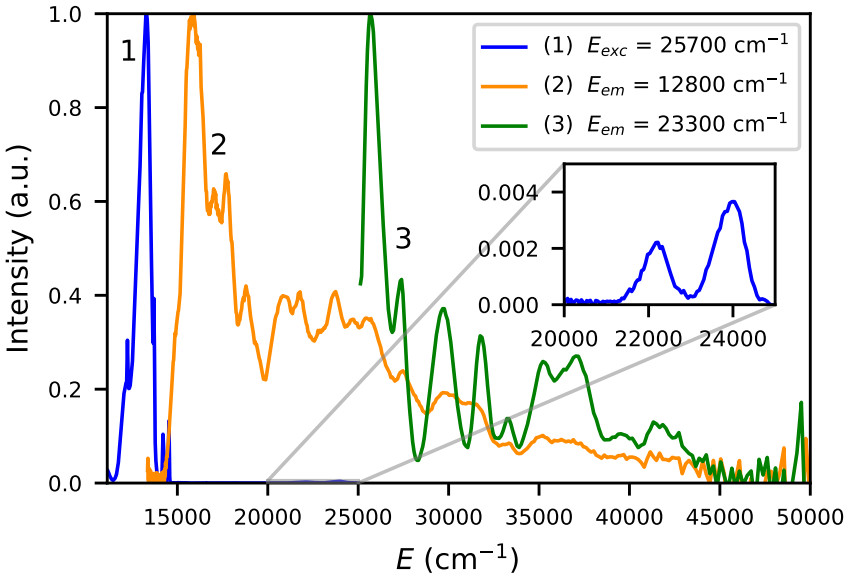

Figure 2.7: Photoluminescence excitation and emission spectra of $CsBa_2I_5$:2%Yb^{2+},1%Sm^{2+} at 10 K. The inset shows an enlarged view of the Yb^{2+} emission between 20,000 cm^{-1} and 25,000 cm^{-1}.

2.3.3. Photoluminescence decay time profiles

Upon excitation at 25,700 cm^{-1}, corresponding to the Yb^{2+} $4f^{14} \rightarrow 4f^{13}[^2F_{7/2}]5d_1$[LS] transition, either spin-allowed emission occurs, or Yb^{2+} relaxes to the $4f^{13}[^2F_{7/2}]5d_1$[HS] state from which the spin-forbidden emission occurs. Additionally, energy can be transferred to Sm^{2+} from both these Yb^{2+} states. 25,700 cm^{-1} photons can also excite Sm^{2+} directly. The dynamics of this system are revealed in the photoluminescence decay time profiles of the Yb^{2+} and Sm^{2+} emissions.

Figure 2.8 shows the photoluminescence decay of $CsBa_2I_5$:0.3%Yb^{2+} (curve 1) and $CsBa_2I_5$:2%Yb^{2+} (curve 2) at room temperature. At this temperature, the spin-allowed and spin-forbidden emission bands strongly overlap, causing both emissions to contribute to the decay time profile. The spin-allowed emission decay time is 0.825 µs for $CsBa_2I_5$:0.3%Yb^{2+}. The spin-allowed emission of $CsBa_2I_5$:2%Yb^{2+} is slightly faster and shows noticable non-exponential behaviour.

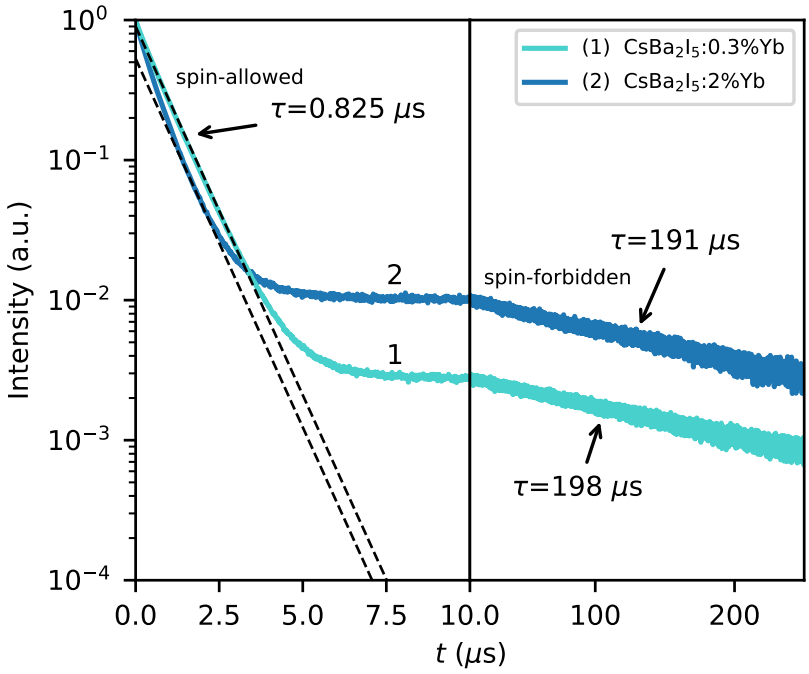

Figure 2.8: Photoluminescence decay time profiles of $CsBa_2I_5$:0.3%Yb^{2+} and $CsBa_2I_5$:2%Yb^{2+} excited at 25,700 cm^{-1} and observed at 24,000 cm^{-1} at room temperature. The left and right side of the figure have different time scales.

The spin-forbidden emission decay times are 198 µs and 191 µs for $CsBa_2I_5$:0.3%Yb^{2+} and $CsBa_2I_5$:2%Yb^{2+}, respectively. This part of the decay time profile is almost perfectly exponential in both samples. The ratio between spin-forbidden to spin-allowed emission intensity is higher in $CsBa_2I_5$:2%Yb^{2+} than in $CsBa_2I_5$:0.3%Yb^{2+}, similar to what is found under X-ray excitation (fig. 2.2).

In samples co-doped with Sm^{2+}, energy is transferred from Yb^{2+} to Sm^{2+}. Photoluminescence decay time profiles of the Yb^{2+} spin-allowed emission in $CsBa_2I_5$:Yb^{2+},Sm^{2+} are shown in Figure 2.9a. Compared to the samples co-doped with Sm^{2+}, $CsBa_2I_5$:2%Yb^{2+} (curve 1) shows almost perfect exponential decay. The Sm^{2+} co-doped samples (curves 2, 3 and 4) show non-exponential decay, indicating that radiationless energy transfer takes place. The rate of energy transfer strongly increases as the Sm^{2+} concentration is increased from 0% (curve 1) to 0.5% (curve 2) to 1% (curve 3), but no significant dependence on the Yb^{2+} concentration is found when comparing $CsBa_2I_5$:2%Yb^{2+},1%Sm^{2+} (curve 3) and $CsBa_2I_5$:5%Yb^{2+},1%Sm^{2+} (curve 4).

For the application as near-infrared scintillator, it is desired that most of the Yb^{2+} excitations are transferred to Sm^{2+}. Radiationless energy transfer competes with Yb^{2+} luminescence. To quantify what fraction of Yb^{2+} excitations is transferred to Sm^{2+} through radiationless energy transfer, the radiationless energy transfer efficiency is estimated using equation 2.2 [18].

$$\eta_{et} = 1 - \frac{\int_0^\infty \Phi_d(t)dt}{\int_0^\infty \Phi_0(t)dt} \tag{2.2}$$

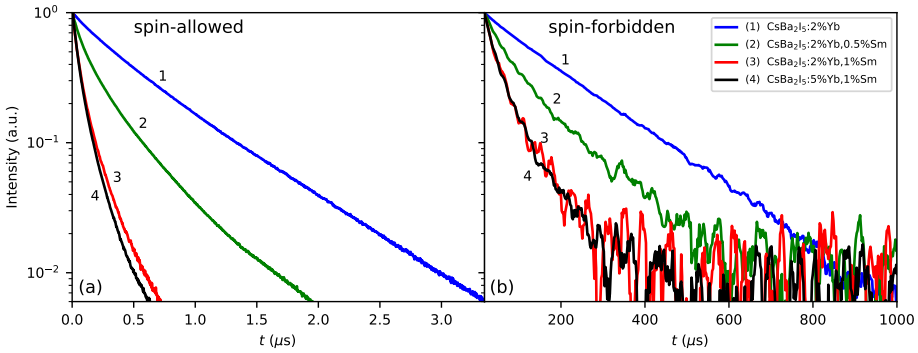

Figure 2.9: Concentration dependent luminescence decay time profiles of Yb^{2+} emission in $CsBa_2I_5$:Yb^{2+},Sm^{2+} after excitation into the $4f^{13}[^2F_{7/2}]5d_1$[LS] state at room temperature. (a): Monitored at the maximum of the $4f^{13}[^2F_{7/2}]5d_1$[LS] → $4f^{14}$ emission at 24,000 cm^{-1}. The decay time profiles are normalised to their value at 0 µs. (b): Monitored at the maximum of the $4f^{13}[^2F_{7/2}]5d_1$[HS] → $4f^{14}$ emission at 22,400 cm^{-1}. The decay time profiles are normalised to their value at 18 µs, chosen as the optimal value to remove the $4f^{13}[^2F_{7/2}]5d_1$[LS] → $4f^{14}$ emission from the image while retaining an almost complete picture of the $4f^{13}[^2F_{7/2}]5d_1$[HS] → $4f^{14}$ decay.

Where $\Phi_d(t)$ is the normalised donor decay time profile and $\Phi_0(t)$ is the normalised decay time profile of the donor without any acceptor ions present. The decay time profile of $CsBa_2I_5$:2%Yb^{2+} (Figure 2.9a curve 1) has been used as an approximation for $\Phi_0(t)$. The estimated radiationless energy transfer efficiencies are 60% for $CsBa_2I_5$:2%Yb^{2+},0.5%Sm^{2+} and 85% for $CsBa_2I_5$:2%Yb^{2+},1%Sm^{2+} and $CsBa_2I_5$:5%Yb^{2+},1%Sm^{2+}.

Figure 2.9b shows the photoluminescence decay time profiles of the Yb^{2+} spin-forbidden emission in $CsBa_2I_5$:Yb^{2+},Sm^{2+}. Similar to Figure 2.9a, $CsBa_2I_5$:2%Yb^{2+} (curve 1) shows almost perfect exponential decay and the decay time profiles of the Sm^{2+} co-doped samples are non-exponential (curves 2, 3 and 4). This shows that radiationless energy transfer also takes place from the Yb^{2+} $4f^{13}[^2F_{7/2}]5d_1$[HS] state to Sm^{2+}. The concentration dependence is nearly identical and thereby the values of the radiationless energy transfer efficiencies are similar. In fact, the only striking difference is the factor of 300 longer timescale of Figure 2.9b compared to Figure 2.9a.

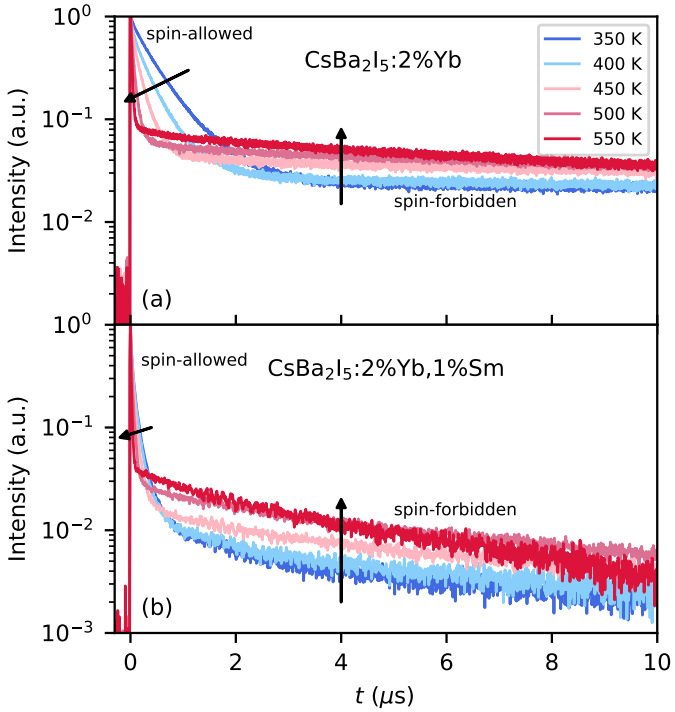

Figure 2.10: Photoluminescence decay time profiles of the Yb^{2+} emission in (a) $CsBa_2I_5$:2%Yb^{2+} and (b) $CsBa_2I_5$:2%Yb^{2+},1%Sm^{2+}. Yb^{2+} is excited in the spin-allowed $4f^{14} \rightarrow 4f^{13}[^2F_{7/2}]5d_1$[LS] excitation band at 25,700 cm^{-1} and monitored at the peak of the spin-forbidden $4f^{13}[^2F_{7/2}]5d_1$[HS] $\rightarrow 4f^{14}$ emission at 22,400 cm^{-1} between 350 K and 550 K.

The photoluminescence decay of the Yb^{2+} emission in $CsBa_2I_5$:2%Yb^{2+} is shown in Figure 2.10a for temperatures between 350 K and 550 K. Similar to Figure 2.8, the fast component is the spin-allowed emission and the slow component is the spin-forbidden emission. When the temperature is increased from 350 K to 550 K, the spin-allowed emission quenches, as seen by rapid shortening of its decay time. Meanwhile, the intensity of the spin-forbidden emission increases.

Figure 2.10b shows the photoluminescence decay of the Yb^{2+} emission in $CsBa_2I_5$:2%Yb^{2+},1%Sm^{2+}. Also here, the spin-allowed emission quenches and the intensity of the spin-forbidden emission increases as temperature is increased from 350 K to 550 K. Both the Yb^{2+} spin-allowed and spin-forbidden decay times are faster than for $CsBa_2I_5$:2%Yb^{2+} in Figure 2.10a. This is due to radiationless energy transfer to Sm^{2+}.

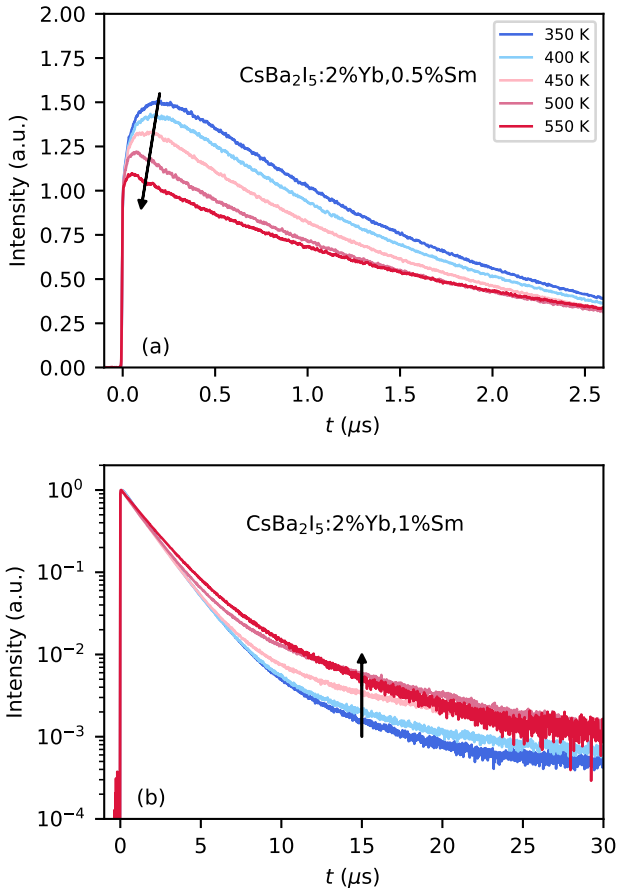

Figure 2.11: Photoluminescence decay time profiles of Sm^{2+} emission excited at 25,700 cm^{-1} and monitored at 13,300 cm^{-1} between 350 K and 550 K. (a) $CsBa_2I_5$:2%Yb^{2+},0.5%Sm^{2+} showing a decrease in energy transfer from the Yb^{2+} $4f^{13}[^2F_{7/2}]5d_1$[LS] state. (b) $CsBa_2I_5$:2%Yb^{2+},1%Sm^{2+} showing an increase in energy transfer from the Yb^{2+} $4f^{13}[^2F_{7/2}]5d_1$[HS] state.

Figure 2.11a shows photoluminescence decay of the Sm^{2+} $4f^5 5d \rightarrow 4f^6$ emission in $CsBa_2I_5$:2%Yb^{2+},0.5%Sm^{2+} excited at 25,700 cm^{-1} between 350 K and 550 K. This energy corresponds to the spin-allowed $4f^{14} \rightarrow 4f^{13}[^2F_{7/2}]5d_1$ [LS] excitation band of Yb^{2+}, meaning that both Yb^{2+} and Sm^{2+} are excited by the laser. The Sm^{2+} ions that are excited directly by the laser will contribute to the intensity of the decay time profile promptly after excitation, while the Sm^{2+} ions that are excited by energy transfer from Yb^{2+} have their contribution delayed. The Sm^{2+} $4f^5 5d \rightarrow 4f^6$ emission decay time profiles are normalised to their value at $t = 0$, keeping the intensity due to direct Sm^{2+} excitation constant. The emission intensity continues to increase in the first 50 to 200 ns after excitation. In this stage, more Sm^{2+} ions are excited by energy transfer from Yb^{2+} than are emitting. The size of this increase in intensity decreases as temperature is raised from 350 K to 550 K.

Figure 2.11b shows the photoluminescence decay of the Sm^{2+} emission in $CsBa_2I_5$:2%Yb^{2+},1%Sm^{2+} between 350 K and 550 K, also excited at 25,700 cm^{-1}. All decay time profiles are normalised to their maximum. The decay time profiles have a slow component at every temperature. The intensity of this slow component increases as temperature is increased from 350 K to 550 K. This indicates that this slow component is caused by slow energy transfer from the $4f^{13}[^2F_{7/2}]5d_1$ [HS] state of Yb^{2+}.

2.4. Discussion

2.4.1. Concentration dependent Yb^{2+} emission

Figures 2.2a and 2.2b show that under X-ray excitation, the ratio of spin-forbidden to spin-allowed emission strongly increases with increasing Yb^{2+} concentration. The same increase in ratio between the spin-forbidden to spin-allowed emission has been observed in Yb^{2+}-doped $SrCl_2$ [23], Cs_4CaI_6 and Cs_4SrI_6 [24]. This phenomenon is also visible in Figure 2.8, where the intensity of the slow component due to spin-forbidden emission is stronger in $CsBa_2I_5$:2%Yb^{2+} than in $CsBa_2I_5$:0.3%Yb^{2+}.

Sekine et al. proposed that self-absorption of the spin-allowed emission causes a concentration dependence of the ratio between spin-forbidden to spin-allowed emission [23]. In this process, spin-allowed emission is reabsorbed by the spin-allowed $4f^{14} \rightarrow 4f^{13}[^2F_{7/2}]5d_1$ [LS] transition of another Yb^{2+} ion. From here, the newly excited Yb^{2+} ion can again decay radiatively, or relax non-radiatively to the $4f^{13}[^2F_{7/2}]5d_1$ [HS] state from which spin-forbidden emission takes place. This self-absorption takes place at the energy where the spin-allowed excitation and spin-allowed absorption bands overlap. Due to the Stokes shift, this is on the high energy side of the spin-allowed emission, which decreases the probability of the spin-allowed emission photons with higher energy exiting the sample. This causes a red-shift of the spin-allowed emission band with increasing Yb^{2+} concentration, which has been observed in $SrCl_2$:Yb^{2+} [23]. This red-shift was not observed for the spin-forbidden emission, as the probability of absorption by the spin-forbidden transition is much lower than by the spin-allowed transition.

Self-absorption causes a photon to be reabsorbed and emitted again at a later time. This causes a lengthening of the observed photoluminescence decay time. The probability of self-absorption scales with the number of Yb^{2+} ions an emitted photon passes on its path leaving the sample, which in turn scales with the samples size and Yb^{2+} concentration [4]. This lengthening of the decay time has been observed in Cs_4CaI_6:Yb^{2+} for

increasing crystal size while keeping the Yb^{2+} concentration constant [24]. However, Figure 2.8 shows that as the Yb^{2+} concentration is increased, the spin-allowed decay time decreases and becomes slightly non-exponential. This indicates that self-absorption cannot be the only process that causes a concentration dependence of the ratio between spin-forbidden to spin-allowed emission.

In Figure 2.5 it is shown that the spin-allowed emission band and the spin-forbidden excitation band overlap at around 24,000 cm^{-1}. According to Förster-Dexter theory, this is the criterium for radiationless energy transfer from the $4f^{13}[^2F_{7/2}]5d_1$[LS] state to the $4f^{13}[^2F_{7/2}]5d_1$[HS] state of another Yb^{2+} ion. The probability of this process scales with the Yb^{2+} concentration. A schematic of this process is depicted in Figure 2.12. The configurational coordinate diagram of a pair of Yb^{2+} ions is shown. Initially, ion 1 is in the $4f^{13}[^2F_{7/2}]5d_1$[LS] state and ion 2 is in the $4f^{14}$ ground state. Radiationless energy transfer from ions 1 to ion 2 is depicted by arrows A. The Stokes shift and exchange splitting have approximately the same value, resulting in arrow A having approximately equal length for ions 1 and 2. After radiationless energy transfer occured, lattice relaxation takes place around both ions (arrows B). The energy dissipated by lattice relaxation makes this process irreversible.

This process also explains the non-exponential decay of the spin-allowed emission in $CsBa_2I_5$:2%Yb^{2+} that is observed in Figure 2.8. The Yb^{2+} $4f^{13}[^2F_{7/2}]5d_1$[LS] state acts as a donor state for the $4f^{13}[^2F_{7/2}]5d_1$[HS] state. The excited Yb^{2+} ions that have many other Yb^{2+} ions nearby have a larger probability of transferring their energy and will on average show a shorter excited state lifetime. With progress of time, the remaining Yb^{2+} ions still in the $4f^{13}[^2F_{7/2}]5d_1$[LS] state are the ones that have no Yb^{2+} ions nearby. This causes the lifetime to become progressively longer as more Yb^{2+} ions decay. The $4f^{13}[^2F_{7/2}]5d_1$[HS] state does not act as a donor state, making its decay time independent of concentration.

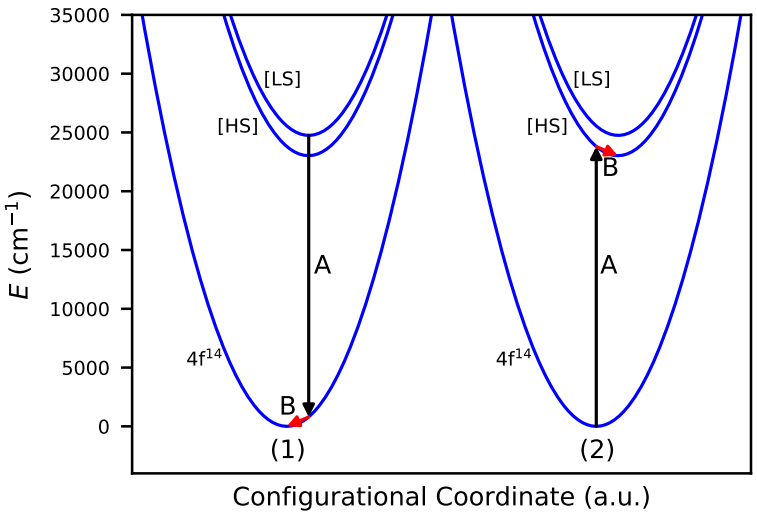

Figure 2.12: Schematic of the energy transfer mechanism from the Yb^{2+} $4f^{13}[^2F_{7/2}]5d_1$[LS] to $4f^{13}[^2F_{7/2}]5d_1$[HS] state.

It is likely that both self-absorption and non-radiative energy transfer between Yb^{2+} ions play a role. Which of the two processes is more prominent depends on the Yb^{2+} concentration and sample size. Both processes change the spin-allowed photoluminescence decay time in opposite directions, but change the ratio between spin-forbidden to spin-allowed emission in the same direction. This allows for a large change in ratio between spin-forbidden and spin-allowed emission intensity while the change in decay time is relatively small.

Figures 2.2c and 2.2d show that the spin-allowed emission quenches when the temperature is increased from 300 K to 450 K until eventually only spin-forbidden emission is left. Quenching of the spin-allowed emission is also observed in Figure 2.10a. This process has been discussed in depth by Suta and Wickleder and is attributed to thermal relaxation from the Yb^{2+} $4f^{13}[^2F_{7/2}]5d_1$[LS] state to the $4f^{13}[^2F_{7/2}]5d_1$[HS] state [29]. Suta and Wickleder found that the temperature at which thermal relaxation becomes competitive with spin-allowed emission depends strongly on type of anion. For iodides this temperature has been observed between 400 K and 500 K [22, 29], which is in agreement with the data presented in Figures 2.2 and 2.10a.

In order to compete with some of the best Eu^{2+}-doped halide scintillators, a light yield of nearly 100,000 ph/MeV is required. This can only be achieved if the luminescence is virtually lossless. Most photons that originate from the spin-forbidden transition will take longer than the shaping time to arrive at the detector. This causes them to be discarded and should be considered lost for applactions in γ-ray spectroscopy. Therefore, the amount of spin-forbidden emission must be kept to a minimum, putting an upper limit on the Yb^{2+} concentration. The best performance of Eu^{2+}-doped halides is often found at Eu^{2+} concentrations between 5% and 10% [8, 10, 34], suggesting that similar Yb^{2+} concentrations would be required to attain optimal results. Therefore, the problem of increasing spin-forbidden emission intensity needs to be addressed to make Yb^{2+}-doped halides competitive with their Eu^{2+}-doped counterparts.

To minimise the spin-forbidden emission, the spin-allowed emission needs to compete more strongly with the relaxation processes from the Yb^{2+} $4f^{13}[^2F_{7/2}]5d_1$[LS] state to the $4f^{13}[^2F_{7/2}]5d_1$[HS] state. This would require careful selection of the proper host material. Thermal relaxation is minimised by choosing a host with low phonon frequencies [29], making iodides the most suitable within the family of halides. Relaxation through energy transfer from the $4f^{13}[^2F_{7/2}]5d_1$[LS] state to the $4f^{13}[^2F_{7/2}]5d_1$[HS] state can be reduced in several ways. One way is to reduce the overlap between the spin-allowed emission band and the spin-forbidden excitation band, i.e. the exchange splitting and Stokes shift need to have different values. Also, a low absorption strength of the Yb^{2+} $4f^{14} \rightarrow 4f^{13}[^2F_{7/2}]5d_1$[HS] excitation band reduces the rate of energy transfer. Lastly, the probability of radiationless energy transfer decreases rapidly with increasing distance between donor and acceptor, so hosts in which the distance between Yb^{2+} sites is relatively large are desired. Additionally, radiationless energy transfer from the Yb^{2+} $4f^{13}[^2F_{7/2}]5d_1$[LS] state to another emission center (e.g. Sm^{2+}) can be used to compete with the relaxation processes to the Yb^{2+} $4f^{13}[^2F_{7/2}]5d_1$[HS] state.

2.4.2. Yb^{2+} as a scintillation sensitiser for Sm^{2+}

Figure 2.13 shows a schematic overview of the energy transfer from Yb^{2+} to Sm^{2+}. The scale of the VRBE scheme in Figure 2.1 has been used. The relevant transitions are based on the results of this article and are further discussed below. The Yb^{2+} spin-allowed (arrow 1) and spin-forbidden emission (arrow 2) and the multiphonon relaxation from the Yb^{2+} $4f^{13}[^2F_{7/2}]5d_1$[LS] state to the $4f^{13}[^2F_{7/2}]5d_1$[HS] state (arrow 3) have been discussed in section 2.4.1.

In samples containing Sm^{2+}, energy transfer from Yb^{2+} to Sm^{2+} takes place. In Figure 2.7 this is shown by the excitation bands of Yb^{2+} (curve 3) being visible in the excitation spectrum of Sm^{2+} (curve 2). In Figure 2.9 it is shown by the photoluminescence decay of Yb^{2+} becoming non-exponential for all samples containing Sm^{2+}. This happens for both the spin-allowed (Figure 2.9a) and spin-forbidden (Figure 2.9b) emissions, meaning radiationless energy transfer takes place from both the Yb^{2+} $4f^{13}[^2F_{7/2}]5d_1$[LS] and $4f^{13}[^2F_{7/2}]5d_1$[HS] states. Energy transfer from the $4f^{13}[^2F_{7/2}]5d_1$[LS] state to Sm^{2+} is depicted in Figure 2.13 by arrows 4. Energy transfer from the $4f^{13}[^2F_{7/2}]5d_1$[HS] state is depicted by arrows 5.

The photoluminescence decay of the Yb^{2+} spin-allowed emission in Figure 2.9a is approximately 300 times faster than the spin-forbidden emission in Figure 2.9b. This is even the case for the samples containing Sm^{2+} where the Yb^{2+} decay is non-exponential, indicating not only luminescence, but also radiationless energy transfer to Sm^{2+} is 300 times faster from the $4f^{13}[^2F_{7/2}]5d_1$[LS] state than from the $4f^{13}[^2F_{7/2}]5d_1$[HS] state. This is predicted by Förster-Dexter theory, as the probability of energy transfer scales with the inverse of the intrinsic luminescence lifetime of the donor state τ_d (equation 2.1).

Both Yb^{2+} donor states have approximately the same energy transfer efficiency. When co-doped with 1% Sm^{2+}, already about 85% of the Yb^{2+} excitations are transferred to Sm^{2+} through radiationless energy transfer. Figure 2.3 shows that the $CsBa_2I_5$:Yb^{2+},Sm^{2+} samples show almost exclusively Sm^{2+} $4f^55d \rightarrow 4f^6[^7F_J]$ emission (arrows 6 in Figure 2.13) under X-ray excitation. The combination of radiationless and radiative energy transfer results in almost complete transfer of energy from Yb^{2+} to Sm^{2+} at a Sm^{2+} concentration low enough to not cause significant self-absorption.

The lifetime of the Sm^{2+} $4f^55d$ state is 2.1 µs in $CsBa_2I_5$ [14], which is longer than the lifetime of the Yb^{2+} $4f^{13}[^2F_{7/2}]5d_1$[LS] state. Because of this, energy transfer from the Yb^{2+} $4f^{13}[^2F_{7/2}]5d_1$[LS] state to Sm^{2+} causes a contribution to the Sm^{2+} emission decay that has a rise time (Figure 2.11a). As temperature is increased from 350 K to 550 K, the intensity of this contribution decreases. This happens at the same temperature as the Yb^{2+} spin-allowed emission quenches due to thermal relaxation in samples not containing Sm^{2+}, indicating that the contribution with rise time is caused by radiationless energy transfer from the Yb^{2+} $4f^{13}[^2F_{7/2}]5d_1$[LS] state to Sm^{2+}.

Radiationless energy transfer from the Yb^{2+} $4f^{13}[^2F_{7/2}]5d_1$[HS] state to Sm^{2+} is not fast enough to make the lifetime of the Yb^{2+} $4f^{13}[^2F_{7/2}]5d_1$[HS] state shorter than the lifetime of the Sm^{2+} $4f^55d$ state. This causes energy transfer from the Yb^{2+} $4f^{13}[^2F_{7/2}]5d_1$[HS] state to create a slow component in the Sm^{2+} emission (fig. 2.11b). As temperature is increased from 350 K to 550 K, the intensity of the slow component increases. Thermal relaxation from the Yb^{2+} $4f^{13}[^2F_{7/2}]5d_1$[LS] to $4f^{13}[^2F_{7/2}]5d_1$[HS] state increases the amount of energy transferred to Sm^{2+} from the $4f^{13}[^2F_{7/2}]5d_1$[HS] state.

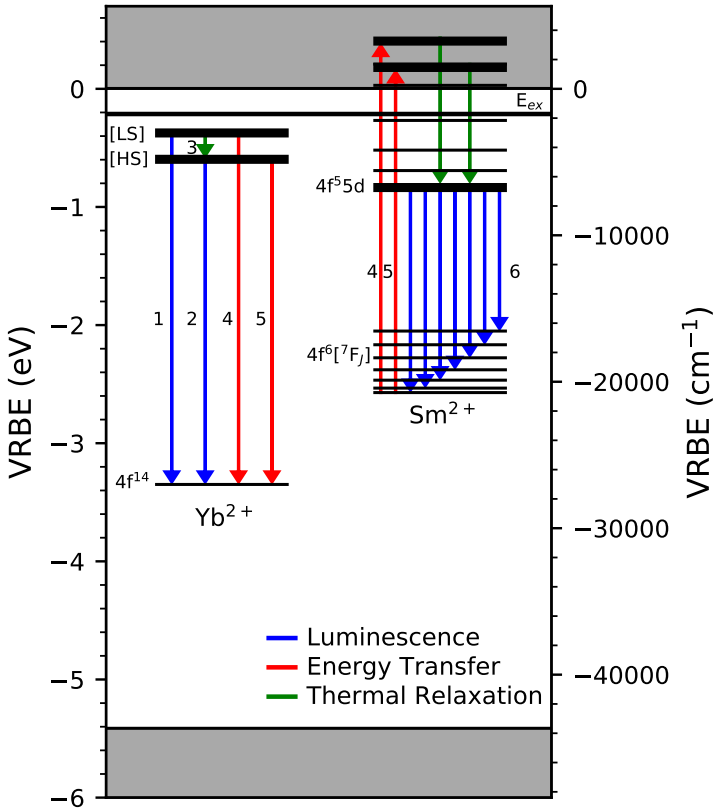

Figure 2.13: Schematic overview of the energy transfer from Yb^{2+} to Sm^{2+}. The energy scale is identical to that of Figure 2.1. The arrows indicate the transitions discussed in this work: (1) Yb^{2+} spin-allowed emission, (2) Yb^{2+} spin-forbidden emission, (3) Thermal relaxation from the Yb^{2+} $4f^{13}[^2F_{7/2}]5d_1$[LS] to $4f^{13}[^2F_{7/2}]5d_1$[HS] state, (4) Energy transfer from the Yb^{2+} $4f^{13}[^2F_{7/2}]5d_1$[LS] state to Sm^{2+}, (5) Energy transfer from the Yb^{2+} $4f^{13}[^2F_{7/2}]5d_1$[HS] state to Sm^{2+}, (6) Sm^{2+} $4f^55d \rightarrow 4f^6[^7F_J]$ emission.

Table 2.2 shows an overview of the scintillation properties of $CsBa_2I_5$ with various dopants. All values were obtained using a shaping time of 10 µs. Most of the light emitted in the slow components of the Yb^{2+}-doped samples falls outside this shaping time and does therefore not contribute to the observed light yield, while this would be crucial for achieving an energy resolution below 2%. As a consequence, an energy resolution of 7.9% was attained with $CsBa_2I_5$:2%Yb^{2+},1%Sm^{2+}, as opposed to the energy resolution of 3.2% attained with $CsBa_2I_5$:2%Eu^{2+},1%Sm^{2+} [14]. Just like the Yb^{2+} spin-forbidden emission of $CsBa_2I_5$:Yb^{2+}, the slow component in the Sm^{2+} emission of $CsBa_2I_5$:Yb^{2+},Sm^{2+} originates from population of the Yb^{2+} $4f^{13}[^2F_{7/2}]5d_1$[HS] state. Therefore, solutions found for Yb^{2+}-doped scintillators will likely also be applicable to Sm^{2+} co-doped scintillators.

Table 2.2: Scintillation properties of $CsBa_2I_5$ samples. R denotes the energy resolution of the 662 keV photopeak and Y denotes the corresponding light yield.

Compound	R (%)	Y (ph/MeV)	Detector	Ref.
$CsBa_2I_5:Eu^{2+}$	2.3	100,000	PMT	[4, 5]
$CsBa_2I_5:2\%Eu^{2+},1\%Sm^{2+}$	3.2	45,000	APD	[14]
$CsBa_2I_5:0.3\%Yb^{2+}$	17.5	58,000	PMT	This work
$CsBa_2I_5:2\%Yb^{2+}$	7.2	39,000	PMT	This work
$CsBa_2I_5:2\%Yb^{2+},1\%Sm^{2+}$	7.9	26,000	APD	This work

2.5. Conclusions

The feasibility of using Yb^{2+} as a scintillation sensitiser for $CsBa_2I_5:Sm^{2+}$ near-infrared scintillators has been assessed. $CsBa_2I_5:Yb^{2+}$ is found to show an increasing spin-forbidden to spin-allowed emission ratio as the Yb^{2+} concentration is increased. Radiationless energy transfer from the $4f^{13}[^2F_{7/2}]5d_1$[LS] state to the $4f^{13}[^2F_{7/2}]5d_1$[HS] state of another Yb^{2+} ion is found to play a significant role in this concentration dependent ratio. It is caused by the spin-allowed $4f^{13}[^2F_{7/2}]5d_1$[LS] $\rightarrow 4f^{14}$ emission band overlapping with the spin-forbidden $4f^{14} \rightarrow 4f^{13}[^2F_{7/2}]5d_1$[HS] excitation band. The spin-forbidden emission is too slow for scintillator applications. This problem can be solved by selecting host materials in which these two bands have less overlap.

Photoluminescence decay time profiles of $CsBa_2I_5:Yb^{2+},Sm^{2+}$ have revealed that the $4f^{13}[^2F_{7/2}]5d_1$[LS] and $4f^{13}[^2F_{7/2}]5d_1$[HS] states of Yb^{2+} both serve as donor states for Sm^{2+} emission. The rates of energy transfer are inversely proportional to the intrinsic luminescence lifetime of the respective excited states. This results in energy transfer from the Yb^{2+} $4f^{13}[^2F_{7/2}]5d_1$[HS] state to Sm^{2+} happening on a 100 µs to 1000 µs timescale, causing a slow component in the Sm^{2+} $4f^5 5d \rightarrow 4f^6$ emission. This slow component is also too slow for scintillator applications. As the slow component is of the same origin as the spin-forbidden emission of Yb^{2+}, it is expected that improvements in Yb^{2+}-doped scintillators will also yield better results for their Sm^{2+} co-doped counterparts.

With only 1% Sm^{2+} co-doping, 85% of the excitations on Yb^{2+} are transferred to Sm^{2+} through radiationless energy transfer. Almost all remaining Yb^{2+} emission is reabsorbed by Sm^{2+} as well, resulting in almost 100% energy transfer. This shows that only a low concentration of Sm^{2+} is required to potentially arrive at a near-infrared scintillator with a light yield similar to those of Eu^{2+}-doped halides, while avoiding the self-absorption problem these scintillators face.

2.6. Acknowledgements

This research was subsidised by the TTW/OTP grant no. 18040 of the Dutch Research Council. The authors would like to thank Daniel Biner, Bern, for the synthesis and crystal growth of the materials.

References

[1] Pieter Dorenbos, Opt. Mater. X. 1 (2019) 100021.

[2] M. S. Alekhin, J. T. M. de Haas, I. V. Khodyuk, K. W. Krämer, P. R. Menge, V. Ouspenski, P. Dorenbos, Appl. Phys. Lett. 102 (2013) 161915.

[3] E. V. D. van Loef, P. Dorenbos, C. W. E. van Eijk, K. Krämer, H. U. Güdel, Appl. Phys. Lett. 79 (2001) 1573.

[4] Mikhail S. Alekhin, Karl W. Krämer, Pieter Dorenbos, J. Lumin. 714 (2013) 13.

[5] Gregory Bizarri, Edith D. Bourret-Courchesne, Zewu Yan, Steve E. Derenzo, IEEE T. Nucl. Sci. 58 (2011) 3403.

[6] R. Hawrami, J. Glodo, K.S. Shah, N. Cherepy, S. Payne, A. Burger, L. Boatner, J. Cryst. Growth. 379 (2013) 63.

[7] M.J. Weber, Nucl. Instrum. Meth. A. 527 (2004) 9.

[8] Jarek Glodo, Edgar V. van Loef, Nerine J. Cherepy, Stephen A. Payne, Kanai S. Shah, IEEE T. Nucl. Sci. 57 (2010) 1228.

[9] Yuntao Wu, Mariya Zhuravleva, Adam C. Lindsey, Merry Koschan, Charles L. Melcher, Nucl. Instrum. Meth. A. 820 (2016) 132.

[10] Mikhail S. Alekhin, Daniel A. Biner, Karl W. Krämer, Pieter Dorenbos, J. Lumin. 145 (2014) 723.

[11] L. Stand, M. Zhuravleva, G. Camarda, A. Lindsey, J. Johnson, C. Hobbs, C.L. Melcher, J. Cryst. Growth. 439 (2016) 93.

[12] R.H.P. Awater, M.S. Alekhin, D.A. Biner, K.W. Krämer, P. Dorenbos, J. Lumin. 212 (2019) 1.

[13] Johan T. M. de Haas, Pieter Dorenbos, IEEE T. Nucl. Sci. 55 (2008) 1086.

[14] Weronika Wolszczak, Karl W. Krämer, Pieter Dorenbos, Phys. Status Solidi R. 13 (2019) 1900158.

[15] D. L. Dexter, J. Chem. Phys. 21 (1953) 836.

[16] Marvin J. Weber, Phys. Rev. B. 4 (1971) 2932.

[17] R. G. Bennett, J. Chem. Phys. 41 (1964) 3037.

[18] Mitio Inokuti, Fumio Hirayama, J. Chem. Phys. 43 (1965) 1978.

[19] Eiichiro Nakazawa, Shigeo Shionoya, J. Chem. Phys. 47 (1967) 3211.

[20] R. D. Shannon, Acta Crystallogr. A. 32 (1976) 751.

[21] Emmanuel Rowe, Pijush Bhattacharya, Eugene Tupitsyn, Michael Groza, Arnold Burger, Nerine J.Cherepy, Steve A. Payne, Benjamin W. Sturm, C. Pédrini, IEEE T. Nucl. Sci. 60 (2013) 1057.

[22] Mikhail S. Alekhin, Daniel A. Biner, Karl W. Krämer, Pieter Dorenbos, Opt. Mater. 37 (2014) 382.

[23] Dai Sekine, Yutaka Fujimoto, Masanori Koshimizu, Daisuke Nakauchi, Takayuki Yanagida, Keisuke Asai, Jpn. J. Appl. Phys. 59 (2020) 012005.

[24] Daniel Rutstrom, Luis Stand, Bogdan Dryzhakov, Merry Koschan, Charles L. Melcher, Mariya Zhuravleva, Opt. Mater. 110 (2020) 110536.

[25] Markus Suta, Claudia Wickleder, J. Lumin. 210 (2019) 210.

[26] P. Dorenbos, J. Alloy. Compd. 341 (2002) 156.

[27] Markus Suta, Tim Senden, Jacob Olchowka, Matthias Adlung, Andries Meijerink, Claudia Wickleder, Phys. Chem. Chem. Phys. 19 (2017) 7188.

[28] Taiju Tsuboi, Donald S. McClure, Wing C. Wong, Phys. Rev. B. 48 (1993) 62.

[29] Markus Suta, Claudia Wickleder, Adv. Funct. Mater. 27 (2016) 1602783.

[30] P. Dorenbos, J. Phys. Condens. Mat. 15 (2003) 575.

[31] Markus Suta, Werner Urland, Claude Daul, Claudia Wickleder, Phys. Chem. Chem. Phys. 18 (2016) 13196.

[32] S. Kück, M. Henke, K. Rademaker, Laser Phys. 11 (2001) 116.

[33] W. Wolszczak, K.W. Krämer, P. Dorenbos, J. Lumin. 222 (2020) 117101.

[34] Daniel Rutstrom, Luis Stand, Merry Koschan, Charles L. Melcher, Mariya Zhuravleva, J. Lumin. 216 (2019) 116740.

[35] Pieter Dorenbos, J. Lumin. 222 (2020) 117164.

[36] Pieter Dorenbos, J. Lumin. 135 (2013) 93.

3

Characterisation of Sm^{2+}-doped $CsYbBr_3$, $CsYbI_3$ and $YbCl_2$ for near-infrared scintillator application

Fast energy transfer from Yb^{2+} to Sm^{2+} is a requirement when using Yb^{2+} as a sensitiser for Sm^{2+} emission for near-infrared scintillator applications. This cannot be achieved through dipole-dipole interactions due to the spin-forbidden nature of the involved Yb^{2+} transition, making the rate of energy transfer too slow for application. This work explores whether exploiting the exchange interaction by increasing the Yb^{2+} concentration to 99% is an effective way to increase the rate at which energy is transferred from Yb^{2+} to Sm^{2+}. The scintillation characteristics of $CsYbBr_3$:1%Sm, $CsYbI_3$:1%Sm and $YbCl_2$:1%Sm single crystals were studied through ^{137}Cs excited pulse height spectra, X-ray excited decay and X-ray excited luminescence spectra. An energy resolution of 7% and a light yield of 30,000 ph/MeV was achieved with $CsYbI_3$:1%Sm. Photoluminescence spectroscopy and decay studies were performed to study the band structure and relaxation dynamics.

The content of this chapter is based on the following publication:
Casper van Aarle, Karl W. Krämer, Pieter Dorenbos, J. Lumin. 251 (2022) 119209.

3.1. Introduction

The energy resolution of a scintillator is an important parameter, as it is a measure for how accurately the energy deposited in a scintillation event can be determined [1,2]. It is most commonly defined as the full width at half maximum of the photopeak of ^{137}Cs 662 keV γ-ray detection in a pulse height spectrum. The current best energy resolution was achieved with $LaBr_3$:Ce,Sr, in which the resolution of 2.0% is close to the fundamental limit determined by photon statistics [3]. Its emission wavelength is around 375 nm, which is where most photomultiplier tubes (PMT) have maximum quantum efficiency. As long as scintillation photons cannot be detected with higher efficiency, the only way to go below 2% energy resolution is developing scintillators with a light yield higher than the 70,000 ph/MeV of $LaBr_3$:Ce,Sr.

Some Eu^{2+} doped halides are reported to have such high light yields. For example SrI_2:Eu and $CsBa_2I_5$:Eu have been reported to emit close to 100,000 ph/MeV and energy resolutions of 2.6% and 2.3% have been achieved with these compounds, respectively [4–9]. However, the drawback of these scintillators is that an Eu^{2+} emission photon can often be reabsorbed by other Eu^{2+} ions that the photon encounters when travelling through the crystal [7, 10–13]. This makes Eu^{2+} doped halides less suitable for applications that require large sized crystals. In order to find a scintillator that truly surpasses $LaBr_3$:Ce,Sr, a scintillator must be found that does not have the self-absorption problem of Eu^{2+}.

Sm^{2+} is a possible candidate as a dopant for such a scintillator. When doped in iodides, its $4f^55d \rightarrow 4f^6$ emission lies typically between 720 nm and 900 nm, which can be detected with an avalanche photodiode (APD) with near 100% quantum efficiency. [14]. Its decay time is usually around 2 µs [15, 16], which is fast enough for application in γ-ray spectroscopy. The $4f^55d \rightarrow 4f^6$ transition of Sm^{2+} can end up on any of the $4f^6[^7F_J]$ states, while absorption only takes place from the $4f^6[^7F_0]$ ground state. Because of this, Sm^{2+} doped scintillators experience less self-absorption than their Eu^{2+} doped counterparts [17]. Due to its broad absorption bands across the entire visible spectrum, Sm^{2+} can easily be sensitised by other lanthanides. Dopants with which high light yields have previously been achieved can thus be used to excite Sm^{2+}. Awater et al. have demonstrated that Eu^{2+} excitations can be transferred efficiently to Sm^{2+} in SrI_2 [17]. Eu^{2+} was later used as a scintillation sensitiser by Wolszczak et al., with which an energy resolution of 3.2% was attained in $CsBa_2I_5$:2%Eu,1%Sm [18]. Other attempts have been made using $CsSrI_3$ and BaBrI as host materials [19].

Recently, Yb^{2+} has gained in popularity as a potential alternative to Eu^{2+} as activator for inorganic scintillators [20–24]. Yb^{2+} in the ground state has a full $4f^{14}$ subshell, which means it has no 4f-4f transitions and the first excited state is of the $4f^{13}5d$ configuration. The spin-orbit coupling of the $4f^{13}$ electrons causes splitting of the $4f^{13}5d$ level into two $4f^{13}[^2F_J]5d$ levels, with J=7/2 or J=5/2. The latter lies at approximately 10,000 cm^{-1} higher energy. The crystal field interaction with the 5d causes splitting into 5 energy levels, labelled $5d_n$ with n=1-5. The exchange interaction between the $4f^{13}$ electrons and the electron in 5d causes further splitting into states with spin S=0 or S=1, referred to as the $4f^{13}[^2F_J]5d_n$[LS] and $4f^{13}[^2F_J]5d_n$[HS] states, respectively. The size of the exchange splitting is approximately 2,000 cm^{-1}, with the [LS] state lying at highest energy [25].

Yb^{2+} emission is mostly observed from the spin-forbidden $4f^{13}[^2F_{7/2}]5d_1$[HS] $\rightarrow 4f^{14}$

transition. When thermal relaxation from the $4f^{13}[^2F_{7/2}]5d_1$[LS] to $4f^{13}[^2F_{7/2}]5d_1$[HS] state is slow enough, spin-allowed $4f^{13}[^2F_{7/2}]5d_1$[LS] $\rightarrow$ $4f^{14}$ emission is also observed. The decay times of these emissions are typically around 1 µs for the spin-allowed emission and 1 ms for the spin-forbidden emission [26], the latter being too slow for scintillator applications as it imposes a severe limitation on the maximum achievable count rate.

We recently studied the feasibility of using Yb^{2+} as a scintillation sensitiser for Sm^{2+} in $CsBa_2I_5$ [27]. It was found that energy transfer from Yb^{2+} to Sm^{2+} takes place through the dipole-dipole interaction and energy can be transferred from both the Yb^{2+} $4f^{13}[^2F_{7/2}]5d_1$[HS] and $4f^{13}[^2F_{7/2}]5d_1$[LS] states. As the rate of energy transfer through dipole-dipole interactions scales with the oscillator strength of the involved transitions [28], energy transfer to Sm^{2+} from the Yb^{2+} $4f^{13}[^2F_{7/2}]5d_1$[HS] state is about 200 times slower than that from the $4f^{13}[^2F_{7/2}]5d_1$[LS] state. This resulted in an unwanted slow component in the decay of the Sm^{2+} $4f^5$5d $\rightarrow$ $4f^6$ emission. It was concluded that where Yb^{2+} doped scintillators are held back by the long decay time of the spin-forbidden $4f^{13}[^2F_{7/2}]5d_1$[HS] $\rightarrow$ $4f^{14}$ transition, scintillators that use Yb^{2+} as a scintillation sensitiser suffer from the same problem.

In this work a solution for the slow energy transfer from Yb^{2+} to Sm^{2+} is explored. The rate of radiationless energy transfer from one ion to another scales strongly with the distance R between the two ions. In the case of the dipole-dipole interaction, the rate scales with R^{-6}, whereas the exchange interaction scales as $\exp(-2R/L)$, where L is approximately the Bohr radius of the involved ions [28]. If the Yb^{2+} excitations are located close enough to a Sm^{2+} ion, the rate of energy transfer to Sm^{2+} is much faster. To achieve this, single crystals of $CsYbBr_3$:1%Sm, $CsYbI_3$:1%Sm and $YbCl_2$:1%Sm are studied, which can be viewed as materials in which the Yb^{2+} doping concentration is increased to 99%. $CsYbBr_3$ ($CaTiO_3$ type structure) and $CsYbI_3$ ($GdFeO_3$ type structure) have perovskite structures similar to those of $CsCaBr_3$ and $CsCaI_3$, in which the Yb^{2+} site has a coordination number of 6 [29, 30]. $YbCl_2$ has a SrI_2 type structure where the Yb^{2+} site has a coordination number of 7 [31]. The aim is that the short distance between neighbouring Yb^{2+} ions allows for migration of excitations towards Sm^{2+}.

The energy transfer process is shown schematically in Figure 3.1. Arrow 1 depicts the excitation of an Yb^{2+} ion. Arrows 2 and 3 depict energy transfer over neighbouring Yb^{2+} ions. Due to the forbidden nature of the Yb^{2+} $4f^{13}[^2F_{7/2}]5d_1$[HS] $\rightarrow$ $4f^{14}$ transition, it is expected that the exchange mechanism plays a large role in the migration of Yb^{2+} excitations. Arrow 4 corresponds to the energy transfer from an Yb^{2+} ion to a Sm^{2+} ion, after which energy is lost through thermal relaxation to the lowest energy $4f^5$5d state along arrow 5. Due to the energy loss in the thermal relaxation process, the excitation cannot be transferred back to Yb^{2+}. Finally, Sm^{2+} emission is observed as indicated by arrow 6.

In addition to solving the problem of slow energy transfer from Yb^{2+} to Sm^{2+}, there may be other benefits to using such high Yb^{2+} concentrations. The high Z number and small ionic radius of Yb^{2+} allows to create crystals with more γ-photon stopping power than most Ln^{2+} doped halide scintillators. Additionally, the $4f^{14}$ ground state of Yb^{2+} lies within the band gap. This reduces the minimal energy required to excite an electron to the conduction band and could potentially result in the emission of more photons per absorbed γ-ray energy.

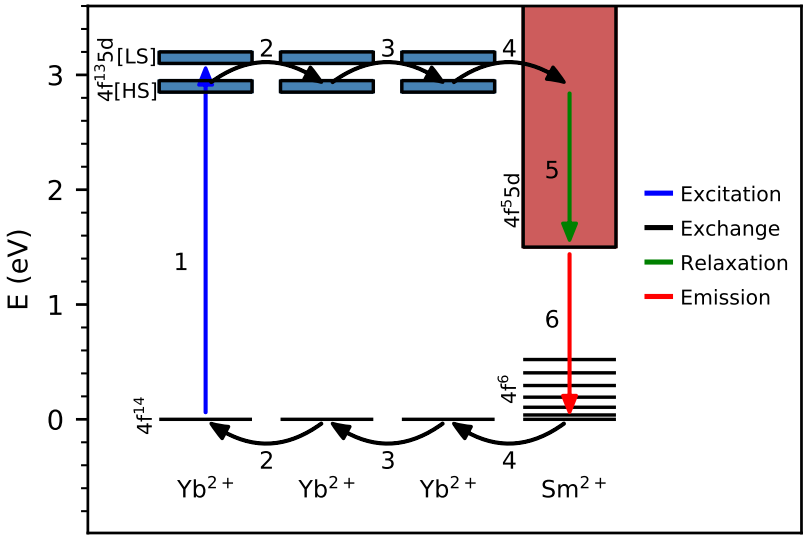

Figure 3.1: Schematic of the energy transfer processes from Yb^{2+} to Sm^{2+}. After initial excitation of an Yb^{2+} ion, the excitation energy migrates over neighbouring Yb^{2+} ions until it is transferred to Sm^{2+} from which emission is observed. The energy scale on the y-axis corresponds to approximate values for the samples studied in this work.

To assess the scintillation performance of the samples, the temperature stability of the scintillators is determined through X-ray excited emission spectra at temperatures ranging from 78 K to 700 K. The room temperature decay times are measured to determine whether the scintillation pulses are fast enough for application. ^{137}Cs excited pulse height spectra have been taken to determine the energy resolution and light yield. Photoluminescence excitation and emission spectra and decay time profiles have been measured to study energy transfer from Yb^{2+} to Sm^{2+}.

3.2. Experimental Techniques

$CsYbBr_3$:1%Sm^{2+}, $CsYbI_3$:1%Sm^{2+}, and $YbCl_2$:1%Sm^{2+} crystals were grown from the binary halides by the vertical Bridgman technique. CsBr (5N, Alfa) and CsI (Merck, suprapur) were dried in high vacuum at 200 °C. YbX_3 with X = Cl, Br were prepared by the ammonium halide method [32]. Yb_2O_3 (6N, Metall Rare Earth Ltd.) and NH_4X (Merck, p.a., sublimed) were dissolved in HX acid (Merck, suprapur) to yield a ternary ammonium rare earth halide, which was dried and decomposed to the YbX_3 halide by heating in vacuum, see equation 3.1.

$$Yb_2O_3 + 7\,NH_4X + HX \rightarrow (NH_4)_3YbX_6 \rightarrow YbX_3 \tag{3.1}$$

For the removal of YbOX traces the YbX_3 halide was sublimed in a sealed Au ampoule in vacuum at 960 °C for $YbCl_3$ and 800 °C for $YbBr_3$. Subsequently, the halide was reduced by Yb metal in a Ta ampoule according to equation 3.2.

$$2\,YbX_3 + Yb \rightarrow 3\,YbX_2 \tag{3.2}$$

The Ta ampoule was sealed under vacuum into a silica ampoule and kept 1 day at 900 °C and 7 days at 750 °C for $YbCl_2$ and 1 day at 970 °C and 7 days at 700 °C for $YbBr_2$.

YbI_2 was prepared from the elements in a silica ampoule sealed under vacuum. Yb (4N, Metall Rare Earth Ltd.) and I_2 (Merck, p.a., sublimed) were slowly heated to 650 °C. One end of the ampoule protruded from the tube furnace to avoid high iodine pressure during the reaction. After the reaction was finished, the ampoule was opened and heated in vacuum to remove excess I_2. The product was sealed in a silica ampoule and purified by Bridgman crystal growth starting at 790 °C.

The samarium halides were prepared by the same methods as described above for ytterbium. SmX_3 were synthesized from Sm_2O_3 (3N, Fluka). $SmCl_3$ was sublimed at 600 °C and $SmBr_3$ at 650 °C in high vacuum. $SmCl_2$ was prepared at 650 °C and $SmBr_2$ at 700 °C using Sm (3N, Alfa). SmI_3 was prepared at 700 °C and sublimed for purification in a silica ampoule under vacuum at 800 °C. The reduction to SmI_2 took place in a Ta ampoule 1 day at 900 °C and 7 days at 600 °C.

The crystal growth was done using a moving furnace and a static ampoule. The stoichiometric mixture of the starting materials was sealed in a Ta ampoule under He by arc welding. The material was molten at 740 °C for $YbCl_2$:1% Sm^{2+}, 680 °C for $CsYbBr_3$:1%Sm^{2+}, and 760 °C for $CsYbI_3$:1%Sm^{2+}. After one day at this temperature, the crystal was grown by moving up the furnace with 0.1 mm/min. During about ten days the sample reached room temperature. Crystals were cleaved from the boules for spectroscopic investigations. The denoted doping level represents the melt composition. Since starting materials and products are highly hygroscopic and sensitive to oxidation, all handling was done under strictly dry and oxygen-free conditions (H_2O and $O_2 < 0.1$ ppm) in glove boxes and sealed sample containers.

X-ray excited luminescence spectra have been measured using an X-ray tube with tungsten anode operated at 79 kV as excitation source. Low energy X-rays were filtered out to avoid radiation damage at the sample surface. The sample was attached to the cold finger of a Janis VPF-700 cryostat. The emission from the sample face of incident X-ray excitation was coupled into an optical fibre and read out with an Ocean Insights QE Pro spectrometer. The optical fibre entrance was placed under a 90°angle with the X-ray tube.

Pulse height spectra were measured with a windowless Advanced Photonix APD (type 630-70-72-510) operated with a 1690 V bias. The temperature of the APD was stabilised at 260 K with two Peltier coolers connected to a Lakeshore 331 temperature controller. The APD output signal was amplified by a Cremat CR-112 pre-amplifier before going into an Ortec 672 spectroscopic amplifier, after which it was read out with an Ortec 926 analog-to-digital converter. The sample was positioned above the PMT surrounded with PTFE powder, using the pressed powder method described by de Haas and Dorenbos [14]. Light yields were determined by comparing the position of the photopeak with the peak generated by 17.8 keV X-rays of ^{241}Am being directly detected by the APD.

X-ray excited decay curves were measured using a time correlated single photon counting method. A PicoQuant LDH-P-C-400M laser diode exciting a Hamamatsu N5084 light excited X-ray tube with tungsten anode operated at 40 kV was used as excitation source. The sample was attached to the cold finger of a Janis VPF-700 cryostat. The sample chamber was kept at a pressure of 10^{-5} mbar to protect hygroscopic samples from exposure to moisture. The scintillation light was detected using an ID Quantique ID100-50 single-photon detector, generating a stop signal. The start and stop signals were processed using an Ortec 567 time-to-amplitude converter of which the output was connected to an Ortec AD413 Quad 8k analog-to-digital converter.

The photoluminescence emission and excitation spectra were measured using a 450 W Xenon lamp as light source. The excitation light passed through a Horiba Gemini 180 monochromator before entering the sample chamber. The emission light from the sample passed through a Princeton Instruments SpectraPro-SP2358 monochromator before being detected by a Hamamatsu R7600-20 PMT. An optical filter was placed between the sample chamber and the emission monochromator to filter out the excitation light. The sample was attached to the cold finger of a closed cycle Helium cryostat.

The photoluminescence decay was measured with an EKSPLA NT230 OPO laser as excitation source. The emission light from the sample passed through a Princeton Instruments SpectraPro-SP2358 monochromator before being detected by a Hamamatsu R7600-20 PMT. The PMT output was read out using a CAEN DT5730 digitiser.

3.3. Results

Figure 3.2a shows the X-ray excited emission spectra of $CsYbBr_3$:1%Sm between 78 K and 700 K. The sample shows broad band emission between 600 nm and 950 nm. Based on comparison with the Eu^{2+} $4f^6 5d \rightarrow 4f^7$ emission in $CsCaBr_3$:Eu located at 433 nm [33], the Sm^{2+} $4f^5 5d \rightarrow 4f^6$ emission is expected at a wavelength of 796 nm [25]. Therefore, the broad emission band is assigned to the Sm^{2+} $4f^5 5d \rightarrow 4f^6$ emission. As temperature is increased from 78 K to 700 K, the emission peak shifts from 790 nm to 765 nm. The strong increase in intensity at 700 K on the long wavelength side of the emission is due to blackbody radiation.

The X-ray excited luminescence spectra of $CsYbI_3$:1%Sm are shown in figure 3.2b. The sample displays a similar wide emission band as $CsYbBr_3$:1%Sm, which is therefore also attributed to the Sm^{2+} $4f^5 5d \rightarrow 4f^6$ emission. In $CsYbI_3$:1%Sm, the Sm^{2+} emission is positioned at about 0.08 eV lower energy compared to $CsYbBr_3$:1%Sm. This is in accordance with the difference between the Eu^{2+} $4f^6 5d \rightarrow 4f^7$ emission energy in $CsCaI_3$:Eu (2.86 eV) [34] and $CsCaBr_3$:Eu (2.78 eV) [33]. Just as in $CsYbBr_3$:1%Sm, the same shift of the Sm^{2+} emission to shorter wavelengths is observed when temperature is increased from 78 K to 700 K.

Figure 3.2c shows the X-ray excited luminescence spectra of $YbCl_2$:1%Sm. The broad emission band between 650 nm and 850 nm is at about 60 nm shorter wavelength compared to $CsYbBr_3$:1%Sm and $CsYbI_3$:1%Sm. As opposed to the Sm^{2+} emission in $CsYbBr_3$:1%Sm and $CsYbI_3$:1%Sm, the Sm^{2+} emission in $YbCl_2$:1%Sm shifts to longer wavelengths when temperature is increased.

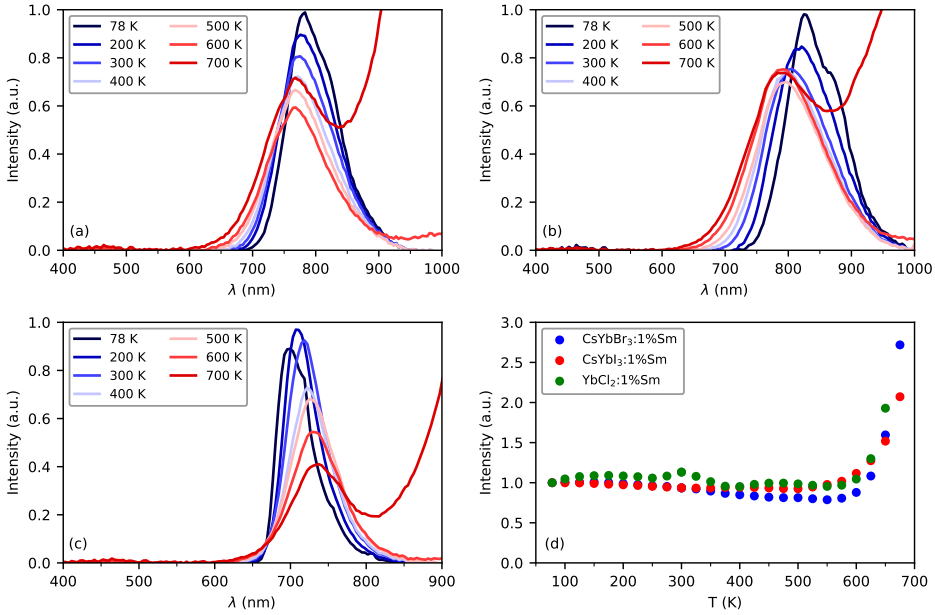

Figure 3.2: X-ray excited emission spectra of (a) $CsYbBr_3$:1%Sm, (b) $CsYbI_3$:1%Sm and (c) $YbCl_2$:1%Sm. (d) shows the emission intensity of all samples integrated from 600 nm to 1000 nm against temperature.

Figure 3.2d shows the emission intensity of all samples integrated from 600 nm to 1000 nm, normalised to the intensity at 78 K. The emission intensity is almost perfectly stable between 78 K and 600 K. The sudden increase at temperatures above 600 K is caused by blackbody radiation overlapping with the Sm^{2+} emission. From figures 3.2a to c it can be seen that even at temperatures up to 700 K, the Sm^{2+} emission does not quench.

The X-ray excited decay curves of all samples are shown in Figure 3.3. The decay curves of $CsYbBr_3$:1%Sm (Fig. 3.3a) and $CsYbI_3$:1%Sm (fig. 3.3b) are fitted with single exponentials with decay times of 2.1 µs and 2.3 µs, respectively. Similar decay times were observed for Sm^{2+} emission in $CsBa_2I_5$:Sm [18] and SrI_2:Sm [17]. It is fast enough for γ-ray spectroscopy as over 99% of the scintillation light is emitted within 10 µs after excitation.

The decay curve of $YbCl_2$:1%Sm (fig. 3.3c) is fitted with a double exponential decay function. The fast component contains 7% of the scintillation light and has a 0.7 µs decay time. The remaining 93% of the scintillation light is emitted in a slow component with decay time of 4.3 µs. With this decay time, 10% of the scintillation light is emitted more than 10 µs after excitation, making the scintillator rather slow for use in γ-ray spectroscopy.

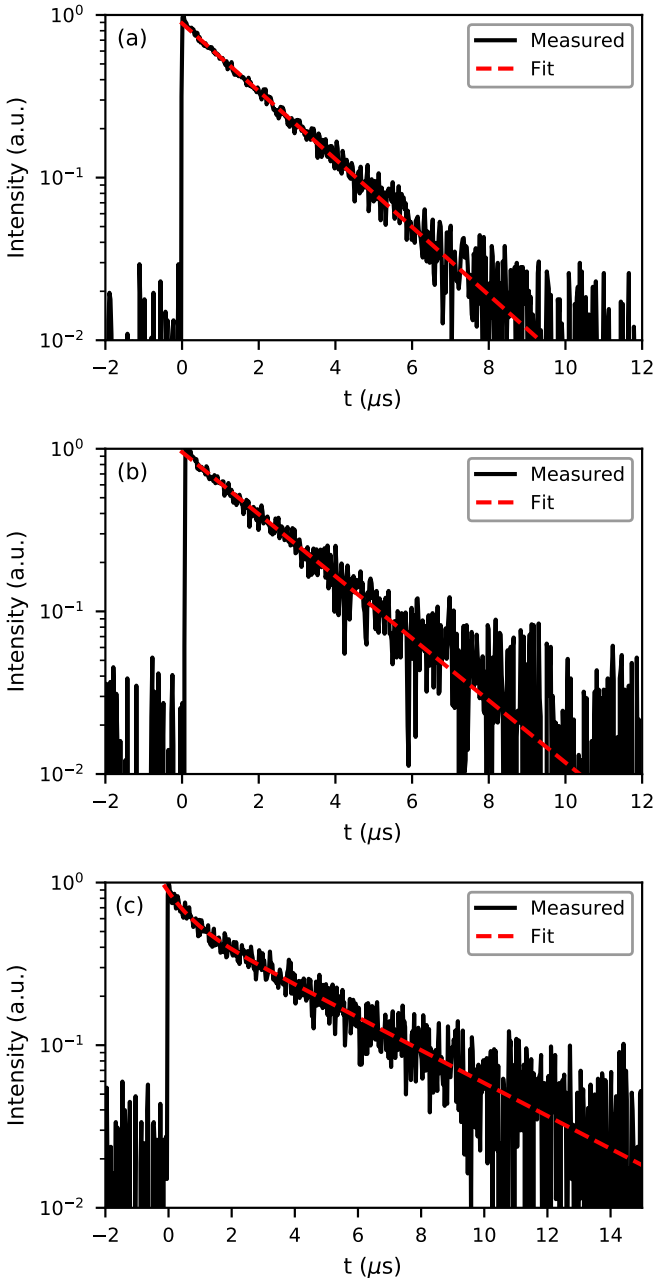

Figure 3.3: X-ray excited decay curves of (a) $CsYbBr_3$:1%Sm, (b) $CsYbI_3$:1%Sm and (c) $YbCl_2$:1%Sm.

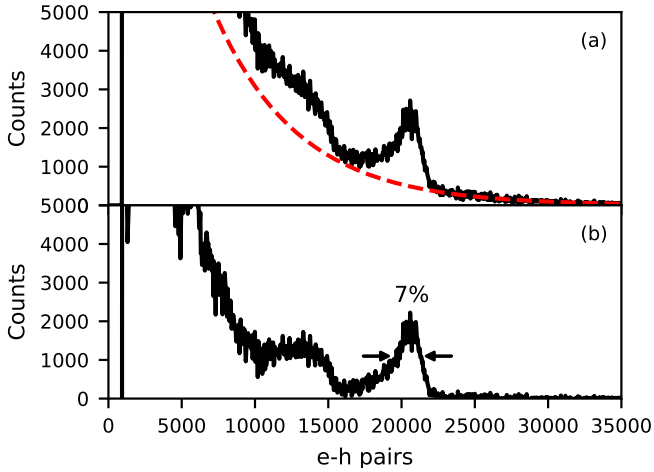

Figure 3.4: Pulse height spectrum of $CsYbI_3$:1%Sm coupled to an APD using a ^{137}Cs γ-ray source. (a) shows the pulse height spectrum as recorded, the red dashed curve indicates an approximate background due to direct γ-ray absorption in the APD, (b) shows the pulse height spectrum after subtraction of the background.

The scintillation performance of the samples was assessed by recording ^{137}Cs excited pulse height spectra with the scintillator crystals coupled to an APD. Only for $CsYbI_3$:1%Sm a photopeak was observed. The result is shown in Figure 3.4a. The x-axis shows the number of primary electron hole pairs created in the APD, which corresponds to the number of photons detected in a scintillation event. In addition to scintillation events, the pulse height spectrum also contains a background of events that originate from the absorption of γ-rays directly in the APD. This background has been roughly approximated with an exponential function, which is depicted by the dotted line. Figure 3.4b shows the pulse height spectrum where this background is subtracted, allowing for easier determination of the energy resolution. Around 20,000 photons are detected in scintillation events that fall in the 662 keV photopeak. The set-up has a quantum efficiency close to 100% at the emission wavelength of $CsYbI_3$:1%Sm [14], therefore the light yield of $CsYbI_3$:1%Sm is estimated to be 30,000 ph/MeV. The FWHM of the photopeak is around 7%.

The photoluminescence emission and excitation spectra of $CsYbBr_3$:1%Sm and $CsYbI_3$:1%Sm at 10 K are shown in Figure 3.5a and 3.5b. They show the same Sm^{2+} emission as the spectra made under X-ray excitation (Fig. 3.2). The slight change in shape of the Sm^{2+} $4f^55d \rightarrow 4f^6$ emission is predominantly caused by the difference in temperature and detector quantum efficiency. The excitation spectrum of the Sm^{2+} emission in both samples displays a shoulder on the long wavelength side of the excitation band around 650 nm. This is often observed as the transition from the Sm^{2+} $4f^6$ ground state to the lowest $4f^55d$ state has a lower oscillator strength than the transition to the $4f^55d$ states that lie at slightly higher energy. Following the notation used by Wood and Kaiser, the shoulder and main excitation band are labelled the Sm A and B bands, respectively. [35].

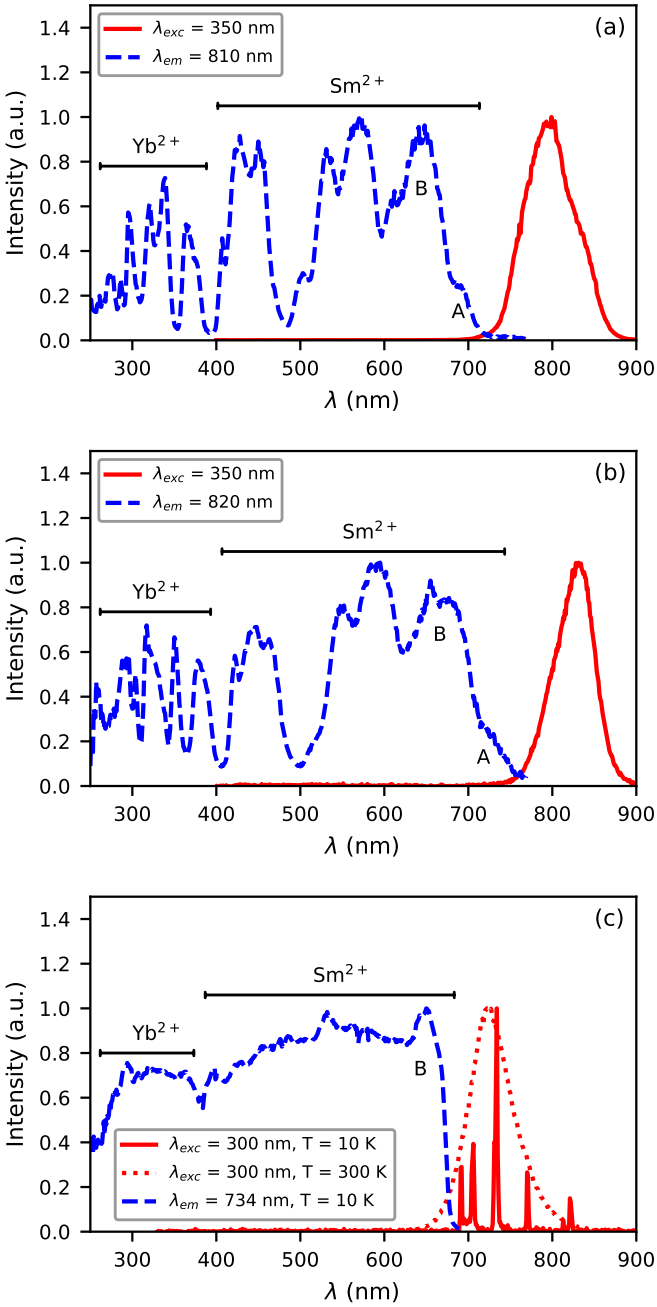

Figure 3.5: Photoluminescence excitation and emission spectra of (a) $CsYbBr_3$:1%Sm, (b) $CsYbI_3$:1%Sm and (c) $YbCl_2$:1%Sm.

Due to the high Yb^{2+} concentration, it is expected that where Yb^{2+} absorbs, the Sm^{2+} excitation bands are not visible in the excitation spectrum. In $CsCaBr_3$:Yb and $CsCaI_3$:Yb, the lowest spin-allowed $4f^{14} \rightarrow 4f^{13}5d$ excitation band of Yb^{2+} is located at 385 nm and 400 nm, respectively [36]. Based on this, the excitation bands between 250 nm and 400 nm are assigned to the $4f^{14} \rightarrow 4f^{13}5d$ transitions of Yb^{2+} for both $CsYbBr_3$:1%Sm and $CsYbI_3$:1%Sm. The position of these excitation bands for $CsYbI_3$:1%Sm is in good agreement with the excitation bands of the intrinsic emission of $CsYbI_3$ measured by Zhao et al. [37] All bands at wavelengths longer than 400 nm are assigned to $4f^6 \rightarrow 4f^5 5d$ transitions of Sm^{2+}.

The emission spectrum of $YbCl_2$:1%Sm (fig. 3.5c) contains exclusively Sm^{2+} $4f^6 \rightarrow 4f^6$ emission at 10 K (solid line), while at 300 K the emission spectrum (dotted line) is entirely $4f^5 5d \rightarrow 4f^6$ emission. This is caused by the $4f^5 5d \rightarrow 4f^6$ emission wavelength of 720 nm being close to the turning point where Sm^{2+} shows exclusively line emission at all temperatures [25]. The excitation spectrum of Sm^{2+} emission in $YbCl_2$:1%Sm emission does not show a detailed structure as $CsYbBr_3$:1%Sm and $CsYbI_3$:1%Sm. In this sample, Yb^{2+} and Sm^{2+} are on a site of low symmetry. The crystal field splitting into five separate 5d levels causes the excitation bands of Sm^{2+} to smear over the entire optical spectrum, similar to what is observed in SrI_2:Sm. [16, 38] The excitation spectrum does not show a resolved Sm A band. Based on the wavelength of the Sm B excitation band, it is estimated that Yb^{2+} starts to absorb around 370 nm.

Upon X-ray excitation, it is unclear what excitation mechanism is most prevalent. Electrons can be excited across the band gap, leaving a hole in the valence band. The small optical band gap of these materials also allows for excitation from the $4f^{14}$ ground state of Yb^{2+} to the conduction band. Eventually, the resulting ionisation should lead to excitation of Sm^{2+}. However, as the Yb^{2+} concentration is much higher than the Sm^{2+} concentration, it is likely that primarily Yb^{2+} is excited and the energy is then transferred to Sm^{2+}. In order to gain insight in the energy transfer from Yb^{2+} to Sm^{2+}, photoluminescence decay curves were measured upon excitation of the divalent lanthanides.

Figure 3.6 shows the photoluminescence decay monitoring the Sm^{2+} emission of (a) $CsYbBr_3$:1%Sm, (b) $CsYbI_3$:1%Sm and (c) $YbCl_2$:1%Sm. The excitation wavelengths are chosen such that a decay trace is recorded when only Sm^{2+} is excited (red curves) and one where almost only Yb^{2+} is excited (blue curves). Even when exciting Yb^{2+}, the Sm^{2+} decay in all 3 compounds is at maximum intensity promptly after excitation. No components with rise time or long decay times are detected. The photoluminescence decay time of $CsYbBr_3$:1%Sm (2.1 µs) and $CsYbI_3$:1%Sm (2.2 µs) correspond well to the decay times under X-ray excitation, as was shown in figure 3.3. The photoluminescence decay time of $YbCl_2$:1%Sm is 5.2 µs, which is slower than the 4.3 µs decay component that was observed under X-ray excitation.

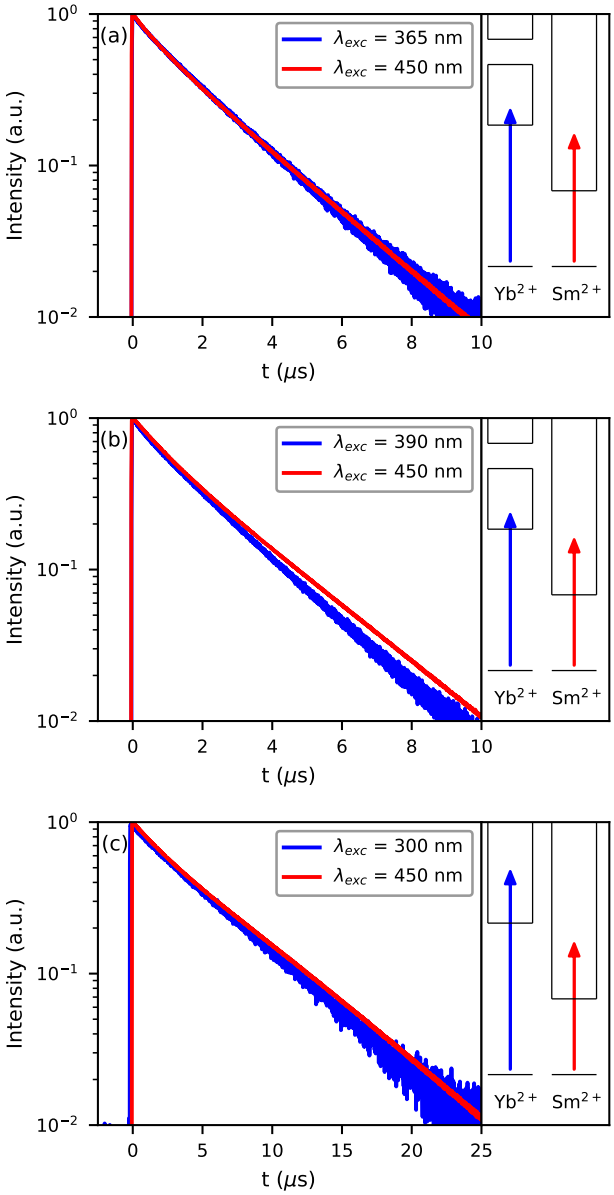

Figure 3.6: Photoluminescence decay curves of (a) $CsYbBr_3$:1%Sm observed at 800 nm, (b) $CsYbI_3$:1%Sm observed at 800 nm, (c) $YbCl_2$:1%Sm observed at 720 nm. The right side of the figures shows schematically what transitions are excited, only the 4f ground state and 5d excited states are drawn. In $CsYbBr_3$:1%Sm and $CsYbI_3$:1%Sm (a and b), the two Yb^{2+} excited states indicate the $4f^{13}[^2F_{7/2}]5d$ and $4f^{13}[^2F_{5/2}]5d$ states.

3.4. Discussion

To gain insight in the scintillation mechanism of $CsYbBr_3$:1%Sm, $CsYbI_3$:1%Sm and $YbCl_2$:1%Sm, vacuum referred binding energy (VRBE) diagrams are shown in figure 3.7. The energy of the divalent lanthanide $4f^n$ ground states is determined by the Eu Coulomb parameter $U(A)$, the tilt parameter $\alpha(A)$ and the nephelauxetic parameter $\beta(2+,A)$, as previously described by Dorenbos [39]. The values of these parameters have been estimated using typical values for compounds with similar anion types [39]. The spectroscopic data of Sm^{2+} presented in this article was used to place the $4f^{n-1}5d$ excited states ($E_{5d}(5,2+,A)$) with respect to the $4f^n$ ground states. The top of the valence band E_V was also estimated with typical values for compounds with the same anion type [40]. Lastly, the bottom of the conduction band E_C was placed 1 eV above the Sm^{2+} $4f^5 5d$ level, which is estimated from the quenching temperature that lies above 700 K. All parameters used to create the VRBE diagram are provided in table 3.1.

Table 3.1: Parameters used to construct the VRBE diagrams in figure 3.7.

Compound A	$CsYbBr_3$	$CsYbI_3$	$YbCl_2$
$U(A)$	6.67	6.25	6.70
$\alpha(A)$	0.095	0.095	0.095
$\beta(2+,A)$	0.92	0.91	0.92
$E^{5d}(5,2+,A)$	-0.9	-0.8	-0.9
$E_V(A)$	-6.7	-5.2	-8.0
$E_C(A)$	0.2	0.2	0.1

The energy of the valence band maximum is highly dependent on anion type, typically reducing the band gap from around 8 eV for chlorides to nearly 5 eV for iodides. However, due to the high concentration of Yb^{2+}, the optical band gap in all these samples is determined by the Yb^{2+} $4f^{14} \rightarrow 4f^{13}[^2F_{7/2}]5d_1$[LS] transition, which is approximately 3.2 eV in all samples. The minimum energy required to excite an electron is thereby greatly reduced, allowing for an increase in the number of electron-hole pairs created in a scintillation event. The valence band consists of the np orbitals (n=3-5) of the halide anions, meaning there are $3 \times 6 = 18$ valence band electrons for every 14 Yb^{2+} 4f electrons in $CsYbBr_3$ and $CsYbI_3$. In $YbCl_2$, there are $2 \times 6 = 12$ valence band electrons for every 14 Yb^{2+} 4f electrons. In a scintillation event an energetic primary electron excites bound electrons into the conduction band. When assuming equal probability for excitation of a valence band electron across the band gap or Yb^{2+} $4f^{14}$ electron into the conduction band, the average energy required to excite an electron in these materials can be calculated. This average energy will be labelled the effective band gap $E_{G\text{-eff}}$ in this work. The energies that correspond to the band gap (E_G), $4f^{13}[^2F_{7/2}]5d_1$[LS] (E_{df}^{Yb2+}) and $E_{G\text{-eff}}$ are shown in Table 3.2.

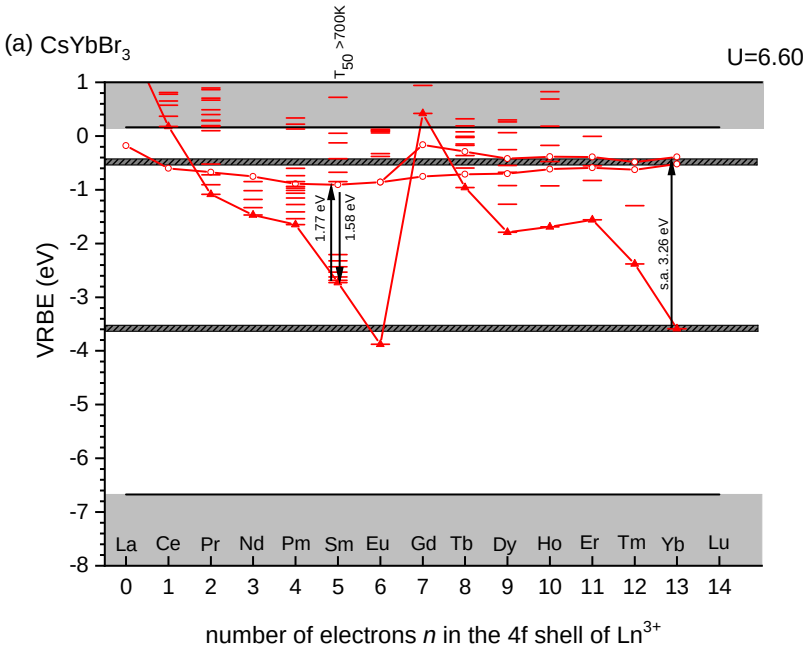
(a) CsYbBr3
U=6.60
T50 >700K
1.77 eV
1.58 eV
s.a. 3.26 eV
VRBE (eV)
1
0
-1
-2
-3
-4
-5
-6
-7
-8
La Ce Pr Nd Pm Sm Eu Gd Tb Dy Ho Er Tm Yb Lu
0 1 2 3 4 5 6 7 8 9 10 11 12 13 14
number of electrons n in the 4f shell of Ln3+

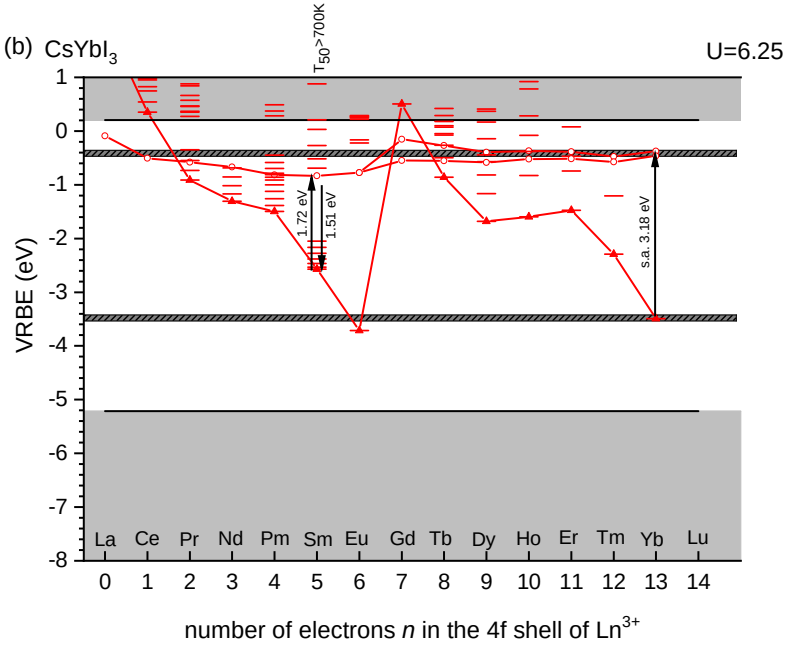
(b) CsYbI3
U=6.25
T50>700K
1.72 eV
1.51 eV
s.a. 3.18 eV
VRBE (eV)
1
0
-1
-2
-3
-4
-5
-6
-7
-8
La Ce Pr Nd Pm Sm Eu Gd Tb Dy Ho Er Tm Yb Lu
0 1 2 3 4 5 6 7 8 9 10 11 12 13 14
number of electrons n in the 4f shell of Ln3+

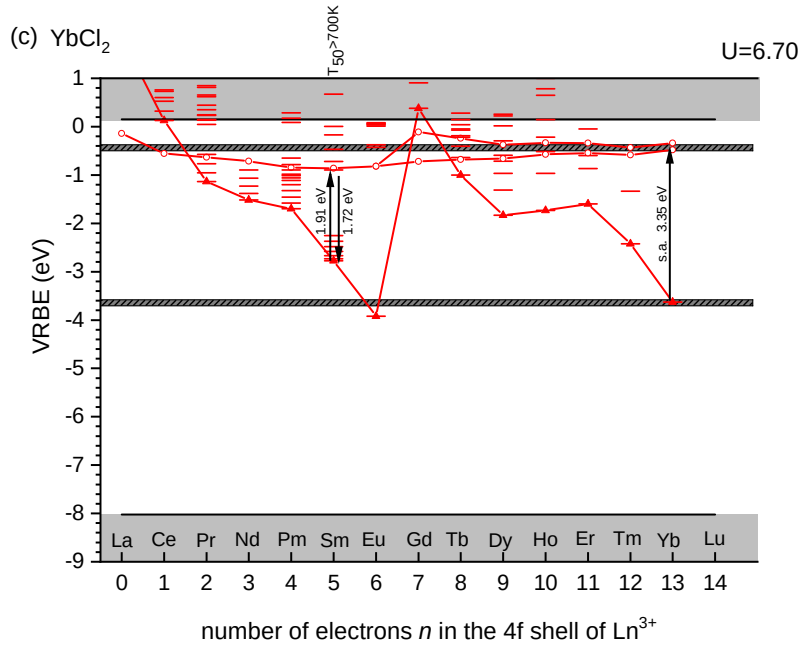

Figure 3.7: VRBE diagrams of (a) $CsYbBr_3$, (b) $CsYbI_3$ and (c) $YbCl_2$. The dark grey horizontal lines indicate the $4f^{14}$ ground state and $4f^{13}[^2F_{7/2}]5d_1$ excited states and are drawn to indicate that Yb^{2+} is part of the host compound.

The theoretical light yield limit Y_{th} in photons/MeV is defined by equation 3.3.

$$Y_{\text{th}} = \frac{10^6}{\beta E_G} \tag{3.3}$$

With β a value between 2 and 3. For the samples discussed in this work, Y_{th} is calculated using the $E_{G\text{-eff}}$ instead of E_G, the values are also shown in Table 3.2. Even though the estimated value of E_G is 1.2 eV larger for $YbCl_2$ than for $CsYbBr_3$, the higher atomic percentage of Yb^{2+} in $YbCl_2$ compared to $CsYbBr_3$ makes the value of Y_{th} almost identical for the two samples. Y_{th} has a value of 69,000 - 104,000 ph/MeV for $CsYbI_3$:1%Sm. However, the pulse height spectrum in figure 3.4 shows that 20,000 photons are detected after photoelectric absorption of a 662 keV γ-ray, which corresponds to a light yield of only 30,000 ph/MeV. Apparently the electron-hole pairs are transferred to Sm^{2+} with low efficiency.

In $CsBa_2I_5$:Yb,Sm, a loss of light yield was found to be caused by slow energy transfer from the Yb^{2+} $4f^{13}[^2F_{7/2}]5d_1$[HS] state to Sm^{2+} [27]. The Yb^{2+} spin-forbidden $4f^{13}[^2F_{7/2}]5d_1$[HS] $\rightarrow$ $4f^{14}$ emission showed photoluminescence decay time of around 100 µs. The Sm^{2+} photoluminescence decay showed a slow component with the same 100 µs decay time. Additionally, the much faster energy transfer from the Yb^{2+} $4f^{13}[^2F_{7/2}]5d_1$[LS] state resulted in a component with risetime in the Sm^{2+} emission.

These energy transfer rates were a consequence of the relatively low concentrations of Yb^{2+} (2% - 5%) and Sm^{2+} (0.5% - 1%) that were used in the $CsBa_2I_5$ samples, which meant energy transfer from Yb^{2+} to Sm^{2+} took place through long range dipole-dipole interactions.

Table 3.2: Energies of the (estimated) band gap E_G, the Yb^{2+} $4f^{14} \rightarrow 4f^{13}[^2F_{7/2}]5d_1$[LS] transition E_{df}^{Yb2+}, the effective band gap $E_{G\text{-eff}}$ and the theoretical light yield limit Y_{th}.

Compound A	$CsYbBr_3$	$CsYbI_3$	$YbCl_2$
E_G (eV)	6.9	5.4	8.1
E_{df}^{Yb2+} (eV)	3.26	3.18	3.35
$E_{G\text{-eff}}$ (eV)	5.7	4.8	6.0
Y_{th} (ph/MeV)	58,000 - 88,000	69,000 - 104,000	56,000 - 83,000

Compared to the previously studied $CsBa_2I_5$:Yb,Sm samples, the Yb^{2+} concentration in the samples discussed in this work is much higher. All samples show exclusively Sm^{2+} emission under X-ray excitation (Fig. 3.2). No Yb^{2+} or other host related emission is observed. Additionally, the X-ray excited decay profiles (Fig. 3.3) show that the Sm^{2+} emission is at maximum intensity promptly after excitation and no slow component is observed. This indicates that Yb^{2+} excitations are able to rapidly migrate through the lattice, facilitating fast energy transfer to Sm^{2+}. This is further confirmed by the photoluminescence decay curves in figure 3.6, where even upon excitation of Yb^{2+}, the maximum intensity of the Sm^{2+} emission is reached without any delay. By increasing the Yb^{2+} concentration to 99%, the light yield losses due to slow energy transfer from Yb^{2+} to Sm^{2+} have been solved. However, as indicated by the lower light yield than would theoretically be achievable in $CsYbI_3$:1%Sm, light yield losses still occur between creation of electron-hole pairs and subsequent excitation of Sm^{2+}.

3.5. Conclusions

The scintillation properties of $CsYbBr_3$:1%Sm, $CsYbI_3$:1%Sm and $YbCl_2$:1%Sm have been evaluated. All samples show exclusively Sm^{2+} $4f^55d \rightarrow 4f^6$ emission under X-ray excitation which does not quench until temperatures higher than 700 K. The scintillation decay times are 2.1 µs, 2.3 µs and 4.6 µs for $CsYbBr_3$:1%Sm, $CsYbI_3$:1%Sm and $YbCl_2$:1%Sm, respectively. The decay curves show that Sm^{2+} reaches maximum intensity promptly after excitation and no slow component has been observed. Increasing the Yb^{2+} concentration to 99% has thus been shown to be an effective way to enable fast energy transfer from Yb^{2+} to Sm^{2+}. The ^{137}Cs excited pulse height spectrum of $CsYbI_3$:1%Sm coupled to an avalanche photodiode resulted in a photopeak with energy resolution of 7%. The light yield of $CsYbI_3$:1%Sm was estimated at 30,000 ph/MeV.

3.6. Acknowledgements

This research was subsidised by the TTW/OTP grant no. 18040 of the Dutch Research Council. The authors would like to thank Daniel Biner, Bern, for the synthesis and crystal growth of the materials.

References

[1] Marvin. J. Weber, J. Lumin. 100 (2002) 35.

[2] Pieter Dorenbos, Opt. Mater. X 1 (2019) 100021.

[3] M. S. Alekhin, J. T. M. de Haas, I. V. Khodyuk, K. W. Krämer, P. R. Menge, V. Ouspenski, P. Dorenbos, Appl. Phys. Lett. 102 (2013) 151915.

[4] L. A. Boatner, J. O. Ramey, J. A. Kolopus, R. Hawrami, W. M. Higgins, E. van Loef, J. Glodo, K. S. Shah, Emmanuel Rowe, Pijush Bhattacharya, Eugene Tupitsyn, Michael Groza, Arnold Burger, N. J. Cherepy, S. A. Payne, J. Cryst. Growth 312 (2010) 1213.

[5] Yuntao Wu, Qi Li, Daniel J. Rutstrom, Ian Greeley, Luis Stand, Matthew Loyd, Merry Koschan, Charles L. Melcher, Nucl. Instrum. Meth. A 954 (2020) 161242.

[6] Nerine J. Cherepy, Giulia Hull, Alexander D. Drobshoff, Stephen A. Payne, Edgar van Loef, Cody M. Wilson, Kanai S. Shah, Utpal N. Roy, Arnold Burger, Lynn A. Boatner, Woon-Seng Choong, William W. Moses, Appl. Phys. Lett. 92 (2008) 083508.

[7] Mikhail S. Alekhin, Daniel A. Biner, Karl W. Krämer, Pieter Dorenbos, J. Lumin. 145 (2014) 723.

[8] E. D. Bourret-Courchesne, G. Bizarri, R. Borade, Z. Yan, S. M. Hanrahan, G. Gundiah, A. Chaudhry, A. Canning, S. E. Derenzo, Nucl. Instrum. Meth. A 612 (2009) 138.

[9] U. Shirwadkar, R. Hawrami, J. Glodo, E. V. D. van Loef, K. S. Shah, IEEE T. Nucl. Sci. 60 (2013) 1011.

[10] Jarek Glodo, Edgar V. van Loef, Nerine J. Cherepy, Stephen A. Payne, Kanai S. Shah, IEEE T. Nucl. Sci. 57 (2010) 1228.

[11] Mikhail S. Alekhin, Karl W. Krämer, Pieter Dorenbos, Nucl. Instrum. Meth. A 714 (2013) 13.

[12] Yuntao Wu, Mariya Zhuravleva, Adam C. Lindsey, Merry Koschan, Charles L. Melcher, Nucl. Instrum. Meth. A 820 (2016) 132.

[13] Daniel Rutstrom, Luis Stand, Merry Koschan, Charles L. Melcher, Mariya Zhuravleva, J. Lumin. 216 (2019) 116740.

[14] Johan T. M. de Haas, Pieter Dorenbos, IEEE T. Nucl. Sci. 55 (2008) 1086.

[15] M. Guzzi, G. Baldini, J. Lumin. 6 (1973) 270.

[16] Mikhail S. Alekhin, Roy H. P. Awater, Daniel A. Biner, Karl W. Krämer, Johan T. M. de Haas, Pieter Dorenbos, J. Lumin. 167 (2015) 347.

[17] R. H. P. Awater, M. S. Alekhin, D. A. Biner, K. W. Krämer, P. Dorenbos, J. Lumin. 212 (2019) 1.

[18] Weronika Wolszczak, Karl W. Krämer, Pieter Dorenbos, Phys. Status Solidi R. 13 (2019) 1900158.

[19] W. Wolszczak, K.W. Krämer, P. Dorenbos, J. Lumin. 222 (2020) 117101.

[20] E. Rowe, E. Tupitsyn, B.Wiggins, P. Bhattacharya, L. Matei, M. Groza, V. Buliga, A. Burger, P. Beck, N.J. Cherepy, S.A. Payne, Cryst. Res. Technol. 48 (2013) 227.

[21] Kohei Mizoi, Miki Arai, Yutaka Fujimoto, Daisuke Nakauchi, Masanori Koshimizu, Takayuki Yanagida, Keisuke Asai, J. Lumin. 227 (2020) 117521.

[22] Kohei Mizoi, Miki Arai, Yutaka Fujimoto, Daisuke Nakauchi, Masanori Koshimizu, Takayuki Yanagida, Keisuke Asai, J. Ceram. Soc. Jpn. 129 (2021) 406.

[23] Daniel Rutstrom, Luis Stand, Bogdan Dryzhakov, Merry Koschan, Charles L. Melcher, Mariya Zhuravleva, Opt. Mater. 110 (2020) 110536.

[24] Dai Sekine, Yutaka Fujimoto, Masanori Koshimizu, Daisuke Nakauchi, Takayuki Yanagida, Keisuke Asai, Jpn. J. Appl. Phys. 59 (2020) 012005.

[25] P. Dorenbos, J. Phys. Condens. Mat. 15 (2003) 575.

[26] Markus Suta, Tim Senden, Jacob Olchowka, Matthias Adlung, Andries Meijerink, Claudia Wickleder, Phys. Chem. Chem. Phys. 19 (2017) 7188.

[27] Casper van Aarle, Karl W. Krämer, Pieter Dorenbos, J. Lumin. 238 (2021) 118257.

[28] D. L. Dexter, J. Chem. Phys. 21 (1953) 836.

[29] Gaby Schilling, Gerd Meyer, Z. Anorg. Allg. Chem. 662 (1992) 759.

[30] Markus Suta, Claudia Wickleder, Adv. Funct. Mater. 27 (2017) 1602783.

[31] Christine A. Voos-Esquivel, Harry A. Eick, J. Solid State Chem. 67 (1987) 291.

[32] G. Meyer, Advances in the Synthesis and Reactivity of Solids, Vol. 2, p.1-16. JAI Press Inc. 1994.

[33] M. Suta, P. Larsen, F. Lavoie-Cardinal, C. Wickleder, J. Lumin. 149 (2014) 35.

[34] Markus Suta, Claudia Wickleder, J. Mater. Chem. C, 3 (2015) 5233.

[35] D. L. Wood, W. Kaiser, Phys. Rev. 126 (1962) 2079.

[36] Markus Suta, Wener Urland, Claude Daul, Claudia Wickleder, Phys. Chem. Chem. Phys., 18 (2016) 13196.

[37] Xinhua Zhao, Yongzhi Deng, Zhonghe Li, Shishua Wang, J. Alloy. Compd. 250 (1997) 405.

[38] Mirosław Karbowiak, Piotr Solarz, Radosław Lisiecki, Witold Ryba-Romanowski, J. Lumin. 195 (2018) 159.

[39] Pieter Dorenbos, J. Lumin. 222 (2020) 117164.

[40] Pieter Dorenbos, J. Lumin. 136 (2013) 122.

4

Avoiding concentration quenching and self-absorption in Cs_4EuX_6 (X = Br, I) by Sm^{2+} doping

The benefits of doping Cs_4EuBr_6 and Cs_4EuI_6 with Sm^{2+} are studied for near-infrared scintillator applications. It is shown that undoped Cs_4EuI_6 suffers from a high probability of self-absorption, which is almost completely absent in Cs_4EuI_6:2%Sm. Sm^{2+} doping is also used to gain insight in the migration rate of Eu^{2+} excitations in Cs_4EuBr_6 and Cs_4EuI_6, which shows that concentration quenching is weak, but still significant in the undoped compounds. Both self-absorption and concentration quenching are linked to the spectral overlap of the Eu^{2+} excitation and emission spectra which were studied between 10 K and 300 K. The scintillation characteristics of Cs_4EuI_6:2%Sm is compared to that of the undoped samples. An improvement of energy resolution from 11% to 7.5% is found upon doping Cs_4EuI_6 with 2%Sm and the scintillation decay time shortens from 4.8 μs to 3.5 μs in samples of around 3 mm in size.

The content of this chapter is based on the following publication:
Casper van Aarle, Karl W. Krämer, Pieter Dorenbos, J. Mater. Chem. C 11 (2023) 2336.

4.1. Introduction

The energy resolution is a key parameter in the development of γ-ray spectrometers. It is defined as the full width at half maximum of the photopeak in a pulse height spectrum and is a measure of how accurately γ-rays from different energies can be resolved. Typically, scintillator energy resolutions are compared under detection of 662 keV γ-rays from a ^{137}Cs source. The current best energy resolution of 2.04% was achieved with $LaBr_3$:Ce,Sr, for which a light yield of 70,000 ph/MeV was reported [1]. The energy resolution of $LaBr_3$:Ce,Sr is close to the fundamental limit based on photon statistics, meaning significant improvements can only be made if more photons are detected in a scintillation event. This stresses the importance of developing high light yield scintillators. After the rediscovery of SrI_2:Eu in 2008 [2], SrI_2:Eu has been further developed resulting in an energy resolution of 2.6% and light yields of up to 115,000 ph/MeV have been reported [3–7]. Among other Eu^{2+}-doped halides, the best energy resolution of 2.3% was achieved with $CsBa_2I_5$:Eu, with reported light yields up to 100,000 ph/MeV [8–11]. This shows that Eu^{2+}-doped halides are potential candidates for achieving an energy resolution below 2%.

Despite these promising characteristics, Eu^{2+}-doped scintillators still suffer from several drawbacks. Light yield and energy resolution typically tend to improve upon initial increase in Eu^{2+} concentration, but above several percent doping with Eu^{2+} these properties start to worsen again [12–16]. This is at least in part caused by the large overlap between the Eu^{2+} excitation and emission spectrum, making Eu^{2+}-doped halides prone to concentration quenching and, in the case of large crystals, self-absorption [3, 17, 18].

Concentration quenching is caused by energy transfer between Eu^{2+} ions. This can take the form of consecutive transfer of a single excitation from one Eu^{2+} to another until it reaches a quenching site, or the excitation energy being lost by transfer to an already excited Eu^{2+} ion after which energy is lost due to relaxation back to the emitting state [19, 20]. Both these processes are strongly dependent on distance between Eu^{2+} ions and their effects can thus be diminished by increasing the distance between Eu^{2+} ions [21]. Aside from reducing the amount of Eu^{2+} doping, this can also be achieved by selecting host compounds which intrinsically have larger distances between the divalent cation sites.

The compounds Cs_4MX_6 (M = Ca, Sr, Eu, Yb; X = Br, I) crystallize in the K_4CdCl_6-type structure with space group $R\bar{3}c$ [22]. They contain a single M^{2+} site with isolated $[MX_6]^{4-}$ octahedra, well separated from each other by Cs^+ cations. Accordingly, the smallest M-M distance of R = 9.0 Å in Cs_4EuI_6 [22–24] is much longer than for corner-sharing perovkites with R = 6.2 Å in $CsEuI_3$ [25]. When only considering the dipole-dipole interaction (scaling with R^{-6} [21]), the expected rate of energy transfer between Eu^{2+} nearest neighbours is around 10 times slower in Cs_4EuI_6 than it is in $CsEuI_3$. Contribution of the exchange interaction will make this difference even larger. Based on this, one would expect that Cs_4MX_6 compounds are much less affected by concentration quenching than their $CsMX_3$ counterparts, which is in line with the light yield increase reported by Wu et al. upon lowering the dimensionality of self-activated Cs_nEuI_{2+n} compounds [24].

Even though concentration quenching can be reduced by careful selection of the host lattice, the problem of self-absorption remains, especially for high Eu^{2+} concentration and large crystal size. A solution of the Eu^{2+} self-absorption problem in scintillators

is the co-doping with Sm^{2+}. With an addition of as little as 1% Sm^{2+}, close to 100% of Eu^{2+} excitations are transferred to Sm^{2+} and almost exclusively Sm^{2+} emission is observed [26, 27]. The Sm^{2+} $4f^5 5d \rightarrow 4f^6$ emission can end up in any of the $4f^6[^7F_J]$ states, while re-absorption can only take place from the $4f^6[^7F_0]$ ground state. Transitions to the $4f^6[^7F_{1\text{-}6}]$ states result in longer wavelength emissions that are less likely to be re-absorbed by other Sm^{2+} ions. In combination with the relatively low Sm^{2+} concentration of around 1%, the probably of self-absorption in Eu^{2+} and Sm^{2+} co-doped materials is greatly reduced compared to scintillators in which Eu^{2+} is the emitting ion [28].

In this work, the benefits of doping Cs_4EuBr_6 and Cs_4EuI_6 with Sm^{2+} are studied in an attempt to solve self-absorption and concentration quenching and thereby develop a near-infrared scintillator. For this, Cs_4EuBr_6 and Cs_4EuI_6 samples were synthesises with Sm^{2+} concentrations ranging from 0% to 2%. The amount of self-absorption is assessed for undoped and Sm^{2+}-doped Cs_4EuI_6 through X-ray excited emission and decay measurements. Energy transfer from Eu^{2+} to Eu^{2+} and from Eu^{2+} to Sm^{2+} is studied through photoluminescence spectroscopy and decay studies. Lastly, the scintillation performance is assessed through ^{137}Cs 662 keV γ-ray excited pulse height spectra.

4.2. Experimental Techniques

Crystals of Cs_4EuBr_6, Cs_4EuI_6, and doped crystals with 0.5% and 2% Sm^{2+} were grown from the binary halides by the vertical Bridgman technique. CsBr (5N, Alfa) and CsI (suprapur, Merck) were dried in high vacuum at 200°C. $EuBr_2$ and $SmBr_3$ were prepared by the ammonium bromide method [29]. The rare earth oxide M_2O_3 (M = Eu, 5N, Metall Rare earth Ltd.; M = Sm, >3N, Fluka) was dissolved in concentrated HBr acid (suprapur, Merck) and an excess of NH_4Br (pro analysis, sublimed, Merck) added in a M to NH_4 ratio of 2 to 7. The solution was dried up on a sand bath to yield the anhydrous ternary compound $(NH_4)_3MBr_6$, which is subsequently decomposed to the binary bromide by heating in vacuum. $EuBr_2$ was obtained at 500°C and used without further purification. $SmBr_3$ was sublimed at 650 °C in a silica apparatus under high vacuum for removal of SmOBr traces. $SmBr_2$ was obtained by reduction of $SmBr_3$ with Sm metal (3N; Alfa) in a Ta ampoule. The Ta-ampoule was sealed by helium arc-welding and enclosed into a silica ampoule under vacuum. The ampoule was heated to 900 °C for 7 days. The rare earth iodides were synthesized from the elements (Eu, 3N; Sm, 3N, both Alfa; I_2, pro analysis, sublimed, Merck) in sealed silica ampoules under vacuum. EuI_2 was obtained at 500 °C and purified by sublimation in an Au ampoule under vacuum at 900 °C. SmI_3 was prepared at 700 °C and sublimed for purification at 800 °C. SmI_2 was prepared from SmI_3 and Sm in a Ta ampoule 1 day at 900 °C and 7 days at 600 °C.

Stoichiometric amounts of the binary halides (about 5 g per sample) were sealed in Ta ampoules, as described above. The ampoules were heated in a Bridgman furnace to 560 °C, i.e., above the congruent melting points of Cs_4EuBr_6 at 545 °C and Cs_4EuI_6 at 540 °C. After 1 day at constant temperature, the crystal growth was started by slowly moving up the furnace. The samples were cooled to RT within about 10 days. Crystals were cleaved from the boules for spectroscopic investigations. The denoted doping level represents the melt composition. Since staring materials and products are highly hygroscopic and sensitive to oxidation, all handling was done under strictly dry and oxygen-free condi-

tions (H_2O and O_2 <0.1 ppm) in glove boxes and sealed sample containers.

X-ray excited emission spectra were measured using an X-ray tube with tungsten anode, operated at 79 kV and aluminium filter to block low energy X-rays for preventing radiation damage at the sample surface. The samples were attached to the cold finger of a Janis VPF-700 cryostat. The emission coming from the sample under a 90°angle with respect to the X-ray beam was coupled into an optical fibre and read out with an Ocean insights QE Pro spectrometer.

X-ray excited decay curves were measured using a time correlated single photon counting method. A start signal was generated upon triggering a PicoQuant LDH-P-C-400M laser diode exciting a Hamamatsu N5084 light excited X-ray tube with tungsten anode operated at 40 kV, creating a 500 ps long pulse of X-rays. Upon detection of a scintillation photon by the ID Quantique ID100-50 single-photon detector, a stop signal was generated. The start and stop signals were processed using an Ortec 567 time-to-amplitude converter of which the output was connected to an Ortec AD114 16k analog-to-digital converter. The sample was attached to the cold finger of a Janis VPF-700 cryostat. The sample chamber was kept at a vacuum of 10^{-5} mbar to protect the hygroscopic sample from moisture.

^{137}Cs 662 keV γ-ray pulse height spectra of undoped samples were recorded using a R1791 photomultiplier tube (PMT) operated at a voltage of -700 V. The unpolished bare crystal was placed on the entrance window of the PMT and was covered with teflon tape. No optical coupling was used. The number of photoelectrons created in a scintillation event was determined by comparing corresponding channel with the single electron response of the PMT. The light yield was calculated using the number of photoelectrons at the maximum of the 662 keV photopeak and correcting for the quantum efficiency and reflectivity of the PMT, using the method described by de Haas and Dorenbos [30].

^{137}Cs excited pulse height spectra of Sm^{2+}-doped samples were recorded using an Advanced Photonix APD (type 630-70-72-510) operated at a bias voltage of 1690 V. The temperature of the APD was stabilised at 260 K. The APD signal was increased by a Cremit CR-112 pre-amplifier. The rest of the electronics are the same as used in the PMT set-up described above. The light yield was determined by comparing the channel of the photopeak with the peak from direct detection of 17.8 keV X-rays of ^{241}Am.

Photoluminescence excitation and emission spectra were measured using a 450 W Xenon lamp and a Horiba Gemini 180 monochromator to excite the sample. Light from the sample was collected at a 90°angle with respect to the incoming excitation light. Reflected excitation light was filtered out with an optical filter. The emission light passed through a Princeton Instruments SpectraPro-SP2358 monochromator, after which it was detected by a Hamamatsu R7600-20 PMT. The sample was attached attached to the cold finger of a closed cycle helium cryostat.

Photoluminescence decay curves were recorded using an EKSPLA NT230 OPO laser to excite the sample with a repetition rate of 100 Hz and pulse duration of 10 ns. The emission passed through a Princeton Instruments SpectraPro-SP2358 monochromator and was detected by a Hamamatsu R7600U-20 PMT. An optical long pass filter was placed at the entrance of the monochromator to filter out the excitation light from the laser. The signal from the PMT was recorded using a CAEN DT5730 digitizer.

4.3. Results

Figures 4.1a and b show the X-ray excited emission spectra between 78 K and 300 K of undoped Cs_4EuBr_6 and Cs_4EuI_6, respectively. Cs_4EuBr_6 shows a single emission band around 450 nm. This emission band is assigned to the Eu^{2+} $4f^6 5d \rightarrow 4f^7$ transition. With increasing temperature, the peak of the emission band shifts to longer wavelengths. This is typically observed in materials with high Eu^{2+} concentration and is ascribed to self-absorption [8, 13, 31]. Cs_4EuI_6 also shows a single emission band that is assigned to the Eu^{2+} $4f^6 5d \rightarrow 4f^7$ transition. The Eu^{2+} emission is located around 470 nm, at about 20 nm longer wavelength than for Cs_4EuBr_6. The emission band shows a similar shift to longer wavelengths with increasing temperature as was observed for Cs_4EuBr_6. The room temperature emission spectra of both samples correspond well to the data reported by Wu et al. [24]. Figure 4.1c shows the integrated emission intensity for Cs_4EuBr_6 and Cs_4EuI_6, normalised to their intensity at 78 K. The emission intensity of Cs_4EuBr_6 decreases by about 25% when temperature is increased from 78 K to 300 K. For Cs_4EuI_6, the emission intensity decreases by about 12%.

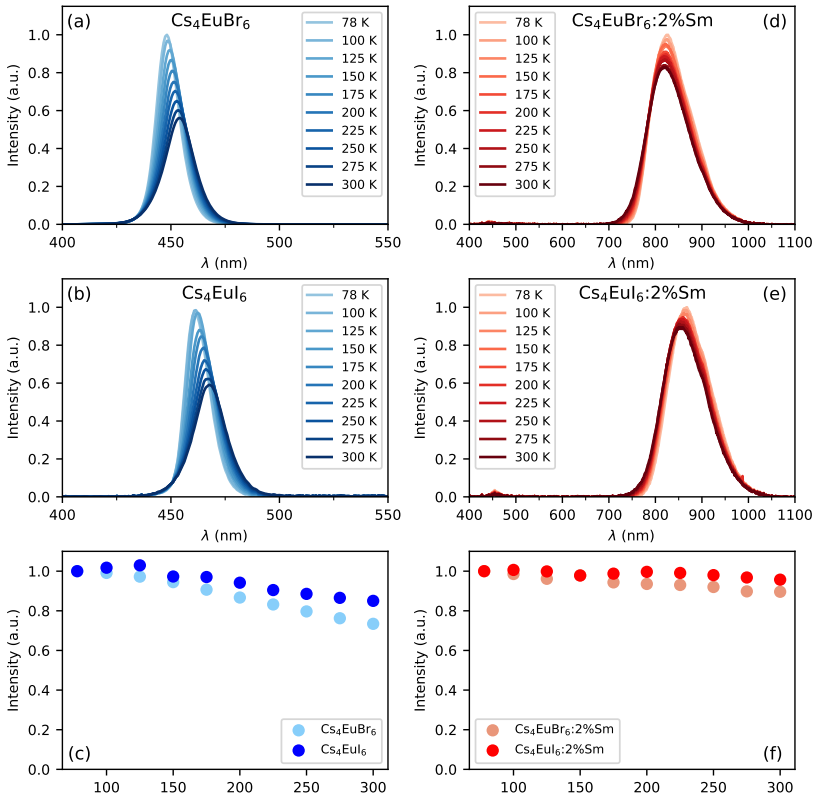

Figure 4.1: X-ray excited emission spectra between 78 K and 300 K for a) Cs_4EuBr_6, b) Cs_4EuI_6, d) Cs_4EuBr_6:2%Sm and e) Cs_4EuI_6:2%Sm. c) and f) show the integrated emission intensities normalised to the intensity at 78 K.

Figures 4.1d and e show the X-ray excited emission spectra between 78 K and 300 K of Cs_4EuBr_6:2%Sm and Cs_4EuI_6:2%Sm, respectively. Cs_4EuBr_6:2%Sm shows a broad emission band around 820 nm, which is assigned to the Sm^{2+} $4f^55d \rightarrow 4f^6$ transitions. With increasing temperature, the peak of the emission band shifts to shorter wavelengths. This is likely caused by thermal expansion of the sample, decreasing the crystal field splitting and thereby elevating the lowest 5d level to higher energies. The observation of the emission peak shifting to shorter wavelengths indicates a low probability of self-absorption of the Sm^{2+} emission. Cs_4EuI_6:2%Sm shows a similar broad emission band around 850 nm, which is also assigned to the Sm^{2+} $4f^55d \rightarrow 4f^6$ transition. Also in this sample, the peak of the Sm^{2+} emission shifts to shorter wavelengths as temperature is increased. In both samples, a small amount of Eu^{2+} emission is visible between 400 nm and 500 nm. The integrated emission intensity of Cs_4EuBr_6:2%Sm and Cs_4EuI_6:2%Sm is shown in Figure 4.1f. Upon increasing the temperature from 78 K to 300 K, the emission intensity remains almost constant compared to the decrease in intensity observed in the undoped samples.

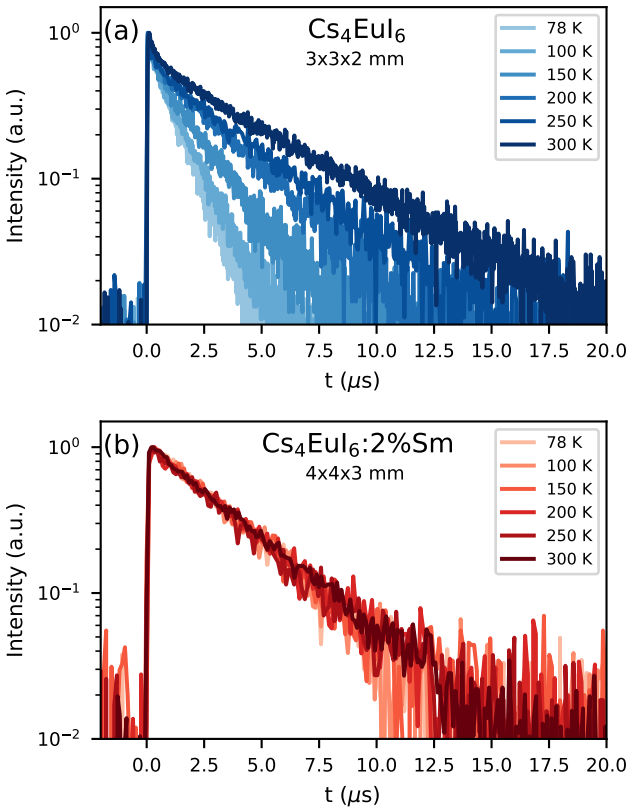

Figure 4.2: X-ray excited decay curves between 78 K and 300 K of a) Cs_4EuI_6 and b) Cs_4EuI_6:2%Sm.

Figure 4.2a shows the X-ray excited decay curves of a 3×3×2 mm^3 Cs_4EuI_6 crystal between 78 K and 300 K. All decay curves show an initial fast component after which they converge to a single exponential of which the decay time increases with temperature. At 78 K, this decay time is 1.19 µs and at 300 K it becomes 4 times slower with a decay time of 4.80 µs. Figure 4.2b shows the X-ray excited decay curves of a 4×4×3 mm^3 Cs_4EuI_6:2%Sm crystal between 78 K and 300 K. A 630 nm long pass filter was placed between the sample and the detector to remove the small amount of remaining Eu^{2+} emission. Unlike the decay curve of undoped Cs_4EuI_6, no fast component is observed in the decay curve. The decay time is also almost independent of temperature and increases marginally from 3.16 µs at 78 K to 3.50 µs at 300 K.

Figure 4.3 shows the ^{137}Cs 662 keV γ-ray pulse height spectra of undoped Cs_4EuBr_6 and Cs_4EuI_6 recorded on a PMT. The photopeak of Cs_4EuBr_6 corresponds to 7,500 photoelectrons being emitted from the photocathode of the PMT. Taking into account the quantum efficiency (25%) and reflectivity (33%) of the PMT, the light yield is estimated around 30,200 ph/MeV. Scintillation events in the photopeak of Cs_4EuI_6 correspond to 5,800 photoelectrons. At its emission wavelength of 470 nm, the quantum efficiency of the PMT is 22% and the reflectivity is 35%. This gives a light yield of 26,100 ph/MeV. Both samples have an energy resolution of 11%.

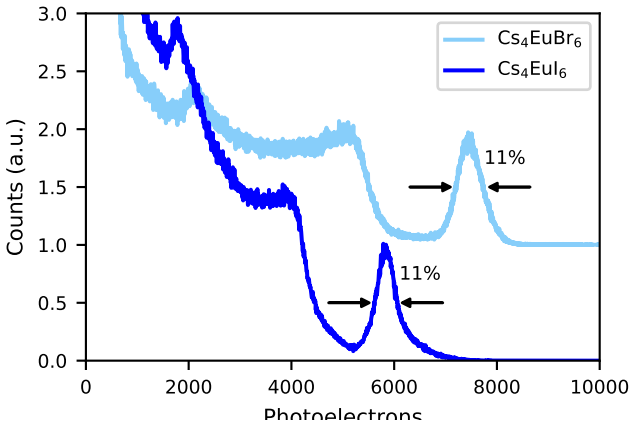

Figure 4.3: ^{137}Cs excited pulse height spectra of Cs_4EuBr_6 and Cs_4EuI_6 measured on a PMT.

Figure 4.4 shows the ^{137}Cs excited pulse height spectrum of Cs_4EuI_6:2%Sm recorded on an APD. In Figure 4.4a, the pulse height spectrum is shown as recorded. On the x-axis, the number of primary electron-hole pairs created in the APD during a scintillation event is set out, which is equal to the amount of detected scintillation photons. This pulse height spectrum contains a background of events that are caused by absorption of γ-rays directly in the APD. The dashed curve is an exponential approximation for this background and has been subtracted from the data to result in the pulse height spectrum displayed in Figure 4.4b. On average, 11,000 photons are detected under the 662 keV photopeak, translating to a light yield of around 16,600 ph/MeV. An energy resolution of 7.5% has been attained.

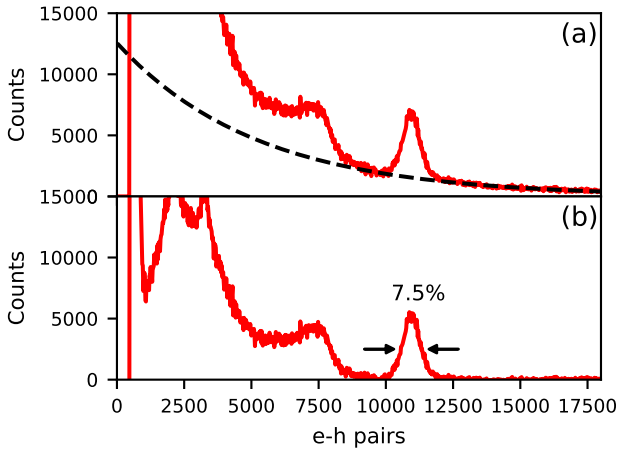

Figure 4.4: ^{137}Cs excited pulse height spectrum of Cs_4EuI_6:2%Sm measured on an APD. a) shows the spectrum as recorded and b) shows the spectrum after background subtraction.

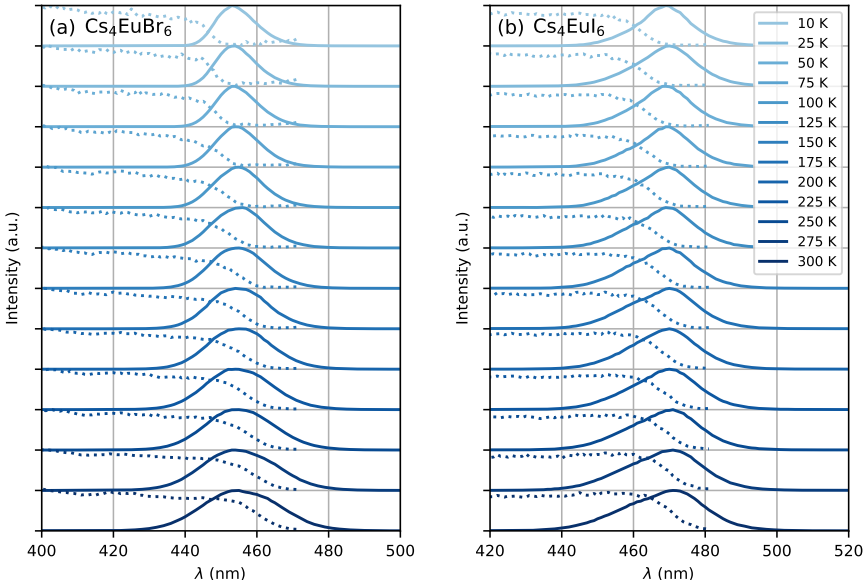

Figure 4.5: Photoluminescence excitation (dotted curve) and emission (solid curve) spectra between 10 K and 300 K of a) Cs_4EuBr_6 and b) Cs_4EuI_6.

Figure 4.5 shows the photoluminescence excitation (dashed curves) and emission (solid curves) spectra of undoped Cs_4EuBr_6 and Cs_4EuI_6 between 10 K and 300 K. As temperature is increased, both samples show an increase in emission bandwidth and the excitation spectra stretch to longer wavelengths. The result is an increase in spectral overlap between the Eu^{2+} emission and Eu^{2+} excitation. This increase in spectral overlap increases the probability that Eu^{2+} emission is re-absorbed by other Eu^{2+}, or that energy is transferred non-radiatively between neighbouring Eu^{2+} ions.

Figure 4.6a shows the photoluminescence excitation and emission spectra of Cs_4EuBr_6:0.5%Sm at 300 K. Both the Eu^{2+} and Sm^{2+} 5d → 4f emission can be detected upon excitation at 350 nm, as shown by curve 1. The Eu^{2+} emission overlaps with the excitation spectrum of the Sm^{2+} emission (curve 3), which indicates that Eu^{2+} can transfer energy to Sm^{2+}. Between 200 nm and 400 nm, the excitation spectrum of the Sm^{2+} 5d → 4f emission shows the same bands as the excitation spectrum of the Eu^{2+} 5d → 4f emission (curve 2). This confirms that energy transfer from Eu^{2+} to Sm^{2+} takes place.

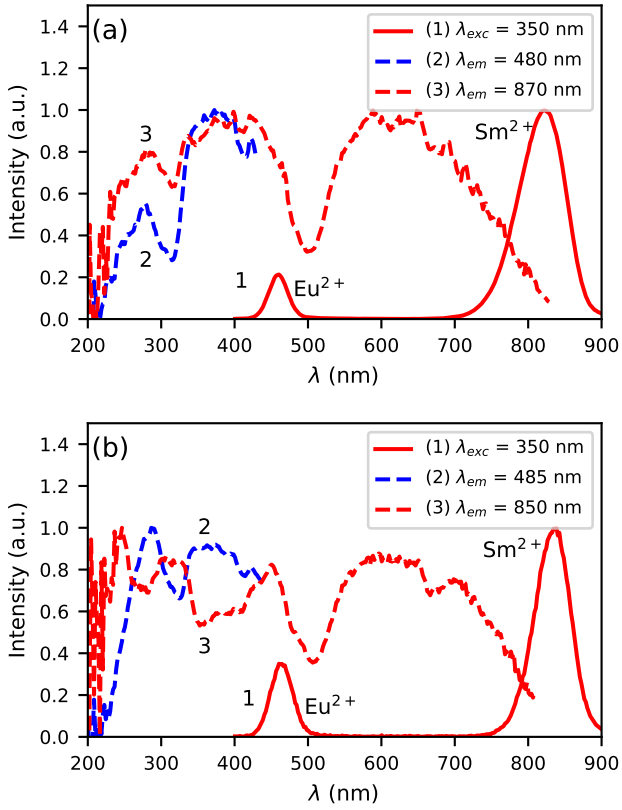

Figure 4.6: Photoluminescence excitation and emission spectra at 300 K of a) Cs_4EuBr_6:0.5%Sm and b) Cs_4EuI_6:0.5%Sm.

In Figure 4.6b, the photoluminescence excitation and emission spectra of Cs_4EuI_6:0.5%Sm are shown. Similar to Cs_4EuBr_6:0.5%Sm, it shows Eu^{2+} and Sm^{2+} 5d → 4f emission upon excitation at 350 nm, as shown by curve 1. In this case though, the excitation spectrum of the Sm^{2+} emission (curve 3) shows dips where the excitation spectrum of the Eu^{2+} emission (curve 2) shows highest intensity. This indicates that energy transfer from Eu^{2+} to Sm^{2+} is inefficient, which is likely due to the low Sm^{2+} concentration is this sample.

Figure 4.7 shows the photoluminescence decay of Eu^{2+} emission in (a) Cs_4EuBr_6:0.5%Sm, (b) Cs_4EuBr_6:2%Sm, (c) Cs_4EuI_6:0.5%Sm and (d) Cs_4EuI_6:2%Sm. All samples show approximately the same behaviour. All decay curves deviate from exponential functions, starting with fast decay and becoming slower as time progresses. The initial fast decay rate is only moderately dependent on temperature. The largest temperature dependence is found in the tail of the decay, making all temperature series fan out. This behaviour strongly resembles that of migrationally accelerated energy transfer, where Eu^{2+} excitations are able to move closer to Sm^{2+} by means of energy transfer between neighbouring Eu^{2+} ions [20, 32]. The initial rising component in the decay curves of Figures 4.7a and b are caused by the laser pulse duration of approximately 10 ns.

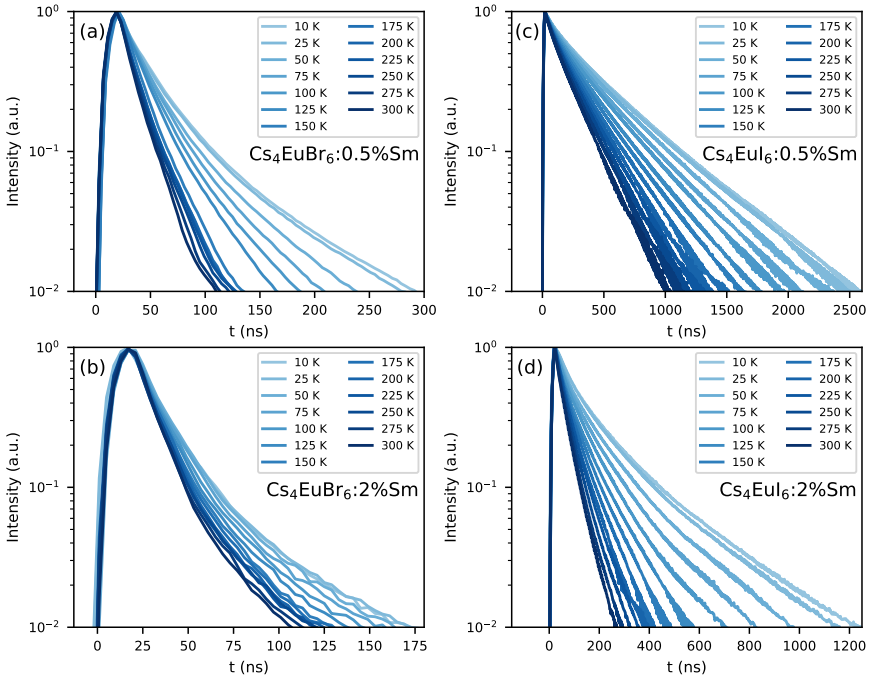

Figure 4.7: Photoluminescence decay of the Eu^{2+} emission upon 400 nm excitation between 10 K and 300 K in a) Cs_4EuBr_6:0.5%Sm, b) Cs_4EuBr_6:2%Sm, c) Cs_4EuI_6:0.5%Sm and d) Cs_4EuI_6:2%Sm.

The lifetime of Eu^{2+} excitations varies strongly between the samples. As the decay curves cannot be approximated with a single exponential function, the 1/e-decay time τ_e is reported. τ_e is defined as the time it takes for the decay curve to decrease by a factor of 1/e starting from its maximum intensity. Increasing the Sm^{2+} concentration in Cs_4EuBr_6 from 0.5% to 2% decreases τ_e from 20 ns to 16 ns. For Cs_4EuI_6, the same increase in Sm^{2+} concentration decreases τ_e from 172 ns to 44 ns. This decrease of τ_e with increasing Sm^{2+} concentration is expected, as a higher Sm^{2+} causes faster non-radiative energy transfer to Sm^{2+}.

Figures 4.8a and b show the photoluminescence decay of Eu^{2+} and Sm^{2+} emission in Cs_4EuBr_6:2%Sm and Cs_4EuI_6:2%Sm, respectively. The excitation wavelength is 350 nm, at which primarily Eu^{2+} is excited. The decay time of the Sm^{2+} emission is 2.82 µs in Cs_4EuBr_6:2%Sm and 3.26 µs in Cs_4EuI_6:2%Sm. The Eu^{2+} emission is strongly quenched by the presence of Sm^{2+}, therefore the inset shows the start of the decay curves on a shorter timescale. Here, it becomes visible that the Sm^{2+} emission intensity increases as the Eu^{2+} emission decays. This shows that excitations are transferred from Eu^{2+} to Sm^{2+}.

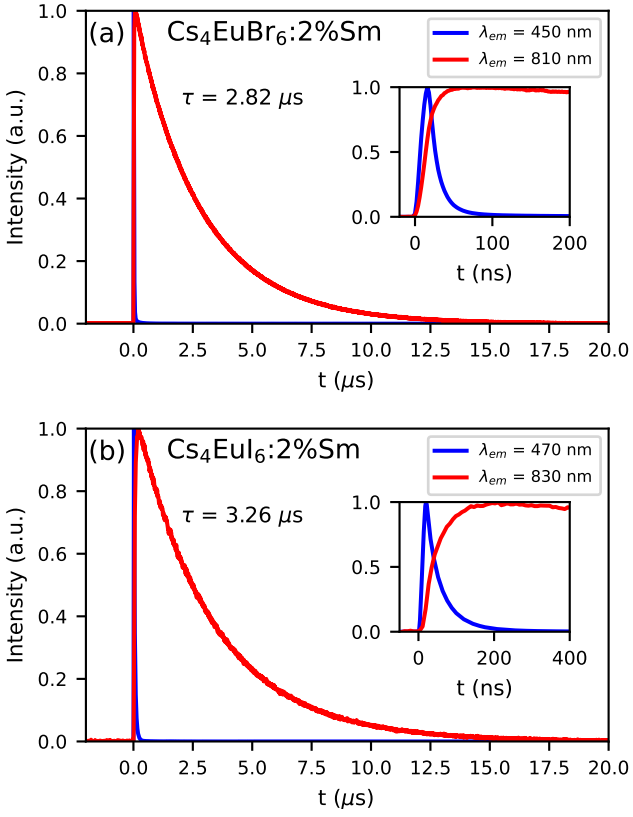

Figure 4.8: Photoluminescence decay of Eu^{2+} and Sm^{2+} emission upon 350 nm excitation at 300 K in a) Cs_4EuBr_6:2%Sm and b) Cs_4EuI_6:2%Sm. The insets show the same decay curve on a shorter time scale.

4.4. Discussion

Both self-absorption and non-radiative energy transfer significantly modify a luminescence decay curve. The luminescence decay can thus yield information on the energy transfer processes in the sample. The probability of both processes scales with the spectral overlap between the excitation band of the absorbing ion and the emission band of the emitting ion. In the case of Eu^{2+} it is shown by Figure 4.5 that temperature induced broadening of the Eu^{2+} excitation and emission bands results in a significant change in spectral overlap between these bands when going from 10 K to 300 K. This increase in spectral overlap occurs both in Cs_4EuBr_6 and Cs_4EuI_6. Based on this, it is expected that the probability of self-absorption and the non-radiative energy transfer rate between neighbouring Eu^{2+} ions increase with temperature. Both these processes typically decrease the light yield of a scintillator, which is in line with the observed decrease of the emission intensity under X-ray excitation, as shown in Figure 4.1c.

Figure 4.2a shows the X-ray excited luminescence decay curves of Cs_4EuI_6. The experiment was performed in reflection mode, i.e., the detector was pointed to the surface of the sample illuminated by X-rays. With an average X-ray energy of around 10 keV, almost all X-rays are absorbed within the first 100 μm below the sample surface; therefore almost all excitations of Eu^{2+} are present close to the surface on the side of the crystal oriented towards the detector. Light emitted into the direction of the detector has a low chance of being re-absorbed, thus the fast component visible in the first few microseconds gives an impression of the intrinsic radiative decay rate of Eu^{2+}. The light which, after being emitted, travels deeper into the crystal has a high probability of being re-absorbed. The absorbed photons can be re-emitted into the direction of the detector and still contibute to the decay curve. The decay curve thereby converges to an exponential decay rate that is longer than the intrinsic radiative decay rate of Eu^{2+}. This decay rate is given by equation 4.1 [33]:

$$\tau = \frac{\tau_r}{1-\eta a} \tag{4.1}$$

Here, τ_r is the radiative lifetime of the luminescence center, in this case Eu^{2+}. η is the quantum efficiency of the luminescence center and a is the average probability that an emitted photon is re-absorbed. a increases with dopant concentration and size of the crystal. Values for τ and a are provided in Table 4.1 for the 3×3×2 mm^3 Cs_4EuI_6 crystal, assuming $\eta = 1$. The value of τ_r was taken as 1.07 μs, which is the photoluminescence (PL) decay time at 10 K. It was assumed that self-absorption is negligible under these conditions. This assumption is justified as the photoluminescence decay time at room temperature converges to the same value of around 1.0 μs upon decreasing the Eu^{2+} concentration to nearly 0% in Cs_4CaI_6 and Cs_4SrI_6 [15]. When increasing the temperature from 78 K to 300 K, τ increases from 1.19 μs to 4.80 μs and accordingly a increases from 0.10 to 0.78. This shows that even in a small crystal of 3×3×2 mm^3, 78% of the emitted photons are re-absorbed.

In the same temperature range, the Sm^{2+} emission of the 4×4×3 mm^3 Cs_4EuI_6:2%Sm sample shows only a marginal increase in τ from 3.16 µs to 3.50 µs. Using equation 4.1, the value of a is calculated for every temperature step. The results are summarised in Table 4.1. Even though the Cs_4EuI_6:2%Sm crystal is significantly larger than the undoped Cs_4EuI_6 crystal, the values of a are around around 10 times lower at every temperature. This shows that the low sensitivity of Sm^{2+} to self-absorption combined with the low Sm^{2+} concentration is an effective way to almost completely solve the self-absorption problem of Cs_4EuI_6.

Table 4.1: Decay times τ under X-ray excitation of Cs_4EuI_6 and Cs_4EuI_6:2%Sm single crystals and the average probability a a scintillation photon is re-absorbed inside the crystal. The first row shows the photoluminescence (PL) decay time at 10 K, which is taken as an approximation for the radiative lifetime τ_r.

	Cs_4EuI_6 (3×3×2 mm^3)		Cs_4EuI_6:2%Sm (4×4×3 mm^3)	
T (K)	τ (µs)	a	τ (µs)	a
10 (PL)	1.07	-	3.12	-
78	1.19	0.10	3.16	0.01
100	1.40	0.24	3.13	0.01
150	2.08	0.49	3.34	0.06
200	2.98	0.64	3.40	0.08
250	3.97	0.73	3.31	0.06
300	4.80	0.78	3.50	0.11

As Eu^{2+} transfers energy to Sm^{2+}, doping the samples with Sm^{2+} introduces a large amount of quenching sites for Eu^{2+}. Insight in the non-radiative energy transfer rate between Eu^{2+} ions can be attained by monitoring the photoluminescence decay of Eu^{2+} in the Sm^{2+}-doped samples, see Figure 4.7. Directly after excitation of Eu^{2+}, the Eu^{2+} excitations are randomly distributed through the lattice. As the rate of non-radiative energy transfer scales with R^{-6}, excited Eu^{2+} ions that happen to be close to Sm^{2+} will transfer their energy to Sm^{2+} with higher probability than those at larger distance. Therefore the Eu^{2+} excitations will be depleted rapidly close to Sm^{2+}. In this stage, corresponding to the first tens of nanoseconds of the decay curves, the rate at which Sm^{2+} can deplete the volume around it is the limiting factor in the decay rate of Eu^{2+}. Once the volume around Sm^{2+} has been depleted, non-radiative energy transfer between Eu^{2+} ions will replenish the excitations in the depleted volumes. At this point, non-radiative energy transfer between Eu^{2+} ions becomes the limiting factor of the Eu^{2+} decay rate and causes the Eu^{2+} decay to slow down.

The rate at which Sm^{2+} depletes the Eu^{2+} excitations around it is almost independent of temperature, because the spectral overlap between the Eu^{2+} emission bands and the Sm^{2+} absorption bands does not change much with temperature. On the other hand, the rate of non-radiative energy transfer between Eu^{2+} ions does depend on temperature, because the spectral overlap between the Eu^{2+} excitation and emission spectra increases with temperature, see Figure 4.5. This is also visible in Figure 4.7; during the depletion of Eu^{2+} excitations close to Sm^{2+} in the first tens of nanoseconds after excitation, the

Eu^{2+} emission decays with approximately the same rate at every temperature. As time further progresses into the hundreds of nanoseconds, non-radiative energy transfer between Eu^{2+} ions becomes the limiting factor of the Eu^{2+} decay; this results in a strong temperature dependence of the decay rate on longer timescales and the decay curves fan out.

The results in Figure 4.7 show that a significant amount of energy transfer between Eu^{2+} ions is observed even for the isolated $[MX_6]^{4-}$ octahedra of Cs_4EuX_6. The light yield reported for undoped Cs_4EuI_6 (53,000 ph/MeV) [24] is still significantly lower than that of the more diluted compounds Cs_4CaI_6:7%Eu (69,000 ph/MeV) and Cs_4SrI_6:9%Eu (78,000 ph/MeV) [15], as reported by the same research group. When cooling Cs_4EuI_6 from 300 K to 78 K, the migration rate of the Eu^{2+} excitations slows down while the light yield increases 10% to 20% (Figure 4.1c). These observations strongly suggest that concentration quenching still plays a role in undoped Cs_4EuBr_6 and Cs_4EuI_6.

Opposed to the undoped samples, Cs_4EuBr_6:2%Sm and Cs_4EuI_6:2%Sm show a much less significant change in intensity in the same temperature range, as shown by Figure 4.1f. Once energy is transferred from Eu^{2+} to Sm^{2+} it cannot be transferred back to Eu^{2+} anymore. If the Sm^{2+} concentration is low enough, the distance between the Sm^{2+} ions is large and energy will not be transferred between Sm^{2+} ions. Aside from avoiding self-absorption, the doping of Eu^{2+} materials with Sm^{2+} effectively reduces concentration quenching.

Compared to the 2.1 μs scintillation decay time of $CsBa_2I_5$:Sm^{2+}, the 3.5 μs decay time of Cs_4EuI_6:2%Sm is on the slow side for Sm^{2+}-doped scintillators. However, due to the strong self-absorption in undoped Cs_4EuI_6, the decay time of Cs_4EuI_6:2%Sm is already faster than that of undoped Cs_4EuI_6 with sample sizes of only a few mm. It is also fast enough for applications in γ-ray spectroscopy, as succesfully shown by the pulse height spectrum in Figure 4.4.

4.5. Conclusions

The benefits of doping Cs_4EuBr_6 and Cs_4EuI_6 with Sm^{2+} have been studied for applications in γ-ray spectroscopy. It has been demonstrated that undoped Cs_4EuI_6 suffers from strong self-absorption. Despite the large distances between neighbouring Eu^{2+} ions, a small amount of concentration quenching has been observed in both Cs_4EuBr_6 and Cs_4EuI_6. Self-absorption and concentration quenching originate from the spectral overlap between the Eu^{2+} excitation and emission spectra.

Both self-absorption and concentration quenching can be avoided by doping these scintillators with 2% Sm^{2+}; this results almost exclusively in Sm^{2+} $4f^55d \rightarrow 4f^6$ emission. Due to the large amounts of self-absorption in the undoped samples, the room temperature scintillation decay time of the Sm^{2+}-doped Cs_4EuI_6 is already faster than that of small-size, undoped Cs_4EuI_6 crystals. The Sm^{2+} emission around 850 nm can be efficiently detected with an avalanche photodiode. Doping Cs_4EuI_6 with 2% Sm^{2+} improved the energy resolution from 11% to 7.5%.

4.6. Acknowledgements

This research was subsidised by the TTW/OTP grant no. 18040 of the Dutch Research Council. The authors would like to thank Daniel Biner, Bern, for the synthesis and crystal growth of the materials.

References

[1] M. S. Alekhin, J. T. M. de Haas, I. V. Khodyuk, K. W. Krämer, P. R. Menge, V. Ouspenski, P. Dorenbos, Appl. Phys. Lett. 102 (2013) 151915.

[2] Nerine J. Cherepy, Giulia Hull, Alexander D. Drobshoff, Stephen A. Payne, Edgar van Loef, Cody M. Wilson, Kanai S. Shah, Utpal N. Roy, Arnold Burger, Lynn A. Boatner, Woon-Seng Choong, William W. Moses, Appl. Phys. Lett. 92 (2008) 083508.

[3] L. A. Boatner, J. O. Ramey, J. A. Kolopus, R. Hawrami, W. M. Higgins, E. van Loef, J. Glodo, K. S. Shah, Emmanuel Rowe, Pijush Bhattacharya, Eugene Tupitsyn, Michael Groza, Arnold Burger, N. J. Cherepy, S. A. Payne, J. Cryst. Growth 312 (2010) 1213.

[4] N. J. Cherepy, B. W. Sturm, O. B. Drury, T. A. Hurst, S. A. Sheets, L. E. Ahle, C. K. Saw, M. A. Pearson, S. A. Payne, A. Burger, L. A. Boatner, J. O. Ramey, E. V. van Loef, J. Glodo, R. Hawrami, W. M. Higgins, K. S. Shah, W. W. Moses, Proc. SPIE 7449 (2009) 74490F.

[5] Leonard Alaribe, Christian Disch, Alex Fauler, Ralf Engels, Egbert Keller, Angelica Cecilia, Tomy dos Santos Rolo, Elias Hamann, Michael Fiederle, IEEE T. Nucl. Sci. 59 (2012) 2193.

[6] R. Hawrami, J. Glodo, K. S. Shah, N. Cherepy, S. Payne, A. Burger, L. Boatner, J. Cryst. Growth 379 (2013) 69.

[7] Yuntao Wu, Qi Li, Daniel J. Rutstrom, Ian Greeley, Luis Stand, Matthew Loyd, Merry Koschan, Charles L. Melcher, Nucl. Instrum. Meth. A 954 (2020) 161242.

[8] Mikhail S. Alekhin, Daniel A. Biner, Karl W. Krämer, Pieter Dorenbos, J. Lumin. 145 (2014) 723.

[9] Gregory Bizarri, Edith D. Bourret-Courchesne, Zewu Yan, Steve E. Derenzo, IEEE T. Nucl. Sci. 58 (2011) 3403.

[10] E. D. Bourret-Courchesne, G. Bizarri, R. Borade, Z. Yan, S. M. Hanrahan, G. Gundiah, A. Chaudhry, A. Canning, S. E. Derenzo, Nucl. Instrum. Meth. A 612 (2009) 138.

[11] U. Shirwadkar, R. Hawrami, J. Glodo, E. V. D. van Loef, K. S. Shah, IEEE T. Nucl. Sci. 60 (2013) 1011.

[12] Kan Yang, Mariya Zhuravleva, Charles L. Melcher, Phys. Status Solidi R 5 (2011) 43.

[13] Yuntao Wu, Mariya Zhuravleva, Adam C. Lindsey, Merry Koschan, Charles L. Melcher, Nucl. Instrum. Meth. A 820 (2016) 132.

[14] Jarek Glodo, Edgar V. van Loef, Nerine J. Cherepy, Stephen A. Payne, Kanai S. Shah, IEEE T. Nucl. Sci. 57 (2010) 1228.

[15] Daniel Rutstrom, Luis Stand, Merry Koschan, Charles L. Melcher, Mariya Zhuravleva, J. Lumin. 216 (2019) 116740.

[16] Mikhail S. Alekhin, Johan T. M. de Haas, Karl W. Krämer, Pieter Dorenbos, IEEE T. Nucl. Sci. 58 (2011) 2519.

[17] Mikhail S. Alekhin, Karl W. Krämer, Pieter Dorenbos, Nucl. Instrum. Meth. A 714 (2013) 13.

[18] Gautam Gundiah, Martin Gascón, Gregory Bizarri, Stephen E. Derenzo, Edith D. Bourret-Courchesne, J. Lumin. 159 (2015) 274.

[19] D. L. Dexter, James H. Schulman, J. Chem. Phys. 22 (1954) 1063.

[20] A. I. Burshteĭn, Sov. Phys. Uspekhi 27 (1984) 579.

[21] D. L. Dexter, J. Chem. Phys. 21 (1953) 836.

[22] Chen Ling, Wang Meitian, Wang Shishua, J. Alloy. Compd. 256 (1997) 112.

[23] L. Stand, M. Zhuravleva, B. Chakoumakos, J. Johnson, M. Loyd, Y. Wu, M. Koschan, C. L. Melcher, J. Cryst. Growth 486 (2018) 162.

[24] Yuntao Wu, Dan Han, Bryan C. Chakoumakos, Hongliang Shi, Shiyou Chen, Mao-Hua Du, Ian Greeley, Matthew Loyd, Daniel J. Rutstrom, Luis Stand, Merry Koschan, Charles L. Melcher, J. Mater. Chem. C 6 (2018) 6647.

[25] Cao Baopeng, Wang Shihua, Zhao Xinhua, J. Alloy. Compd. 181 (1992) 511.

[26] Weronika Wolszczak, Karl W. Krämer, Pieter Dorenbos, Phys. Status Solidi R. 13 (2019) 1900158.

[27] Casper van Aarle, Karl W. Krämer, Pieter Dorenbos, J. Lumin. 238 (2021) 118257.

[28] R. H. P. Awater, M. S. Alekhin, D. A. Biner, K. W. Krämer, P. Dorenbos, J. Lumin. 212 (2019) 1.

[29] G. Meyer, Advances in the Synthesis and Reactivity of Solids, Vol. 2, p.1-16. JAI Press Inc. 1994.

[30] Johan T. M. de Haas, Pieter Dorenbos, IEEE T. Nucl. Sci. 55 (2008) 1086.

[31] L. Stand, M. Zhuravleva, G. Camarda, A. Lindsey, J. Johnson, C. Hobbs, C. L. Melcher, J. Cryst. Growth 439 (2016) 93.

[32] Marvin J. Weber, Phys. Rev. B 4 (1971) 2932.

[33] Winicjusz Drozdowski, Andrzej J. Wojtowicz, Nucl. Instrum. Meth. A 486 (2002) 412.

5

Light yield and thermal quenching of Ce^{3+} and Pr^{3+} co-doped $LaBr_3$:Sm^{2+} near-infrared scintillators

$LaBr_3$:Ce^{3+} is a compound with excellent scintillation properties, but its ultraviolet emission does not match well with the detection efficiency curves of silicon based photodetectors. In this work, Sm^{2+} is studied as an activator for $LaBr_3$ as its near-infrared emission can be detected with close to 100% efficiency by such photodetectors. $LaBr_3$:Sm^{2+} single crystals were grown with and without co-doping of Ce^{3+} or Pr^{3+}. The samples were studied by means of X-ray excited and photoluminescence spectroscopy at temperatures between 10 K and 300 K. Their spectroscopic properties are compared to $LaBr_3$:Ce^{3+} and $LaBr_3$:Eu^{2+}. The effect of using Ce^{3+} or Pr^{3+} as scintillation sensitiser for Sm^{2+} is assessed. It is found that energy transfer from host to Sm^{2+} greatly improves upon Ce^{3+} co-doping, but the quenching temperature of the Sm^{2+} emission decreases. The quenching mechanism of both the Ce^{3+} and Sm^{2+} emission in $LaBr_3$ is elaborated on. Furthermore, the effect of charge compensating defects on the light yield and spectroscopic properties is discussed.

The content of this chapter is based on the following publication:
Casper van Aarle, Nils Roturier, Daniel A. Biner, Karl W. Krämer, Pieter Dorenbos, Opt. Mater. 145 (2023) 114375.

5.1. Introduction

When $LaBr_3$:Ce^{3+} was first discovered as a γ-ray scintillator in 2001, it was found to have a light yield of 61,000 ph/MeV and an energy resolution of 2.8% at 662 keV was attained [1]. Its high light yield and fast decay time of 30 ns make $LaBr_3$:Ce^{3+} suitable for medical imaging applications where high time resolution and count rates are required, such as time-of-flight positron emission tomography [2] and photon-counting computed tomography [3]. Its energy resolution makes it possible to discriminate between γ-rays with smaller energy difference than what is achieved with more commonly used NaI:Tl^+ scintillators. $LaBr_3$:Ce^{3+} is therefore also suitable for use in γ-ray spectrometers [4] and radio-isotope identification devices [5]. These days, $LaBr_3$:Ce^{3+} scintillation crystals are widely available as commercial products.

Another useful property of $LaBr_3$:Ce^{3+} is its exceptionally large Stokes shift of 0.54 eV [6] resulting in low self-absorption losses [7], which is favourable for applications where large crystals are required. Even in large crystals of $CeBr_3$ self-absorption losses are minimal [7, 8]. The reason behind this large Stokes shift has been studied by Andriessen et al. [9]. $LaBr_3$ has the UCl_3 type crystal structure, the same as $CeBr_3$ and $PrBr_3$, in which the cation has 9 fold coordination. Upon further decrease of the cation size, e.g. $NdBr_3$, compounds start to crystallise in the $PuBr_3$ type structure, where the cation has 8 fold coordination [10]. Ab initio calculations have shown that upon 4f → 5d excitation of Ce^{3+}, the corresponding decrease in its ionic radius causes deformation of the direct environment of Ce^{3+}. One bromide ion is pushed away and the other 8 are pulled towards Ce^{3+}, effectively reducing the coordination number to 8 [9]. This increases the crystal field splitting and moves the lowest 5d excited state to even lower energy without the usual broadening of the Ce^{3+} emission bands, decreasing the overlap between the Ce^{3+} emission and its absorption bands.

In 2013, significant improvements were made to $LaBr_3$:Ce^{3+} by means of Sr^{2+} co-doping. The co-doping greatly improved the scintillator's proportionality and resulted in a slight increase in light yield to 78,000 ph/MeV. When coupled to a Hamamatsu R6231-100 photomultiplier tube (PMT), the attained energy resolution of 2.04% was close to the fundamental limit achievable when 24,000 scintillation photons are being detected [11]. Further improvement of the energy resolution thus requires increasing the number of detected photons.

The number of detected photons is determined by the light yield of a scintillator and the detector efficiency. Only 31% of the scintillation photons were detected when recording the 2.04% energy resolution pulse height spectrum [11]. Silicon based photodetectors, such as avalanche photodiodes (APD) or silicon photomultipliers (SiPM) typically have much higher detection efficiencies which can reach close to 100% in the visible and NIR part of the spectrum. For wavelengths shorter than 400 nm, the detection efficiency of such photodetectors is typically lower due to a rapid increase in the absorption coefficient of silicon, causing scintillation photons to be absorbed in the dead layer of the detector. In the case of $LaBr_3$:Ce^{3+},Sr^{2+}, this reduces the number of detected photons by approximately 20% [12]. A solution to this problem would be the use of activators that emit at wavelengths longer than 400 nm.

Some activators other than Ce^{3+} have already been attempted for $LaBr_3$, among which are Pr^{3+} and Eu^{2+}. $LaBr_3$:Pr^{3+} shows exclusively Pr^{3+} $4f^2$ → $4f^2$ line emission with a decay

time of 11 µs. An energy resolution of 3.2% and light yield of over 60,000 ph/MeV have been observed when coupled to an APD [13]. $LaBr_3$:Eu^{2+} shows Eu^{2+} $4f^6 5d \rightarrow 4f^7$ broad band emission around 430 nm. A light yield of 43,000 ph/MeV and energy resolution of 6% have been reported [14].

Sm^{2+} is another potential candidate as an activator for $LaBr_3$. Its energy levels are shown in Figure 5.1 together with those of Ce^{3+}, Pr^{3+}, and Eu^{2+}. The energy of the lowest $4f^{n-1}5d$ levels ($5d_1$) of Ce^{3+} and Eu^{2+} are based on their $4f^{n-1}5d \rightarrow 4f^n$ emission wavelengths in $LaBr_3$ [6]. The energy of the $5d_1$ levels of Pr^{3+} and Sm^{2+} are calculated using their constant energy difference to Ce^{3+} and Eu^{2+}, respectively [15, 16].

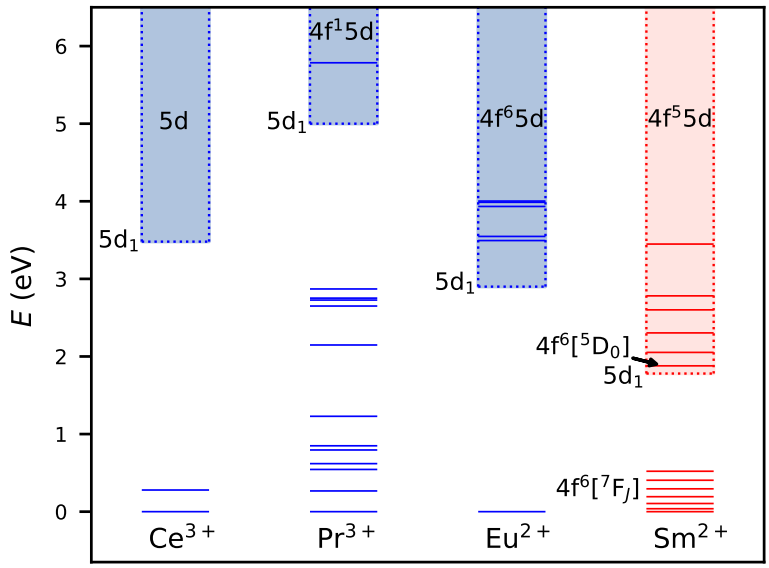

Figure 5.1: Diagram showing the energy levels of Ce^{3+}, Pr^{3+}, Eu^{2+}, and Sm^{2+} in $LaBr_3$. The horizontal lines represent $4f^n$ levels. The ranges of the $4f^{n-1}5d$ levels are shown by coloured bands.

At room temperature, Sm^{2+} shows exclusively $4f^6[^5D_0] \rightarrow 4f^6[^7F_J]$ line emission when the $5d_1$ level lies more than about 0.2 eV above the $4f^6[^5D_0]$ level. When the $5d_1$ level lies below the $4f^6[^5D_0]$ level, exclusively $4f^5 5d \rightarrow 4f^6$ broad band emission is observed. In compounds where the $5d_1$ level lies less than 0.2 eV above the $4f^6[^5D_0]$ level, the $4f^6 \rightarrow 4f^6$ and $4f^5 5d \rightarrow 4f^6$ emissions are often observed simultaneously. The ratio between the $4f^6 \rightarrow 4f^6$ and $4f^5 5d \rightarrow 4f^6$ emission is temperature dependent. With increasing temperature, the $4f^6 \rightarrow 4f^6$ emission lines decrease in intensity and $4f^5 5d \rightarrow 4f^6$ emission intensity increases. In compounds where Sm^{2+} shows exclusively $4f^5 5d \rightarrow 4f^6$ emission at room temperature, $4f^6 \rightarrow 4f^6$ line emission is often still observed at cryogenic temperatures. For any given temperature, the intensity of these $4f^6 \rightarrow 4f^6$ emission lines decreases with decrease of the $5d_1$ level energy.

The Sm^{2+} $4f^55d \rightarrow 4f^6$ emission typically lies in the near-infrared part of the spectrum and can therefore be efficiently detected by silicon based photodetectors. Its decay time lies between 1.5 µs and 15 µs [17, 18], which is fast enough for application in low count rate γ-ray spectroscopy. Compounds with exclusively Sm^{2+}-doping have been reported to show light yields of up to 33,000 ph/MeV [19]. A benefit to using Sm^{2+} is that $4f^55d \rightarrow 4f^6$ emission may have any of the ^7F_J levels as final state, while absorption exclusively takes place from the $^7F_0$ ground state. As a consequence, self-absorption losses in Sm^{2+}-doped scintillators are minimal, especially if the Sm^{2+} concentration can remain low [20].

Radiationless energy transfer is possible when the emission bands of a sensitiser overlap with the absorption bands of an acceptor [21]. Since the Sm^{2+} $4f^55d \rightarrow 4f^6$ emission lies in the infrared, its $4f^6 \rightarrow 4f^55d$ absorption bands cover the entire visible spectrum. This makes it possible to sensitise Sm^{2+} with many different co-dopants. Efficient sensitisation of Sm^{2+} by Eu^{2+} for scintillation was first demonstrated in SrI_2:Eu^{2+},Sm^{2+}, where it was found that almost all Eu^{2+} excitations are transferred non-radiatively to Sm^{2+} upon co-doping with as little as 0.5% Sm^{2+} [18]. The same strategy has yielded an energy resolution of 3.2% and light yield of 45,000 ph/MeV when coupling a $CsBa_2I_5$:2%Eu^{2+},%Sm^{2+} crystal to an APD [22].

In this work the feasibility of using Sm^{2+} as a dopant in $LaBr_3$ is assessed. Additionally, the effect of using Ce^{3+} or Pr^{3+} as a scintillation sensitiser is explored. A comparison is made with the spectroscopic and scintillation properties of $LaBr_3$:Eu^{2+}. For this study, $LaBr_3$ samples were synthesised with a 1% doping concentration of Sm^{2+} or Eu^{2+}. Two Sm^{2+}-doped samples were co-doped with 5% Ce^{3+} or 1% Pr^{3+}. Additionally, $CeBr_3$:1%Sm is studied. The scintillation characteristics are assessed through X-ray excited emission spectra. Thermoluminescence (TL) measurements are performed to study the effect of charge compensating defects. Lastly, photoluminescence measurements are performed to study the energy transfer from host and sensitiser to Sm^{2+} and to determine the location of the Sm^{2+} $5d_1$ level.

5.2. Experimental Techniques

Crystals of $LaBr_3$ and $CeBr_3$ doped with Ce^{3+}, Pr^{3+}, Sm^{2+}, and/or Eu^{2+} were grown from the binary halides MBr_3 (M = La, Ce, Pr) and MBr_2 (M = Sm, Eu) by the vertical Bridgman technique. The binary halides MBr_3 (M = La, Ce, Pr, Sm, Eu) were prepared by the ammonium bromide method [23]. The rare earth oxide (La_2O_3, 5N; CeO_2, 5N; Pr_6O_{11}, 5N5; Eu_2O_3, 5N, all from Metall Rare earth Ltd.; Sm_2O_3, > 3N, Fluka) was dissolved in concentrated HBr acid (47%, suprapur, Merck) and an excess of NH_4Br (p.a., sublimed, Merck) added in a M to NH_4 ratio of 2 to 7. The solution was dried up on a sand bath to yield the anhydrous ternary compound $(NH_4)_3MBr_6$, which is subsequently decomposed to MBr_3 by heating in vacuum. $LaBr_3$, $CeBr_3$, $PrBr_3$, and $SmBr_3$ were sublimed in a silica apparatus under high vacuum for purification. $EuBr_2$ was obtained by heating $EuBr_3$ in vacuum at 500 °C and used without further purification. $SmBr_2$ was obtained by reduction of $SmBr_3$ with Sm metal (3N; Alfa) in a Ta ampoule. The Ta ampoule was sealed by helium arc-welding and enclosed into a silica ampoule under vacuum. The ampoule was heated to 900 °C for 7 days.

Stoichiometric amounts of the binary halides (about 5 g per sample) were sealed in Ta ampoules. An inert ampoule, such as Ta, is required to maintain a pure Sm^{2+} state in the crystal. $LaBr_3$:1% Eu^{2+} was grown in a silica ampoule, since Eu^{2+} is less sensitive to oxidation than Sm^{2+}. The ampoules were heated in a Bridgman furnace to 800 °C ($LaBr_3$) or 750 °C ($CeBr_3$), respectively, i.e., above the congruent melting point of the host material. After 1 day at constant temperature, the crystal growth was started by slowly moving up the furnace. The samples were cooled to room temperature within about 10 days. Crystals were cleaved from the boules for spectroscopic investigations. The denoted doping level represents the melt composition. Since starting materials and products are highly hygroscopic and sensitive to oxidation, all handling was done under strictly dry and oxygen-free conditions (H_2O and $O_2 < 0.1$ ppm) in glove boxes and sealed sample containers. Experiments on $LaBr_3$ and $CeBr_3$ without divalent dopants were performed on samples of which the synthesis was previously reported in literature: $LaBr_3$:5%Ce^{3+} [24], $LaBr_3$:0.5%Pr^{3+} [6], and $CeBr_3$ [25].

X-ray excited emission spectra were recorded using a Varex VF-80JM X-ray tube with tungsten anode operated at 80 kV and 1 mA. A 1 mm thick copper filter was used to filter out the low energy X-rays that otherwise may cause radiation damage to the sample. The samples were mounted directly on the cold finger of a Janis He or N_2 cryostat and placed in front of the X-ray tube. The sample chamber was kept at a pressure below 10^{-4} mbar during operation. The sample emission was monitored under a 90°angle with respect to the X-ray beam and was collected through an Ocean Optics QP600-2-VIS optical fibre before being detected using an Ocean Optics QE65Pro spectrometer. Spectra were corrected for the optical fibre attenuation and spectrometer sensitivity. The temperature of the sample was controlled using a Lakeshore temperature controller.

For light yield measurements, a sample holder with fused silica window was filled with small grains of the studied sample. An identical sample holder was filled with small grains of a $LaBr_3$:Ce^{3+} reference sample with known light yield of 76,000 ph/MeV [24]. Light yields were determined by taking the integral of the X-ray excited emission spectrum of the studied sample and comparing it to that of the reference sample at room temperature. The reference sample was mounted on the same cryostat as the studied sample to ensure the geometry of the setup was identical between the measurements.

Thermoluminescence measurements were performed on the same experimental setup as the X-ray excited emission spectra. Samples were given an X-ray dose by irradiating the sample for 10 minutes at 10 K. After irradiation, the X-ray tube was turned off and a constant heating rate of 15 K/min was applied. The emission spectra were continuously measured by the spectrometer and the integral of the spectra was taken to find the total intensity.

Photoluminescence excitation and emission spectra were measured using a 450 W Xenon lamp and Horiba Gemini 180 monochromator as excitation source. The samples were mounted directly on the cold finger of a Janis He or N_2 cryostat and the sample chamber was kept at a pressure below 10^{-4} mbar during the experiment. Emission light from the sample first passed through an optical filter to block the excitation light before passing through a SpectraPro-SP2358 monochromator. For excitation spectra, the emission light was detected using a Hamamatsu R7600U-20 PMT. The excitation spectra were corrected for the intensity of the Xenon lamp. For emission spectra, the the emission was

detected by a Hamamatsu C9100-13-EM-CCD camera. The temperature was controlled using a Lakeshore temperature controller.

Photoluminescence decay curves were measured using an EKSPLA NT230 OPO laser as excitation source, with a pulse width of 6 ns and repetition rate of 100 Hz. The temperature of the samples was controlled in an identical way as for the photoluminescence excitation and emission spectra. The excitation light was filtered out using an optical filter, after which the emission light passed through a SpectraPro-SP2358 monochromator before being detected by a Hamamatsu R7600U-20 PMT. The signal from the PMT was converted to a digital signal using a CAEN DT5730 digitizer.

5.3. Results

As the effect of co-doping $LaBr_3$:Sm^{2+} with Ce^{3+} and Pr^{3+} is studied, spectroscopic results on $LaBr_3$:5%Ce^{3+} and $LaBr_3$:0.5%Pr^{3+} are also presented to yield information on the role of these dopants in the scintillation mechanism. Figure 5.2a shows the X-ray excited emission spectrum of $LaBr_3$:5%Ce^{3+}. The two strong emission bands around 380 nm are ascribed to the Ce^{3+} 5d → 4f transitions. The weak band around 440 nm was previously assigned to self-trapped exciton (STE) emission of $LaBr_3$ [6].

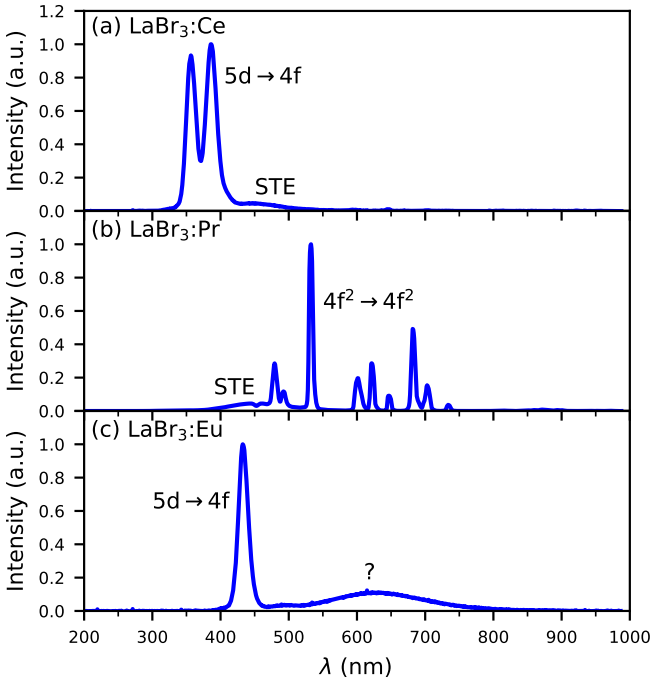

Figure 5.2: X-ray excited emission spectra of a) $LaBr_3$:5%Ce^{3+}, b) $LaBr_3$:0.5%Pr^{3+}, and c) $LaBr_3$:1%Eu^{2+} at 10 K.

The emission spectrum of $LaBr_3$:0.5%Pr^{3+} is shown in Figure 5.2b. The spectrum contains predominantly sharp emission lines that are ascribed to the Pr^{3+} $4f^2 \rightarrow 4f^2$ transitions. It shows a weak broad band around 440 nm, similar to the STE emission observed in $LaBr_3$:Ce^{3+}.

$LaBr_3$:1%Eu^{2+} is studied for comparison with $LaBr_3$:Sm^{2+}, as Eu^{2+} has the same valence and similar ionic radius as Sm^{2+} and is spectroscopically more simple. Figure 5.2c shows the X-ray excited emission spectrum of $LaBr_3$:1%Eu^{2+}. It shows an intense emission band with a maximum at 430 nm, which is assigned to the $4f^65d \rightarrow 4f^7$ transition [6]. Additionally, a broad emission band of unknown origin is observed between 500 nm and 800 nm.

Figure 5.3a shows the X-ray excited emission spectra of $LaBr_3$:1%Sm^{2+}. At 10 K it shows almost exclusively sharp line emission between 680 nm and 850 nm that corresponds to the $4f^6[^5D_0] \rightarrow 4f^6[^7F_J]$ transitions of Sm^{2+}. When increasing the temperature to 100 K, a broad band with a maximum at 790 nm appears and the intensity of the line emission decreases. Based on the Eu^{2+} $4f^65d \rightarrow 4f^7$ emission wavelength, the Sm^{2+} $4f^55d \rightarrow 4f^6$ emission wavelength is expected near 750 nm [16]. Therefore, the broad band is assigned to the Sm^{2+} $4f^55d \rightarrow 4f^6$ emission. At 200 K, the $4f^6 \rightarrow 4f^6$ lines have completely disappeared and the $4f^55d \rightarrow 4f^6$ has gained further in intensity. Between 200 K and 300 K, the intensity of the $4f^55d \rightarrow 4f^6$ decreases and at 300 K only 20% of the intensity remains.

Figure 5.3b shows the X-ray excited emission spectra of $LaBr_3$:5%Ce^{3+},1%Sm^{2+}. The emission spectrum at 10 K again shows Sm^{2+} $4f^6 \rightarrow 4f^6$ line emission, but the $4f^55d \rightarrow 4f^6$ is already visible at this temperature as well. This shows that Ce^{3+} doping slightly lowers the Sm^{2+} $4f^55d$ energy level with respect to the $4f^6[^5D_0]$ level, likely caused by an increase in crystal field splitting strength. In addition to the Sm^{2+} emission, weak Ce^{3+} $5d \rightarrow 4f$ emission bands are visible between 350 nm and 420 nm. Again, upon increasing the temperature the Sm^{2+} $4f^6 \rightarrow 4f^6$ emission decreases in intensity while the $4f^55d \rightarrow 4f^6$ emission increases until it quenches between 200 K and 300 K.

The X-ray excited emission spectra for $LaBr_3$:1%Pr^{3+},1%Sm^{2+} are shown in Figure 5.3c. At all temperatures, the spectrum contains intense Pr^{3+} $4f^2 \rightarrow 4f^2$ lines in addition to the Sm^{2+} emission, indicating that transfer from Pr^{3+} is inefficient. At 10 K, it can be seen at 825 nm that still a Sm^{2+} $4f^6 \rightarrow 4f^6$ line is visible on top of the $4f^55d \rightarrow 4f^6$ emission, but at higher temperatures this has already disappeared. As opposed to $LaBr_3$:1%Sm^{2+} and $LaBr_3$:5%Ce^{3+},1%Sm^{2+}, the intensity of the Sm^{2+} $4f^55d \rightarrow 4f^6$ emission is highest at 10 K and steadily decreases upon increase of temperature.

In Figure 5.3d, the X-ray excited emission spectra of $CeBr_3$:1%Sm^{2+} are shown. Similar to $LaBr_3$:5%Ce^{3+},1%Sm^{2+}, it shows weak Ce^{3+} $5d \rightarrow 4f$ emission between 350 nm and 420 nm. The increase in Ce^{3+} concentration compared to $LaBr_3$:5%Ce^{3+},1%Sm^{2+} has lowered the Sm^{2+} $4f^55d$ level even further and the Sm^{2+} emission around 790 nm now contains exclusively $4f^55d \rightarrow 4f^6$ emission already at 10 K. Upon increase of the temperature, the Sm^{2+} emission rapidly quenches and is already completely gone at 200 K. As opposed to $LaBr_3$:5%Ce^{3+},1%Sm^{2+}, the Ce^{3+} $5d \rightarrow 4f$ emission intensity also decreases with increasing temperature, which is ascribed to energy transfer between Ce^{3+} ions increasing the rate of energy transfer to Sm^{2+}.

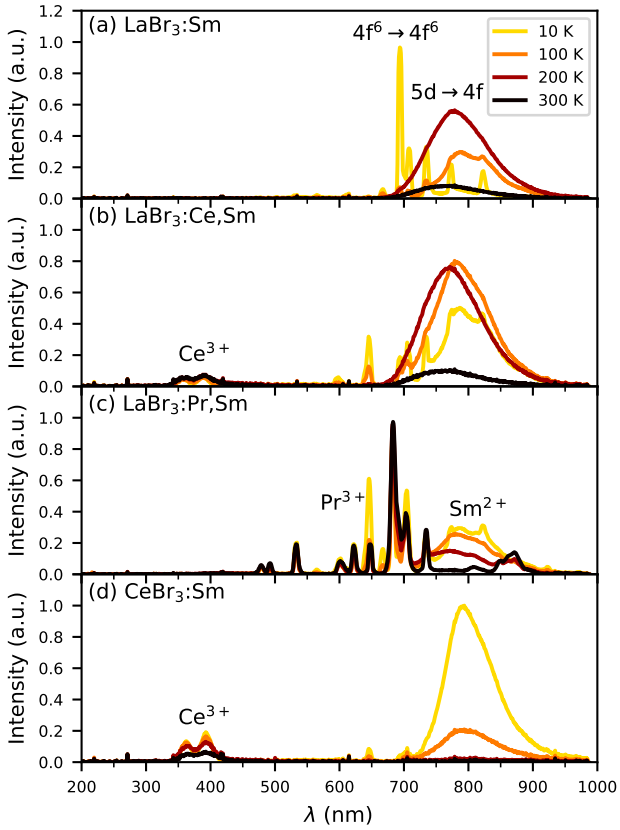

Figure 5.3: X-ray excited emission spectra of a) $LaBr_3$:1%Sm^{2+}, b) $LaBr_3$:5%Ce^{3+},1%Sm^{2+}, c) $LaBr_3$:1%Pr^{3+},1%Sm^{2+}, and d) $CeBr_3$:1%Sm^{2+}.

To further investigate the quenching of Sm^{2+} emission, the integrated emission intensity under X-ray excitation of various compounds is plotted against temperature in Figure 5.4. Figure 5.4a shows the X-ray excited intensity of Ce^{3+} emission in $LaBr_3$:5%Ce^{3+} and $CeBr_3$. $LaBr_3$:5%Ce^{3+} shows stable emission intensity ranging all the way from 10 K to 600 K. Above 600 K, the intensity drops due to thermal quenching. The value at which the intensity reaching 50% of its maximum values (T_{50}) falls outside the range of the experimental setup. The quenching curve is extrapolated using the a single barrier Arrhenius equation and the T_{50} value is estimated to be 715 K.

For $CeBr_3$, the intensity slowly decreases over the entire temperature range, which was also observed by Awater et al. [26] and similar to what was observed for Ce^{3+} emission in $CeBr_3$:Sm^{2+}. In undoped $CeBr_3$, the Ce^{3+} excitations are not lost to Sm^{2+}, but the gradual decrease is ascribed to temperature enhanced concentration quenching. Around 600 K, a steeper decline of the intensity is observed, which is the temperature at which thermal quenching sets in. The value for T_{50} is around 675 K, slightly lower than for $LaBr_3$:5%Ce^{3+}.

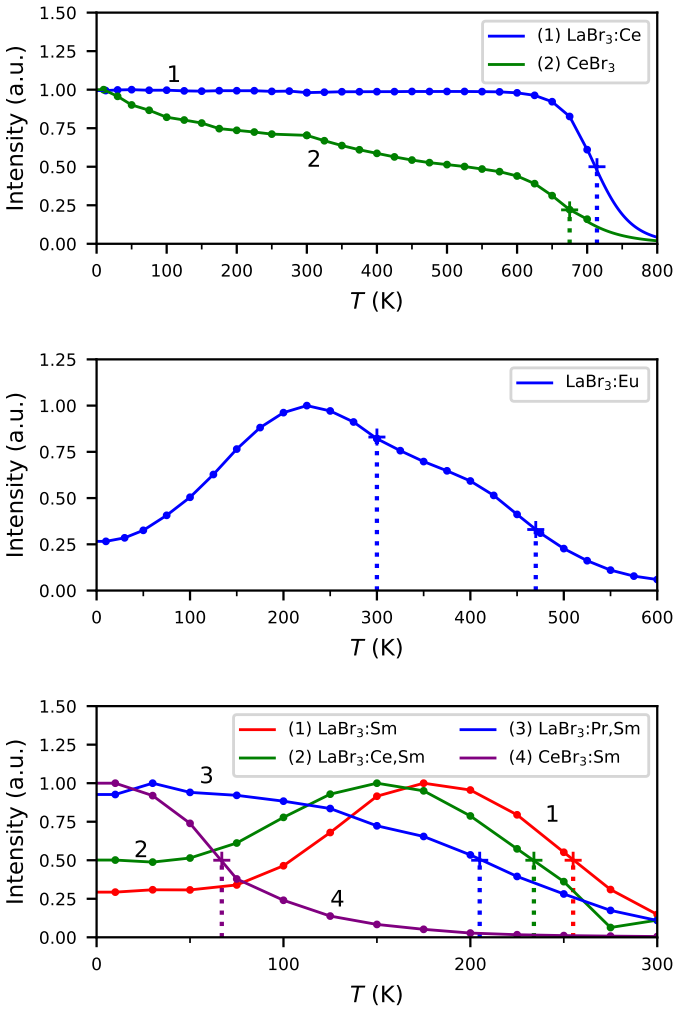

Figure 5.4: Integrated X-ray excited emission intensities of a) $LaBr_3$:5%Ce and $CeBr_3$, b) $LaBr_3$:1%Eu^{2+} and c) $LaBr_3$:1%Sm^{2+}, $LaBr_3$:5%Ce^{3+},1%Sm^{2+}, $LaBr_3$:1%Pr^{3+},1%Sm^{2+} and $CeBr_3$:1%Sm^{2+}.

Figure 5.4b shows the X-ray excited emission intensity of $LaBr_3$:Eu^{2+}. When going from 10 K to 225 K, the emission becomes 4 times more intense, very similar to what was observed in $LaBr_3$:Ce^{3+} co-doped with Ca^{2+}, Sr^{2+} or Ba^{2+}, indicating the formation of electron traps when doping $LaBr_3$ with divalent cations [24]. Further increasing the temperature above 225 K causes the intensity to decrease again due to thermal quenching. The intensity drops in two steps, one with a T_{50} value of approximately 300 K, the other around 470 K. This suggests there are multiple Eu^{2+} sites present in the sample.

Figure 5.4c shows the X-ray excited emission intensity of the four Sm^{2+}-doped samples. Just like $LaBr_3$:1%Eu^{2+}, the emission intensity of $LaBr_3$:1%Sm^{2+} (curve 1) becomes 4 times more intense upon increasing the temperature from 10 K to 200 K. Further increasing the temperature beyond 200 K causes thermal quenching and rapidly decreases the intensity. The emission intensity of $LaBr_3$:1%Sm^{2+} however does not drop in two steps, as was observed for $LaBr_3$:1%Eu^{2+}. T_{50} is reached at 255 K.

$LaBr_3$:5%Ce^{3+},1%Sm^{2+} (curve 2) shows similar behaviour to $LaBr_3$:1%Sm^{2+}. Increasing the temperature from 10 K initially causes the intensity to increase after which thermal quenching starts. The increase in intensity between 10 K and 150 K is however two times less than for $LaBr_3$:1%Sm^{2+}, which could be caused by Ce^{3+} competing with traps at capturing electrons from the conduction band. Another difference is that thermal quenching begins at approximately 25 K lower temperature compared to $LaBr_3$:1%Sm^{2+}, giving a T_{50} value of 235 K.

The intensity of $LaBr_3$:1%Pr^{3+},1%Sm^{2+} gradually decreases upon increase of the temperature from 10 K to 300 K. No clear onset of thermal quenching is observed. The total intensity reached 50% of its maximum value at 205 K. Lastly, the $CeBr_3$:Sm^{2+} emission intensity also exclusively decreases upon heating from 10 K. The quenching behaviour is not as gradual as in $LaBr_3$:1%Pr^{3+},1%Sm^{2+} and resembles that of the thermal quenching of $LaBr_3$:1%Sm^{2+}, but occurring at 185 K lower temperature, giving a T_{50} value of 70 K. The T_{50} values of all compounds are provided in Table 5.1.

For each compound, the light yield was determined at the temperature at which the X-ray excited emission spectrum has its highest intensity, and also at 300 K. Both light yield values are provided in Table 5.1. The sample with the lowest light yield of 7,000 ph/MeV is $LaBr_3$:Sm^{2+}, recorded at 175 K. Co-doping with 5% Ce^{3+} resulted in a significant increase to 25,000 ph/MeV, but the maximum intensity was attained at 150 K. For $CeBr_3$:1%Sm, a further increase to 34,000 ph/MeV is observed, but now at 10 K. This indicates the effectiveness of using Ce^{3+} as a scintillation sensitiser for Sm^{2+} in $LaBr_3$, but also shows its negative effect on the quenching temperature. At room temperature, thermal quenching causes the light yields of the Sm^{2+}-doped samples to be lower than their maximum value. However, even though $LaBr_3$:5%Ce^{3+},1%Sm^{2+} quenches at lower temperature than $LaBr_3$:1%Sm^{2+}, the room temperature light yield of the 5% Ce^{3+} co-doped sample is still higher than the sample without Ce^{3+} co-doping.

Table 5.1: Overview of maximum light yield Y_{max} determined at temperature T_{max}, the light yield at 300 K Y_{300K} and quenching temperature T_{50} of $LaBr_3$-type samples with various dopants.

Sample	Y_{max} (ph/MeV)	T_{max} (K)	Y_{300K} (ph/MeV)	T_{50} (K)
$LaBr_3$:Ce^{3+}	76,000	10-600	76,000 [24]	715
$CeBr_3$	78,000	10	55,000 [25]	675
$LaBr_3$:1%Eu^{2+}	21,000	225	17,000	300, 470
$LaBr_3$:1%Sm^{2+}	7,000	175	1,000	255
$LaBr_3$:5%Ce^{3+},1%Sm^{2+}	25,000	150	3,000	235
$LaBr_3$:1%Pr^{3+},1%Sm^{2+}	17,000	10	2,000	205
$CeBr_3$:1%Sm^{2+}	34,000	10	0	70

In both $LaBr_3$:Ce^{3+} and $CeBr_3$ that were co-doped with Ca^{2+}, Sr^{2+} or Ba^{2+}, the decrease in light yield when cooling below room temperature was observed together with shallow electron traps creating TL glow peaks between 50 K and 300 K [24, 26]. The origin of these electron traps was suggested to be Br^- vacancies forming as charge compensation for the divalent ions incorporated in the lattice. To investigate whether this is also the case for Eu^{2+} and Sm^{2+} samples, TL glow curves are shown in Figure 5.5. Glow peaks are observed for $LaBr_3$:1%Eu^{2+}, $LaBr_3$:1%Sm^{2+} and $LaBr_3$:5%Ce^{3+},1%Sm^{2+} at temperatures where the light yield increases under X-ray excitation in Figure 5.4c. No TL signal above noise level was found for $LaBr_3$:1%Pr^{3+},1%Sm^{2+} and $CeBr_3$:1%Sm^{2+}, which both show maximal intensity under X-ray excitation at 10 K.

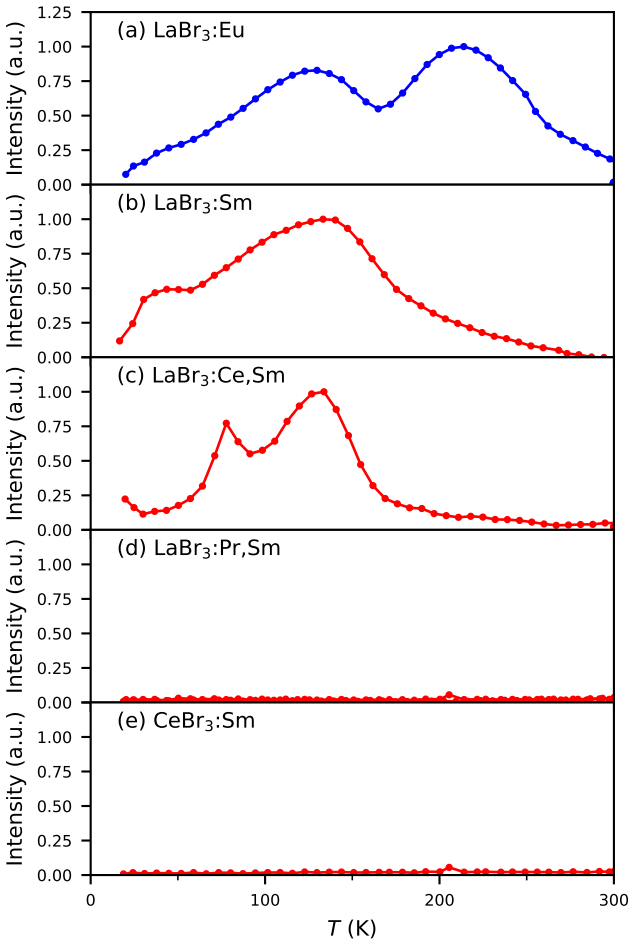

Figure 5.5: Thermoluminescence glow curves with 15 K/min heating rate of a) $LaBr_3$:1%Eu^{2+}, b) $LaBr_3$:1%Sm^{2+}, c) $LaBr_3$:5%Ce^{3+},1%Sm^{2+}, d) $LaBr_3$:1%Pr^{3+},1%Sm^{2+} and e) $CeBr_3$:1%Sm^{2+}.

A Br^- vacancy sitting next to Eu^{2+} or Sm^{2+} would turn the regular 9 fold coordinated site into an 8 fold coordinated site and thereby remove the relaxation mechanism causing the unusually large Stokes shift. To study this, photoluminescence excitation and emission measurements were performed. Figure 5.6a shows the photoluminescence emission and excitation spectra of $LaBr_3$:5%Ce^{3+}. The emission spectrum (curve 1) shows the Ce^{3+} 5d → 4f emission bands between 350 nm and 425 nm. The STE emission around 440 nm is not visible under photoexcitation at 295 nm. The excitation spectrum (curve 2) shows the 5 Ce^{3+} bands between 250 nm and 350 nm split up due to the crystal field splitting. The Stokes shift is determined to be 0.58 eV. The band between 210 nm and 250 nm is the host exciton band of $LaBr_3$ [6].

Figure 5.6b shows the photoluminescence emission and excitation spectra of $LaBr_3$:1%Eu^{2+}. Under excitation at 300 nm, the emission spectrum (curve 1) shows only the Eu^{2+} $4f^6 5d \rightarrow 4f^7$ emission band. The broad band emission around 600 nm observed under X-ray excitation in Figure 5.2c is not visible here, showing that this emission does not originate from Eu^{2+}. The excitation spectrum (curve 2) features no clear structure. Based on the small bend in the excitation spectrum near 380 nm, the band corresponding to excitation into the Eu^{2+} $5d_1$ level is approximated at 385 nm, giving a Stokes shift of 0.35 eV. This is in good agreement with the expectation that the Eu^{2+} Stokes shift is 0.61 times that of Ce^{3+} [27] and suggests that most of the Eu^{2+} emission comes from the same 9 fold coordinated sites that Ce^{3+} occupies in $LaBr_3$. The excitation spectrum of the Eu^{2+} emission shows a sudden drop in intensity at 230 nm where the host exciton band of $LaBr_3$ is located. This indicates that energy transfer from host excitons to Eu^{2+} is inefficient and is in line with the significantly lower value for the light yield compared to $LaBr_3$:Ce^{3+} given in Table 5.1.

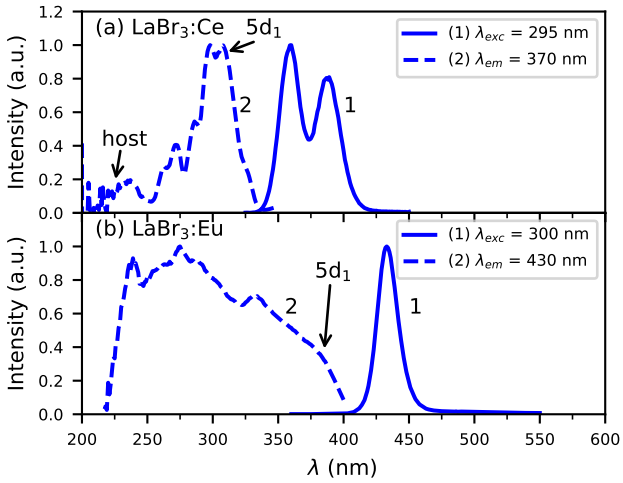

Figure 5.6: Photoluminescence excitation and emission spectra at 10 K of a) $LaBr_3$:5%Ce^{3+} and b) $LaBr_3$:1%Eu^{2+}. No Eu^{2+} emission is observed when exciting the $LaBr_3$ host.

Figure 5.7a shows the photoluminescence emission and excitation spectra of $LaBr_3$:1%Sm^{2+} at 10 K. Similar to under X-ray excitation in Figure 5.3a, the emission spectrum (curve 1) shows exclusively Sm^{2+} $4f^6 \rightarrow 4f^6$ lines between 690 nm and 850 nm. The excitation spectrum (curve 2) shows that Sm^{2+} absorbs across the entire visible spectrum, but shows a sudden drop in intensity at 230 nm similar to what was observed for $LaBr_3$:1%Eu^{2+}. The low light yield given in Table 5.1 can therefore be explained by inefficient energy transfer from host excitons to Sm^{2+}.

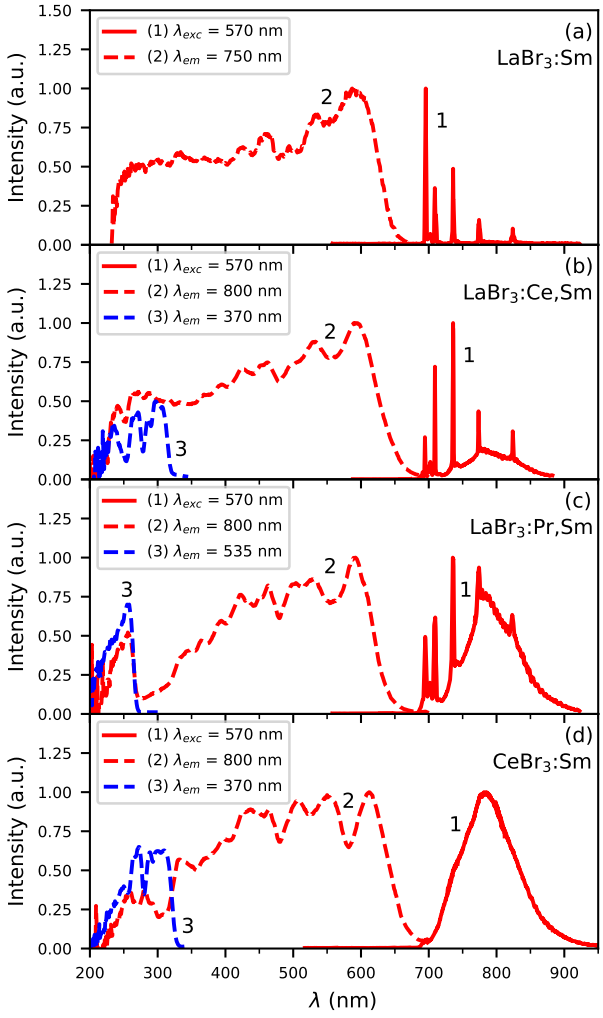

Figure 5.7: Photoluminescence excitation and emission spectra at 10 K of a) $LaBr_3$:1%Sm^{2+}, b) $LaBr_3$:5%Ce^{3+},1%Sm^{2+}, c) $LaBr_3$:1%Pr^{3+},1%Sm^{2+} and d) $CeBr_3$:1%Sm^{2+}. The bands of Ce^{3+} and Pr^{3+} are visible in the excitation spectrum of Sm^{2+} in co-doped samples.

In Figure 5.7b, the photoluminescence emission and excitation spectra of $LaBr_3$:5%Ce^{3+},1%Sm^{2+} at 10 K are shown. The emission spectrum (curve 1) shows Sm^{2+} $4f^6 \rightarrow 4f^6$ lines on top of a weak $4f^5 5d \rightarrow 4f^6$ band. This implies that the Sm^{2+} $5d_1$ level is shifted to slightly lower energies as a result of Ce^{3+} co-doping. The excitation spectrum of the Sm^{2+} emission (curve 2) shows the structure of the Ce^{3+} excitation bands between 200 nm and 340 nm. For comparison, curve 3 shows the excitation spectrum of the Ce^{3+} emission in this sample. The excitation spectrum of the Sm^{2+} emission no longer shows a sudden drop at 230 nm. This indicates that host excitons can transfer their energy to Ce^{3+} which in turn can pass it on to Sm^{2+}. This is in line with the increase in light yield observed when co-doping $LaBr_3$:1%Sm^{2+} with Ce^{3+}, as shown in Table 5.1.

Figure 5.7c shows the photoluminescence emission and excitation spectra of $LaBr_3$:1%Pr^{3+},1%Sm^{2+} at 10 K. The emission spectrum (curve 1) shows a further increase in the ratio of Sm^{2+} $4f^5 5d \rightarrow 4f^6$ to $4f^6 \rightarrow 4f^6$ emission compared to the $LaBr_3$:5%Ce^{3+},1%Sm^{2+} sample. The excitation spectrum of the Sm^{2+} emission (curve 2) shows an intense band around 250 nm, which is also visible in the excitation spectrum of the Pr^{3+} emission (curve 3). This band is assigned to the Pr^{3+} CT band [6]. From this can be concluded that also Pr^{3+} serves as an intermediate step in energy transfer from host exciton to Sm^{2+}.

Lastly, Figure 5.7d shows the photoluminescence emission and excitation spectra of $CeBr_3$:1%Sm^{2+} at 10 K. Just like under X-ray excitation, exclusively Sm^{2+} $4f^5 5d \rightarrow 4f^6$ emission is visible in the emission spectrum (curve 1), indicating that the Sm^{2+} $5d_1$ level is further shifted to lower energies. The excitation spectrum of the Sm^{2+} emission (curve 2) shows an anti-correlation with the excitation spectrum of the Ce^{3+} emission (curve 3). This means that energy transfer is inefficient, which can be caused by saturation effects due to the high absorption strength of $CeBr_3$ combined with a low Sm^{2+} concentration.

The decay dynamics of Sm^{2+} can give insight in the presence of multiple sites and the decay time is also an important characteristic for application. Therefore, photoluminescence decay curves of $LaBr_3$:Sm^{2+} are shown in Figure 5.8 upon excitation at 570 nm. Figure 5.8a shows the decay curves between 10 K and 150 K. At 10 K (curve 1), the decay shows strong non-exponential behaviour containing an initial fast component with a decay time faster than 100 ns. Gradually, the decay slows down and a slow component of around 100 µs appears. Upon increasing the temperature to 150 K (curve 4), the fast component gradually disappears and the slow component becomes faster.

On a timescale of the first few µs after excitation, the temperature dependent behaviour is more complex. For this, a zoom in of the first 3 µs of the decay curves shown in Figure 5.8a is shown in Figure 5.8b. Here it becomes visible that upon increasing the temperature from 10 K to 50 K, the fast component becomes even faster and a plateau develops in the luminescence decay curve between 0.2 µs and 1 µs. Upon increasing the temperature further to 100 K and 150 K, this plateau develops into a build up of the signal, indicating the $4f^5 5d$ level becomes more populated, likely from crossover from the $4f^6[^5D_0]$ level. The fast component however still persists while this build up with slower time constant develops. This behaviour can only be explained with multiple Sm^{2+} sites being present in the sample, some of which create the fast component and others cause the build up in signal.

The decay curves in Figure 5.8c are collected at temperatures between 150 K and 300 K, which is the temperature range in which thermal quenching of the X-ray excited emission takes place (Figure 5.4c). Going from 150 K (curve 4) to 200 K (curve 5), the strong non-exponential behaviour disappears, coinciding with the disappearing of the $4f^6 \rightarrow 4f^6$ lines in the X-ray excited emission spectrum in Figure 5.3a. However, the decay curves are still not well described by single exponential functions, again hinting towards the presence of multiple sites. Increasing the temperature further above 200 K causes the decay time to rapidly become shorter, which confirms that this is the temperature range in which thermal quenching takes place.

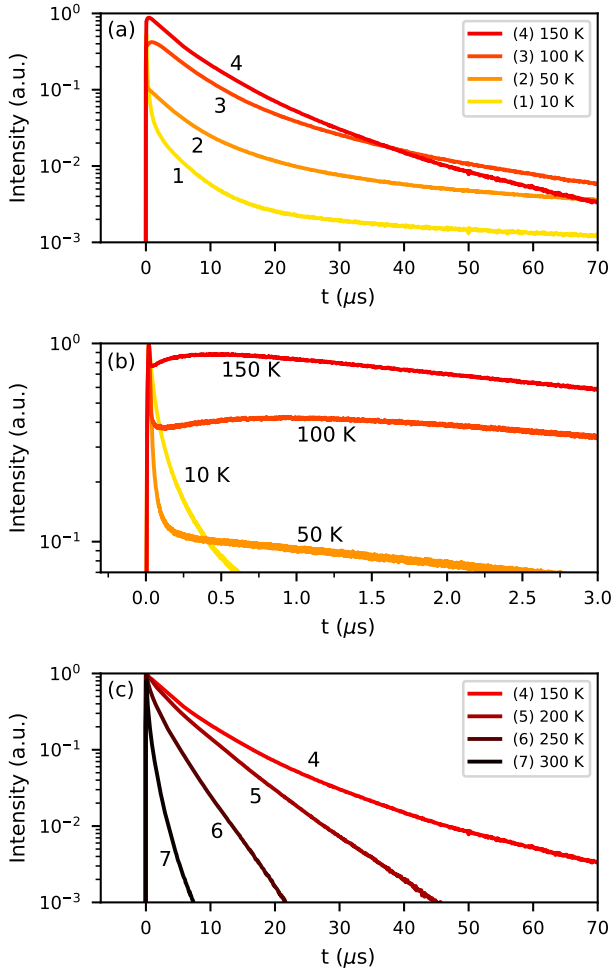

Figure 5.8: Photoluminescence decay curves of $LaBr_3$:1%Sm^{2+} excited at 570 nm and observed at 800 nm, a) between 10 K and 150 K, b) between 10 K and 150 K on a shorter timescale, c) between 150 K and 300 K.

5.4. Discussion

Incorporating divalent ions such as Sm^{2+} in a $LaBr_3$ lattice requires charge compensation, as was previously discussed by Alekhin et al. [24, 28]. It was found that co-doping $LaBr_3$:Ce^{3+} with Ca^{2+}, Sr^{2+}, or Ba^{2+} creates two additional Ce^{3+} sites, creates electron traps that cause TL peaks between 78K and 300 K, and decreases the light yield below room temperature. The suggested charge compensation mechanism was the creation of Br^- vacancies. The decrease in light yield below room temperature (Figure 5.4a and b) and accompanying TL peaks (Figure 5.5) were also observed for $LaBr_3$:1%Eu^{2+}, $LaBr_3$:1%Sm^{2+}, and $LaBr_3$:5%Ce^{3+},1%Sm^{2+}. As Eu^{2+} and Sm^{2+} have the same charge and a similar ionic radius as Sr^{2+}, the same mechanism of charge compensation in the form of Br^- vacancies can be expected here.

Intuitively, Br^- vacancies would locate right next to the divalent dopant ion. Along the series $LaBr_3$, $CeBr_3$, $PrBr_3$, $NdBr_3$, the rare earth ion radius decreases. As a result, the crystal structure of the MBr_3 bromide changes from the UCl_3 structure for M = La - Pr to the $PuBr_3$ structure for M = Nd and the coordination number of the rare earth ion is reduced from nine to eight, respectively. As Eu^{2+} and Sm^{2+} have larger ionic radii than La^{3+}, they prefer a higher coordination number and occupy the regular cation site with 9-fold coordination, rather than the neighborhood of a Br^- vacancy with a reduced coordination number of eight. The analysis of the Stokes shift of Eu^{2+} suggests that most of the emission comes from the 9 fold coordinated site, even though the photoluminescence decay of Sm^{2+} showed that multiple sites are still present in the $LaBr_3$:1%Sm^{2+} sample.

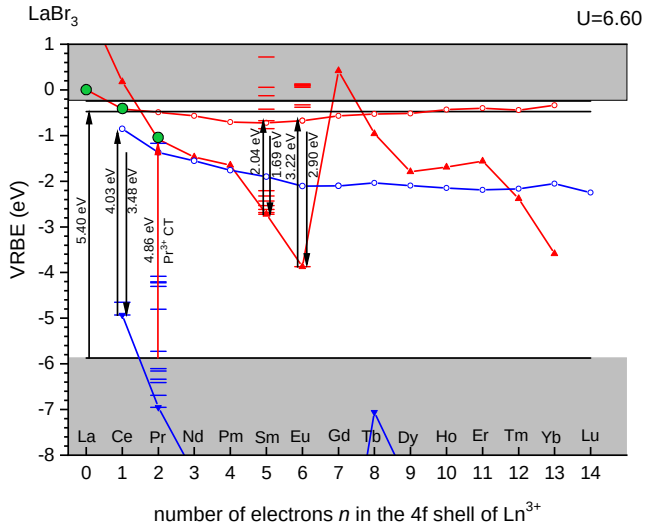

Figure 5.9: VRBE diagram of lanthanide levels in $LaBr_3$, for details see the text in Discussion. The $5d_1$ levels of Eu^{2+} and Sm^{2+} are located closer to the conduction band bottom than that of Ce^{3+}, explaining the lower quenching temperatures.

To rationalise the quenching mechanism of Sm^{2+} in $LaBr_3$, a vacuum referred binding energy (VRBE) diagram has been constructed, which is shown in Figure 5.9. The parameters used for constructing the diagram are summarised in Table 5.2. The band gap E_G of $LaBr_3$ is estimated from the exciton band according to ref. [29]. The $4f^n \rightarrow 4f^{n-1}5d$ transition energies of Ce^{3+} and Sm^{2+} (E_{5d}^{Ce3+} and E_{5d}^{Sm2+}) are based on spectroscopic data presented in this work and extrapolated to other lanthanides using refs. [15, 16]. The triangles connected by the zigzag curves indicate the lowest $4f^n$ states of trivalent (blue) and divalent (red) lanthanides. The dots indicate their respective $5d_1$ states. The excited $4f^n$ states of Ce^{3+}, Pr^{3+}, Sm^{2+} and Eu^{2+} are shown by horizontal lines. The arrows indicate transitions observed spectroscopically in this work. The resulting diagram shows that the $4f^{n-1}5d$ levels of Eu^{2+} and Sm^{2+} lie well above that of Ce^{3+} and thereby closer to the conduction band, while also the T_{50} of Eu^{2+} and Sm^{2+} is much lower than that of Ce^{3+} (Figure 5.4). This suggests that thermal quenching takes place via ionisation to the conduction band.

In $PrBr_3$, the T_{50} of the Ce^{3+} emission is 300 K. Birowosuto et al. suggested that quenching of Ce^{3+} emission in $PrBr_3$:Ce^{3+} happens through charge transfer from the 5d excited state of Ce^{3+} to the Pr^{2+} ground state [30]. The ground state of Pr^{2+} is the $4f^3$ ground state, which lies well below the conduction band minimum in $LaBr_3$. Creating Pr^{2+} in $PrBr_3$ is analogous to placing an electron at the bottom of the conduction band, which implies that the conduction band minimum of $PrBr_3$ lies at approximately 1 eV lower energy compared to that of $LaBr_3$. Assuming the valence band maximum at the same energy in $LaBr_3$ and $PrBr_3$, the conduction band minimum of $PrBr_3$ can be estimated using the Pr^{3+} CT band in $LaBr_3$. From this reasoning follows that quenching of Ce^{3+} emission in $PrBr_3$ also occurs via ionisation to the conduction band.

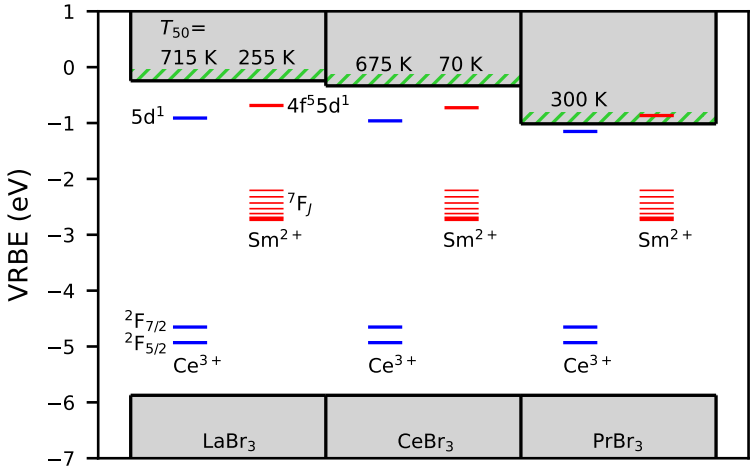

Figure 5.10: VRBE diagram for Ce^{3+} and Sm^{2+} in $LaBr_3$, $CeBr_3$, and $PrBr_3$. The lowering of the conduction band bottom along the series decreases the quenching temperature of Ce^{3+} and Sm^{2+} $4f^{n-1}5d \rightarrow 4f^n$ emissions.

To illustrate the change in conduction band minimum and its relation to T_{50}, Figure 5.10 has been constructed where the Ce^{3+} and Sm^{2+} energy levels are shown in the band gap of $LaBr_3$, $CeBr_3$ and $PrBr_3$ together with the T_{50} values of the Ce^{3+} and Sm^{2+} emission. It is assumed that the U parameter and CT transition energy of Eu^{3+} (E_{CT}^{Eu3+}) and consequently the valence band maximum are constant between the compounds. The values of E_{5d}^{Ce3+} and E_{5d}^{Sm2+} are adjusted to spectroscopic data, only E_{5d}^{Sm2+} in $PrBr_3$ is estimated based on the redshift of the Ce^{3+} 5d level. The conduction band minimum of $CeBr_3$ is estimated from the change in quenching temperature (ΔT_{50}) of the Ce^{3+} emission compared to that in $LaBr_3$ and $PrBr_3$ through equation 5.1 [31]:

$$\Delta T_{50} = \frac{11600}{\ln(\tau_v \Gamma_0)} \Delta E \tag{5.1}$$

Here, τ_v is radiative lifetime of Ce^{3+} and Γ_0 is approximately the highest phonon frequency in $LaBr_3$. The used values for τ_v and Γ_0 is are 30 ns [1] and 5×10^{12} Hz [32], respectively. ΔE is the energy gap between the Ce^{3+} 5d level and the conduction band bottom. All parameters required to construct Figure 5.10 are also summarised in Table 5.2.

Table 5.2: Parameters used for constructing the VRBE diagram in Figure 5.10. All values are given in units of eV.

Host	U	E_G	E_{CT}^{Eu3+}	E_{5d}^{Ce3+}	E_{5d}^{Sm2+}
$LaBr_3$	6.60 [33]	5.63	2.09 [33]	4.02	2.04
$CeBr_3$	6.60 [33]	5.54	2.09 [33]	3.97	2.00
$PrBr_3$	6.60 [33]	4.86	2.09 [33]	3.78 [30]	1.86

Figure 5.10 shows that the conduction band minimum decreases in energy when changing the host cation from La^{3+} to Ce^{3+} to Pr^{3+}, while simultaneously T_{50} decreases. The energy of the conduction band minimum follows the same trend as that of the ground state energy of La^{2+}, Ce^{2+}, and Pr^{2+} marked with green circles in the VRBE diagram in Figure 5.9. This also explains why T_{50} of the Sm^{2+} emission decreases upon co-doping $LaBr_3$:1%Sm^{2+} with Ce^{3+}, as upon co-doping with Ce^{3+} a gradual decrease in conduction band energy is expected. In the case of $LaBr_3$:1%Pr^{3+},1%Sm^{2+} the quenching of Sm^{2+} emission is a gradual process and no distinct quenching temperature was observed. This is likely caused by the low Pr^{3+} concentration. The quenching temperature of a Sm^{2+} ion then depends on the distance to the nearest Pr^{3+} ion, giving a large distribution of quenching temperatures. As the Sm^{2+} $4f^5$5d level lies close to the Pr^{2+} $4f^3$ ground state, the quenching is indeed expected to start from temperatures as low as 10 K. Sm^{2+} would then likely not show any emission at all in $PrBr_3$ due to the $4f^5$5d state lying in the conduction band.

Despite reducing the quenching temperature of Sm^{2+}, co-doping $LaBr_3$:Sm^{2+} with Ce^{3+} or Pr^{3+} as scintillation sensitiser drastically increases its light yield, as can be seen in Table 5.1. Pr^{3+} does not transfer its energy efficiently to Sm^{2+}, as still a lot of Pr^{3+} emission is present in Figure 5.3c. However, the intensity of the Ce^{3+} emission is low in Figures 5.3b and d, indicating that Ce^{3+} is a suitable sensitiser.

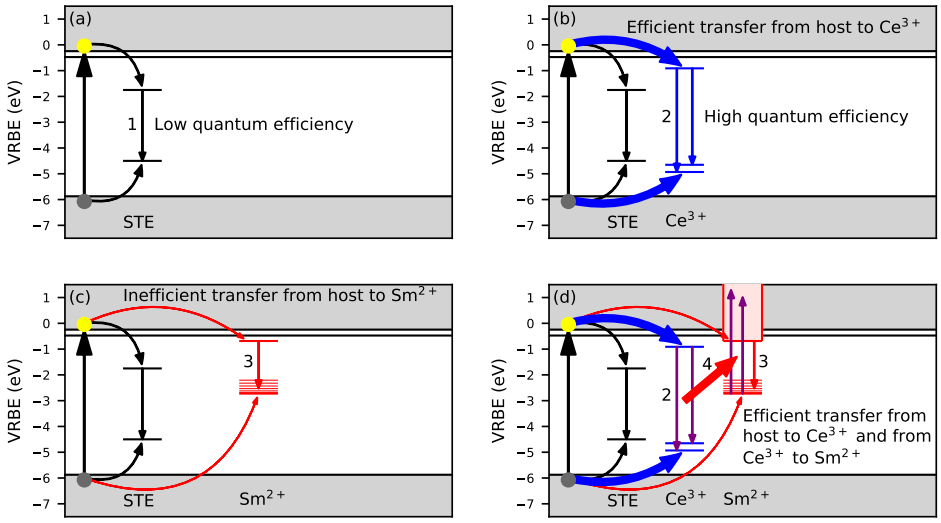

Figure 5.11: Diagram showing the scintillation sensitising mechanism of Ce^{3+}. a) Undoped $LaBr_3$ shows low quantum efficiency STE emission, b) doping with Ce^{3+} introduces an efficient route of energy transfer from host to Ce^{3+} and creates stable emission at room temperature, c) energy transfer from host to Sm^{2+} is inefficient and d) efficient transfer from host to Ce^{3+} and subsequent energy transfer from Ce^{3+} to Sm^{2+} creates an efficient route of energy transfer from host to Sm^{2+}.

The mechanism of sensitisation is portrayed in Figure 5.11. Figure 5.11a shows the case of undoped $LaBr_3$, where most of the emission is STE emission, indicated by arrow 1. The STE emission energy is drawn accurately, but the position of the energy levels within the band gap is chosen arbitrarily. Below 150 K, the light yield of undoped $LaBr_3$ is the same as that of $LaBr_3$:Ce^{3+}, but the emission is thermally quenched with a T_{50} of 225 K [34]. Doping $LaBr_3$ with Ce^{3+} creates the situation of Figure 5.11b. The transfer of electrons and holes to Ce^{3+} competes with STE formation and almost all emission comes from Ce^{3+} with doping concentrations of a few percent, indicated by arrows 2.

When doping $LaBr_3$ with 1% Sm^{2+}, the situation of Figure 5.11c is created. Sm^{2+} emission is visible, as indicated by arrow 3, but the light yield has drastically dropped to only 7,000 ph/MeV at its maximum at 175 K. Additionally, the intensity of the excitation spectrum of Sm^{2+} emission in $LaBr_3$:1%Sm^{2+} drops to zero upon exciting the $LaBr_3$ host below 230 nm (Figure 5.7a). These two observations indicate that energy transfer from the host to Sm^{2+} is inefficient.

When co-doping $LaBr_3$:1%Sm^{2+} with 5% Ce^{3+} (Figure 5.11d), electrons and holes can again be efficiently transferred to Ce^{3+}. This is confirmed by the remaining Ce^{3+} emission in the X-ray excited spectra in Figure 5.3b, displaying that Ce^{3+} gets excited during the scintillation process. As the 5d → 4f emission bands of Ce^{3+} overlap with the $4f^6$ → $4f^5$5d excitation bands of Sm^{2+}, most of the Ce^{3+} excitations are transferred to

Sm^{2+} through radiationless energy transfer, indicated by arrow 4. In this way, the efficient transfer from host to Ce^{3+} is used to sensitise Sm^{2+} and the light yield increases from 7,000 ph/MeV for $LaBr_3$:1%Sm^{2+} to 25,000 ph/MeV for $LaBr_3$:5%Ce^{3+},1%$Sm^{2.+}$. The same inefficient transfer from host to lanthanide is also seen in $LaBr_3$:1%Eu^{2+} and it can therefore be expected that co-doping with Ce^{3+} improves its light yield as well.

5.5. Conclusions

The possibility of using Sm^{2+} as an activator for $LaBr_3$ has been investigated. The Sm^{2+} emission wavelength is found to be in the optimal range for readout with silicon based photodetectors. However, energy transfer from the $LaBr_3$ host to both Eu^{2+} and Sm^{2+} is inefficient, but can be greatly improved by using Ce^{3+} as a scintillation sensitiser. The light yield of $LaBr_3$:1%Sm^{2+} improved from 7,000 ph/MeV to 25,000 ph/MeV upon co-doping with 5% Ce^{3+}. Host excitations are efficiently transferred to Ce^{3+}, which in turn transfers its excitations to Sm^{2+}. Energy transfer from Pr^{3+} to Sm^{2+} was shown to be inefficient. The downside of using Ce^{3+} or Pr^{3+} as a co-dopant is that it decreases the quenching temperature of Sm^{2+}. All Sm^{2+}-doped samples experienced thermal quenching already below room temperature. Doping $LaBr_3$ with Eu^{2+} and Sm^{2+} creates charge compensating defects similar to what is seen upon Sr^{2+} co-doping. These defects act as electron traps and reduce the light output below room temperature.

5.6. Acknowledgements

This research was subsidised by the TTW/OTP grant no. 18040 of the Dutch Research Council.

References

[1] E. V. D. van Loef, P. Dorenbos, C. W. E. van Eijk, K. Krämer, H. U. Güdel, Appl. Phys. Lett. 79 (2001) 1573.

[2] M. E. Daube-Witherspoon, S. Surti, A. Perkins, C. C. M. Kyba, R. Wiener, M. E. Werner, R. Kulp, J. S. Karp, Phys. Med. Biol. 55 (2010) 45.

[3] Stefan J. van der Sar, David Leibold, Stefan E. Brunner, Dennis R. Schaart, Proc. SPIE 12304 (2022) 123040A.

[4] A. Kozyrev, I. Mitrofanov, A. Owens, F. Quarati, J. Benkhoff, B. Bakhtin, F. Fedosov, D. Golovin, M. Litvak, A. Malakhov, M. Mokrousov, I. Nuzhdin, A. Sanin, V. Tretyakov, A. Vostrukhin, G. Timoshenko, V. Shvetsov, C. Granja, T. Slavicek, S. Pospisil, Rev. Sci. Intrum. 87 (2016) 085112.

[5] B. D Milbrath, B. J. Choate, J. E. Fast, W. K. Hensley, R. T. Kouzes, J. E. Schweppe, Nucl. Instrum. Meth. A 572 (2007) 774.

[6] P. Dorenbos, E. V. D. van Loef, A. P. Vink, E. van der Kolk, C. W. E. van Eijk, K. W. Krämer, H. U. Güdel, W. M. Higgins, K. S. Shah, J. Lumin. 117 (2006) 147.

[7] David N. ter Weele, Dennis R. Schaart, Pieter Dorenbos, IEEE T. Nucl. Sci. 61 (2014) 683.

[8] F. G. A. Quarati, P. Dorenbos, J. van der Biezen, Alan Owens, M. Selle, L. Parthier, P. Schotanus, Nucl. Instrum. Meth. A 729 (2013) 596.

[9] J. Andriessen, E. van der Kolk, P. Dorenbos, Phys. Rev. B 76 (2007) 075124.

[10] W. H. Zachariasen, Acta Crystallogr. 1 (1948) 265.

[11] M. S. Alekhin, J. T. M. de Haas, I. V. Khodyuk, K. W. Krämer, P. R. Menge, V. Ouspenski, P. Dorenbos, Appl. Phys. Lett. 102 (2013) 151915.

[12] Johan T. M. de Haas, Pieter Dorenbos, IEEE T. Nucl. Sci. 55 (2008) 1086.

[13] J. Glodo, R. Farrell, E. V. D. van Loef, W. M. Higgins, K. S. Shah, IEEE Nucl. Sci. Conf. R. (2005) 98.

[14] Daniel Rutstrom, Robyn Collette, Luis Stand, Matthew Loyd, Yuntao Wu, Merry Koschan, Charles L. Melcher, Mariya Zhuravleva, J. Cryst. Growth 483 (2018) 251.

[15] P. Dorenbos, J. Lumin. 91 (2000) 155.

[16] P. Dorenbos, J. Phys. Condens. Mat. 15 (2003) 575.

[17] Laura C. Dixie, Andrew Edgar, Murray C. Bartle, J. Lumin. 149 (2014) 91.

[18] R. H. P. Awater, M. S. Alekhin, D. A. Biner, K. W. Krämer, P. Dorenbos, J. Lumin. 212 (2019) 1.

[19] Daisuke Nakauchi, Yutaka Fujimoto, Takumi Kato, Noriaki Kawaguchi, Takayuki Yanagida, Crystals 12 (2022) 517.

[20] Casper van Aarle, Karl W. Krämer, Pieter Dorenbos, J. Mater. Chem. C 11 (2023) 2336.

[21] D. L. Dexter, J. Chem. Phys. 21 (1953) 836.

[22] Weronika Wolszczak, Karl W. Krämer, Pieter Dorenbos, Phys. Status Solidi R. 13 (2019) 1900158.

[23] G. Meyer, Advances in the Synthesis and Reactivity of Solids, JAI Press Inc., 1994, vol. 2, pp. 1–16.

[24] Mikhail S. Alekhin, Daniel A. Biner, Karl W. Krämer, Pieter Dorenbos, J. Appl. Phys. 113 (2013) 224904.

[25] F. G. A. Quarati, M. S. Alekhin, K. W. Krämer, P. Dorenbos, Nucl. Instrum. Meth. A 735 (2014) 655.

[26] Roy H. P. Awater, Karl W. Krämer, P. Dorenbos, IEEE T. Nucl. Sci. 62 (2015) 2343.

[27] P. Dorenbos, J. Phys. Condens. Mat. 15 (2003) 4797.

[28] Mikhail S. Alekhin, Sandra Weber, Karl W. Krämer, Pieter Dorenbos, J. Lumin. 145 (2014) 518.

[29] P. Dorenbos, J. Lumin. 111 (2005) 89.

[30] M. D. Birowosuto, P. Dorenbos, C. W. E. van Eijk, K. W. Krämer, H. U. Güdel, J. Phys. Condens. Matter. 19 (2007) 256209.

[31] Pieter Dorenbos, J. Mater. Chem. C, 2023, Advance Article.

[32] Isaac Richman, Robert A. Satten, Eugene Y. Wong, J. Chem. Phys. 39 (1963) 1833.

[33] Pieter Dorenbos, Aday Josef, Johan T. M. de Haas, Karl W. Krämer, J. Lumin. 208 (2019) 463.

[34] E. V. D. van Loef, P. Dorenbos, C. W. E. van Eijk, K. W. Krämer, H. U. Güdel, Nucl. Instrum. Meth. A 486 (2002) 254.

6

Lengthening of the Sm^{2+} $4f^55d \rightarrow 4f^6$ decay time through interplay with the $4f^6[^5D_0]$ level and its analogy to Eu^{2+} and Pr^{3+}

Recent research activity on Sm^{2+}-doped compounds has significantly increased the amount of available data on $4f^55d \rightarrow 4f^6$ decay times. This enabled the systematic comparison of spectroscopic and time resolved luminescence data to theoretical models describing the interplay between the $4f^55d$ and $4f^6[^5D_0]$ excited states on the observed decay time. A Boltzmann distribution between the population of the excited states is assumed, introducing a dependence of the observed $4f^55d \rightarrow 4f^6$ decay time on the energy gap between the $4f^55d$ and $4f^6[^5D_0]$ levels and temperature. The model is used to interpret the origin of the large variation in reported $4f^55d \rightarrow 4f^6$ decay times through literature, and links their temperature dependence to applications such as luminescence thermometry and near-infrared scintillation. The model is further applied to the analogous situation of close lying $4f^{n-1}5d$ and $4f^n$ states in Eu^{2+} ($^6P_{7/2}$) and Pr^{3+} ($^1S_0$).

The content of this chapter is based on the following publication:
Casper van Aarle, Karl W. Krämer, Pieter Dorenbos, J. Lumin. 266 (2024) 120329.

6.1. Introduction

Sm^{2+}-doped compounds have been explored for many purposes throughout the past decades. Spectroscopic data on Sm^{2+} has been valuable for fundamental understanding of the lanthanide energy levels in compounds and the electronic transitions between them [1–3]. Applications such as spectral hole burning for digital memory [4, 5], solid state lasers [6–8], X-ray storage phosphors [9, 10], luminescent solar concentrators [11, 12], and pressure sensors [13–15] have been explored. In recent years, two of the most researched topics are the development of near-infrared scintillators [16–19] and luminescence thermometers [20–22].

A configurational coordinate diagram showing the energy levels of Sm^{2+} is shown in Figure 7.2. The ground state is $4f^6[^7F_0]$, which is part of the $4f^6[^7F_J]$ multiplet. About 14,500 cm^{-1} above the ground state lies the $4f^6[^5D_0]$ level. Sm^{2+} can show emission from the $4f^6[^5D_0] \rightarrow 4f^6[^7F_J]$ transitions yielding multiple narrow emission lines ranging from 680 nm to 850 nm, each line corresponding to a different $4f^6[^7F_J]$ final state. The energy difference between the $4f^6$ levels is almost independent of host compound and therefore the emission lines always lie at approximately the same wavelength.

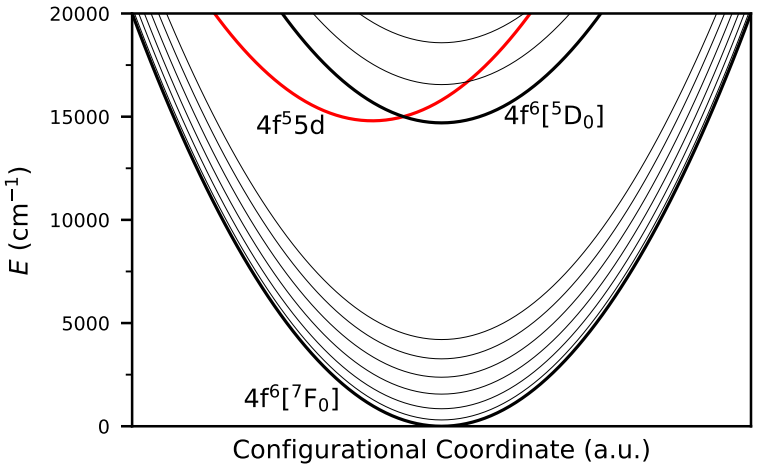

Figure 6.1: Configurational coordinate diagram of Sm^{2+}. The black parabola are $4f^6$ states, the red parabola is the $4f^55d$ state.

Sm^{2+} also has states of the $4f^55d$ configuration that lie close to the $4f^6[^5D_0]$ level. In this work, only the lowest $4f^55d$ level is considered, the energy of which does strongly depend on compound and can therefore be located at higher or lower energies than drawn in Figure 7.2. In some compounds, Sm^{2+} shows $4f^55d \rightarrow 4f^6$ broad band emission instead of the $4f^6 \rightarrow 4f^6$ line emission. This happens when the $4f^55d$ states lies below the $4f^6[^5D_0]$ level or low enough that it is thermally populated, which is the case when the $4f^55d \rightarrow 4f^6$ emission lies at approximately 670 nm or longer wavelength [23]. Many of the compounds in which the $4f^55d \rightarrow 4f^6$ emission wavelength lies around this transition point at 670 nm still show $4f^6 \rightarrow 4f^6$ line emission at cryogenic temperatures.

Luminescence thermometry relies on measuring a property Q of the luminescent center with known dependence on the temperature T. For Sm^{2+}-based thermometers, Q is often chosen to be the luminescence intensity ratio (LIR) between the $4f^5 5d \rightarrow 4f^6$ and $4f^6 \rightarrow 4f^6$ emission [24, 25], or the decay time τ of any of the two emissions [26]. It is desired that Q varies strongly with temperature as this allows for more sensitive temperature measurement. This can be expressed as a figure of merit called the relative sensitivity.

$$S_r = \left| \frac{1}{Q} \frac{dQ}{dT} \right| \times 100\% \tag{6.1}$$

Both when using LIR or τ as measured property, compounds are typically selected where the $4f^5 5d$ level lies above the $4f^6[^5D_0]$ level. In that case, thermal excitation from the long lived $4f^6[^5D_0]$ level with a radiative lifetime time of milliseconds to the $4f^5 5d$ level with a radiative lifetime of microseconds causes large changes in τ upon temperature increase and simultaneously the spectrum rapidly changes from $4f^6 \rightarrow 4f^6$ line emission to broad band $4f^5 5d \rightarrow 4f^6$ emission [27, 28].

For the development of near-infrared scintillators, Sm^{2+} is a promising activator as its emission wavelength is efficiently detected by silicon based photodetectors such as avalanche photodiodes and silicon photomultipliers [18]. It can be doped in the same hosts as the more conventional Eu^{2+} activator and can even be used as co-dopant to solve the self-absorption problems that Eu^{2+}-doped scintillators typically face [29]. For scintillator applications, it is necessary that the compound emits its light quickly, so that the scintillator is ready to detect a new γ-ray without overlap of the scintillation pulses. This means the $4f^5 5d \rightarrow 4f^6$ emission with its short τ is desirable and therefore development of near-infrared scintillators has largely focussed on compounds in which the $4f^5 5d$ level lies below the $4f^6[^5D_0]$ level.

As the energy difference between the $4f^6$ levels are almost independent of compound, the energy difference between the $4f^5 5d$ level and the $4f^6[^5D_0]$ level can be conveniently approximated by only knowing the $4f^5 5d \rightarrow 4f^6$ emission wavelength. One problem is however that compounds which show exclusively $4f^5 5d \rightarrow 4f^6$ emission at room temperature still shows large variation in τ. Values have been reported between 1.5 µs [30] and 35 µs [31]. For scintillator applications such as γ-ray spectroscopy, an order of magnitude slower decay time is extremely undesirable, underlining the importance of a reliable prediction for τ. Unfortunately, the mechanism behind this large variation in τ has not yet been studied.

Feofilov and Tolstoi showed that a level system of two excited states in thermal equilibrium can be used to describe the temperature dependence of the Sm^{2+} decay time. The system is shown schematically in Figure 6.2. State 1 lies at energy E_1 above the ground state, has degeneracy g_1 and an intrinsic radiative lifetime τ_1. The same applies to State 2, having its own energy E_2, degeneracy g_2 and intrinsic lifetime τ_2. The energy difference between States 1 and 2 is defined as $\Delta E = E_2 - E_1$. When both excited states are in thermal equilibrium, emission from both states will have the same decay time, which is given by Equation 6.2 [32].

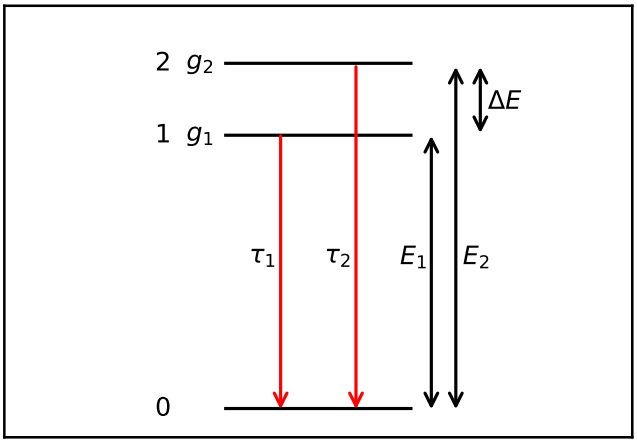

Figure 6.2: 3 level system with ground state 0 and excited states 1 and 2. Excited states 1 (here, Sm^{2+} $4f^6[^5D_0]$) and 2 (Sm^{2+} $4f^5$5d) are in thermal equilibrium and their respective degeneracies are g_1 and g_2. Their intrinsic lifetimes are τ_1 and τ_2. $\Delta E \equiv E_2 - E_1$ is the energy difference between the excited states.

$$\tau(T,\Delta E) = \frac{1 + \frac{g_2}{g_1} e^{\frac{-\Delta E}{kT}}}{\tau_1^{-1} + \tau_2^{-1} \frac{g_2}{g_1} e^{\frac{-\Delta E}{kT}}} \tag{6.2}$$

When using this system to describe Sm^{2+}, State 1 and 2 correspond to the $4f^6[^5D_0]$ and $4f^5$5d states, respectively. The model assumes that all transitions to the ground state are radiative and thermal population of other levels such as the close lying $4f^6[^5D_1]$ state is neglected. Equation 6.2 has been succesfully used to model the temperature dependence of the decay time of Sm^{2+} emission in many compounds of the MX_2 (M = Ca, Sr, Ba; X = F, Cl, Br) family, which often show a transition from $4f^6 \rightarrow 4f^6$ line emission to $4f^5$5d $\rightarrow 4f^6$ broad band emission upon increase of temperature [32–35].

Showing $4f^{n-1}$5d $\rightarrow 4f^n$ broad band emission in some compounds and $4f^n \rightarrow 4f^n$ line emission in others is not exclusively a property of Sm^{2+}, as it is also observed for Eu^{2+} and Pr^{3+}. Figure 6.3a shows a configurational coordinate diagram for Eu^{2+}. In most compounds, the $4f^6$5d level lies well below the $4f^7[^6P_{7/2}]$ level and only $4f^6$5d $\rightarrow 4f^7$ emission is observed. When the $4f^6$5d level lies above 28,500 cm^{-1}, such as in SrFCl and BaFCl, $4f^7[^6P_{7/2}] \rightarrow 4f^7[^8S_{7/2}]$ line emission can be observed [36, 37]. This mostly happens at 78 K or lower temperatures, as the distance between the $4f^6$5d and $4f^7[^6P_{7/2}]$ level is typically smaller than 500 cm^{-1}. Some examples of compounds in which emission from the $4f^7[^6P_{7/2}]$ level is observed at room temperature are reported in literature [38–44], most of which belong to the $AMgF_3$ (A = Na, K, Rb, Cs) family of compounds. It is believed that in these compounds the $4f^6$5d level is located more than 1000 cm^{-1} above the $4f^7[^6P_{7/2}]$ level because Eu^{2+} occupies the monovalent A cation site with small crystal field split-

ting. It has been reported that in some compounds where the $4f^6 5d$ level lies close to the $4f^7[^6P_{7/2}]$ level, the Eu^{2+} $4f^6 5d \rightarrow 4f^7$ emission decay time becomes longer than the typical intrinsic Eu^{2+} decay time of 0.5 µs to 1 µs [45, 46]. For these compounds, Equation 6.2 has been used to determine ΔE between the $4f^6 5d$ and $4f^7[^6P_{7/2}]$ level from the $4f^6 5d \rightarrow 4f^7$ emission decay time [44, 47, 48]. This shows that the transition from broad band emitters to line emitters in Eu^{2+} is analogous to that of Sm^{2+}. Of the dopants discussed in this work, Eu^{2+} is the one for which by far the most spectroscopic data is available. The temperature dependence of its emission intensities and decay times have been extensively reviewed by Adachi [49].

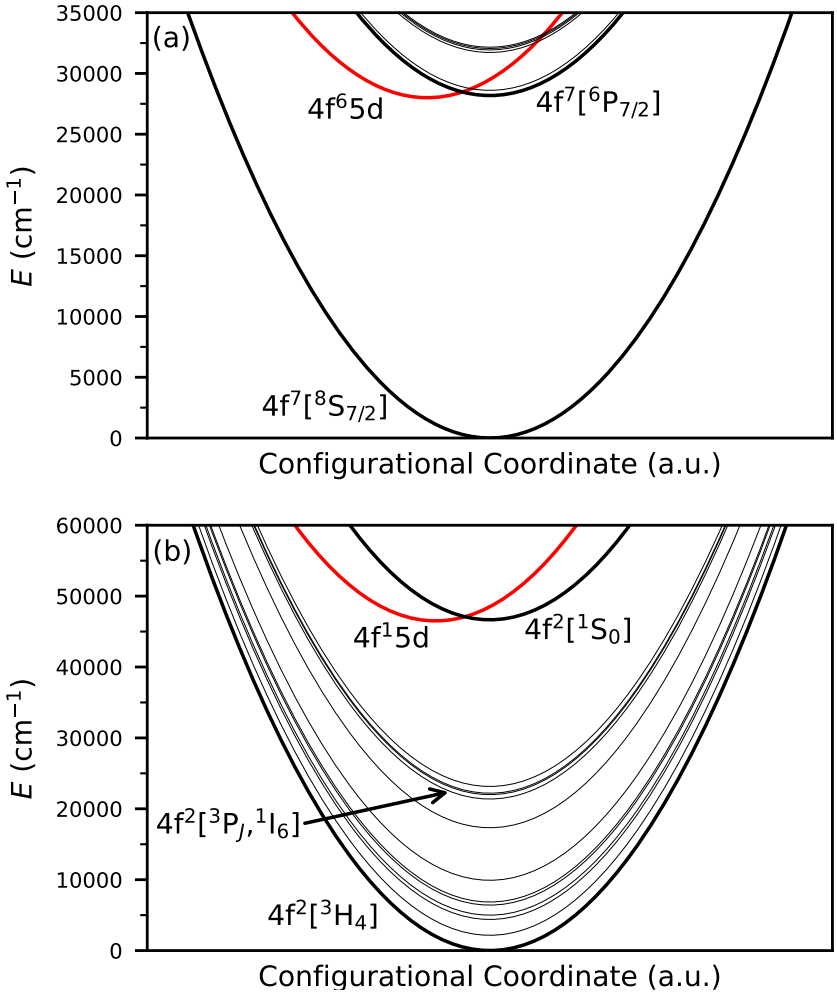

Figure 6.3: Configurational coordinate diagram of a) Eu^{2+} and b) Pr^{3+}. The black parabola are $4f^6$ states, the red parabolas are their respective $4f^{n-1}5d$ states.

For Pr^{3+} a configurational coordinate diagram is shown in figure 6.3b. The $4f^15d$ level can lie above or below the $4f^2[^1S_0]$ level at about 47,000 cm^{-1}. In compounds where the $4f^15d$ level lies below the $4f^2[^1S_0]$ level, the energy gap between the $4f^15d$ level and the lower lying $4f^2[^3P_J]$ and $[^1I_6]$ levels is too large for non-radiative relaxation processes to be efficient and therefore $4f^15d \rightarrow 4f^2$ emisson is observed. Compounds in which the $4f^15d$ level lies above the $4f^2[^1S_0]$ level show exclusively $4f^2 \rightarrow 4f^2$ line emission [50]. In compounds such as $LiLaP_4O_{12}$ and $LaPO_4$, Pr^{3+} only shows line emission at cryogenic temperatures and $4f^15d \rightarrow 4f^2$ emission appears upon increase of temperature [51, 52]. In for example LaF_3, YF_3 and $SrAl_{12}O_{19}$, emission from the $4f^2[^1S_0]$ level can also be observed at room temperature [53–55]. Emission from the $4f^2[^1S_0]$ level can leave Pr^{3+} in the $4f^2[^1I_6]$ state [56], after which emission can subsequently take place from the $4f^2[^3P_0]$ state. Because of this, many Pr^{3+} compounds that show $4f^2[^1S_0]$ emission have been researched for their photon cascade emission, where two photons in the visible part of the spectrum are emitted after absorption of a single UV photon [57–59]. Compounds in which Pr^{3+} shows $4f^15d \rightarrow 4f^2$ emission at room temperature have been heavily researched for scintillation due to their exceptionally fast decay time of between 10 ns and 20 ns [60–62]. An overview of Pr^{3+}-doped compounds, their characteristics depending on the energy of the $4f^15d$ level relative to the $4f^2[^1S_0]$ level, and their application can be found in the works of Srivastava [63].

In this work, data on Sm^{2+} and Eu^{2+}-doped compounds showing $4f^{n-1}5d \rightarrow 4f^n$ emission are compiled to show the relation between emission wavelength and decay time. This relation is compared to a model of a three level system assuming a Boltzmann equilibrium between the populations of the $4f^{n-1}5d$ and excited $4f^n$ levels. The results are used to explain the large variation in Sm^{2+} $4f^55d \rightarrow 4f^6$ decay times reported in literature. The model is also used to predict the temperature dependence of this decay time as a function of $4f^55d \rightarrow 4f^6$ emission wavelength and the outcome is compared to the experimental data. The applicability of this model to development of new luminescence thermometers is discussed and new constraints are formulated to predict whether a Sm^{2+}-doped compound is a potential candidate for near-infrared scintillator applications. Lastly, an attempt has been made to predict the $4f^15d \rightarrow 4f^2$ decay time of Pr^{3+}-doped compounds.

6.2. Theory

When the population of the Sm^{2+} $4f^55d$ and $4f^6[^5D_0]$ levels are in thermal equilibrium, the ratio between the total number of ions in these respective states, N_{5d} and N_{4f}, can be expressed according to a Boltzmann distribution:

$$\frac{N_{4f}(t,T,\Delta E)}{N_{5d}(t,T,\Delta E)} = \frac{g_{4f}}{g_{5d}} e^{\frac{\Delta E}{kT}} \tag{6.3}$$

Here, $\Delta E = E_{5d} - E_{4f}$, which is the energy difference between the respective $4f^55d$ and $4f^6[^5D_0]$ states. g_{5d} and g_{4f} are their respective degeneracies. While N_{5d} and N_{4f} depend on time due to radiative decay, the ratio between them is independent of time as excited Sm^{2+} ions rapidly alternate between the two excited states. As the degeneracy of the

excited states can vary from compound to compound and is generally unknown, it is assumed that $\frac{g_{4f}}{g_{5d}} = 1$ in the rest of this work.

Figure 6.4 schematically shows how ΔE is determined in this work. The parabola represent the electronic states of Sm^{2+} similar to the configurational coordinate diagram in Figure 7.2, but this time only the three states taken into account within this model are drawn. The arrows indicate the relevant energy differences within the diagram. E_{4f} is the energy difference between the $4f^6[^7F_0]$ and $4f^6[^5D_0]$ states, which is found from the emission wavelength of the $4f^6[^5D_0] \rightarrow 4f^6[^7F_0]$ emission line λ_{4f} according to:

$$E_{4f} = \frac{hc}{\lambda_{4f}} \tag{6.4}$$

Where h is the Planck constant and c the speed of light. Within this work, we will use $\lambda_{4f} = 687$ nm (14550 cm^{-1}) for all compounds. Following Figure 6.4, E_{5d} is given by Equation 6.5:

$$E_{5d} = E_{5d}^{em} + \frac{1}{2}\Delta S = \frac{hc}{\lambda_{5d}} + \frac{1}{2}\Delta S \tag{6.5}$$

Here, E_{5d}^{em} is the energy of the $4f^5 5d \rightarrow 4f^6$ transition, which can be found from its emission wavelength λ_{5d}. ΔS is the Stokes shift between absorption and emission. Most compounds in which λ_{5d} of Sm^{2+} is close to 687 nm are iodides or bromides. On average, ΔS in these compounds is approximately 2000 cm^{-1} [64] and will be assumed that value in all other compounds as well.

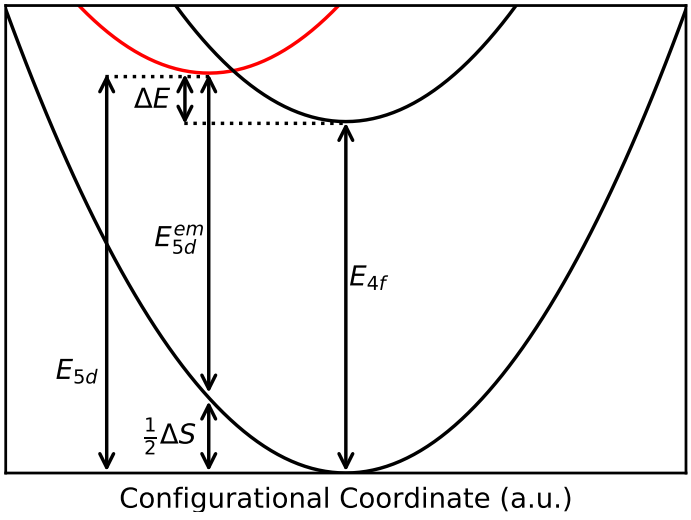

Figure 6.4: Configurational coordinate diagram showing how the energy difference between the $4f^5 5d$ and $4f^6[^5D_0]$ states $\Delta E \equiv E_{5d} - E_{4f}$ is calculated from the transition energies E_{4f} and E_{5d}^{em} and the Stokes shift ΔS.

Thermal equilibrium implies that phonon mediated transitions between the $4f^5 5d$ and $4f^6[^5D_0]$ levels are much faster than radiative decay to the ground state. In that case, the excited state of a single Sm^{2+} ion can be described as having a probability p_{5d} of being in the $4f^5 5d$ state and p_{4f} of being in the $4f^6[^5D_0]$ state, according to Equations 6.6 and 6.7:

$$p_{5d}(T,\Delta E) = \frac{N_{5d}}{N_{5d}+N_{4f}} = \frac{1}{e^{\frac{\Delta E}{kT}}+1} \tag{6.6}$$

$$p_{4f}(T,\Delta E) = \frac{N_{4f}}{N_{5d}+N_{4f}} = \frac{1}{e^{\frac{-\Delta E}{kT}}+1} \tag{6.7}$$

When two levels are not in thermal equilibrium, they both decay with their own intrinsic radiative lifetime. These are labelled τ_{5d} and τ_{4f} for the $4f^5 5d$ and $4f^6[^5D_0]$ levels, respectively. When they are in thermal equilibrium, they both show single exponential decay with the same decay time constant. In that case, the decay time can be found by a weighted average of τ_{5d} and τ_{4f}, where the weights are given by p_{5d} and p_{4f}:

$$\frac{1}{\tau(T,\Delta E)} = \frac{p_{5d}}{\tau_{5d}} + \frac{p_{4f}}{\tau_{4f}} \tag{6.8}$$

τ_{4f} is approximated to be 1 ms for all compounds. It is asssumed that $\tau_{5d} \propto \lambda^3$ as predicted by the standard theory on luminescence decay [65] and based on the available decay time data at wavelengths longer than 750 nm it is approximated to be 3 µs at 850 nm [18, 66–68]. τ_{5d} is then found by Equation 6.9:

$$\tau_{5d} = 3\left(\frac{\lambda_{5d}}{850\text{ nm}}\right)^3 \mu s \tag{6.9}$$

Equation 6.10 is found when combining Equations 6.6-6.8. This equation is identical to Equation 6.2, the one found by Feofilov and Tolstoi [32], except for omission of the terms describing the degeneracy of the states. This shows that both their model and the one described in this work are the same.

$$\tau(T,\Delta E) = \frac{1+e^{\frac{-\Delta E}{kT}}}{\tau_{4f}^{-1}+\tau_{5d}^{-1}e^{\frac{-\Delta E}{kT}}} \tag{6.10}$$

Depending on the ratio between p_{5d} and p_{4f}, emission can be observed from both excited states. The luminescence intensity ratio between the $4f^5 5d \rightarrow 4f^6$ and $4f^6 \rightarrow 4f^6$ emission intensities (I_{5d} and I_{4f}) can be found using Equation 6.3, τ_{4f} and τ_{5d} and is expressed as:

$$\frac{I_{4f}}{I_{5d}} = \frac{\tau_{5d}}{\tau_{4f}} e^{\frac{\Delta E}{kT}} = \frac{\tau_{5d}}{\tau_{4f}} \frac{p_{4f}}{p_{5d}} \tag{6.11}$$

The same model applies for Eu^{2+} and Pr^{3+}, but different input parameters are required. For Eu^{2+}, λ_{4f} corresponds to the $4f^7[^6P_{7/2}] \rightarrow 4f^7[8S_{7/2}]$ transition and a value of 360 nm (27800 cm^{-1}) is used [44]. The $4f^7 \rightarrow 4f^7$ emission is mostly observed in oxides and fluorides. ΔS of the $4f^6 5d \rightarrow 4f^7$ emission in these compounds is typically larger than in the bromides and iodides for which the Stokes shift of the Sm^{2+} $4f^5 5d \rightarrow 4f^6$ emission was

estimated. Therefore, ΔS was determined to be on average 3000 cm^{-1} [64]. Just like for Sm^{2+}, τ_{4f} was taken to be 1 ms [44] and τ_{5d} was assumed to be 0.5 µs at 450 nm.

In the case of Pr^{3+}, a value of λ_{4f} = 213 nm (46900 cm^{-1}) applies for the $4f^2[^1S_0] \rightarrow 4f^2[^3H_4]$ transition [69]. Similar to Eu^{2+}, emission from the $4f^2[^1S_0]$ is also typically observed in fluorides and oxides, but ΔS for Pr^{3+} is larger than for Eu^{2+} [70], so an average ΔS of 4000 cm^{-1} is used [63, 71]. The transitions from the $4f^2[^1S_0]$ state of Pr^{3+} are typically much faster than the $4f^n \rightarrow 4f^n$ transitions of Eu^{2+} and Sm^{2+}, so the value of τ_{4f} was taken to be 1 µs [53–55]. The approximated value for τ_{5d} is 15 ns at 230 nm [65]. The input parameters for the model of all lanthanides are summarised in Table 6.1.

Table 6.1: Input parameters for the model describing the $4f^{n-1}5d \rightarrow 4f^n$ decay times for Sm^{2+}, Eu^{2+} and Pr^{3+}.

Lanthanide	λ_{4f} (nm)	ΔS (cm^{-1})	τ_{4f} (µs)	τ_{5d} (µs)
Sm^{2+}	687	2000	1000	$3\left(\frac{\lambda_{5d}}{850\ nm}\right)^3$
Eu^{2+}	360	3000	1000	$0.5\left(\frac{\lambda_{5d}}{450\ nm}\right)^3$
Pr^{3+}	213	4000	1	$0.015\left(\frac{\lambda_{5d}}{230\ nm}\right)^3$

6.3. Experimental Techniques

$YbCl_2$:1%Sm^{2+} crystals were grown from the melt of binary starting materials in a Ta ampoule, as previously described in [67]. The growth of $CsBa_2I_5$:0.5%Sm^{2+} crystals in a silica ampoule was previously described in [18, 66]. Cs_4EuI_6:0.5%Sm^{2+} crystals were grown from the melt in a Ta ampoule, as previously described in [68]. YbFBr:1%Sm^{2+} was synthesized from YbF_3, $YbBr_2$, $SmBr_2$, and Yb. YbF_3 was prepared from Yb_2O_3 (Metall Rare Earth Ltd., 6N) and concentrated HF acid (Merck, suprapur, 40%). The oxide was reacted with HF acid in a Teflon beaker, dried on a sand bath, and treated by an Ar and HF gas stream in a glassy carbon boat at 450 °C inside an alloy 600 apparatus for fluorination and removal of oxygen traces. $YbBr_3$ and $SmBr_3$ were prepared from the oxides (Sm_2O_3, Fluka, 3N) via the NH_4Br synthetic route [72] and sublimed under high vacuum in a silica apparatus for removal of oxygen impurities, as previously described, e.g., in [67]. The trihalides were reduced with the respective metal (Sm, Yb, Alfa, 3N) in a Ta ampoule to obtain the dihalides $YbBr_2$ and $SmBr_2$. Ta ampoules were sealed by He-arc welding and protected in silica ampoules under vacuum. Stoichiometric amounts of YbF_3, $YbBr_2$, $SmBr_2$, and a small excess of Yb were sealed in a Ta ampoule, heated to 1080 °C, and slowly cooled by 3 K/h to 700 °C and 6 K/h to room temperature. All handling of starting materials and products was done in glove boxes or sealed sample containers under strictly dry and oxygen-free conditions.

For photoluminescence emission spectra, the sample was excited using a 450 W Xenon lamp in combination with a Horiba Gemini 180 monochromator. Quartz glass ampoules containing the samples under He gas were mounted directly on the cold finger of a Janis He cryostat and placed in a sample chamber. A Lakeshore Model 331 temperature

controller was used to change the sample temperature. Emission light from the sample passed through an optical filter to block the excitation light before entering an optical fibre connected to an Ocean Insight QEPro spectrometer. The resulting spectra were corrected for the transmission of the optical fibre and sensitivity of the spectrometer.

Photoluminescence decay curves were measured using an EKSPLA NT230 OPO laser as excitation source with a repetition rate of 100 Hz and pulse duration of 10 ns. The temperature of the samples was controlled in an identical way as for the photoluminescence emission spectra. The emission light from the sample passed through an optical filter, after which it was detected using a SpectraPro-SP2358 monochromator and a Hamamatsu R7600U-20 PMT. The signal from the PMT was converted to a digital signal using a CAEN DT5724F digitizer.

6.4. Results

To illustrate the complex temperature dependence of Sm^{2+} emission, the photoluminescence emission and decay of two seemingly similar compounds are compared. The first compound is $YbCl_2$:1%Sm^{2+}. Its photoluminescence emission spectra between 10 K and 300 K at an excitation wavelength of 500 nm are shown in Figure 6.5a. At 10 K, $YbCl_2$:1%Sm^{2+} shows $4f^6 \rightarrow 4f^6$ line emission on top of broad band $4f^5 5d \rightarrow 4f^6$ emission. Upon increasing the temperature to 100 K, the $4f^6 \rightarrow 4f^6$ lines gradually disappear. From 100 K onwards, $4f^6 \rightarrow 4f^6$ lines are no longer visible and the emission spectrum only contains the $4f^5 5d \rightarrow 4f^6$ broad band emission. The maximum of the $4f^5 5d \rightarrow 4f^6$ emission band shows a small shift to longer wavelengths as temperature increases and is 727 nm at 300 K. This results in a value of ΔE = 200 cm^{-1}, meaning the $4f^5 5d$ state lies just above the $4f^6[^5D_0]$ state.

The decay curves of the $4f^5 5d \rightarrow 4f^6$ emission monitored at 720 nm are shown in Figure 6.5b. At 10 K, the emission consists of a decay component too fast for the response time of the setup (10 ns) and a slow component with a decay time of 430 µs. A fast and slow component with similar decay times were also observed in BaBrI:Sm^{2+} by Sofich et al. and in $BaCl_2$:Sm^{2+} by He et al. (ΔE = 1460 cm^{-1} and ΔE = 1710 cm^{-1}) [73, 74]. He et al. ascribed the slow component to thermal repopulation of the $4f^5 5d$ state from the $4f^6[^5D_0]$ state, as both the $4f^5 5d \rightarrow 4f^6$ and the $4f^6 \rightarrow 4f^6$ had the same decay time. The fast component is much faster than the intrinsic decay time of the Sm^{2+} emission, indicating the decay is accelerated by out-of-equilibrium processes, as discussed below in Section 6.5. As ΔE is positive, the fast decay is ascribed to $4f^5 5d \rightarrow 4f^6$ emission in the out-of-equilibrium situation. Rapid thermal relaxation to the lower lying $4f^6[^5D_0]$ state eventually leads to the Boltzmann distribution with long decay time. Upon increasing the temperature, the intensity of the fast component decreases until it is no longer visible at 100 K, the same temperature at which the $4f^6 \rightarrow 4f^6$ lines disappear in the emission spectrum in Figure 6.5a. Simultaneously, the decay time of the slow component steadily decreases, indicating that the rate of thermal repopulation from $4f^6[^5D_0]$ to $4f^5 5d$ increases with temperature.

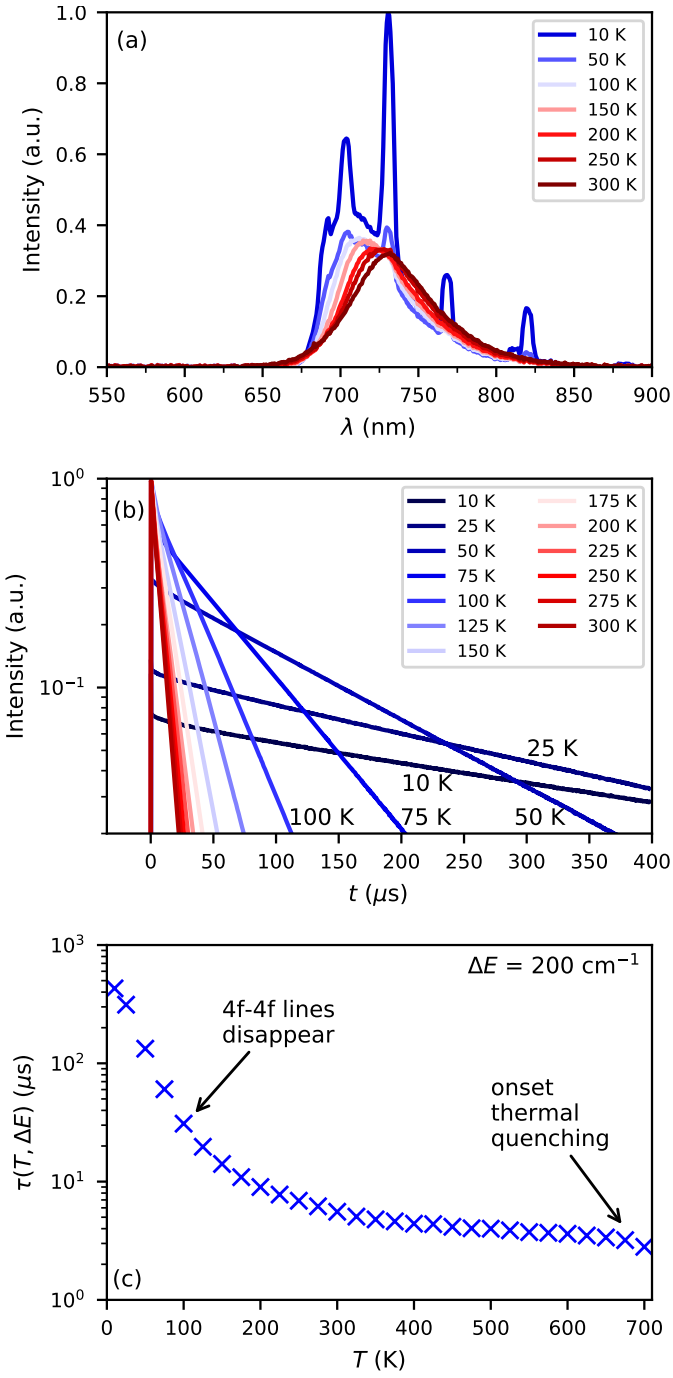

Figure 6.5: $YbCl_2$:1%Sm^{2+} excited at 500 nm into the $4f^5$5d state, a) Photoluminescence emission spectra, b) Photoluminescence decay curves monitored at 720 nm, and c) Decay times of Sm^{2+} emission versus temperature.

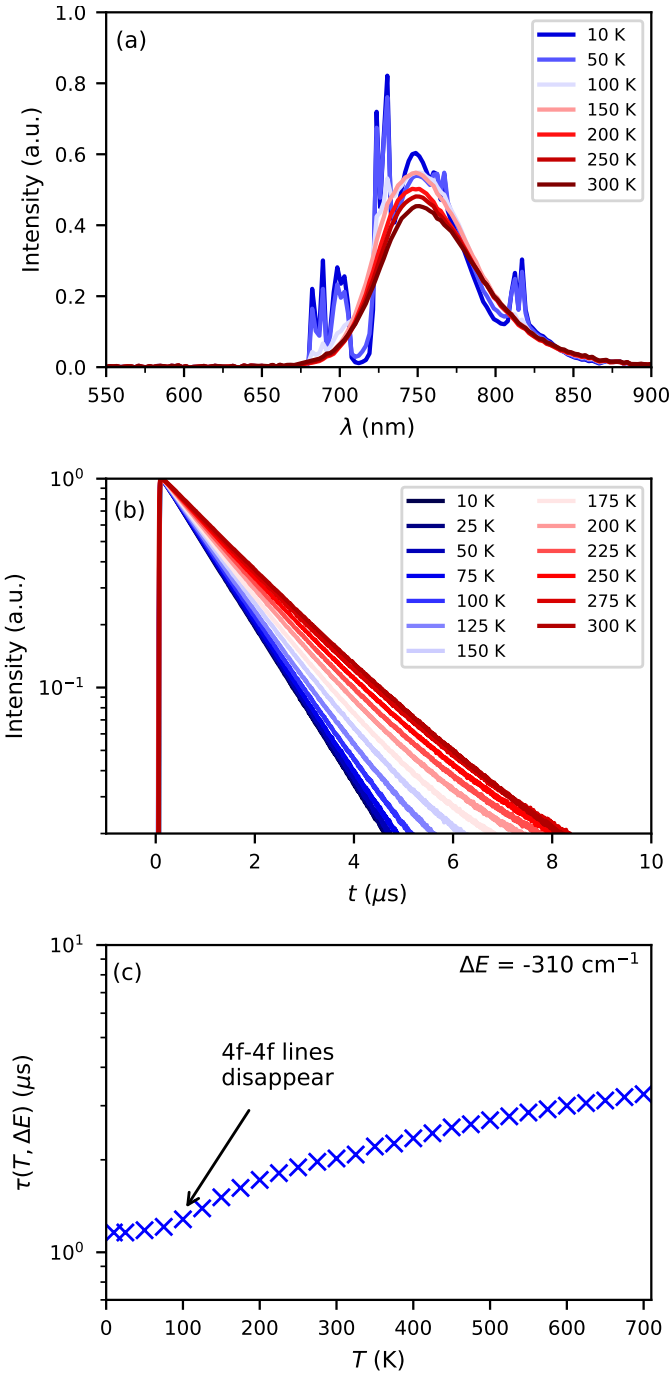

Figure 6.6: $CsBa_2I_5$:0.5%Sm^{2+} excited at 500 nm into the $4f^55d$ state, a) Photoluminescence emission spectra, b) Photoluminescence decay curves monitored at 750 nm, and c) Decay times of Sm^{2+} emission versus temperature.

The decay time constants of the $4f^5 5d \rightarrow 4f^6$ emission as a function of temperature are shown in Figure 6.5c. For temperatures between 10 K and 100 K, only the decay time values of the slow component are included. It shows that at 100 K, the lowest temperature at which only $4f^5 5d \rightarrow 4f^6$ emission is visible in the emission spectrum, the decay time is still shortening rapidly. A further increase in temperature to 500 K further shortens the decay time by almost an order of magnitude after which it stabilises. Around 700 K, another decrease in decay time associated with the onset of thermal quenching is observed. These results show that when an emission spectrum at room temperature contains exclusively $4f^5 5d \rightarrow 4f^6$ emission, the rate of thermal repopulation from the $4f^6[^5D_0]$ state can still lengthen the decay time observed for the $4f^5 5d \rightarrow 4f^6$ emission. Similar temperature dependence of the decay time was previously observed in $SrCl_2:Sm^{2+}$ and $SrBr_2:Sm^{2+}$ [35].

The second example is $CsBa_2I_5$:0.5%Sm^{2+}. Figure 6.6a shows the photoluminescence emission spectra between 10 K and 300 K excited at 500 nm. Similar to the photoluminescence emission spectra of $YbCl_2$:1%Sm^{2+}, the 10 K emission spectrum shows $4f^6 \rightarrow 4f^6$ line emission on top of broad band $4f^5 5d \rightarrow 4f^6$ emission. The $4f^6 \rightarrow 4f^6$ line emission intensity again descreases upon increase of temperature and from 100 K onwards, exclusively $4f^5 5d \rightarrow 4f^6$ emission is visible in the emission spectrum. The temperature dependence of the emission spectra shows no large difference between $YbCl_2$:1%Sm^{2+} and $CsBa_2I_5$:0.5%Sm^{2+}, however the emission band maximum of λ_{5d} = 755 nm implies with Equation 6.5 that ΔE = -310 cm^{-1}, which means that the $4f^5 5d$ level now lies below the $4f^6[^5D_0]$ level.

Figure 6.6b shows the corresponding decay curves of the $4f^5 5d \rightarrow 4f^6$ emission, excited at 500 nm and monitored at 750 nm. As opposed to rapid shortening of the decay time with increasing temperature that was seen in $YbCl_2$:1%Sm, the Sm^{2+} emission in $CsBa_2I_5$:0.5%Sm^{2+} gradually lengthens as temperature is increased. Apparently the change of sign of ΔE can cause an extreme difference in the decay dynamics that is not necessarily manifest in the photoluminescence emission spectra of the two samples. Figure 6.6c shows the decay time constants of the $4f^5 5d \rightarrow 4f^6$ emission as a function of temperature. The temperature at which the $4f^6 \rightarrow 4f^6$ emission lines disappear coincides with the temperature at which the decay time starts to lengthen.

To further investigate the interplay between the $4f^5 5d$ and $4f^6[^5D_0]$ levels, data on $\tau(300\,K, \Delta E)$ measured on the Sm^{2+} $4f^5 5d \rightarrow 4f^6$ emission in various compounds have been compiled in Table 6.2. A plot of $\tau(300\,K, \Delta E)$ versus λ_{5d} is shown in Figure 6.7. ΔE is negative for $\lambda_{5d} > 740$ nm. In this wavelength range the data points are well described by a λ_{5d}^3 trend line. At $\lambda_{5d} < 740$ nm, where ΔE is positive, the λ_{5d}^3 trend is broken and τ starts to rapidly increase.

The calculated values of $\tau(300\,K, \Delta E)$ using Equation 6.10 are shown by the black dotted line in Figure 6.7. The model follows the data well and accurately predicts that $\tau(300\,K, \Delta E)$ increases when $\lambda_{5d} < 740$ nm and also the steepness of this increase corresponds well to the data. It also explains why no data points were found for $\lambda_{5d} < 650$ nm, as this is where $\tau(300\,K, \Delta E)$ converges to the 1 ms value of τ_{4f}, and then following Equations 6.10 and 6.11 those compounds show exclusively $4f^6 \rightarrow 4f^6$ emission.

Table 6.2: Room temperature decay times $\tau(300\,\mathrm{K}, \Delta E)$ of Sm^{2+} $4f^5 5d \rightarrow 4f^6$ emission in various compounds. λ_{5d} denotes the wavelength of the $4f^5 5d \rightarrow 4f^6$ emission band maximum and $\Delta E = E_{5d} - E_{4f}$ in the configurational coordinate diagram.

Compound	λ_{5d} (nm)	ΔE (cm^{-1})	$\tau(300\,\mathrm{K}, \Delta E)$ (µs)	ref.
$BaCl_2$	655	1710	1700	[74]
$BaCl_2$:12.5%La	655	1710	100	[75]
KY_3F_{10}	660	1600	230	[76]
$Sm(AlCl_4)_2$	660	1600	275	[31]
YbFBr	662	1550	409	This work
BaBrI	666	1460	2150	[73]
BaFI	675	1260	350	[77, 78]
$Sr_{0.7}Ba_{0.3}Cl_2$	680	1150	15	[79]
$SrCl_2$	690	940	13	[35]
CsBr	695	830	15	[80]
$SrBr_2$	702	690	13	[35]
$Sm(AlBr_4)_2$	712	490	35	[31]
$KSrPO_4$	715	430	390	[81]
$YbCl_2$	727	200	5.2	[67]
KCl	730	140	4.3	[20]
SrI_2	740	43	1.5	[17, 30, 35]
$CsBa_2I_5$	755	-310	2.1	[18, 66]
$CsYbBr_3$	780	-740	2.1	[67]
$CsYbI_3$	800	-1060	2.3	[67]
Cs_4EuBr_6	820	-1360	3.5	[68]
Cs_4EuI_6	848	-1760	3.5	[68]

To further explore the different types of temperature behaviour of $\tau(T, \Delta E)$, 4 compounds with different ΔE are analysed in Figure 6.8. Figure 6.8a shows the configurational coordinate diagram of Sm^{2+} in 4 different compounds. The black parabola represent the $4f^6$ states and are the same for all compounds. Parabola 1 represents the $4f^5 5d$ state for λ_{5d} = 662 nm (ΔE = 1550 cm^{-1}), which corresponds to YbFBr:1%Sm^{2+}. Parabola 2 correspond to λ_{5d} = 727 nm (ΔE = 200 cm^{-1}), which is the case for $YbCl_2$:1%Sm^{2+}. Parabola 3 has λ_{5d} = 755 nm (ΔE = -310 cm^{-1}), corresponding to $CsBa_2I_5$:0.5%Sm^{2+}. Lastly, parabola 4 represents the situation for λ_{5d} = 848 nm (ΔE = -1760 cm^{-1}), which is the case for Cs_4EuI_6:0.5%Sm^{2+}.

The experimental values of $\tau(T, \Delta E)$ as a function of temperature for these 4 compounds are shown in Figure 6.8b. Curve 1 shows the experimental data for YbFBr:1%Sm^{2+}. Below 175 K, $\tau(T, 1550\,cm^{-1})$ could not be accurately determined by measuring the $4f^5 5d \rightarrow 4f^6$ emission as its intensity was too low. Therefore, data points between 10 K and 150 K were determined from the $4f^6 \rightarrow 4f^6$ emission decay time. The data points at 150 K and 175 K have approximately the same value, which confirms that $\tau(T, 1550\,cm^{-1})$ is the same for both the $4f^5 5d \rightarrow 4f^6$ and $4f^6 \rightarrow 4f^6$ emission.

$\tau(T, 1550\ \text{cm}^{-1})$ remains almost constant until 350 K, after which it starts to gradually decrease. This means that up to 300 K, the emission spectrum mostly consists of $4f^6 \rightarrow 4f^6$ lines, as was also observed by Schipper and Blasse [82].

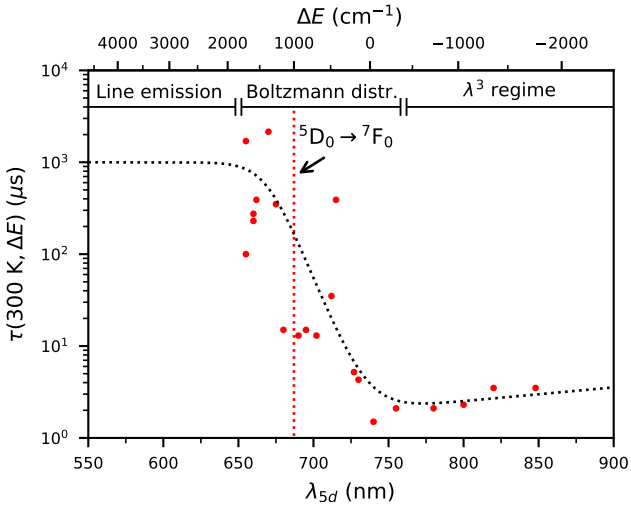

Figure 6.7: Room temperature decay times of Sm^{2+} $4f^55d \rightarrow 4f^6$ emission in various compounds. The red dashed line indicates the energy of the $4f^6[^5D_0] \rightarrow 4f^6[^7F_0]$ transition.

Curve 2 shows the experimental data for $YbCl_2$:1%Sm^{2+} (ΔE = 200 cm^{-1}), which are the same as shown in Figure 6.5c. Opposed to YbFBr:1%Sm^{2+}, $\tau(T, 200\ \text{cm}^{-1})$ of $YbCl_2$:1%Sm^{2+} starts to decrease already from 10 K onwards and converges to around 3.5 µs at 500 K. Curve 3 shows $\tau(T, -310\ \text{cm}^{-1})$ for $CsBa_2I_5$:0.5%Sm^{2+}, which are the same as shown in Figure 6.6c, and shows the steady increase in $\tau(T, -310\ \text{cm}^{-1})$ from 1.2 µs at 10 K to 3.2 µs at 700 K. Lastly, Curve 4 shows the experimental data for Cs_4EuI_6:0.5%Sm^{2+}. Its value for $\tau(T, -1760\ \text{cm}^{-1})$ slowly increases from 2.9 µs to 3.4 µs from 10 K to 700 K. Its value at 10 K is higher than that of $CsBa_2I_5$:0.5%Sm^{2+} and it has a smaller temperature dependence.

The calculated temperature behaviour of $\tau(T, \Delta E)$ for all 4 compounds is shown in Figure 6.8c. Curve 1 corresponds to ΔE = 1550 cm^{-1} (YbFBr:1%Sm^{2+}). $\tau(T, 1550\ \text{cm}^{-1})$ is stable at 1 ms from 0 K until almost 300 K. This value of 1 ms corresponds to τ_{4f} set in the model and means thermal population from the $4f^6[^5D_0]$ to the $4f^55d$ state is extremely unlikely and even when it occurs, thermal relaxation back down to the $4f^6[^5D_0]$ state will be much faster than emission. Above 300 K, $\tau(T, 1550\ \text{cm}^{-1})$ starts to decrease as there is enough thermal energy to excite Sm^{2+} from the $4f^6[^5D_0]$ to the $4f^55d$ state. The temperature at which this occurs agrees reasonably well with the experimental data in Figure 6.8b. $\tau(T, 1550\ \text{cm}^{-1})$ decreases less in the calculated data than in the experimental data. This may be caused by the close lying $4f^6[^5D_1]$ level in combination with the onset of thermal quenching, which can for example be seen by the more rapid downturn in the final step from 675 K to 700 K in the experimental data.

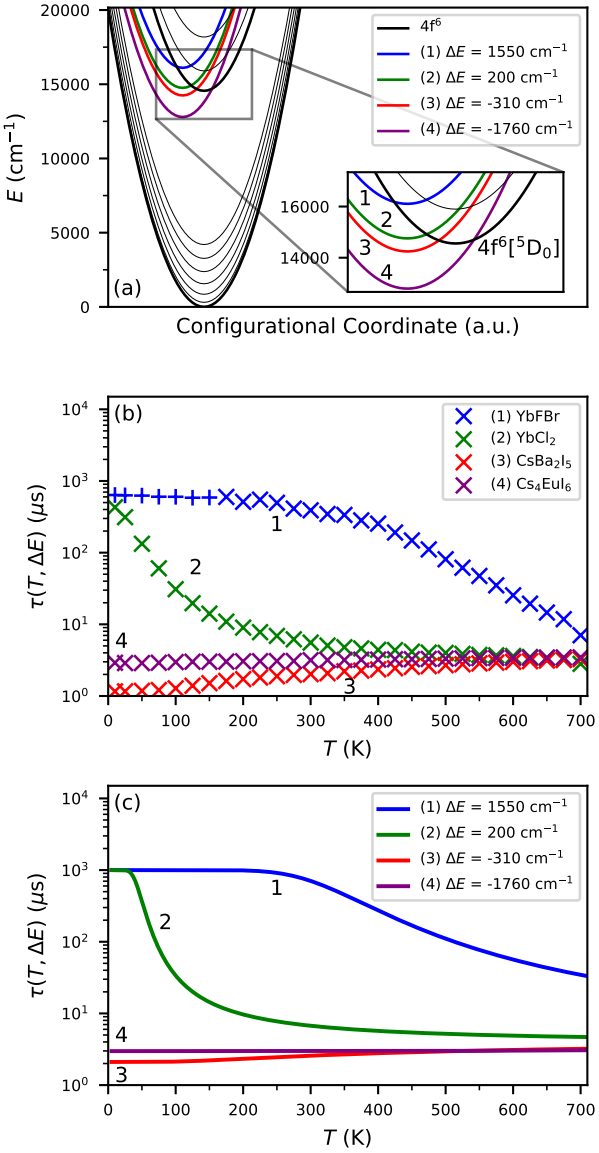

Figure 6.8: Decay times of Sm^{2+} $4f^5 5d \rightarrow 4f^6$ emission as a function of temperature. a) The configurational coordinate diagrams show the energy difference between the $4f^5 5d$ and $4f^6[^5D_0]$ levels for all four compounds. b) Experimentally observed temperature dependence of $\tau(T, \Delta E)$. Datapoints marked with "+" indicate $4f^6 \rightarrow 4f^6$ decay times. c) The calculated temperature dependence of $\tau(T, \Delta E)$.

Curve 2 corresponds to ΔE = 200 cm^{-1} ($YbCl_2$:1%Sm^{2+}). Its behaviour is similar to Curve 1, where $\tau(T, 200\ \text{cm}^{-1})$ is first 1 ms over an initial temperature range and then rapidly decreases as enough thermal energy becomes available to excite Sm^{2+} from the $4f^6[^5D_0]$ to the $4f^55d$ state. However, as ΔE is almost 8 times smaller than for Curve 1, all changes happen at 8 times lower temperature. This can be understood from Equation 6.10, in which the exponent in the denominator is responsible for most of the temperature dependence. A ΔE that is 8 times smaller requires an 8 times lower temperature for the same change in $\tau(T, \Delta E)$. As a result, the range in which $\tau(T, 200\ \text{cm}^{-1})$ is stable at 1 ms stops well below 50 K, shortly after which the $4f^6 \rightarrow 4f^6$ lines disappear from the emission spectrum in Figure 6.5a. The subsequent decrease in $\tau(T, 200\ \text{cm}^{-1})$ is also 8 times as steep compared to $\tau(T, 1550\ \text{cm}^{-1})$. This calculated data accurately explains that the difference between the temperature dependence of $\tau(T, \Delta E)$ of YbFBr:1%Sm^{2+} and $YbCl_2$:1%Sm^{2+} is primarily driven by their difference in ΔE.

Curve 3 shows the calculated temperature behaviour for ΔE = -310 cm^{-1} ($CsBa_2I_5$:0.5%Sm^{2+}). As ΔE is now negative, the $4f^55d$ state will be preferentially occupied at low temperatures and therefore $\tau(T, -310\ \text{cm}^{-1}) = \tau_{5d}$ at 0 K, almost 3 orders of magnitude faster than for Curves 1 and 2. Upon increase of the temperature, $\tau(T, -310\ \text{cm}^{-1})$ becomes longer as the $4f^6[^5D_0]$ state starts to become populated, similar to what is observed in the experimental data on $CsBa_2I_5$:0.5%Sm^{2+} (Figure 6.8b). This means that lengthening of $\tau(T, -310\ \text{cm}^{-1})$ with increasing temperature is an intrinsic property of Sm^{2+} when ΔE is negative and has a small magnitude. At 10 K, a value of $\tau(T, -310\ \text{cm}^{-1})$ is around 2 µs for the calculated curve, while the experimental data on $CsBa_2I_5$:0.5%Sm^{2+} show 1.2 µs at 10 K, meaning τ_{5d} has been estimated too high for this compound. $\tau(T, -310\ \text{cm}^{-1})$ increases with temperature and reaches a value of 3.2 µs at 700 K, indicating the $4f^6[^5D_0]$ state becomes more populated.

Finally, Curve 4 shows the situation for ΔE = -1760 cm^{-1} (Cs_4EuI_6:0.5%Sm^{2+}). At 0 K, $\tau(T, -1760\ \text{cm}^{-1})$ is significantly longer than for Curve 3. This is caused by the λ_{5d}^3 dependence of τ_{5d}. This is also observed in the experimental data in Figure 6.8b. As ΔE is almost 6 times as large as for Curve 3, the change in $\tau(T, -1760\ \text{cm}^{-1})$ is again spread out over a 6 times larger temperature range than $\tau(T, -310\ \text{cm}^{-1})$. The result is that $\tau(T, -1760\ \text{cm}^{-1})$ seems almost independent of temperature. This is also in line with the experimental data, where the smallest temperature dependence of $\tau(T, \Delta E)$ of all samples is found in Cs_4EuI_6:0.5%Sm^{2+}.

The model has also been applied to Eu^{2+} and Pr^{3+} and its results are shown in Figure 6.9. $\tau(300\ \text{K}, \Delta E)$ data measured on the Eu^{2+} $4f^65d \rightarrow 4f^7$ emission have been collected. Only data were used in which the effects of thermal quenching, concentration quenching, and self-absorption were minimal. The $\tau(300\ \text{K}, \Delta E)$ values are shown in Table 6.3 and plotted against λ_{5d} in Figure 6.9, together with those of Sm^{2+}. The calculated curves of $\tau(300\ \text{K}, \Delta E)$ for Sm^{2+} (Curve 1), Eu^{2+} (Curve 2), and Pr^{3+} (Curve 3) are also shown in Figure 6.9, using the input parameters from Table 6.1.

For $\lambda_{5d} > 400$ nm the calculated values of $\tau(300\ \text{K}, \Delta E)$ for Eu^{2+} are primarily described by the λ^3 dependence of τ_{5d} and the Eu^{2+} data scatter nicely around it. When $\lambda_{5d} <$ 400 nm, the calculated values shows an increase in $\tau(300\ \text{K}, \Delta E)$ and converge to the value of 1 ms that corresponds to τ_{4f} around 350 nm. The wavelength range in which $\tau(300\ \text{K}, \Delta E)$ increases is more narrow than for Sm^{2+}, which is solely caused by the non-

linear conversion from an energy to wavelength scale. On an energy scale, both ranges would have equivalent size. In the wavelength range between 350 nm and 400 nm, some compounds show a longer $\tau(300\,\mathrm{K}, \Delta E)$ value than the typical decay times for τ_{5d} of between 0.5 µs and 1 µs. These data points follow the calculcated increase in $\tau(300\,\mathrm{K}, \Delta E)$ well and thereby show that this model can be effectively applied to Eu^{2+}.

For Pr^{3+}, the resulting relation between $\tau(300\,\mathrm{K}, \Delta E)$ and λ_{5d} is shown by Curve 3 in Figure 6.9. Unfortunately, no $\tau(300\,\mathrm{K}, \Delta E)$ data could be found that confirms that the model can be applied to Pr^{3+} as well. Data on Pr^{3+} $4f^1 5d \rightarrow 4f^2$ decay times near 225 nm are scarce, which is likely due to experimental difficulty as it requires measuring decay times of around 10 ns with a vacuum UV excitation source. The temperature dependent decay times of the Pr^{3+} $4f^2[^1S_0]$ state in $LaPO_4$ and $LiLaP_4O_{12}$ were reported by Srivastava et al. and shows similar temperature dependence as the $4f^5 5d \rightarrow 4f^6$ emission of Sm^{2+} in $YbCl_2$ [51, 52]. The compounds show respective emission wavelengths λ_{5d} of 228 nm and 217 nm and fall precisely within the wavelength range where the $\tau(300\,\mathrm{K}, \Delta E)$ increases. Unfortunately, no data on the room temperature decay times were presented and it cannot be verified that the two states are in thermal equilibrium.

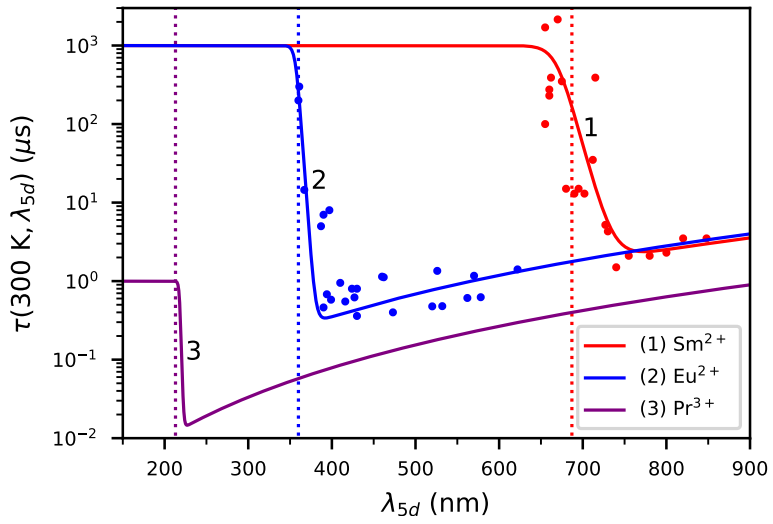

Figure 6.9: Room temperature decay times of $4f^{n-1}5d \rightarrow 4f^n$ emission of (1) Sm^{2+}, (2) Eu^{2+}, and (3) Pr^{3+} against wavelength.

Table 6.3: Room temperature decay times $\tau(300\,\mathrm{K}, \Delta E)$ of Eu^{2+} $4f^6 5d \rightarrow 4f^7$ emission in various compounds. λ_{5d} denotes the wavelength of the $4f^6 5d \rightarrow 4f^7$ emission band maximum and $\Delta E = E_{5d} - E_{4f}$ in the configurational coordinate diagram.

Compound	λ_{5d} (nm)	ΔE (cm^{-1})	$\tau(300\,\mathrm{K}, \Delta E)$ (µs)	ref.
$SrAlF_5$	360	1500	200	[44]
$LiBaAlF_6$	361	1420	300	[83]
SrB_4O_7	367	970	14.5	[84]
SrFCl	387	-440	5.0	[85]
BaFCl	390	-640	7.0	[85]
$SrMgP_2O_7$	390	-640	0.46	[86]
BaFBr	394	-900	0.68	[45]
$SrAl_{12}O_{19}$	397	-1090	8	[48, 87]
$BaCl_2$	399	-1220	0.58	[85]
$SrCl_2$	410	-1890	0.95	[85]
SrF_2	416	-2240	0.55	[85]
CaF_2	424	-2690	0.8	[85]
SrI_2	427	-2860	0.7	[88]
$CaCl_2$	430	-3020	0.8	[85]
$CsBa_2I_5$	430	-3020	0.36	[89]
Cs_4SrI_6	460	-4540	1.14	[90]
Cs_4CaI_6	462	-4630	1.12	[90]
$BaAl_2S_4$	473	-5140	0.4	[91]
$KLuS_2$	520	-7050	0.48	[92]
$CsCaF_3$	526	-7270	1.35	[93]
$SrGa_2S_4$	532	-7480	0.48	[94]
$CaGa_2S_4$	562	-8480	0.61	[95]
$LiSrSiO_4$	570	-8730	1.17	[96]
Sr_3SiO_5	578	-8980	0.63	[97]
$Rb_3YSi_2O_7$	622	-10200	1.41	[98]

6.5. Discussion

The described decay time model of Equation 6.10 only holds when the Sm^{2+} $4f^5 5d$ level and $4f^6[^5D_0]$ level are in thermal equilibrium. An example of an out-of-equilibrium situation is encountered in Figure 6.5b, where the photoluminescence decay of $YbCl_2$:1%Sm^{2+} shows a <10 ns fast component between 10 K and 100 K in addition to the slow component that was visible at all temperatures. Only the origin of the slow component is described by the decay time model expressed by Equation 6.10. The origin of the fast component is illustrated by the left schematic of Figure 6.10. Sm^{2+} is optically excited into one of the higher lying $4f^5 5d$ levels, corresponding to arrow A. After this, relaxation to the lower lying levels through arrows B and C will result in a distribution over the $4f^5 5d$ and $4f^6[^5D_0]$ levels that does not necessarily match the distribution that corresponds to Boltzmann statistics. Using Equation 6.7 with ΔE = 200 cm^{-1} and T = 100 K,

the Boltzmann distribution is established when $p_{4f} = 95\%$ and consequently $p_{5d} = 5\%$. It is therefore likely that the initial distribution contains an overpopulation of Sm^{2+} ions in the $4f^5 5d$ state.

Nonradiative decay to the $4f^6[^5D_0]$ state via arrow D with rate k_{21} and radiative decay to the ground state via arrow E with rate τ_{5d}^{-1} will make the excited Sm^{2+} population converge to the Boltzmann distribution. The fast component in Figure 6.5b is then an indication of how fast the population converges to the Boltzmann distribution and its decay time τ_f is given by Equation 6.12.

$$\frac{1}{\tau_f} = \frac{1}{\tau_{5d}} + k_{21} \tag{6.12}$$

As τ_{5d} is approximately 2 µs and τ_f in Figure 6.5b is <10 ns, k_{21} has by far the largest contribution to this decay time, even at 10 K. k_{21} is typically caused by the interconfigurational crossing of the $4f^5 5d$ and $4f^6[^5D_0]$ states and therefore the rate is expected to increase with temperature. As a consequence, the time it takes for the excitations to reach a Boltzmann distribution will become even shorter at higher temperatures until the fast component can no longer be observed.

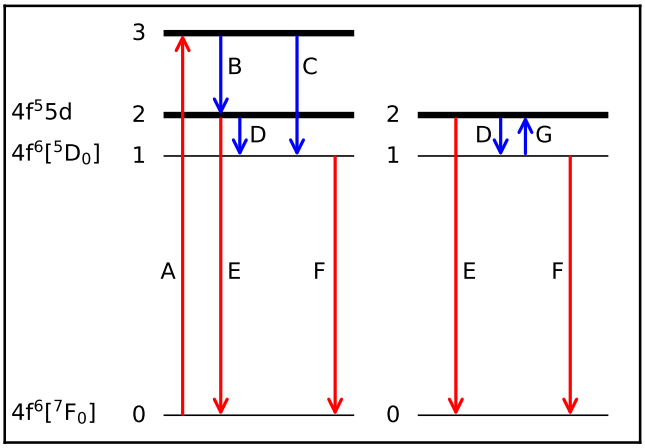

Figure 6.10: Schematic showing the origin of the fast component in the luminescence decay of Sm^{2+}. Left: Directly after excitation an excess of $4f^5 5d$ excitations causes a fast component and Right: Situation after Boltzmann distribution between the $4f^5 5d$ and $4f^6[^5D_0]$ states is established.

After the fast component has disappeared, the Boltzmann distribution has been established and the schematic on the right of Figure 6.10 applies. The electronic configuration of the Sm^{2+} ions is constantly switching between the $4f^5 5d$ and $4f^6[^5D_0]$ states through arrows D and G. At any point in time, the probability to find a Sm^{2+} ion in each of the two states now corresponds to p_{5d} in Equation 6.6 and p_{4f} in Equation 6.7. In this situation, radiative decay is possible from both excited states via arrows E and F. In $YbCl_2$:1%Sm^{2+} at 100 K however, where $p_{4f} = 95\%$ and $p_{5d} = 5\%$, the emission spectrum shows almost exclusively $4f^5 5d \rightarrow 4f^6$ emission. This can be understood from Equation 6.11. As τ_{5d} is

roughly 500 times shorter than τ_{4f} for Sm^{2+}, Sm^{2+} ions will prefentially decay through the $4f^5 5d \rightarrow 4f^6$ transition and less than 4% of the total emission intensity comes from the $4f^6 \rightarrow 4f^6$ emission. At 300 K, this will even be less than 0.5%. When not specifically looking for the presence of $4f^6 \rightarrow 4f^6$ lines by employing spectroscopic techniques with high wavelength resolution and exceptional signal to noise ratio, these $4f^6 \rightarrow 4f^6$ lines will likely go unnoticed and only broad band $4f^5 5d \rightarrow 4f^6$ emission will be observed.

For luminescence thermometry, a large relative sensitivity S_r is acquired when $\tau(T, \Delta E)$ rapidly changes with temperature (see Equation 6.1). It can be seen in Figure 6.8 that the largest changes in $\tau(T, \Delta E)$ are found when ΔE is positive and its magnitude is small. It was for example recently found that doping SrB_4O_7 with Eu^{2+} for luminescent thermometer applications results in much higher S_r values than what is achieved with Sm^{2+}-doping in SrB_4O_7 [84]. One cause for this is that in SrB_4O_7, the ΔE between the $4f^7[^6P_{7/2}]$ and $4f^6 5d$ states of Eu^{2+} (130 cm^{-1} [99]) is almost 25 times smaller than ΔE between the $4f^6[^5D_0]$ and $4f^5 5d$ states of Sm^{2+} (3100 cm^{-1} [25]). This shifts the temperature at which S_r has its maximum value from roughly 550 K [26] to around 20 K [84], but simultaneously increases the maximum achievable S_r value by the same factor 25. Sójka et al. reported an S_r value of over 10% at 20 K in SrB_4O_7:Eu^{2+} [84], compared to the 3.3% at 550 K reported for SrB_4O_7:Sm^{2+} [26]. By monitoring the luminescence intensity ratio between the the Eu^{2+} $4f^n \rightarrow 4f^n$ emission with that of Sm^{2+}, Zheng et al. achieved S_r values of over 40% at temperatures below 20 K [100]. This shows that the high S_r values at cryogenic temperatures are a direct consequence of a small ΔE.

Another small contribution to the larger S_r can be found in the shorter τ_{5d} of the Eu^{2+} $4f^{n-1}5d \rightarrow 4f^n$ emission compared to that of Sm^{2+}, which is primarily due to the shorter λ_{5d}. The total change in $\tau(T, \Delta E)$ is approximately the difference between τ_{4f} and τ_{5d}. This difference increases as τ_{5d} becomes smaller. A larger change in $\tau(T, \Delta E)$ in turn results in higher values of S_r, which means that Eu^{2+} should give larger values for S_r than Sm^{2+} when they have the same ΔE.

For scintillators there is a strong preference for materials with a short $\tau(300\,K, \Delta E)$. Wolszczak et al. formulated a criterion for using Sm^{2+} as a dopant for scintillation saying that it must exclusively show $4f^5 5d \rightarrow 4f^6$ emission, resulting in a restriction of $\lambda_{5d} >$ 698 nm [101]. From Figure 6.7 it can be seen that this criterion should be formulated more strictly. The model presented in this work predicts that around λ_{5d} = 700 nm, τ is already over an order of magnitude longer than it is at its minimum value around 750 nm. A better criterion would therefore be that λ_{5d} should be no shorter than 730 nm. Going to longer wavelengths than 750 nm, the decay time lengthens again due to the λ_{5d}^3 dependence. This lengthening is however much less severe and should not impose a restriction on what λ_{5d} can be used. Looking at Table 6.2, it can be seen that the criterion of $\lambda_{5d} > 730$ nm is often achieved in iodides (large nephelauxetic effect) or compounds in which Sm^{2+} sits on a site with octahedral symmetry (large crystal field splitting).

$\lambda_{5d} > 730$ nm implies that ideally ΔE is negative for scintillators. For negative ΔE, the $4f^6 \rightarrow 4f^6$ emission is often completely absent at all temperatures. An increase in temperature promotes Sm^{2+} to the slowly decaying $4f^6[^5D_0]$ level and thereby lengthens $\tau(T, \Delta E)$. This effect is most prominent when the magnitude of ΔE is small, as can be seen by the differences in curves 3 and 4 in Figure 6.8. While lengthening of $\tau(T, \Delta E)$ is an intrinsic property of Sm^{2+} in compounds like $CsBa_2I_5$, it strongly resembles the effect of

self-absorption. When Sm^{2+} emits a photon in the wavelength range where other Sm^{2+} ions can reabsorb it, there is a probability that the photon is reabsorbed before leaving the material. It then again takes time for the newly excited Sm^{2+} to emit a photon, lengthening the decay time and increasing the probability of luminescence quenching. This effect is detrimental for applications in which large crystals are required, as a photon travelling through the crystal encounters more Sm^{2+} ions before exiting the crystal, increasing the probability of self-absorption. Lengthening of the decay time with increasing temperature is often ascribed to self-absorption, as absorption and emission bands broaden and the overlap between them grows, increasing the probability that a photon is re-absorbed. With the knowledge that the lengtening of $\tau(T, \Delta E)$ with increasing temperature is an intrinsic property of Sm^{2+}, it is more reliable to probe the probability of self-absorption comparing samples of different sizes or Sm^{2+} concentrations, rather than relying on temperature dependent data.

Even though $\tau(300\ \mathrm{K}, \Delta E)$ values are suitable for scintillation for $\lambda_{5d} > 730$ nm, some additional restrictions on λ_{5d} might be imposed by the choice of photodetector. Silicon based photodetectors typically show optimal performance between 400 nm and 800 nm, where almost all undetected photons are reflected from the detector. These photons can be recovered by wrapping the scintillor and detector combination in reflective material, giving the photons a second chance to be detected [102]. At wavelengths longer than 800 nm, silicon starts to become transparent and transmission losses occur. Even detectors optimised for near-infrared detection show a sharp drop in quantum efficiency between 900 nm and 950 nm. When a significant part of the Sm^{2+} emission spectrum lies beyond 950 nm, the number of detected photons decreases, which worsens the energy resolution. The longest wavelength emitting scintillator in Table 6.2 is Cs_4EuI_6:Sm^{2+} with λ_{5d} = 848 nm [68]. The Sm^{2+} $4f^55d \rightarrow 4f^6$ emission in this compound shows a tail extending beyond 1000 nm, meaning losses already occur when coupling it to a silicon based photodetector. Losses are expected to be minimal for compounds with $\lambda_{5d} < 800$ nm. This means that the ideal λ_{5d} for near-infrared scintillators with silicon based photodetecetor read out sits in a narrow window from 730 nm to 800 nm. It is worth pointing out that the currently best performing NIR scintillator $CsBa_2I_5$:2%Eu^{2+},1%Sm^{2+} with its λ_{5d} of 755 nm lies within this window and even close to the minimum value of $\tau(300\ \mathrm{K}, \Delta E)$.

6.6. Conclusions

The effect of a Boltzmann distribution establishing between population of the Sm^{2+} $4f^55d$ and $4f^6[^5D_0]$ levels on $4f^55d \rightarrow 4f^6$ decay time has been modelled and compared with data from literature. It is found that when the maximum of the $4f^55d \rightarrow 4f^6$ emission wavelength is shorter than 730 nm, the probability to find an excited Sm^{2+} in the $4f^6[^5D_0]$ state becomes large enough that it lengthens the decay time of the $4f^55d \rightarrow 4f^6$ emission. This effect becomes more pronounced at shorter $4f^55d \rightarrow 4f^6$ emission wavelengths. Experimental evidence is also provided which shows that the model can be applied to the $4f^65d$ and $4f^7[^6P_{7/2}]$ levels of Eu^{2+}. The $4f^65d \rightarrow 4f^7$ decay time becomes longer when its emission wavelength is shorter than 400 nm. For Pr^{3+}, it is predicted that the $4f^l5d \rightarrow 4f^2$ decay time becomes longer below 220 nm.

The model is used to explain large variations in the temperature dependence of the

Sm^{2+} $4f^5 5d \rightarrow 4f^6$ emission decay time. When the $4f^5 5d$ level lies above the $4f^6[^5D_0]$ level, the $4f^6[^5D_0]$ level is primarily populated at low temperatures. Luminescence decay becomes faster upon increase of temperature as the $4f^5 5d$ level is thermally populated. The total change in decay time can be as large as 3 orders of magnitude. When the $4f^5 5d$ level lies below the $4f^6[^5D_0]$ level, the luminescence decay becomes slower upon increase of temperature. In both scenarios, the rate at which the decay time changes with temperature scales approximately with the inverse of the energy difference between the $4f^5 5d$ and $4f^6[^5D_0]$ levels, meaning faster changes are observed when the two levels lie close together. This information can be used for the development of luminescent thermometers.

For near-infrared scintillators, it has been determined that the decay time becomes too long when the $4f^5 5d \rightarrow 4f^6$ emission wavelengths is shorter than 730 nm. When the emission wavelength becomes longer than 800 nm, unrecoverable losses will occur in silicon based photodetectors. Therefore the optimal wavelength window for Sm^{2+}-doped near-infared scintillators is between 730 nm and 800 nm.

6.7. Acknowledgements

This research was subsidized by the TTW/OTP grant no. 18040 of the Dutch Research Council. The authors would like to thank Daniel Biner, Bern, for the synthesis and crystal growth of the materials.

References

[1] D. L. Wood, W. Kaiser, Phys. Rev. 126 (1962) 2079.

[2] G. Baldini, M .Cartoceti, M. Guzzi, Solid State Commun. 8 (1970) 1697.

[3] M. Guzzi, G. Baldini, J. Lumin. 6 (1973) 270.

[4] R. Jaaniso, H. Bill, Europhys. Lett. 16 (1991) 569.

[5] Changjiang Wei, Keith Holliday, Alfred J. Meixner, Mauro Croci, Urs P. Wild, J. Lumin. 50 (1991) 89.

[6] W. Kaiser, C. G. B. Garrett, D. L. Wood, Phys. Rev. 123 (1961) 766.

[7] V. K. Koniukhov, V. Marchenko, A. Prokhorov, IEEE J. Quantum Electron. 2 (1966) 541.

[8] Yu. A. Anan'ev, A. A. Mak, B. M. Sedov, J. Exp. Theor. Phys. (U.S.S.R.) 52 (1967) 12.

[9] Hans Riesen, Wieslaw A. Kaczmarek, Inorg. Chem. 46 (2007) 7235.

[10] Go Okada, Noriaki Ikenaga, Yasuhiro Koguchi, Takayuki Yanagida, Safa Kasap, Hidehito Nanto, Mater. Res. Bull. 159 (2023) 112107.

[11] David de Vries, Sadiq van Overbeek, Evert P. J. Merkx, Erik van der Kolk, J. Lumin. 225 (2020) 117321.

[12] L. J. B. Erasmus, P. F. Smet, R. E. Kroon, D. Poelman, J. J. Terblans, J. J. Joos, D. Van der Heggen, H. C. Swart, ACS Photonics 10 (2023) 609.

[13] A. Lacam, C. Chateau, J. Appl. Phys. 66 (1989) 366.

[14] Paola Comodi, Pier Francesco Zanazzi, J. Appl. Crystallogr. 26 (1993) 843.

[15] Teng Zheng, Marcin Runowski, Przemysław Woźny, Stefan Lis, Victor Lavin, J. Mater. Chem. C, 8 (2020) 4810.

[16] Laura Catherine Dixie, Andrew Edgar, Colin Murray Bartle, Nucl. Instrum. Methods A 753 (2014) 131.

[17] R. H. P. Awater, M. S. Alekhin, D. A. Biner, K. W. Krämer, P. Dorenbos, J. Lumin. 212 (2019) 1.

[18] Weronika Wolszczak, Karl W. Krämer, Pieter Dorenbos, Phys. Status Solidi R. 13 (2019) 1900158.

[19] Daisuke Nakauchi, Yutaka Fujimoto, Takumi Kato, Noriaki Kawaguchi, Takayuki Yanagida, Crystals 12 (2022) 517.

[20] Claudio Yamamoto Morassuti, Simone Finoto, Junior Reis Silva, Sandro Marcio Lima, Luis Humberto da Cunha Andrade, Phys. Status Solidi B 257 (2020) 1900484.

[21] Aleksandar Ćirić, Stevan Stojadinović, Zoran Ristić, Ivana Zeković, Sanja Kuzman, Željka Antić, Miroslav D. Dramićanin, Adv. Mater. Technol. 6 (2021) 2001201.

[22] Chenwei Xu, Chenxia Li, Degang Deng, Jianxun Lu, Hua Yu, Le Wang, Xufeng Jing, Shiqing Xu, Chunxu Shao, Inorg. Chem. 61 (2022) 7989.

[23] P. Dorenbos, J. Phys. Condens. Matter 15 (2003) 575.

[24] Jianghao Xiong, Mingshu Zhao, Xiaotian Han, Zhongmin Cao, Xiantao Wei, Yonghu Chen, Changkui Duan, Min Yin, Sci. Rep. 7 (2017) 41311.

[25] Benedikt Bendel, Markus Suta, J. Mater. Chem. C. 10 (2022) 13805.

[26] Zhongmin Cao, Xiantao Wei, Lu Zhao, Yonghu Chen, Min Yin, ACS Appl. Mater. Interfaces 8 (2016) 34546.

[27] Francis K. Fong, Howard V. Lauer, Charles R. Chilver, J. Chem. Phys. 63 (1975) 366.

[28] Laura C. Dixie, Andrew Edgar, Michael F. Reid, J. Lumin. 132 (2012) 2775.

[29] Pieter Dorenbos, Opt. Mater. X. 1 (2019) 100021.

[30] Mikhail S. Alekhin, Roy H. P. Awater, Daniel A. Biner, Karl W. Krämer, Johan T. M. de Haas, Pieter Dorenbos, J. Lumin. 167 (2015) 347.

[31] T. C. Schäfer, J. R. Sorg, A. E. Sedykh, K. Müller-Buschbaum, Chem. Commun. 57 (2021) 11984.

[32] P. P. Feofilov, N. M. Tolstoi, Opt. Spectrosc. 13 (1962) 164.

[33] A. S. M. Mahbub'ul Alam, B. Di Bartolo, Phys. Lett. 25A (1967) 157.

[34] L. L. Chase, Stephen A. Payne, Gary D. Wilke, J. Phys. C Solid State 20 (1987) 953.

[35] Mirosław Karbowiak, Piotr Solarz, Radosław Lisiecki, Witold Ryba-Romanowski, J. Lumin. 195 (2018) 159.

[36] J. L. Sommerdijk, J. M. P. J. Verstegen, A. Bril, J. Lumin. 8 (1974) 502.

[37] J. Sytsma, G. Blasse, J. Lumin. 51 (1992) 283.

[38] J. M. P. J. Verstegen, J. L. Sommerdijk, J. Lumin. 9 (1974) 297.

[39] J. L. Sommerdijk, A. Bril, J. Lumin. 11 (1976) 363.

[40] D. K. Sardar, W. A. Sibley, R. Alcala, J. Lumin. 27 (1982) 401.

[41] R. Alcala, D. K. Sardar, W. A. Sibley, J. Lumin. 27 (1982) 273.

[42] S. Mahlik, K. Wisniewski, M. Grinberg, Hyo Jin Seo, J. Non-Cryst. Solids 356 (2010) 1888.

[43] J. J. Schuyt, G. V. M. Williams, J. Lumin. 204 (2018) 472.

[44] R. A. Hewes, M. V. Hoffman, J. Lumin. 3 (1971) 261.

[45] J. P. Spoonhower, M. S. Burberry, J. Lumin. 43 (1989) 221.

[46] S. H. M. Poort, A. Meijerink, G. Blasse, J. Phys. Chem. Solids 58 9 (1997) 1451.

[47] A. Meijerink, J. Lumin. 55 (1993) 125.

[48] D. Dutczak, T. Jüstel, C. Ronda, A. Meijerink, Phys. Chem. Chem. Phys. 17 (2015) 15236.

[49] Sadao Adachi, ECS J. Solid State Sci. Technol. 12 (2023) 016002.

[50] Fangtian You, Shihua Huang, Chunxia Meng, Dawei Wang, Jianhua Xu, Yan Huang, Guobin Zhang, J. Lumin. 122-123 (2007) 58.

[51] A. M. Srivastava, A. A. Setlur, H. A. Comanzo, M. E. Hannah, P. A. Schmidt, U. Happek, J. Lumin. 129 (2009) 126.

[52] A. M. Srivastava, A. A. Setlur, H. A. Comanzo, W. W. Beers, U. Happek, P. Schmidt, Opt. Mater. 23 (2011) 292.

[53] L. R. Elias, Wm. S. Heaps, W. M. Yen., Phys. Rev. B 8 (1973) 4989.

[54] P. A. Rodnyi, P. Dorenbos, G. B. Stryganyuk, A. S. Voloshinovskii, A. S. Potapov, C. W. E. van Eijk, J. Phys. Condens. Matter 15 (2003) 719.

[55] P. Vergeer, V. Babin, A. Meijerink, J. Lumin. 114 (2005) 267.

[56] E. van der Kolk, P. Dorenbos, C. W. E. van Eijk, A. P. Vink, C. Fouassier, F. Guillen, J. Lumin. 97 (2002) 212.

[57] R. Pappalardo, J. Lumin. 14 (1976) 159.

[58] A. M. Srivastava, D. A. Doughty, W. W. Beers, J. Electrochem. Soc. 142 (1996) 4113.

[59] S. Kück, I. Sokólska, M. Henke, M. Döring, T. Scheffler, J. Lumin. 102-103 (2003) 176.

[60] M. Nikl, H. Ogino, A. Yoshikawa, E. Mihokova, J. Pejchal, A. Beitlerova, A. Novoselov, T. Fukuda, Chem. Phys. Lett. 410 (2005) 218.

[61] M. Trevisani, K. V. Ivanovskikh, F. Piccinelli, A. Speghini, M. Bettinelli, ECS Trans. 41 (37) (2012) 11.

[62] Vladimir A. Pustovarov, Konstantin V. Ivanovskikh, Yulya E. Khatchenko, Qiufeng Shi, Marco Bettinelli, Radiat. Meas. 123 (2019) 39.

[63] A. M. Srivastava, J. Lumin. 169 (2016) 445.

[64] P. Dorenbos, J. Lumin. 104 (2003) 239.

[65] Aleksander Zych, Matthijs de Lange, Celso de Mello Donegá, Andries Meijerink, J. Appl. Phys. 112 (2012) 013536.

[66] Casper van Aarle, Karl W. Krämer, Pieter Dorenbos, J. Lumin. 238 (2021) 118257.

[67] Casper van Aarle, Karl W. Krämer, Pieter Dorenbos, J. Lumin. 251 (2022) 119209.

[68] Casper van Aarle, Karl W. Krämer, Pieter Dorenbos, J. Mater. Chem. C 11 (2023) 2336.

[69] W. J. Schipper, G. Blasse, J. Lumin. 59 (1994) 377.

[70] P. Dorenbos, J. Phys. Condens. Matter 15 (2003) 4797.

[71] P. Dorenbos, J. Lumin. 91 (2000) 155.

[72] G. Meyer, Advances in the Synthesis and Reactivity of Solids, Vol. 2, p. 1-16. JAI Press Inc. 1994.

[73] D. Sofich, R. Shendrik, A. Rusakov, A. Shalaev, A. Myasnikova, AIP Conf. Proc. 2392 (2021) 040004.

[74] Zhi-yi He, Yong-shen Wang, Sun Li, Xu-rong Xu, J Lumin. 97 (2002) 102.

[75] Laura C. Dixie (2013): Samarium doped alkaline earth halides as red-emitting scintillators and phosphors. Victoria University of Wellington. Thesis. https://doi.org/10.26686/wgtn.17005837.v1

[76] Mitsuo Yamaga, Shin-ichiro Tsuda, Jon-Paul R. Wells, Thomas P. J. Han, J. Ceram. Process. Res. 15 (2014) 167.

[77] T. Penhouet, H. Hagemann, J. Alloys Compd. 451 (2008) 74.

[78] Prodipta Pal, Tiphaine Penhouët, Vincenza D'Anna, Hans Hagemann, J. Lumin. 142 (2013) 66.

[79] Laura C. Dixie, Andrew Edgar, Murray C. Bartle, J. Lumin. 149 (2014) 91.

[80] Go Okada, Yutaka Fujimoto, Hironori Tanaka, Safa Kasap, Takayuki Yanagida, J. Rare Earths 34 (2016) 769.

[81] Yanlin Huang, Weifang Kai, Yonggang Cao, Kiwan Jang, Ho Sueb Lee, Ilgon Kim, Eunjin Cho, J. Appl. Phys. 103 (2008) 053501.

[82] W J. Schipper, G. Blasse, J. Solid State Chem. 94 (1991) 418.

[83] J. L. Sommerdijk, P. Vries, A. Bril, Philips J. Res. 33 (1978) 117.

[84] Małgorzata Sójka, Marcin Runowski, Teng Zheng, Andrii Shyichuk, Dagmara Kulesza, Eugeniusz Zych, Stefan Lis, J. Mater. Chem. C 10 (2022) 1220.

[85] Takao Kobayasi, Stanley Mroczkowski, James F. Owen, Lothar H. Brixner, J. Lumin. 21 (1980) 247.

[86] Jin He, Rui Shi, Zhiqiang Wang, Minsi Li, Tsun-Kong Sham, Lianshe Fu, Adv. Opt. Mater. 10 (2022) 2101751.

[87] J. M. P. J. Verstegen, J. L. Sommerdijk, A. Bril, J. Lumin. 9 (1974) 420.

[88] Jarek Glodo, Edgar V. van Loef, Nerine J. Cherepy, Stephen A. Payne, Kanai S. Shah, IEEE Trans. Nucl. Sci. 57 (2010) 1228.

[89] Mikhail S. Alekhin, Daniel A. Biner, Karl W. Krämer, Pieter Dorenbos, J. Lumin. 145 (2014) 723.

[90] Daniel Rutstrom, Luis Stand, Merry Koschan, Charles L. Melcher, Mariya Zhuravleva, J. Lumin. 216 (2019) 116740.

[91] C. Barthou, R. B. Jabbarov, P. Benalloul, C. Chartier, N. N. Musayeva, B. G. Tagiev, O. B. Tagiev, J. Electrochem. Soc. 153 (2006) G253.

[92] V. Jarý, L. Havlák, J. Bárta, E. Mihóková, M. Nikl, Chem. Phys. Lett. 574 (2013) 61.

[93] U. Happek, M. Aycibin, A. M. Srivastava, H. A. Comanzo, S. Camardello, ECS Trans. 25 (2009) 39.

[94] C. Chartier, C. Barthou, P. Benalloul, J. M. Frigerio, J. Lumin. 111 (2005) 147.

[95] Paul Benalloul, Carlos Barthou, Claude Fouassier, Anatoly N. Georgobiani, Leonid S. Lepnev, Yusuf N. Emirov, Alex N. Gruzintsev, Bakhadur G. Tagiev, Oktay. B. Tagiev, Rasim. B. Jabbarov, J. Electrochem. Soc. 150 (2003) G62.

[96] Hong He, Renli Fu, Yongge Cao, Xiufeng Song, Zhengwei Pan, Xinran Zhao, Qingbo Xiao, Ran Li, Opt. Mater. 32 (2010) 632.

[97] Hyun Kyoung Yang, Hyeon Mi Noh, Byung Kee Moon, Jung Hyun Jeong, Soung Soo Yi, Ceram. Int. 40 (2014) 12503.

[98] Jianwei Qiao, Lixin Ning, Maxim S. Molokeev, Yu-Chun Chuang, Qinyuan Zhang, Kenneth R. Poeppelmeier, Zhiguo Xia, Angew. Chem. 131 (2019) 11645.

[99] A. Meijerink, J. Nuyten, G. Blasse, J. Lumin. 44 (1989) 19.

[100] Teng Zheng, Małgorzata Sójka, Przemysław Woźny, Inocencio R. Martín, Víctor Lavín, Eugeniusz Zych, Stefan Lis, Peng Du, Laihui Luo, Marcin Runowski, Adv. Opt. Mater. 10 (2022) 2201055.

[101] W. Wolszczak, K.W. Krämer, P. Dorenbos, J. Lumin. 222 (2020) 117101.

[102] Johan T. M. de Haas, Pieter Dorenbos, IEEE Trans. Nucl. Sci. 55 (2008) 1086.

7

Fundamental light yield limits of lanthanide doped scintillators for high resolution γ-ray spectroscopy

The development of scintillation detectors with sub 2% energy resolution runs into the fundamental limitation of Poisson statistics. Significant improvement of the energy resolution therefore requires an increase in the number of detected scintillation photons. This can be achieved by developing higher light yield scintillators, which requires the use of compounds with smaller band gap than are currently being used. For compounds doped with Eu^{2+}, Sm^{2+}, or Ce^{3+}, this work presents an assessment of how small these band gaps can become. A distinction is made between what band gaps can be reached with halide and chalcogenides compounds. Furthermore, the development of intrinsically activated scintillators is discussed. As most of the discussed compounds emit at wavelengths longer than 500 nm, it is suggested that scintillation detectors with significantly better energy resolution than 2% need to use silicon based photodetectors instead of photomultiplier tubes.

7.1. Introduction

For high resolution γ-ray spectroscopy, high purity germanium (HPGe) detectors offer an energy resolution far superior to any scintillation detector. They can reach an energy resolution of 0.3% at 662 keV [1] compared to the 6% of a NaI:Tl^+ scintillation detector [2]. However, their applicability is often hindered by their many drawbacks. They are expensive [3, 4], need to be kept at cryogenic temperatures all the time [5], have a lower stopping power than scintillation detectors, and are prone to radiation damage [6, 7]. Scintillation detectors are much cheaper and do not suffer from all the other impracticalities, but the severely worse energy resolution makes them unfit for many applications where their energy resolution is insufficient.

The development of high energy resolution scintillators such as $LaBr_3$:Ce^{3+} has enabled the use of scintillation detectors for many applications where both NaI:Tl^+ and HPGe would be unfit. For example, the energy resolution of $LaBr_3$:Ce^{3+} detectors is good enough to resolve the close lying energy peaks such as ^{134}Cs (605 keV) and ^{137}Cs (662 keV), or ^{154}Eu (1,274 keV) and ^{60}Co (1,333 keV), which has been valuable for monitoring of radioisotopes at the Fukushima Dai-ichi nuclear powerplant [8, 9]. It is expected that further improvement of the energy resolution of scintillation detectors will allow for the use of γ-ray spectroscopy in many more scenarios where this technique is currently unavailable.

The energy resolution R of a scintillation detector can be expressed according to Equation 7.1.

$$R^2 = \frac{2.35^2}{N_{dp}} + R_{np}^2 + R_{det}^2 \tag{7.1}$$

Here, N_{dp} is the number of detected photons during a scintillation event. The first term corresponds to the contribution of Poisson statistics in photon detection to the energy resolution (R_{stat}^2). The second term, R_{np}^2, corresponds to how much the nonproportionality of the scintillator's response to different γ-ray energies contributes to the energy resolution. Lastly, R_{det}^2 encapsulates all other noise contributions, such as crystal inhomogeneity and detector noise. Alekhin et al. reported the current best energy resolution of 2.04% at 662 keV, which was attained with $LaBr_3$:Ce^{3+},Sr^{2+} [10]. It improved on the energy resolution attained with standard $LaBr_3$:Ce^{3+} (2.8% [11]) mainly by improving the scintillators proportionality; decreasing R_{np}. 24,000 photons were detected during a scintillation pulse that fell within the 2.04% energy resolution photopeak, meaning R_{stat} =1.52%. Using Equation 7.1, it is then found that all other terms only contribute 1.36% to the energy resolution. The energy resolution is therefore mainly limited by N_{dp}. It can thus be concluded that the only way to develop a scintillation detector with significantly better energy resolution than 2.0% is to increase the number of detected scintillation photons.

There are two methods to increase the number of detected scintillation photons. The first method is to increase the efficiency with which scintillation photons are detected. Scintillation photons are usually detected using a photomultiplier tube (PMT). PMTs however have a limited quantum efficiency (QE) of typically no more than 40%, which is defined as the probability a photon is detected when it hits the entrance window of the PMT. The QE curve of a Hamamatsu R6231-100 PMT, the same type as was used

to attain the 2.04% energy resolution with $LaBr_3:Ce^{3+},Sr^{2+}$, is shown in Figure 7.1. The optimal QE of around 35% is at wavelengths between 320 nm and 420 nm. Typically the scintillator is optically coupled to the PMT entrance window and the combination is wrapped in reflective material. The optical coupling allows scintillation photons to be trapped in the PMT entrance window due to total internal reflection. The reflective material gives scintillation photons that are initially reflected off the PMT entrance window a second chance at being detected. Both strategies contribute to increasing the total photon detection efficiency (PDE) of the detector system [12]. When recording the record 2.04% energy resolution pulse height spectrum with $LaBr_3:Ce^{3+},Sr^{2+}$, the PDE was just under 50%, which means still more than half of the scintillation photons remained undetected [10]. R_{stat} can therefore be reduced from 1.52% to 1.05% by using a detector system with a PDE of 100%.

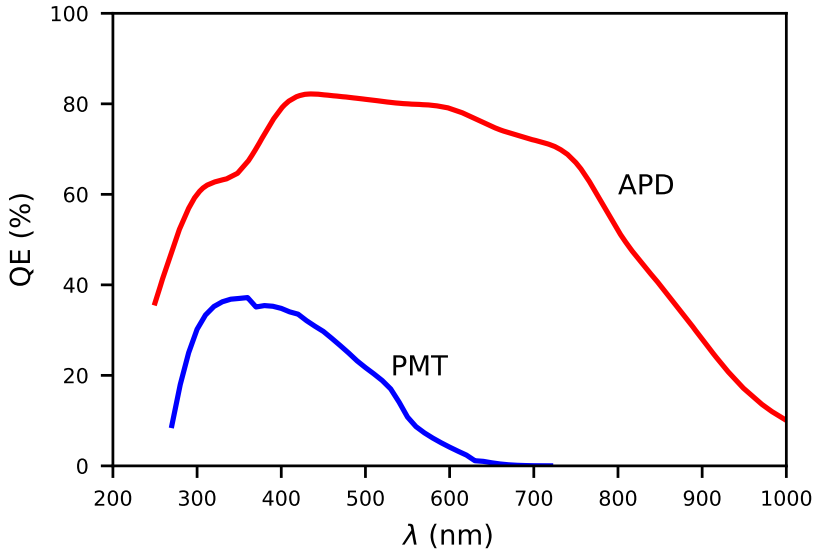

Figure 7.1: Quantum efficiency curves of a Hamamatsu R6231-100 super bialkali PMT and Advanced Photonix 630-70-72-510 APD. The PMT has an optimal detection efficiency between 320 nm and 420 nm, the APD has an optimal detection efficiency between 400 nm and 800 nm.

Some detectors that typically have much higher QE than a PMT are the silicon based photodetectors. Figure 7.1 also shows the QE of an avalanche photodiode (APD), again the same type as was used by Alekhin et al. to assess the scintillation properties of $LaBr_3:Ce^{3+},Sr^{2+}$. Its QE reaches over 80% around 400 nm and is much higher than that of the PMT over the entire wavelength range. Between 400 nm and 800 nm, the detection losses of an APD are almost purely from reflected photons. Therefore, by using the same method of wrapping the scintillator and detector in a highly reflective material, a PDE of nearly 100% can be attained in this wavelength range [12]. APDs however have several large drawbacks. Absorption of low energy X-rays in the APD generates electronic pulses stronger than from the scintillation pulse of an X-ray first absorbed in the

scintillator. They also have much lower gain and larger noise contribution than a PMT, and this gain is even strongly temperature dependent. Therefore, these devices need to be temperature stabilised to prevent gain drift. A more practical detector that does not require temperature stabilisation is the silicon photomultiplier (SiPM). SiPMs can now reach excellent QE values of over 60% [13, 14], also outperforming PMTs. The field of silicon based photomultipliers is rapidly developing and further improvements in the QE of devices can be expected in the near future [15].

The other method to increase the number of detected photons is to develop scintillators with higher light yields. The maximum achievable light yield of a scintillator Y_{max} is inversely proportional to its band gap E_g in eV according to Equation 7.2.

$$Y_{\text{max}}(\text{ph/MeV}) = \frac{10^6}{\beta E_g} \tag{7.2}$$

Here, β is a constant with a value typically between 2 and 3 [16]. A value of $\beta = 2.5$ is used for the rest of this work. Based on the 5.7 eV band gap of $LaBr_3$:Ce^{3+} [17], its Y_{max} is calculated to be 70,000 ph/MeV. A light yield of around 75,000 ph/MeV is often reported [18–20], which means that the light yield of $LaBr_3$:Ce^{3+} is already at its theoretical maximum. Higher light yields can therefore not be attained by further optimisation of crystal growth. Other compounds with which energy resolutions below 3% have been attained often also already show a light yield close to their theoretical maximum. Two examples are SrI_2:Eu^{2+}, $CsBa_2I_5$:Eu^{2+}. These compounds have a band gap of 5.5 eV [21] and 5.4 eV [22], respectively. Light yields of 80,000 ph/MeV or higher have been reported for both compounds [22–27]. It can therefore be concluded that the only way to attain a higher light yield is to develop scintillators with a smaller band gap.

The Y_{max} value of a scintillator is directly related to its band gap and is not directly linked to the type of activator. However, it is required that the activator shows emission in the host compound. For the $4f^{n-1}5d \rightarrow 4f^n$ transitions there are two main criteria that must be met for an activator to show emission. The first is that the emitting $4f^{n-1}5d$ level lies at least approximately 0.5 eV below the conduction band minimum in order to avoid thermal quenching of emission at room temperature. The second criterium is that the emission spectrum of the dopant does not overlap with the absorption of the host compound, as otherwise the emitted photons will be reabsorbed by band gap absorption. Dorenbos estimated the fundamental light yield limit of Ce^{3+}, Pr^{3+}, and Eu^{2+}-doped scintillators using this second criterium [28]. A correlation between the $4f^{n-1}5d \rightarrow 4f^n$ transition energy E_{df} and the band gap E_{g} was observed. It was demonstrated that the second criterium is violated when the band gap becomes too small. The point at which this violation occurs was used as an indication for the smallest band gap of compounds in which Ce^{3+}, Pr^{3+}, and Eu^{2+} can still emit.

Due to the correlation between E_{df} and E_{g}, it is expected that the smallest band gap Ce^{3+} and Eu^{2+}-doped scintillators no longer emit in the optimal wavelength range for PMTs. This makes such compounds more compatible for read out with silicon based photodetectors. A transition to silicon based photodetectors makes the development of near-infrared (NIR) emitting scintillators become interesting. One of the most promising NIR emitting activators for scintillator applications is Sm^{2+}, for which the fundamental light yield limits have not yet been assessed.

Figure 7.2 compares the electronic states of (a) Ce^{3+} doped in $LaBr_3$, (b) Eu^{2+} doped in $CsBa_2I_5$, and (c) Sm^{2+} doped in $CsBa_2I_5$. Ce^{3+} shows 2 emission bands, corresponding to the transitions from the 5d state to the 4f[$^2F_{5/2}$] and 4f[$^2F_{7/2}$] states. The $4f^6 5d \rightarrow 4f^7$ transition of Eu^{2+} only has one final state, so Eu^{2+} shows a single emission band. The ground state being the only final state combined with the typically smaller Stokes shift of divalent lanthanides compared to trivalent lanthanides [29] gives rise to a high probability of self-absorption. This typically lengthens the decay time and worsens the energy resolution of large Eu^{2+}-doped scintillators with high Eu^{2+} concentration [30]. A problem that is less prominent in Ce^{3+}-doped scintillators.

Sm^{2+} has the $4f^6$[$^7F_0$] ground state configuration. Directly above the ground state lie the other $4f^6$[^7F_J] levels (J = 1-6). The next excited state with the $4f^6$ configuration has the $^5D_0$ term. In many compounds Sm^{2+} shows $4f^6 \rightarrow 4f^6$ line emission from this state with a decay time of around 1 ms. In compounds where the $4f^5 5d$ state of Sm^{2+} lies close to the $4f^6$[$^5D_0$] state, Sm^{2+} can also show $4f^5 5d \rightarrow 4f^6$ broad band emission. As the $4f^5 5d \rightarrow 4f^6$ emission is much faster than the $4f^6 \rightarrow 4f^6$ emission, it is required that Sm^{2+} shows $4f^5 5d \rightarrow 4f^6$ emission when used as an activator in scintillators. Due to the requirement of the $4f^5 5d$ state lying below the $4f^6$[$^5D_0$] state, Sm^{2+}-doped scintillators will always emit in the NIR. Sm^{2+}-doped scintillators are therefore not suitable for read out with a PMT, but as long as most of the emission spectrum lies at wavelengths shorter than 800 nm, it can be efficiently read out using a silicon based photodetector.

The decay time of the Sm^{2+} $4f^5 5d \rightarrow 4f^6$ emission is typically around 2 µs [31]. The shortest decay time observed so far is found in SrI_2, corresponding to 1.5 µs at an emission wavelength of 740 nm [32–34]. This is still slow compared to the decay time of other activators that are typically used for scintillator applications. The $4f^{n-1}5d \rightarrow 4f^n$ emission of Ce^{3+} and Pr^{3+}-doped scintillators has a decay time in the order of tens of ns [28, 35], about 100 times faster than Sm^{2+}. Even the commercial NaI:Tl^+ has a decay time of 250 ns [36], about 10 times faster than Sm^{2+}. The decay time of Sm^{2+} can only compete with Eu^{2+}, which intrinsically lies between 0.5 µs and 1 µs [37]. While the intrinsic decay time of Eu^{2+} emission is shorter than that of Sm^{2+}, the large probability of self-absorption can sometimes lengthen the Eu^{2+} beyond that of Sm^{2+} [34, 38].

In this work, the smallest possible band gap of compounds in which lanthanide dopants still emit is determined, similar to the works of Dorenbos [28]. In addition to Ce^{3+} and Eu^{2+}, for which a larger data set than in [28] is provided, Sm^{2+} is also discussed as an alternative activator. Besides quenching by ionisation to the conduction band, interconfigurational crossover to the ground state is taken into consideration. Furthermore, the data are separated for different classes of compounds, e.g., lanthanide doped halides or lanthanide doped chalcogenides. Self-activated compounds, in which lanthanides do not show $4f^{n-1}5d \rightarrow 4f^n$ emission, are also included in the analysis. From these band gap values, the theoretical light yield limit and their expected emission wavelength are determined for each class of compounds. It is then determined whether R_{stat} can be improved and a strategy towards developing higher resolution scintillators is formulated per class of compound.

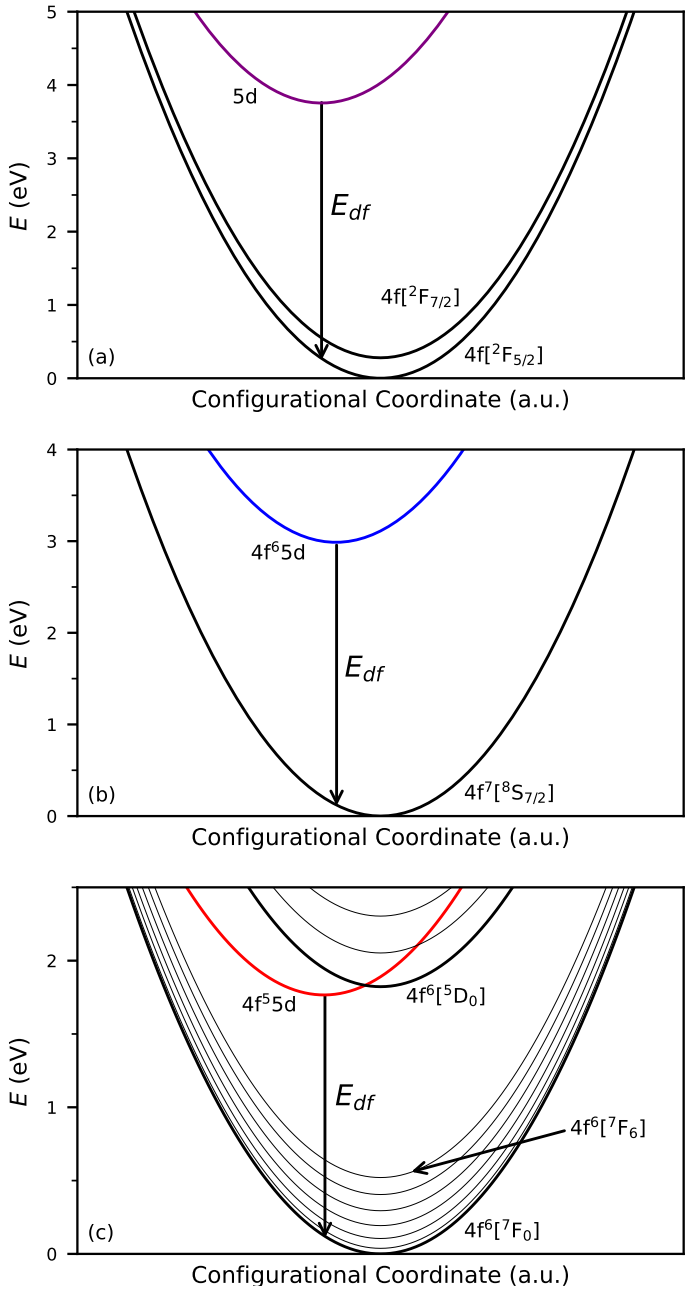

Figure 7.2: Configurational coordinate diagram of (a) Ce^{3+} in $LaBr_3$, (b) Eu^{2+} in $CsBa_2I_5$, and (c) Sm^{2+} in $CsBa_2I_5$.

7.2. Light yield of lanthanide doped halides

Over the years, an extended still largely unpublished database on lanthanide spectroscopy has been collected by P. Dorenbos that provides the E_{df} and E_g values for lanthanides doped in many hundreds of different inorganic compounds. Figure 7.3a shows E_{df} versus E_g for Eu^{2+}. Line 1 corresponds to $E_{df} = E_g$ and line 2 corresponds to the line where $E_{df} = E_g - 0.5$ eV, the requirement that ensures no Eu^{2+} emission is reabsorbed by the host compound. According to expectation, all datapoints fulfil this requirement and lie below line 2. Line 3 is a linear fit to the data. The E_g value at which line 2 and line 3 intersect corresponds to the smallest possible band gap of compounds in which Eu^{2+} can still show luminescence. This happens at a value of $E_g = 2.5$ eV. Using Equation 7.2, this gives a Y_{max} value of Eu^{2+}-doped scintillators of 160,000 ph/MeV. This is approximately two times higher than what is currently achieved with compounds such as SrI_2:Eu^{2+} and $CsBa_2I_5$:Eu^{2+}.

In Figure 7.3b, E_{df} versus E_g is shown for Sm^{2+}. There is not enough data available for Sm^{2+} to make a reliable fit. The Sm^{2+} emission wavelength can however be predicted from the Eu^{2+} emission wavelength in the same host compound. Line 3 has therefore been constructed by translating line 3 of Eu^{2+} in Figure 7.3a down by 1.22 eV [39]. By doing this, the datapoints for the iodide compounds group together just above line 3 between E_g values of 5 eV and 7 eV, similar like they do for Eu^{2+} in Figure 7.3a.

For Sm^{2+} there is an additional requirement that must be met for it to show emission at room temperature. When the energy of the $4f^5 5d$ state becomes too low, the energy barrier for thermal quenching to the $4f^6[^7F_J]$ multiplet becomes small enough that it can occur at room temperature. The state with the highest energy in this multiplet, $4f^6[^7F_6]$, lies approximately 0.5 eV above the ground state [40]. Taking into account the Stokes shift and requiring a sufficiently large gap between the $4f^6[^7F_6]$ and $4f^5 5d$ states to ensure a high enough activation energy to the interconfigurational crossing point, it is estimated that Sm^{2+} will quench when E_{df} gets below 1 eV. This is represented by line 4, where it is expected that only room temperature Sm^{2+} emission is found in datapoints that lie above this line. This mechanism applies specifically to Sm^{2+} emission and does not play a role in the quenching of Eu^{2+} emission.

One datapoint is found below line 4, corresponding to SrS:Sm^{2+}. It is indeed reported that the Sm^{2+} emission in SrS is quenched at room temperature [41] while the Eu^{2+} emission is not [42]. Knowing that the $4f^{n-1}5d$ levels of Eu^{2+} and Sm^{2+} always have approximately the same energy gap to the conduction band minimum [43], it is clear that quenching of the Sm^{2+} emission does not happen through thermal ionisation to the conduction band. A configurational coordinate diagram of the Eu^{2+} and Sm^{2+} energy levels in SrS is shown in Figure 7.4. For Eu^{2+}, the activation energy required for quenching through the interconfigurational crossing point is multiple eV, which is only accessible far above room temperature. For Sm^{2+} however, it is in the order of 100 meV, which corresponds to a quenching temperature well below room temperature [44], in accordance with the experimental observation. This confirms that at such low E_{df} values, quenching of the Sm^{2+} emission indeed occurs due to the proximity of the $4f^5 5d$ state to the $4f^6[^7F_J]$ multiplet.

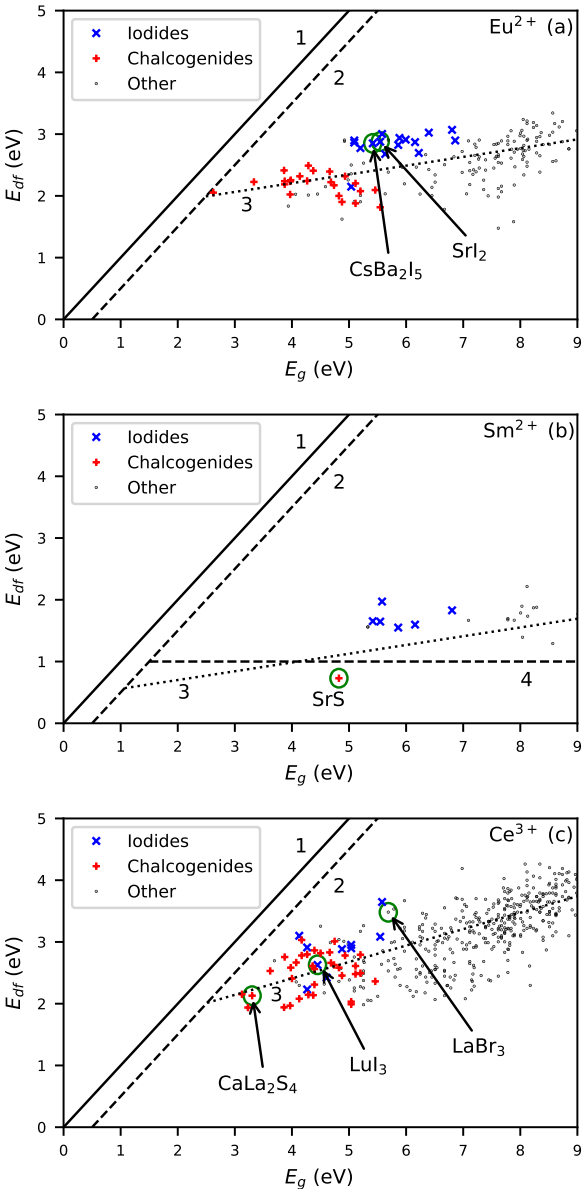

Figure 7.3: Energy of the $4f^{n-1}5d \rightarrow 4f^n$ transition E_{df} of (a) Eu^{2+}, (b) Sm^{2+}, and (c) Ce^{3+} versus the band gap E_g of the host compound. Line 1 represents $E_{df} = E_g$, and line 2 $E_{df} = E_g - 0.5$ eV. Line 3 is a linear fit through the data. Line 4 in (b) represents the minimum E_{df} to prevent quenching of luminescence via the Sm^{2+} $4f^6[^7F_J]$ multiplet. Emission is only expected in compounds that lie below line 2, and in (b) above line 4.

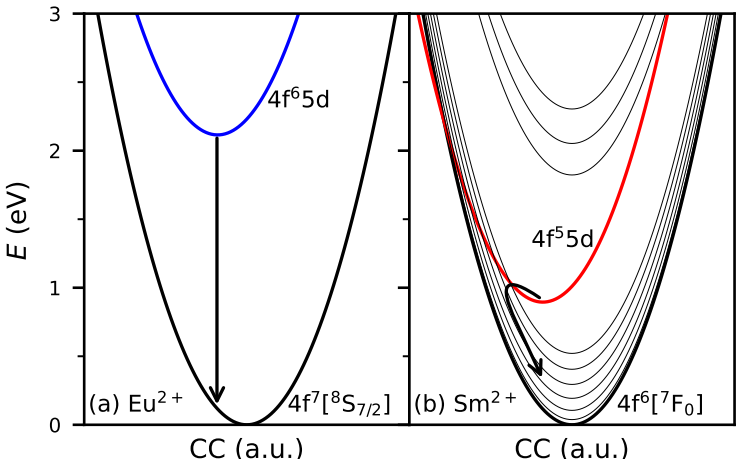

Figure 7.4: Configurational coordinate (CC) diagram of (a) Eu^{2+} and (b) Sm^{2+}-doped in SrS. The diagrams are constructed based on data from [42]. The small energy difference between the Sm^{2+} $4f^5$5d state and $4f^6[^7F_J]$ multiplet causes the Sm^{2+} emission to quench at lower temperature than the Eu^{2+} emission.

The consequence of this quenching mechanism is that the smallest band gap of compounds in which Sm^{2+} still shows luminescence does not correspond to the E_g value at which line 3 intersects line 2 in Figure 7.3b. Instead, it corresponds to the E_g value at which line 3 intersects line 4, which happens at a higher E_g value of 4.1 eV. This band gap gives a Y_{max} of 98,000 ph/MeV. Because of this, Eu^{2+} can show emission in compounds of smaller band gap than Sm^{2+}. Consequently, higher light yields can be attained with Eu^{2+}-doped scintillators than with Sm^{2+}-doped scintillators.

Figure 7.3c shows E_{df} versus E_g for Ce^{3+}. While for E_g values around 9 eV, E_{df} for Ce^{3+} is almost 0.5 eV larger than for Eu^{2+}, it decreases more rapidly. Line 3 therefore crosses line 2 at approximately the same E_g value of 2.5 eV. For this reason, the Y_{max} value of Ce^{3+}-doped scintillators is 160,000 ph/MeV, similar to that of Eu^{2+}-doped scintillators.

Research to high light yield scintillators has largely limited itself to halide compounds. The reason for this is that it is relatively easy to synthesise large single crystals from a melt for many of these compounds. The smallest band gaps among halides are found in iodide compounds. The iodides are denoted with "×" in Figure 7.3. Among the Eu^{2+} and Sm^{2+}-doped iodides (Figure 7.3a and 7.3b), the smallest band gaps are about 5 eV. For Ce^{3+} (Fig. 7.3c), the smallest band gaps that are found are about 4 eV.

To understand why there is no Eu^{2+} and Ce^{3+} emission reported for iodides with smaller band gaps, the diagram in Figure 7.5a is constructed. It shows the position of the valence band maximum, conduction band minimum, and lanthanide energy levels on a vacuum referred binding energy (VRBE) scale. The energies do not correspond to any real compounds, but to a theoretical ideal iodide compound that has the smallest possible band gap and still shows $4f^{n-1}5d \rightarrow 4f^n$ emission of the lanthanide activators. The VRBE of the bands and energy levels are estimated based on spectroscopic data from the aforementioned database.

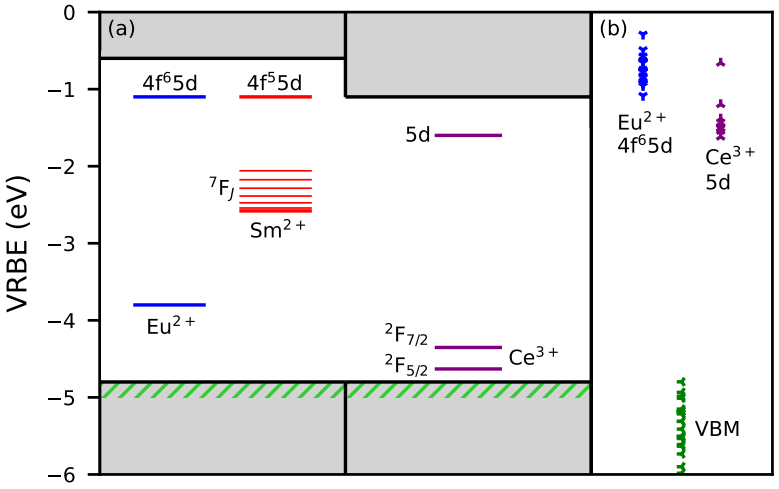

Figure 7.5: a) VRBE diagram illustrating the iodide compound with the smallest possible band gap in which Eu^{2+}, Sm^{2+} and Ce^{3+} still show emission. The valence band maximum cannot reach above -4.8 eV in iodides and the energy difference between the $4f^{n-1}5d$ state and conduction band minimum must be at least 0.5 eV. b) The range in VRBE of the valence band maxima (VBM), and Eu^{2+} and Ce^{3+} $4f^{n-1}5d$ levels in iodides.

7

The valence band maximum (VBM) of iodide compounds in the database was estimated according to the methods described in [45] and their values are shown in Figure 7.5b. The valence band maximum rarely exceeds a VRBE of -5 eV [45–47], the highest value of -4.8 eV was taken as the value for which the smallest possible band gaps can be achieved. For emission to be stable at room temperature, the emitting $4f^{n-1}5d$ level must lie at least 0.5 eV below the conduction band minimum [44]. The VRBE of the Eu^{2+} and Ce^{3+} $4f^{n-1}5d$ levels in iodide compounds are estimated according to [48] and also shown in Figure 7.5b. For Eu^{2+}, the lowest VRBE of -1.1 eV is found in $CsMgI_3$. The small Mg^{2+} site causes the crystal field splitting strength to be large for an iodide compound, resulting in a low VRBE. It is therefore unlikely that a compounds with much lower Eu^{2+} $4f^6 5d$ VRBE will be found and therefore this is taken as lowest possible value. For Ce^{3+}, the lowest 5d VRBE of -1.6 eV is found in LaI_3 and similarly this is taken as the lowest possible value. This places the lowest allowable conduction band minimum around -0.6 eV and -1.1 eV for Eu^{2+} and Ce^{3+}, respectively. As the Sm^{2+} $4f^5 5d$ level always lies at approximately the same energy as the $4f^6 5d$ level of Eu^{2+} [43], the lowest conduction band minimum for Sm^{2+} also has a VRBE of -0.6 eV.

Now the situation is created where neither the valence band maximum can shift to higher energies nor the conduction band minimum can shift the lower energies. It can thus be concluded that Eu^{2+} and Sm^{2+} will not show emission in iodides with a band gap smaller than 4.2 eV, and that Ce^{3+} will not show emission in iodides witha band gap smaller than 3.7 eV. The latter being in accordance with the Ce^{3+} emission being quenched at room temperature in LaI_3, which has a band gap of 3.3 eV [49].

A band gap of 4.2 eV is still larger than the band gap below which thermal quenching of Sm^{2+} through relaxation from the $4f^5$5d level to the $4f^6[^7F_J]$ multiplet is expected. Therefore, when limiting the search to iodide compounds, Eu^{2+} and Sm^{2+}-doped scintillators can reach an equal Y_{max} of 95,000 ph/MeV. Unfortunately, this means that Eu^{2+}-doped halide scintillators already operate near their theoretical maximum light yield and improvements are expected to be severely limited. For these compounds, further development of their Sm^{2+} counterparts is still a fruitful strategy to combat the inherent self-absorption problems of Eu^{2+}, as it can be expected that similar light yields can be attained using Sm^{2+} as an activator. For Ce^{3+}-doped halide scintillators, Y_{max} is about 108,000 ph/MeV. An example of a compound that gets close to this theoretical limit is LuI_3:Ce^{3+}, with a band gap of 4.4 eV [50] and light yield around 100,000 ph/MeV [51,52]. In theory, Ce^{3+}-doped iodide scintillators can thus reach higher light yields than those doped with Eu^{2+} or Sm^{2+}. Consequently, there is more room for improvement for Ce^{3+}-doped iodides beyond the current standard of $LaBr_3$:Ce^{3+}.

Sm^{2+} shows emission in compounds containing Eu^{2+} or Yb^{2+} as host cation [38,53]. This offers a unique opportunity to develop higher light yield Sm^{2+}-doped halide scintillators. To illustrate this, a VRBE diagram of YbI_2 is shown in Figure 7.6. YbI_2 is isostructural to CaI_2 [54] and both Yb^{2+} and Ca^{2+} have nearly identical ionic radius [55]. The band gap of YbI_2 cannot be measured spectroscopically due to the strong Yb^{2+} $4f^{14} \rightarrow 4f^{13}$5d absorption bands. For simplicity, the conduction band minimum and valence band maximum are therefore assumed to have the same VRBE for both compounds. The VRBE of the $4f^n$ ground states and valence band maximum are estimated. The band gap of CaI_2 is 5.3 eV [56], giving a Y_{max} value of 77,000 ph/MeV.

When present in high concentrations, the Yb^{2+} $4f^{14}$ ground state forms a narrow band of occupied states that lies within the band gap. This is denoted by the grey horizontal line through the Yb^{2+} $4f^{14}$ ground state in Figure 7.6. The optical band gap of such compounds therefore corresponds to the Yb^{2+} $4f^{14} \rightarrow 4f^{13}$5d transition [57], which is 3.0 eV in YbI_2 [58]. In undoped compounds of this type, the emission of Eu^{2+} or Yb^{2+} is typically weak due to concentration quenching [38,53,59–61]. However, when doped with Sm^{2+}, the concentration quenching of the Eu^{2+} or Yb^{2+} emission helps with the migration of excitations to Sm^{2+}. Once an excitation arrives on Sm^{2+}, it relaxes to the emitting $4f^5$5d state, preventing back transfer to Eu^{2+} or Yb^{2+}. The Sm^{2+} emission lies at significantly longer wavelength than the optical band gap and can therefore escape the scintillator.

During a scintillation event in conventional scintillation materials, electrons are promoted from the valence band to the conduction band. In the Eu^{2+} and Yb^{2+}-based compounds, electrons can also be promoted from the $4f^n$ ground state of Eu^{2+} or Yb^{2+} to the conduction band. As the energy gap between the $4f^n$ ground state and the conduction band is smaller than from the valence band to the conduction band, more electron-hole pairs can be created in this way. The largest effect is expected in a compound containing the largest amount of $4f^n$ electrons compared to valence band electrons, which is YbI_2. When naively assuming that any of the 14 4f electrons from Yb^{2+} have equal probability to cross the optical band gap as any of the 12 5p electrons from I^- have to be promoted to the conduction band, the average energy it takes to promote any electron to the conduction band is 4.1 eV. This yields a Y_{max} value of 98,000 ph/MeV, a 25% increase over that of CaI_2.

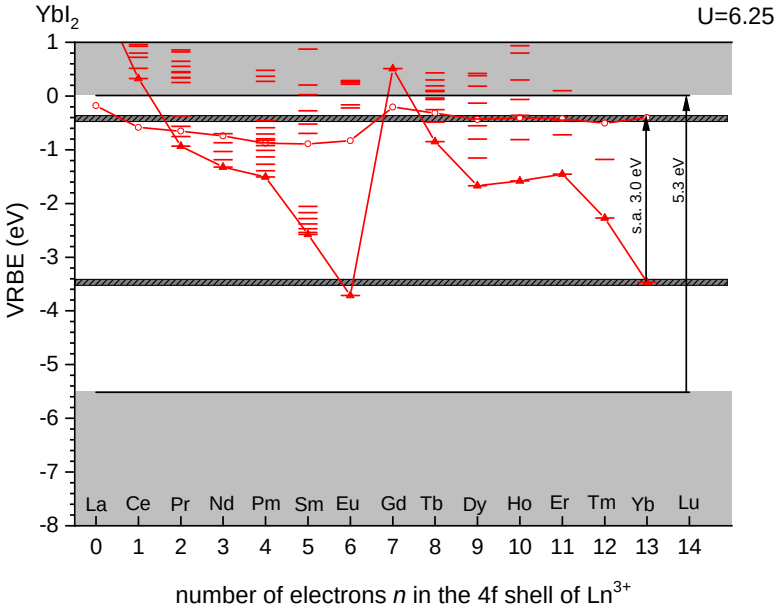

Figure 7.6: VRBE diagram of YbI_2. The horizontal lines around -3.5 eV and -0.5 eV correspond to the Yb2+ $4f^{14}$ ground state and $4f^{13}5d$ excited state, respectively. The transition between these states forms the optical band gap of this compound. The near-infrared Sm^{2+} emission is not absorbed by the host compound.

7

7.3. Light yield of smaller band gap compounds

It has become clear that current lanthanide doped halide scintillators already operate near their maximum achievable light yield. The limiting factor in their light yield is the VRBE of the valence band maximum that cannot be much higher than -5 eV in iodides, while decrease of the conduction band minimum quenches the $4f^{n-1}5d \rightarrow 4f^n$ emission of the lanthanides. Based on this, there appear to be two methods to surpass this limit and develop a scintillator with even smaller band gap. The first is to decrease the band gap by substituting cations for ones that lower the conduction band minimum. The second is decreasing the band gap by moving away from halides and substituting the anions for ones that allow for $4f^{n-1}5d \rightarrow 4f^n$ emission in smaller band gap compounds. Attempts at both strategies are found in literature and have their own merits and obstacles.

One recent example of small band gap compounds is the development of Hf^{4+}-based halides such as Cs_2HfCl_6 and Cs_2HfI_6. These compounds have a band gap of 5.8 eV [62] and 2.6 eV [63], respectively. The emission wavelength changes with anion type and Cs_2HfCl_6 emits around 400 nm [64], while Cs_2HfI_6 emits around 700 nm [65]. This indicates that the emission wavelength is related to the size of the band gap. The emission in these compounds typically has a decay time in the µs range [64,66,67]. One benefit of

this emission mechanism is the large Stokes shift of nearly 1 eV [63,68,69]. This allows for efficient luminescence in a self-activated compound due to the absence of concentration quenching and simultaneously preventing any problems with self-absorption [70]. When the aim is to keep these compounds compatible with silicon based photodetectors, it is important that most of the emission spectrum remains at shorter wavelength than 800 nm. With a Stokes shift of 1 eV, the minimal band gap is about 2.5 eV, meaning Cs_2HfI_6 is already close to the ideal band gap for these type of compounds. With such a small band gap, Y_{max} can reach 160,000 ph/MeV. In practice, the light yield of this compound was estimated to be 64,000 ph/MeV and an energy resolution of 4.2% has been achieved by read out with an APD [66].

A change in band gap from 4 - 5 eV to 2.5 eV that is realised by changing the host cations implies that the VRBE of the conduction band minimum shifts to lower energy by about 2 eV. The VRBE of $4f^{n-1}5d$ levels of lanthanide dopants vary typically only around 1 eV between different compounds [48]. Therefore, the energy gap between the $4f^{n-1}5d$ levels and the conduction band minimum is expected to decrease. The positions of the valence band maximum and conduction band minimum of Cs_2HfI_6 are shown in Figure 7.7, together with those of $LaBr_3$ and SrI_2 for comparison, which are taken from [45]. Due to lack of available spectroscopic data, the valence band maximum is assumed to lie at -5 eV, the typical value for iodides. The 2.6 eV band gap then places the conduction band minimum at -2.4 eV, which corresponds reasonable well with the conduction band minimum of other hafnate compounds [48, 71]. As the VRBE of Eu^{2+} and Ce^{3+} $4f^{n-1}5d$ levels are expected to lie above -2 eV, it explains why no $4f^{n-1}5d \rightarrow 4f^n$ emission was observed when doping Cs_2HfI_6 with these lanthanides [65].

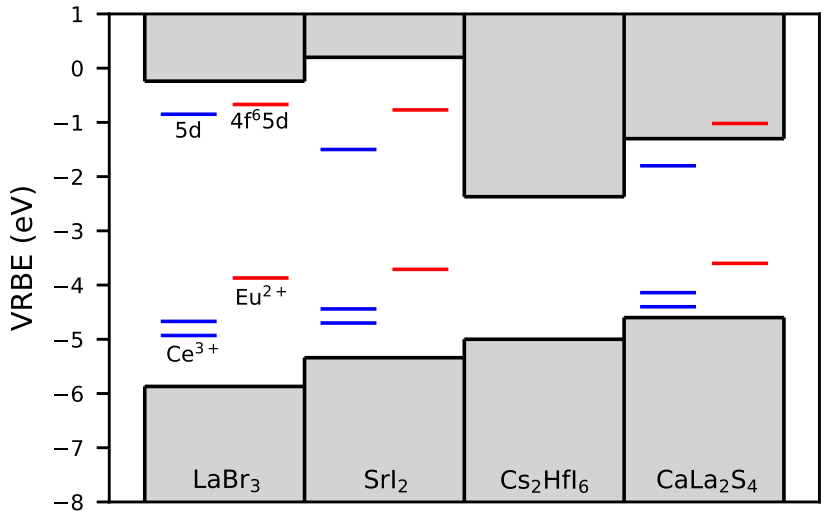

Figure 7.7: VRBE of the Ce^{3+} and Eu^{2+} energy levels with respect to the valence band maximum and conduction band minimum in various compounds.

Another recent example is the development of Cu^+-based halide scintillators, such as

$Cs_3Cu_2I_5$ [72] and $CsCu_2I_3$ [73]. These compounds have a band gap of 3.8 eV and 3.5 eV, respectively [74]. Similar to the Hf^{4+}-based halides, they have a Stokes shift of approximately 1 eV, making self-absorption and concentration quenching losses minimal. The decay time of their emission is approximately 1 μs. The benefit of these compounds is that they are virtually non-hygroscopic, but like many other self-activated compounds, thermal quenching of the luminescence often occurs at a relatively low temperature. The emission of $Cs_3Cu_2I_5$ starts to quench around 290 K [75], making it still an efficient emitter at room temperature. Light yields of around 30,000 ph/MeV have been reported [72, 76], and an energy resolution of 3.4% has been attained [72]. It has been shown that the light yield further improves upon doping with Tl^+ [76, 77]. For $CsCu_2I_3$, the emission starts to quench already at 200 K [73]. Despite the 50% light loss due to thermal quenching, a 4.8% energy resolution was attained by coupling $CsCu_2I_3$ to an APD [74]. It was estimated that the light yield is around 60,000 ph/MeV at 200 K.

The last class of self-activated scintillators in which there is currently a high research activity are the Pb^{2+}-based halide compounds. Among these are compounds such as $CsPbBr_3$ and the many organic-inorganic hybrid compounds, where the monovalent Cs^+ ions are replaced by organic molecules [78]. The band gap of these compounds is extremely variable and strongly depends on the type of anion it contains. Band gaps smaller than 2.5 eV can easily be attained in iodides [79]. Typically, these compounds show very fast near band gap emission or broad band emission that is related to self-trapped excitons [80]. Unfortunately, the small Stokes shift of the near band gap emission has a high self-absorption probability [81–84]. For γ-ray spectroscopy, it is therefore important to look for compounds that emit primarily through self-trapped excitons, the Stokes shift of which is again often around 1 eV [79, 80, 83]. This means that just like for the Hf^{4+} and Cu^+-based compounds, the optimal band gap is about 2.5 eV.

Besides the self-activated compounds, Figure 7.3a and c show that there also exist many compounds with smaller band gaps than iodides that still show $4f^{n-1}5d \rightarrow 4f^n$ emission for Eu^{2+} and Ce^{3+}. Most of these compounds belong to the chalcogenides, which are denoted by "+" in the figure. It was determined that the smallest possible band gap lies around 2.5 eV for both activators, which coincidentally corresponds to the optimal band gap for intrinsically activated scintillators.

Out of the chalcogenides, most research has been performed on sulfides. Unfortunately, most of this research is not performed on single crystals. Rare-earth sulfides can often crystalise in many stoichiometries, which tends to introduce sulfide vacancies [85]. They have melting points sometimes in excess of 2000 °C [86–88]. The binary rare earth sulfides can exist in many phases [89] and ternary rare earth sulfides often melt incongruently [86]. All these things combined make it difficult to grow large single crystals from a melt using techniques such as the Bridgman or Czochralski method. For this reason, often chemical vapour transport [90] or flux method [91] are used for synthesis of single crystals. Both methods cause random nucleation in the reaction vessel, limiting the size of crystals grown by these techniques to typically about 1 mm^3, which is too small for almost all applications.

Among compounds that are grown through chemical vapour transport are ϵ-Lu_2S_3:Ce^{3+} [92] and β-La_2S_3 [93]. Both show Ce^{3+} emission at room temperature. The scintillation performance of sub-mm sized ϵ-Lu_2S_3:Ce^{3+} crystals was assessed [92]. With a band gap of 4 eV, Y_{max} is equal to 100,000 ph/MeV. In practice, the light yield was estimated to be around 28,000 ph/MeV. The most researched family of compounds grown with the flux methods is $ALnS_2$ (A = K, Rb; Ln = La, Gd, Lu, Y), which has been extensively reviewed by Jarý et al. [91]. Eu^{2+} and Ce^{3+} show emission at room temperature in many of these compounds. The light yield of $KLuS_2$:Eu^{2+} and $KLuS_2$:Ce^{3+} was estimated to be 36,000 ph/MeV and 24,000 ph/MeV, respectively.

Growing large single crystals is however not a strict requirement for scintillators. A prime example of this is development of Ce^{3+}-doped garnet transparent ceramics which sometimes even show better scintillation properties than their monocrystalline counterparts [94–96]. Transparent ceramics of rare-earth sulfides with a cubic crystal structure have been extensively studied for use as infrared window material for wavelengths between 8 μm to 14 μm [97]. Typically, sulfides with the Th_3P_4 structure are selected, among which are γ-La_2S_3 [98] and $CaLa_2S_4$ [85]. The Ce^{3+} 5d → 4f[$^2F_{5/2}$] emission is reported to lie at 582 nm in $CaLa_2S_4$ and was observed at room temperature [99]. With a band gap of 3.2 eV, it has one of the smallest band gaps of the compounds shown in Figure 7.3c and, yielding a Y_{max} value of 125,000 ph/MeV.

The VRBE scheme of $CaLa_2S_4$ is also included in Figure 7.7. The $4f^n$ ground states energies of Eu^{2+} and Ce^{3+} are estimated according to [43,100]. The energy of the $4f^{n-1}5d$ states are based on spectroscopic data from absorption spectra [99]. The energy at the top of the valence band is roughly estimated from the Pr^{3+} charge transfer band in $KLuS_2$ [91]. The resulting conduction band minimum falls between the Eu^{2+} and Ce^{3+} $4f^{n-1}5d$ states, which is in line with the observation of room temperature Ce^{3+} emission and absence of Eu^{2+} emission [99]. As can be seen from the long Ce^{3+} emission wavelength, the VRBE of the Ce^{3+} 5d state lies close to -2 eV, giving room for a much lower conduction band minimum compared to for example $LaBr_3$. Simultaneously, the valence band maximum in sulfides can reach above -5 eV. It is the combination of these two effects that is required to attain Ce^{3+} emission in compounds with a much smaller band gap than is observed in iodides.

7.4. Improving the energy resolution

The primary goal of finding scintillator materials with higher light yield than $LaBr_3$ is to detect more photons during a scintillation event and thereby reducing the first term (R_{stat}) in Equation 7.1. This does not mean that a better energy resolution will be achieved, but merely that R_{stat} is no longer the limiting factor. It is therefore instructive to compare R_{stat} for different Y_{max} values and detection efficiency for each class of compounds. The comparison is shown in Table 7.1. It is chosen to compare the size of R_{stat} for detector systems with a PDE of 50% and 100%, as this illustrates the gain in R_{stat} that can be made starting from the current record holding energy resolution measured by Alekhin et al. [10].

Table 7.1: The maximum achievable light yield Y_{max}, the R_{stat} values for a 662 keV γ-ray scintillation pulse in a detector with 50% and 100% PDE, and the expected range of the emission spectrum λ_{em} for the smallest band gap scintillators of each compound class.

Compound class	Y_{max} (ph/MeV)	$R_{stat,50\%}$ (%)	$R_{stat,100\%}$ (%)	λ_{em} (nm)
$LaBr_3$:Ce^{3+},Sr^{2+}	70,000	1.54	1.09	340 - 410
Eu^{2+}-doped halides	95,000	1.33	0.94	400 - 500
Sm^{2+}-doped halides	98,000	1.30	0.92	700 - 900
Ce^{3+}-doped halides	108,000	1.24	0.88	450 - 700
E_g = 2.5 eV	160,000	1.02	0.72	500 - 900

The R_{stat} value of $LaBr_3$:Ce^{3+},Sr^{2+} at a PDE of 50% approximates the 2.04% energy resolution measurement of Alekhin et al. [10]. When 24,000 scintillation photons were detected, R_{stat} corresponds to 1.52%, close to the 1.54% that is calculated from the Y_{max} value in Table 7.1. By increasing the PDE from 50% to 100%, R_{stat} will decrease by a factor $\sqrt{2}$, resulting in an R_{stat} value of 1.09%. Alekhin et al. also reported the energy resolution attained when using a temperature stabilised APD as photodetector. As most of the emission wavelength of $LaBr_3$:Ce^{3+},Sr^{2+} lies at wavelengths shorter than 400 nm, the PDE was approximately 85% instead of the 100% attainable at wavelengths longer than 400 nm [12]. This increase in detection efficiency lowered R_{stat} to 1.18%. Despite the decrease in R_{stat}, the energy resolution remained 2.0%. From this can be concluded that the APD introduces more noise and larger R_{det} in the measurement than a PMT, but that at least the same energy resolution can be attained, even when the emission wavelength is not optimal for detection with an APD.

Y_{max} of the Eu^{2+}-doped halides is 95,000 ph/MeV, 35% higher than that of $LaBr_3$:Ce^{3+},Sr^{2+}. These light yields have also been attained in for example SrI_2:Eu^{2+} and $CsBa_2I_5$:Eu^{2+}. Despite the higher light yield than $LaBr_3$:Ce^{3+},Sr^{2+}, the best energy resolution attained with Eu^{2+}-doped halides is 2.3%, measured with $CsBa_2I_5$:Eu^{2+} [22]. Pulse height spectra have shown that the number of photons detected with Eu^{2+}-doped halides can significantly exceed that of $LaBr_3$:Ce^{3+} [23]. From this can be concluded that the energy resolution attained with Eu^{2+}-doped halides is not yet limited by R_{stat}. It was found that the proportionality of $CsBa_2I_5$:Eu^{2+} is worse than that of $LaBr_3$:Ce^{3+},Sr^{2+} for low γ-ray energies [22]. It then follows that the best strategy towards better energy resolution with Eu^{2+}-doped halides is improving their proportionality, either by finding more proportional compounds or co-doping of existing compounds. Unfortunately, Eu^{2+}-doped halides inherently suffer from self-absorption. This lengthens the decay time and worsens the energy resolution for large crystals, and is therefore an additional problem that should be addressed. If further improvement in R_{stat} are at some point required, it can only be attained by switching to photodetectors with a higher QE than a PMT, such as silicon based photodetectors. As the Eu^{2+} $4f^6 5d \rightarrow 4f^7$ emission typically lies at wavelengths longer than 400 nm, it falls within the optimal wavelength range for these detectors.

As was shown in Figure 7.5a, the maximum attainable light yield in halide compounds is in principle the same for Sm^{2+} doping as for Eu^{2+}. However, Sm^{2+} can emit in halides with a high concentration of Eu^{2+} and Yb^{2+} cations, potentially resulting in slightly

higher light yields. The best energy resolution attained with a Sm^{2+}-doped scintillator is 3.2%, which was achieved with $CsBa_2I_5:Eu^{2+},Sm^{2+}$ and read out with an APD [101]. Its light yield was determined to be 45,000 ph/MeV, approximately half that of $CsBa_2I_5:Eu^{2+}$. When a Sm^{2+}-doped scintillator with light yield around 100,000 ph/MeV is found, R_{stat} becomes about 0.2% lower than for $LaBr_3:Ce^{3+},Sr^{2+}$. While Sm^{2+}-doped scintillators are not suitable to be coupled to a PMT, their emission is more efficiently detected with a silicon based photodetector than the emission of $LaBr_3:Ce^{3+},Sr^{2+}$. In principle, this should make it possible to attain an energy resolution below 2% using Sm^{2+}-doped scintillators.

The real advantage of Sm^{2+} as an activator however is the much lower probability of self-absorption of its emission compared to Eu^{2+}. Therefore, the energy resolution is not expected to degrade as much when large Sm^{2+}-doped scintillation crystals are used. Developing Sm^{2+}-doped halides with similar light yield and proportionality as current Eu^{2+}-doped halides might therefore be a good strategy to attain better energy resolution while avoiding the inherent problems the Eu^{2+}-doped halides face.

Figure 7.5 also showed that Ce^{3+} can emit in halide compounds with a band gap of around 3.7 eV, which is 0.5 eV smaller band gap than for Eu^{2+} and Sm^{2+}. Therefore, Y_{max} is 108,000 ph/MeV, almost 15% larger than that of Eu^{2+}-doped halides. Similar to Sm^{2+}, the use of Ce^{3+}-doped halides has the additional advantage of a low self-absorption probability. Additionally, the Ce^{3+} decay time is almost two orders of magnitude faster than that of Eu^{2+} and Sm^{2+}. Following the correlation between band gap and emission wavelength shown in Figure 7.3, it is expected that the Ce^{3+} emission shifts to longer wavelengths in compounds approaching a 3.7 eV band gap. For example, the $LuI_3:Ce^{3+}$ emission spectrum extends beyond 600 nm [51]. Other high light yield Ce^{3+}-doped iodides, such as $YI_3:Ce^{3+}$ and $GdI_3:Ce^{3+}$ emit at even longer wavelengths [52]. As shown by Figure 7.1, this falls within the wavelength range where there QE of a PMT is very low. Because of this, silicon based photodetectors will also be required to optimally exploit the high light yield of these compounds.

Lastly, there are the compounds that can reach a 2.5 eV band gap. Among these are the intrinsically activated scintillators based on for example Hf^{4+}, Cu^{+} or Pb^{2+} cations, and the Eu^{2+} and Ce^{3+}-doped sulfides. Potentially these compounds can reach light yields up to 160,000 ph/MeV and combined with a PDE of 100%, R_{stat} can be more than halved to 0.72%. However, there has not yet been a demonstration of one of these compounds actually exceeding the light of lanthanide doped halides. Even if an unexpectedly bright scintillator is found, it is questionable how meaningful such a low R_{stat} really is. It is likely that the other contributions in Equation 7.1 will still limit the energy resolution to values above 2%, especially in light of the difficulty to synthesise some of these compounds. A band gap of 2.5 eV corresponds to a wavelength of approximately 500 nm and a large Stokes shift is required. Because of this, it can be said with certainty that these compounds will also not be suitable for read out with a PMT, and again silicon based photodetectors will be required for efficient read out.

7.5. Conclusions

The highest achievable light yield for different classes of compounds was assessed. The smallest band gaps of halide compounds in which Eu^{2+} and Sm^{2+} can emit is around 4.2 eV, for Ce^{3+} it is around 3.7 eV. This corresponds to light yield maxima of 95,000 ph/MeV and 108,000 ph/MeV, respectively. It was found that Eu^{2+}-doped halides have already reached close to their maximum light yield and further improvements in energy resolution are only expected from improved proportionality or reduced self-absorption. Virtually all Eu^{2+}-doped halides emit at wavelengths shorter than 500 nm and are suitable for read out with a PMT. Sm^{2+}-doped halides can reach the same light yield as Eu^{2+}-doped halides, but emit in the near-infrared and therefore require silicon based photodetectors for efficient detection of the scintillation light, which can efficiently detect wavelengths up to 800 nm. Sm^{2+}-doped scintillators are judged to be a promising low self-absorption alternative to their Eu^{2+}-doped counterparts. While Ce^{3+}-doped halides can still significantly improve their light yield from the 70,000 ph/MeV of $LaBr_3$:Ce^{3+}, the emission spectrum of these compounds is however expected to largely fall at wavelengths longer than 500 nm, making them no longer suitable for efficient read out with a PMT.

Both Eu^{2+} and Ce^{3+} can emit in even smaller band gap compounds than the 4.2 eV and 3.7 eV of their respective halides, such as for example in sulfides. Both activators can still emit in compounds with a band gap of around 2.5 eV. This does not work for Sm^{2+}, as its $4f^5 5d \rightarrow 4f^6$ emission will quench to the ^7F_J multiplet. Scintillators with a band gap close to 2.5 eV can also be realised using self-activated halides. The band gap in these compounds is reduced by lowering of the conduction band minimum, which quenches lanthanide $4f^{n-1}5d \rightarrow 4f^n$ emission. For these compounds, a large Stokes shift is required to avoid self-absorption, meaning their emission wavelength will lie around 700 nm. Therefore, the smallest band gap compounds in all discussed classes of compounds, with exception of the Eu^{2+}-doped halides, are expected to emit at wavelengths that are too long for read out with a PMT. This stresses the importance of developing scintillation detectors in which the scintillator is read out using silicon based photodetectors.

7.6. Acknowledgements

This research was subsidised by the TTW/OTP grant no. 18040 of the Dutch Research Council.

References

[1] Alan Owens, Nucl. Instrum. Meth. A 238 (1985) 473.

[2] Giulia Hull, Woon-Seng Choong, William W. Moses, Gregory Bizarri, John. D. Valentine, Stephen A. Payne, Nerine J. Cherepy, Bryan W. Reutter, IEEE. T. Nucl. Sci. 56 (2009) 331.

[3] James H. Ely, Edward R. Siciliano, Richard T. Kouzes, IEEE Nucl. Sci. Conf. R. (2004) 1584.

[4] David C. Stromswold, Edward R. Siciliano, John E. Schweppe, James H. Ely, Brian D. Milbrath, Richard T. Kouzes, Bruce D. Geelhood, IEEE Nucl. Sci. Conf. R. (2004) 1065.

[5] G. A. Armantrout, IEEE T. Nucl. Sci. 19 (1972) 289.

[6] F. Quarati, S. Brandenburg, E. J. Buis, P. Dressler, S. Kraft, M. O. Lampert, R. W. Ostendorf, Alan Owens, A. Peacock, P. Quirin, D. Quirion, Nucl. Instr. Meth. A 610 (2009) 354.

[7] Masaaki Kaburagi, Kenji Shimazoe, Yutaka Otaka, Mizuki Uenomachi, Kei Kamada, Kyoung Jin Kim, Masao Yoshino, Ysuhiro Shoji, Akira Yoshikawa, Hiroyuki Takahashi, Yatsuo Torii, Nucl. Instrum. Meth. A 971 (2020) 164118.

[8] Yokihisa Sanada, Tadashi Orita, Tatsuo Torii, Appl. Radiat. Isot. 118 (2016) 308.

[9] M. Nancekievill, A. R. Jones, M. J. Joyce, B. Lennox, S. Watson, J. Katakura, K. Okumura, S. Kamada, M. Katoh, K. Nishimura, IEEE. T. Nucl. Sci. 65 (2018) 2565.

[10] M. S. Alekhin, J. T. M. de Haas, I. V. Khodyuk, K. W. Krämer, P. R. Menge, V. Ouspenski, P. Dorenbos, Appl. Phys. Lett. 102 (2013) 151915.

[11] E. V. D. van Loef, P. Dorenbos, C. W. E. van Eijk, K. Krämer, H. U. Güdel, Appl. Phys. Lett. 79 (2001) 1573.

[12] Johan T. M. de Haas, Pieter Dorenbos, IEEE T. Nucl. Sci. 55 (2008) 1086.

[13] G. Zappalà, F. Acerbi, A. Ferri, A. Gola, G. Paternoster, N. Zorzi, C. Piemonte, J. Instrum. 11 (2016) P08014.

[14] Fabio Acerbi, Stefan Gundacker, Nucl. Instrum. Meth. A 926 (2019) 16.

[15] S. Vinogradov, Nucl. Instrum. Meth. A 1045 (2023) 167596.

[16] D. J. Robbins, J. Electrochem. Soc. 127 (1980) 2694.

[17] E. V. D. van Loef, P. Dorenbos, C. W. E. van Eijk, K. W. Krämer, H. U. Güdel, Phys. Rev. B 68 (2003) 045108.

[18] E. V. D. van Loef, P. Dorenbos, C. W. E. van Eijk, K. W. Krämer, H. U. Güdel, Nucl. Instrum. Meth. A 486 (2002) 254.

[19] W. M. Higgins, A. Churilov, E. van Loef, J. Glodo, M. Squillante, K. Shah, J. Cryst. Growth 310 (2008) 2085.

[20] Mikhail S. Alekhin, Daniel A. Biner, Karl W. Krämer, Pieter Dorenbos, J. Appl. Phys. 113 (2013) 224904.

[21] Mikhail S. Alekhin, Daniel A. Biner, Karl W. Krämer, Pieter Dorenbos, Opt. Mater. 37 (2014) 382.

[22] Mikhail S. Alekhin, Daniel A. Biner, Karl W. Krämer, Pieter Dorenbos, J. Lumin. 145 (2014) 723.

[23] Nerine J. Cherepy, Giulia Hull, Alexander D. Drobshoff, Stephen A. Payne, Edgar van Loef, Cody M. Wilson, Kanai S. Shah, Utpal N. Roy, Arnold Burger, Lynn A. Boatner, Woon-Seng Choong, William W. Moses, Appl. Phys. Lett. 92 (2008) 083508.

[24] Leonard Alaribe, Christian Disch, Alex Fauler, Ralf Engels, Egbert Keller, Angelica Cecilia, Tomy dos Santos Rolo, Elias Hamann, Michael Fiederle, IEEE T. Nucl. Sci. 59 (2012) 2193.

[25] L. A. Boatner, J. O. Ramey, J. A. Kolopus, R. Hawrami, W. M. Higgins, E. van Loef, J. Glodo, K. S. Shah, Emmanuel Rowe, Pijush Bhattacharya, Eugene Tupitsyn, Michael Groza, Arnold Burger, N. J. Cherepy, S. A. Payne, J. Cryst. Growth 312 (2010) 1213.

[26] E. D. Bourret-Courchesne, G. Bizarri, R. Borade, Z. Yan, S. M. Hanrahan, G. Gundiah, A. Chaudhry, A. Canning, S. E. Derenzo, Nucl. Instrum. Meth. A 612 (2009) 138.

[27] U. Shirwadkar, R. Hawrami, J. Glodo, E. V. D. van Loef, K. S. Shah, IEEE T. Nucl. Sci. 60 (2013) 1011.

[28] Pieter Dorenbos, IEEE T. Nucl. Sci. 57 (2010) 1162.

[29] P. Dorenbos, J. Phys. Condens. Mat. 15 (2003) 4797.

[30] Mikhail S. Alekhin, Karl W. Krämer, Pieter Dorenbos, Nucl. Instrum. Meth. A 714 (2013) 13.

[31] Casper van Aarle, Karl W. Krämer, Pieter Dorenbos, J. Lumin. 266 (2024) 120329.

[32] Mikhail S. Alekhin, Roy H. P. Awater, Daniel A. Biner, Karl W. Krämer, Johan T. M. de Haas, Pieter Dorenbos, J. Lumin. 167 (2015) 347.

[33] Mirosław Karbowiak, Piotr Solarz, Radosław Lisiecki, Witold Ryba-Romanowski, J. Lumin. 195 (2018) 159.

[34] R. H. P. Awater, M. S. Alekhin, D. A. Biner, K. W. Krämer, P. Dorenbos, J. Lumin. 212 (2019) 1.

[35] Aleksander Zych, Matthijs de Lange, Celso de Mello Donegá, Andries Meijerink, J. Appl. Phys. 112 (2012) 013536.

[36] J. S. Schweitzer, W. Ziehl, IEEE T. Nucl. Sci. 30 (1983) 380.

[37] S. H. M. Poort, A. Meijerink, G. Blasse, J. Phys. Chem. Solids 58 9 (1997) 1451.

[38] Casper van Aarle, Karl W. Krämer, Pieter Dorenbos, J. Mater. Chem. C 11 (2023) 2336.

[39] P. Dorenbos, J. Phys. Condens. Mat. 15 (2003) 575.

[40] D. L. Wood, W. Kaiser, Phys. Rev. 126 (1962) 2079.

[41] Lawrence H. Robins, J. Ari Tuchman, Phys. Rev. B 57 (1998) 12094.

[42] Nobuhiko Yamashita, Osamu Harada, Kaizo Nakamura, Jpn. J. Appl. Phys. 34 (1995) 5539.

[43] Pieter Dorenbos, J. Lumin. 222 (2020) 117164.

[44] Pieter Dorenbos, J. Mater. Chem. C 11 (2023) 8129.

[45] Pieter Dorenbos, Aday Josef, Johan T. M. de Haas, Karl W. Krämer, J. Lumin. 208 (2019) 463.

[46] Pieter Dorenbos, J. Lumin. 136 (2013) 122.

[47] Pieter Dorenbos, Opt. Mater. 69 (2017) 8.

[48] E. G. Rogers, P. Dorenbos, ECS J. Solid State Sci. Technol. 3 (2014) R173.

[49] A. Bessiere, P. Dorenbos, C. W. E. van Eijk, K. W. Krämer, H. U. Güdel, C. de Mello Donega, A. Meijerink, Nucl. Instrum. Meth. A 537 (2005) 22.

[50] A. M. Srivastava, Opt. Mater. 30 (2008) 1567.

[51] M. D. Birowosuto, P. Dorenbos, C. W. E. van Eijk, K. W. Krämer, H. U. Güdel, J. Appl. Phys. 99 (2006) 123520.

[52] E. V. van Loef, W. M. Higgins, J. Glodo, A. V. Churilov, K. S. Shah, J. Cryst. Growth 310 (2008) 2090.

[53] Casper van Aarle, Karl W. Krämer, Pieter Dorenbos, J. Lumin. 251 (2022) 119209.

[54] W. Lasocha, C. A. Voos-Esquivel, S. A. Hodorowicz, B. Y. Kim, H. A. Eick, J. Solid State Chem. 74 (1988) 67.

[55] R. D. Shannon, Acta Crystallogr. A 32 (1976) 751.

[56] S. S. Novosad, Tech. Phys. 44 (1999) 124.

[57] Xinhua Zhao, Yongzhi Deng, Zhonghe Li, Shishua Wang, J. Alloy. Compd. 250 (1997) 405.

[58] E. Rogers, P. Dorenbos, J. T. M. de Haas, E. van der Kolk, J. Phys. Condens. Mat. 24 (2012) 275502.

[59] Kan Yang, Mariya Zhuravleva, Charles L. Melcher, Phys. Status Solidi R 5 (2011) 43.

[60] Yuntao Wu, Dan Han, Bryan C. Chakoumakos, Hongliang Shi, Shiyou Chen, Mao-Hua Du, Ian Greeley, Matthew Loyd, Daniel J. Rutstrom, Luis Stand, Merry Koschan, Charles L. Melcher, J. Mater. Chem. C 6 (2018) 6647.

[61] Daniel Rutstrom, Luis Stand, Merry Koschan, Charles L. Melcher, Mariya Zhuravleva, J. Lumin. 216 (2019) 116740.

[62] Keiichiro Saeki, Yutaka Fujimoto, Masanori Koshimizu, Takayuki Yanagida, Keisuke Asai, Appl. Phys. Express 9 (2016) 042602.

[63] Shohei Kodama, Shunsuke Kurosawa, Kotaro Fujii, Masatomo Yashima, Akihiro Yamaji, Akira Yoshikawa, J. Alloys Compd. 970 (2024) 172506.

[64] Arnold Burger, Emmanuel Rowe, Michael Groza, Kristle Morales Figueroa, Nerine J. Cherepy, Patrick R. Beck, Steven Hunter, Stephen A. Payne, Appl. Phys. Lett. 107 (2015) 143505.

[65] Shohei Kodama, Shunsuke Kurosawa, Akihiro Yamaji, Jan Pejchal, Robert Král, Yuji Ohashi, Kei Kamada, Yuui Yokota, Martin Nikl, Akira Yoshikawa, J. Cryst. Growth 492 (2018) 1.

[66] Shohei Kodama, Shunsuke Kurosawa, Maki Ohno, Akihiro Yamaji, Masao Yoshino, Jan Pejchal, Robert Král, Yuji Ohashi, Kei Kamada, Yuui Yokota, Martin Nikl, Akira Yoshikawa, Radiat. Meas. 124 (2019) 54.

[67] Serge Nagorny, Physics 3 (2021) 320.

[68] John. F. Ackerman, Mat. Res. Bull. 19 (1984) 783.

[69] V. Vanecek, R. Kral, J. Paterek, V. Babin, V. Jary, J. Hybler, S. Kodama, S. Kurosawa, Y. Yokota, A. Yoshikawa, M. Nikl, J. Cryst. Growth 533 (2020) 125479.

[70] D. L. Dexter, James H. Schulman, J. Chem. Phys. 22 (1954) 1063.

[71] Pieter Dorenbos, J. Lumin. 151 (2014) 224.

[72] Shuangliang Cheng, Alena Beitlerova, Romana Kucerkova, Martin Nikl, Guohao Ren, Yuntao Wu, Phys. Status Solidi R. 14 (2020) 2000374.

[73] Shuangliang Cheng, Alena Beitlerova, Romana Kucerkova, Eva Mihokova, Martin Nikl, Zhengyang Zhou, Guohao Ren, Yuntao Wu, ACS Appl. Mater. Interfaces 13 (2021) 12198.

[74] J. Jasper van Blaaderen, Liselotte A. van den Brekel, Karl W. Krämer, Pieter Dorenbos, Chem. Mater. 35 (2023) 9623.

[75] Qian Yao, Jiaming Li, Xuesong Li, Xiaoxin Zheng, Zungang Wang, Xutang Tao, Adv. Opt. Mater. 10 (2022) 2201161.

[76] Dongsheng Yuan, ACS Appl. Mater. Interfaces 12 (2020) 38333.

[77] Luis Stand, Daniel Rutstrom, Merry Koschan, Mao-Hua Du, Charles Melcher, Urmila Shirwadkar, Jarek Glodo, Edgar Van Loef, Kanai Shah, Mariya Zhuravleva, Nucl. Instrum. Meth. A 991 (2021) 164963.

[78] M. D. Birowosuto, D. Cortecchia, W. Drozdowski, K. Brylew, W. Lachmanski, A. Bruno, C. Soci, Sci. Rep. 6 (2016) 37254.

[79] Aozhen Xie, Francesco Maddalena, Marcin E. Witkowski, Michal Makowski, Benoit Mahler, Winicjusz Drozdowski, Stuart Victor Springham, Philippe Coquet, Christophe Dujardin, Muhammad Danang Birowosuto, Cuong Dang, Chem. Mater. 32 (2020) 8530.

[80] Romain Gautier, Michael Paris, Florian Massuyeau, J. Am. Chem. Soc. 141 (2019) 12619.

[81] Yang Li, Wenyi Shao, Xiaoping Ouyang, Zhichao Zhu, Hang Zhang, Xiao Ouyang, Bo Liu, Qiang Xu, J. Phys. Chem. C 123 (2019) 17449.

[82] Richard T. Williams, Weronika W. Wolszczak, Xiaoheng Yan, David L. Carroll, ACS Nano 14 (2020) 5161.

[83] Jacob Jasper van Blaaderen, Francesco Maddalena, Cuong Dang, Muhammad Danang Birowosuto, Pieter Dorenbos, J. Mater. Chem. C 10 (2022) 11598.

[84] J. Jasper van Blaaderen, Stefan van der Sar, Djulia Onggo, Md Abdul K. Sheikh, Dennis R. Schaart, Muhammad D. Birowosuto, Pieter Dorenbos, J. Lumin. 263 (2023) 120012.

[85] K. J. Saunders, T. Y. Wong. T. M. Hartnett, R. W. Tustison, R. L. Gentilman, SPIE Proc. 683(1986) 72.

[86] O. V. Andreev, P. V. Miodushevscy, R. Serlenga, N. N. Parsukov, J. Phase Equilib. Diffus. 26 (2005) 109.

[87] O. V. Andreev, O. Yu. Mitroshin, N. A. Khritokhin, I. A. Razumkova, Russ. J. Inorg. Chem. 53 (2008) 440.

[88] Charles Boury, Antoine Allanore, Sci. Rep. 11 (2021) 18189.

[89] Klaus-Jürgen Range, Kurt G. Lange, Hubert Drexler, Comments Inorg. Chem. 3 (1984) 171.

[90] M. Leiss, J. Phys. C: Solid State Phys. 13 (1980) 151.

[91] V. Jarý, L. Havlák, J. Bárta, E. Mihóková, M. Buryi, M. Nikl, J. Lumin. 170 (2016) 718.

[92] J. C. van't Spijker, P. Dorenbos, C. P. Allier, C. W. E. van Eijk, A. R. H. F. Ettema, G. Huber, Nucl. Instrum. Meth. B 134 (1998) 304.

[93] E. G. Scharmer, M. Leiß, G. Huber, J. Lumin. 24 (1981) 751.

[94] Takayuki Yanagida, Hiromitsu Takahashi, Takeshi Ito, Daisuke Kasama, Teruaki Enoto, Mitsuhiro Sato, Shinya Hirakuri, Motohide Kokubun, Kazuo Makishima, Takagimi Yanagitani, Hideki Yagi, Takashi Shigeta, Takashi Ito, IEEE. T. Nucl. Sci. 52 (2005) 1836.

[95] Takayuki Yanagida, Yutaka Fujimoto, Yuui Yokota, Kei Kamada, Satoko Yanagida, Akira Yoshikawa, Hideki Yagi, Takagimi Yanagitani, Radiat. Meas. 46 (2011) 1503.

[96] Takayuki Yanagida, Kei Kamada, Yutaka Fujimoto, Hideki Yagi, Takagimi Yanagitani, Opt. Mater. 35 (2013) 2480.

[97] P. N. Kumta, S. H. Risbud, J. Mater. Sci. 29 (1994) 1135.

[98] Prashant N. Kumta, Subhash H. Risbud, J. Mater. Res. 8 (1993) 1394.

[99] Masako Matsumura Yuta, William B. White, J. Electrochem. Soc. 139 (1992) 2347.

[100] Pieter Dorenbos, J. Lumin. 135 (2013) 93.

[101] Weronika Wolszczak, Karl W. Krämer, Pieter Dorenbos, Phys. Status Solidi R. 13 (2019) 1900158.

Summary

The energy resolution of the highest resolution scintillation detectors is currently limited by Poisson statistics in the number of detected photons, meaning further improvement is only possible when more photons are detected [1]. Conventionally, scintillators are designed for read out with photomultiplier tubes (PMT). The photon detection efficiency that can be reached with PMTs hardly ever exceeds 50% [2], meaning about half of the photons remains undetected. Silicon based photodetectors, such as avalanche photodiodes (APD) or silicon photomultipliers (SiPM), have higher detection efficiencies than a PMT. The use of such detectors improves the photon statistics and makes it possible to attain a better energy resolution than currently available. To attain optimal detection efficiency, the emission wavelength of a scintillator needs to be matched to the peak sensitivity of the photodetector. For PMTs, this peak sensitivity almost always lies in the UV to blue part of the electromagnetic spectrum. For this reason, some of the best energy resolutions are attained with scintillators such as $LaBr_3$:Ce^{3+} and SrI_2:Eu^{2+}, which emit at 380 nm [3] and 435 nm [4], respectively.

Silicon based photodetectors are usually inefficient at wavelengths shorter than 400 nm, but are ideal for detecting wavelengths between 400 nm and 800 nm. Many Ce^{3+}-doped halide scintillators emit at wavelengths shorter than 400 nm, resulting in a loss of light. The emission wavelength of Eu^{2+}-doped halide scintillators often lies at wavelengths longer than 400 nm, but almost all these compounds suffer from a high probability of self-absorption. Being able to efficiently detect wavelengths up to 800 nm makes Sm^{2+} an interesting alternative activator, a lanthanide which emits in the near-infrared (NIR) part of the electromagnetic spectrum. Awater et al. demonstrated that co-doping SrI_2:5%Eu^{2+} with as little as 0.5% Sm^{2+} replaces virtually all Eu^{2+} emission by NIR Sm^{2+} emission. This drastically reduces the probability of self-absorption [5]. Wolszczak et al. attained an energy resolution of 3.2% by employing the same strategy and mounting $CsBa_2I_5$:2%Eu^{2+},1%Sm^{2+} on a temperature stabilised APD [6]. These results make further research into Sm^{2+} as an activator for scintillators interesting. As Sm^{2+}-doped scintillators are still largely unexplored, the research goal of this dissertation is to formulate design criteria for such scintillators.

The good results attained with Eu^{2+} and Sm^{2+} co-doping called for further research into what other lanthanides could be used to sensitise Sm^{2+}. Chapter 2 starts this off in an attempt to sensitise Sm^{2+} with Yb^{2+}, by co-doping them in the same $CsBa_2I_5$ host. When Yb^{2+} is used as an activator, it often shows both spin-allowed and spin-forbidden $4f^{13}5d \rightarrow 4f^{14}$ emission, with respective decay times in the µs and ms range. The spin-forbidden emission is much too slow for scintillator applications. When using Yb^{2+} as a sensitiser for Sm^{2+} and both are present in low concentrations (not more than several %), it was found that energy transfer from Yb^{2+} to Sm^{2+} happens through dipole-dipole interactions. These dipole-dipole interactions involve the same spin-allowed and spin-

forbidden transitions as the Yb^{2+} $4f^{13}5d \rightarrow 4f^{14}$ emission. The result is that part of the excitations from Yb^{2+} is transferred to Sm^{2+} on a ms timescale, which hinders its use as as sensitiser for scintillator applications. In Chapter 3, it is demonstrated that this slow energy transfer can be solved for very high Yb^{2+} concentrations. For this, the compounds $YbCl_2$:1%Sm^{2+}, $CsYbBr_3$:1%Sm^{2+} and $CsYbI_3$:1%Sm^{2+} were studied. It was found that the network of close lying Yb^{2+} ions rapidly exchange excitations and transfer them to Sm^{2+} on a sub ns timescale.

The rapid transfer of excitations among Yb^{2+} or Eu^{2+} in materials containing a high concentration of these ions typically causes concentration quenching. However, compounds in the Cs_4MX_6:Eu^{2+} (M = Ca, Sr; X = Br, I) family show good scintillation properties up to dopant concentrations of 100% and their light yield decreases only slightly upon increasing the dopant concentration from 10% to 100% [7, 8]. The lack of concentration quenching is largely attributed to the large (9 Å) interatomic distances between the Eu^{2+} ions. In Chapter 4, Cs_4EuX_6 (X = Br, I) was doped with Sm^{2+}. It could be found that Eu^{2+}-Eu^{2+} energy transfer still takes place at such large interatomic distances, but happens at a timescale similar to Eu^{2+} radiative decay. Due to the high Eu^{2+} concentration in these compounds, the Eu^{2+} emission has a high probability of being reabsorbed. This high self-absorption probability makes the scintillation properties of crystals deteriorate with increasing crystal size. With a concentration of 2% Sm^{2+}, almost all Eu^{2+} was replaced by Sm^{2+} emission and virtually no self-absorption was observed anymore and the energy resolution improved from 11% to 7.5%. It could therefore be shown that Sm^{2+} (co-)doping is an effective solution to the self-absorption problems of Eu^{2+}-doped scintillators.

The use of Eu^{2+} as a sensitiser for Sm^{2+} allows the knowledge of Eu^{2+}-doped scintillators to be applied to the development of Sm^{2+}-doped scintillators. If trivalent lanthanides can also be used as scintillation sensitisers, many more potential host materials and dopant combinations would become available. Therefore, Chapter 5 explores the use of Ce^{3+} and Pr^{3+} as scintillation sensitisers for Sm^{2+}. $LaBr_3$ is chosen as a host as both Ce^{3+} and Pr^{3+} dopants have already been shown to yield exceptional scintillation characteristics in this compound. Unfortunately, it was found that the emission of Sm^{2+} is thermally quenched at room temperature. Additionally, energy transfer from the $LaBr_3$ host to Sm^{2+} is inefficient, resulting in a light yield of only 7,000 ph/MeV for $LaBr_3$:1%Sm^{2+} at 175 K. Co-doping with 5% Ce^{3+} introduces a new route of energy transfer from the $LaBr_3$ host to Sm^{2+}, where Ce^{3+} gets excited from the host and transfers this excitation to Sm^{2+}. This increases the light yield to 25,000 ph/MeV, but at the cost of decreasing the quenching temperature of the Sm^{2+} emission even further. Furthermore it is found that Pr^{3+} quenches the emission of Sm^{2+} even stronger than Ce^{3+} does. So while evidence is found that co-doping with sensitisers can be an effective strategy to increase the light yield of Sm^{2+}-doped scintillators, the use of Ce^{3+} and Pr^{3+} as sensitisers does not seem practical as they tend to quench the Sm^{2+} emission.

To match a scintillator to a photodetector, the scintillator's emission wavelength is of key importance. Additionally, the decay time of the emission must be as short as possible as long decay times limit the count rate of a scintillation detector. To make the search for the ideal Sm^{2+}-doped scintillator more efficient, Chapter 6 discusses the relation between Sm^{2+} $4f^55d \rightarrow 4f^6$ emission wavelength and its decay time. It is found that the

close lying $4f^5$5d and $4f^6[^5D_0]$ states are in thermal equilibrium. In compounds where the $4f^5$5d level lies at higher energy than the $4f^6[^5D_0]$ level, it is found that Sm^{2+} often still shows almost exclusively $4f^5$5d → $4f^6$ emission. Since in these compounds Sm^{2+} spends the majority of its time in the $4f^6[^5D_0]$ state, its decay time becomes significantly longer. To avoid excessive lengthening, it is determined that the $4f^5$5d → $4f^6$ emission must lie at 730 nm or longer wavelength. However, for efficient detection with silicon based photodetectors, it is crucial that the majority of the emission lies at wavelengths shorter than 800 nm. The ideal wavelength range for the Sm^{2+} $4f^5$5d → $4f^6$ emission is therefore identified to lie between 730 nm and 800 nm.

Finally, it is assessed what energy resolution can ultimately be achieved with Sm^{2+}-doped scintillators. For this, Chapter 7 compares the fundamental light yield limits of Sm^{2+}-doped scintillators with other scintillator categories. The comparison is made with Eu^{2+} and Ce^{3+}-doped halides and sulfides, and intrinsically activated compounds. It is found that Sm^{2+} luminescence is quenched in compounds with a band gap smaller than approximately 4.1 eV, while Eu^{2+} and Ce^{3+} can still emit in compounds with a band gap of about 2.5 eV. When limiting the search to halide compounds, it was shown that luminescence of Sm^{2+} and Eu^{2+} is quenched when the band gap is smaller than 4.2 eV, for Ce^{3+} this occurs at a band gap of 3.7 eV. This means that the maximum attainable light yield with halide scintillators is the same for Sm^{2+} and Eu^{2+}-doping. In these compounds, the main benefit of using Sm^{2+} instead of Eu^{2+} is to solve the inherent self-absorption problems that Eu^{2+}-doped scintillators face. Light yields significantly higher than 100,000 ph/MeV cannot be found in lanthanide doped halides. Such high light yields will only be found in intrinsically activated halides or lanthanide doped chalcogenides. The highest light yield scintillators of all types discussed in Chapter 7 (with exception of the Eu^{2+}-doped halides) are most suited for read out with silicon based photodetectors, as their emission wavelengths are expected to be too long for efficient detection with PMTs.

References

[1] M. S. Alekhin, J. T. M. de Haas, I. V. Khodyuk, K. W. Krämer, P. R. Menge, V. Ouspenski, P. Dorenbos, Appl. Phys. Lett. 102 (2013) 151915.

[2] Johan T. M. de Haas, Pieter Dorenbos, IEEE T. Nucl. Sci. 55 (2008) 1086.

[3] P. Dorenbos, E. V. D. van Loef, A. P. Vink, E. van der Kolk, C. W. E. van Eijk, K. W. Krämer, H. U. Güdel, W. M. Higgins, K. S. Shah, J. Lumin. 117 (2006) 147.

[4] Edgar V. van Loef, Cody M. Wilson, Nerine J. Cherepy, Giulia Hull, Stephen A. Payne, Woon-Seng Choong, William W. Moses, Kana S. Shah, IEEE T. Nucl. Sci. 56 (2009) 869.

[5] R. H. P. Awater, M. S. Alekhin, D. A. Biner, K. W. Krämer, P. Dorenbos, J. Lumin. 212 (2019) 1.

[6] Weronika Wolszczak, Karl W. Krämer, Pieter Dorenbos, Phys. Status Solidi R. 13 (2019) 1900158.

[7] Daniel Rutstrom, Luis Stand, Merry Koschan, Charles L. Melcher, Mariya Zhuravleva, J. Lumin. 216 (2019) 116740.

[8] Yuntao Wu, Dan Han, Bryan C. Chakoumakos, Hongliang Shi, Shiyou Chen, Mao-Hua Du, Ian Greeley, Matthew Loyd, Daniel J. Rutstrom, Luis Stand, Merry Koschan, Charles L. Melcher, J. Mater. Chem. C 6 (2018) 6647.

Samenvatting

De energieresolutie van de hoogste resolutie scintillatiedetectoren wordt momenteel gelimiteerd door Poisson statistiek in het aantal gedetecteerde fotonen. Dat betekent dat verbetering enkel mogelijk is wanneer meer fotonen worden gedetecteerd [1]. Scintillatoren worden van oudsher ontwikkeld om uitgelezen te worden door middel van een fotomultiplicatorbuis {Engels: photomultiplier tube} (PMT). De fotondetectie-efficiëntie die met PMTs kan worden bereikt is zelden hoger dan 50% [2], waardoor een groot aantal fotonen ongedetecteerd blijft. Silicium gebaseerde fotodetectoren zoals lawinefotodiode {Engels: avalanche photodiodes} (APD) of silicium fotomultiplicatoren {Engels: silicon photomultipliers} (SiPM) hebben een hogere detectie-efficiëntie dan een PMT. Het gebruik van zulke detectoren verbetert de fotonstatistiek en maakt het mogelijk de energieresolutie te verbeteren. Om de detectie-efficiëntie te optimaliseren is het nodig de emissiegolflengte van een scintillator af te stemmen met de golflengte waarop de fotodetector het meest gevoelig is. Voor PMT's ligt de maximale gevoeligheid bijna altijd in het UV of blauwe deel van het electromagnetische spectrum. Om die reden worden de beste energieresoluties bereikt met scintillatoren zoals $LaBr_3$:Ce^{3+} en SrI_2:Eu^{2+}, die licht uitzenden bij respectievelijk 380 nm [3] en 435 nm [4].

Silicium gebaseerde fotodetectoren zijn typisch inefficiënt bij golflengten korter dan 400 nm, maar zijn ideaal voor het detecteren van golflengten tussen de 400 nm en 800 nm. Veel Ce^{3+}-gedoteerde halide scintillatoren zenden licht uit bij golflengten korter dan 400 nm, wat resulteert in het verlies van licht. De emissiegolflengte van Eu^{2+}-gedoteerde halide scintillatoren ligt vaak wel bij golflengten langer dan 400 nm, maar bijna al deze verbindingen hebben last van een hoge kans op zelfabsorptie. De mogelijkheid golflengten tot 800 nm efficiënt te detecteren maakt Sm^{2+} een interessant alternatief als activator, een lanthanide die in het nabij-infrarode {Engels: near-infrared} (NIR) deel van het electromagnetisch spectrum uitzendt. Awater et al. hebben aangetoond dat het co-doteren van SrI_2:5%Eu^{2+} met slechts 0.5% Sm^{2+} ervoor zorgt dat bijna alle Eu^{2+} emissie wordt vervangen door NIR Sm^{2+} emissie. De kans op zelfabsorptie neemt daarmee drastisch af [5]. Wolszczak et al. hebben een energieresolutie van 3.2% bereikt door gebruik te maken van deze strategie en $CsBa_2I_5$:2%Eu^{2+},1%Sm^{2+} op een temperatuurgestabiliseerde APD te bevestigen [6]. Deze resultaten maken het interessant om het gebruik van Sm^{2+} als een activator voor scintillatie verder te onderzoeken. Er is nog weinig bekend over Sm^{2+}-gedoteerde scintillatoren, daarom is het doel van dit proefschrift het formuleren van de ontwerpcriteria van zulke scintillatoren.

De goede resultaten van Eu^{2+} en Sm^{2+} co-dotering riepen op tot verder onderzoek naar welke andere lanthanides kunnen worden gebruikt voor het sensibiliseren van Sm^{2+}. Hoofdstuk 2 begint hieraan met een poging Sm^{2+} te sensibiliseren met Yb^{2+}, door ze beide in hetzelfde $CsBa_2I_5$ gastrooster te co-doteren. Wanneer Yb^{2+} als activator wordt gebruikt zendt het zowel spin-toegestane als spin-verboden $4f^{13}5d \rightarrow 4f^{14}$ emissie uit,

met respectievelijke vervaltijden in het µs en ms bereik. De spin-verboden emissie is veel te traag voor scintillatietoepassingen. Wanneer Yb^{2+} wordt gebruikt als sensibilisator voor Sm^{2+} en de concentratie van beide lanthanides laag is (niet meer dan enkele %), werd er gevonden dat de energieoverdracht van Yb^{2+} naar Sm^{2+} plaatsvindt door middel van dipool-dipool interacties. Deze dipool-dipool interacties bevatten dezelfde spin-toegestane en spin-verboden transities als de Yb^{2+} $4f^{13}5d \rightarrow 4f^{14}$ emissie. Hierdoor wordt een deel van de excitaties van Yb^{2+} op een ms tijdschaal naar Sm^{2+} overgedragen, wat Yb^{2+} ongeschikt maar als sensibilisator voor scintillatietoepassingen. In Hoofdstuk 3 wordt aangetoond dat dit probleem kan worden verholpen door gebruik te maken van zeer hoge Yb^{2+} concentraties. Hiervoor zijn de verbindingen $YbCl_2$:1%Sm^{2+}, $CsYbBr_3$:1%Sm^{2+} en $CsYbI_3$:1%Sm^{2+} bestudeerd. Er werd gevonden dat het netwerk van naburige Yb^{2+} ionen snel excitaties met elkaar uitwisselen en ze zo op een sub-ns tijdschaal naar Sm^{2+} transporteren.

De snelle overdracht van excitaties tussen Yb^{2+} of Eu^{2+} in materialen die een hoge concentratie van deze ionen bevatten zorgt typisch voor concentratiedoving. Verbindingen in de Cs_4MX_6:Eu^{2+} (M = Ca, Sr; X = Br, I) familie hebben echter goede scintillatie-eigenschappen voor doteringconcentraties tot en met 100% en hun lichtopbrengst neem slechts een klein beetje af tijdens het verhogen van de doteringconcentratie van 10% naar 100% [7, 8]. De afwezigheid van concentratiedoving is grotendeels te wijten aan de grote (9 Å) interatomische afstanden tussen de Eu^{2+} ionen. Door Cs_4EuX_6 (X = Br, I) te doteren met Sm^{2+} wordt in Hoofdstuk 4 vastgesteld dat er nog steeds Eu^{2+}-Eu^{2+} energieoverdracht optreedt bij zulke grote interatomische afstanden, maar dat de tijdschaal waarop het plaatsvindt ongeveer gelijk is aan die van het radiatief verval van Eu^{2+}. Door de hoge Eu^{2+} concentratie in deze verbindingen heeft de Eu^{2+} emissie een hoge kans om opnieuw in het kristal geabsorbeerd te worden. Deze hoge kans op zelfabsorptie verslechtert de scintillatie-eigenschappen van grotere kristallen. Door het doteren met 2% Sm^{2+} is bijna alle emissie van Eu^{2+} vervangen door dat van Sm^{2+} en de aanwezigheid van zelfabsorptie kon vrijwel niet meer worden waargenomen. De energieresolutie verbeterde tevens van 11% naar 7.5%. Daarmee kon worden aangetoond dat Sm^{2+} (co-)dotering een effectieve manier is om de problemen van zelfabsorptie van Eu^{2+}-gedoteerde scinatilloren op te lossen.

Het gebruik van Eu^{2+} als sensibilisator voor Sm^{2+} zorgt ervoor dat de kennis over Eu^{2+}-gedoteerde scintillatoren kan worden toegepast op de ontwikkeling van Sm^{2+}-gedoteerde scintillatoren. Als trivalente lanthaniden ook kunnen worden gebruikt als scintillatiesensibilasator, zouden veel meer gastrooster- en doteringcombinaties beschikbaar komen. Daarom verkent Hoofdstuk 5 het gebruik van Ce^{3+} en Pr^{3+} als scintillatiesensibilisator voor Sm^{2+}. $LaBr_3$ is gekozen als gastrooster omdat zowel Ce^{3+} als Pr^{3+}-dotering exceptioneel goede scintillatie-eigenschappen oplevert in deze verbinding. Helaas werd er gevonden dat de Sm^{2+} thermisch is gedoofd bij kamertemperatuur. Daarbij komt dat het $LaBr_3$ gastroosters erg inefficiënt excitaties overdraagt aan Sm^{2+}, waardoor de lichtopbrengst van $LaBr_3$:1%Sm^{2+} slechts 7,000 ph/MeV bedraagt bij een temperatuur van 175 K. Co-dotering met 5% Ce^{3+} introduceert een nieuwe route van energieoverdracht van het $LaBr_3$ gastrooster naar Sm^{2+}, waarin Ce^{3+} eerst de excitatie van het gastrooster overneemt en daarna overdraagt aan Sm^{2+}. Dit verhoogt de lichtopbrengst naar 25,000 ph/MeV, maar dat gaat ten koste van de dovingstemperatuur die hierdoor

verder daalt. Daarnaast werd er gevonden dat Pr^{3+} de Sm^{2+} emissie nog sterker dooft dan Ce^{3+}. Dus terwijl er bewijs is gevonden dat co-doteren met sensibilisatoren een effectieve strategie kan zijn om de lichtopbrengst van Sm^{2+}-gedoteerde scintillatoren te verhogen, lijkt het gebruik van Ce^{3+} en Pr^{3+} als sensibilisator niet handig omdat ze de Sm^{2+} emissie doven.

Het is cruciaal om de emissiegolflengte van een scintillator en de maximale detectie-efficiëntie van een fotodetector op elkaar af te stemmen. Tevens moet de vervaltijd van de emissie zo kort mogelijk zijn, omdat een lange vervaltijd de telsnelheid van een scintillatiedetector limiteert. Om de zoektocht naar de ideale Sm^{2+}-gedoteerde scintillator efficiënter te maken wordt in Hoofdstuk 6 de relatie tussen de Sm^{2+} $4f^5 5d \rightarrow 4f^6$ emissiegolflengte en haar vervaltijd bediscussieerd. Er is gevonden dat de nabijgelegen $4f^5 5d$ en $4f^6[^5D_0]$ toestanden in thermisch evenwicht zijn. In verbindingen waar de $4f^5 5d$ toestand bij hogere energie ligt dan de $4f^6[^5D_0]$ toestand werd gevonden dat Sm^{2+} vaak alsnog bijna alleen $4f^5 5d \rightarrow 4f^6$ emissie uitzendt. Omdat Sm^{2+} in deze verbindingen zich een groot deel van de tijd in de $4f^6[^5D_0]$ toestand bevindt wordt de vervaltijd signifcant langer. Om overmatige verlenging van de vervaltijd te voorkomen is er bepaald dat de $4f^5 5d \rightarrow 4f^6$ emissiegolflengte langer moet zijn dan 730 nm. Echter is het voor detectie met silicium gebaseerde fotodetectoren belangrijk dat het merendeel van de emissie niet bij een golflengte langer dan 800 nm ligt. Hieruit kon worden geconcludeerd dat de ideale golflengte voor de $4f^5 5d \rightarrow 4f^6$ emissie tussen de 730 nm en 800 nm ligt.

Als laatste is er bepaald watvoor energieresolutie potentieel kan worden gehaald met Sm^{2+}-gedoteerde scintillatoren. Hiervoor vergelijkt Hoofstuk 7 de fundamentale limieten in lichtopbrengst van Sm^{2+}-gedoteerde scintillatoren met andere categorieën scintillatoren. De vergelijking wordt gemaakt met Eu^{2+} en Ce^{3+}-gedoteerde haliden en sulfiden, en intrinsiek geactiveerde verbindingen. Er is gevonden dat Sm^{2+} luminescentie wordt gedoofd in verbindingen met een bandkloof kleiner dan ongeveer 4.1 eV, terwijl Eu^{2+} en Ce^{3+} nog kunnen emiteren in verbindingen met een bandkloof nabij 2.5 eV. Wanneer slechts naar halide verbindingen wordt gekeken blijkt dat zowel Sm^{2+} als Eu^{2+} luminescentie wordt gedoofd zodra de bandkloof kleiner wordt dan 4.2 eV, terwijl dit voor Ce^{3+} pas bij 3.7 eV plaatsvindt. Dit betekent dat de maximaal haalbare lichtopbrengst van halide scintillatoren hetzelfde is voor Sm^{2+} als voor Eu^{2+}-dotering. In deze verbindingen is de grootste reden voor het gebruik van Sm^{2+} in plaats van Eu^{2+} het oplossen van de inherente zelfabsorptie problemen van Eu^{2+}-gedoteerde scintillatoren. Lichtopbrengsten veel hoger dan 100,000 ph/MeV kunnen niet worden bereikt met lanthanide gedoteerde halides. Zulke hoge lichtopbrengsten kunnen slechts worden gevonden in intrinsiek geactiveerde haliden of lanthanide gedoteerde chalcogeniden. De scintillatoren met de hoogste lichtopbrengst van alle scintillator categorieën die in Hoofdstuk 7 (met uitzondering van de Eu^{2+}-gedoteerde haliden) worden besproken zijn voornamelijk geschikt voor het uitlezen met silicium gebaseerde fotodetectoren, gezien wordt verwacht dat hun emissiegolflengte te lang is voor efficiënte detectie met een PMT.

References

[1] M. S. Alekhin, J. T. M. de Haas, I. V. Khodyuk, K. W. Krämer, P. R. Menge, V. Ouspenski, P. Dorenbos, Appl. Phys. Lett. 102 (2013) 151915.

[2] Johan T. M. de Haas, Pieter Dorenbos, IEEE T. Nucl. Sci. 55 (2008) 1086.

[3] P. Dorenbos, E. V. D. van Loef, A. P. Vink, E. van der Kolk, C. W. E. van Eijk, K. W. Krämer, H. U. Güdel, W. M. Higgins, K. S. Shah, J. Lumin. 117 (2006) 147.

[4] Edgar V. van Loef, Cody M. Wilson, Nerine J. Cherepy, Giulia Hull, Stephen A. Payne, Woon-Seng Choong, William W. Moses, Kana S. Shah, IEEE T. Nucl. Sci. 56 (2009) 869.

[5] R. H. P. Awater, M. S. Alekhin, D. A. Biner, K. W. Krämer, P. Dorenbos, J. Lumin. 212 (2019) 1.

[6] Weronika Wolszczak, Karl W. Krämer, Pieter Dorenbos, Phys. Status Solidi R. 13 (2019) 1900158.

[7] Daniel Rutstrom, Luis Stand, Merry Koschan, Charles L. Melcher, Mariya Zhuravleva, J. Lumin. 216 (2019) 116740.

[8] Yuntao Wu, Dan Han, Bryan C. Chakoumakos, Hongliang Shi, Shiyou Chen, Mao-Hua Du, Ian Greeley, Matthew Loyd, Daniel J. Rutstrom, Luis Stand, Merry Koschan, Charles L. Melcher, J. Mater. Chem. C 6 (2018) 6647.

Acknowledgements

There are many people without whom this dissertation would likely never have existed, at least not in its current form. All these people deserve a thank you and a short personal message. The obvious first person to express my gratitude to is my promotor, Pieter. During the past 4 years you guided me through this project in exactly the right way. Jasper and I often joked that the best meetings were the ones where you would send us away with a bunch of keywords and let us figure things out by ourselves afterwards. Furthermore, you put a lot of effort in correcting my terrible writing, which hopefully has gotten better over the years. You recently jokingly called it a "Casperian sentence" when you would cross out 5 of my words and replaced it with 1. If the readers of this dissertation do not understand what a "Casperian sentence" is, it means you did your job well. But perhaps most importantly, you gave me the space to just do my own thing. You trusted that, despite the fact that I could often dive into fundamental problems deeper than what would be useful for the project, I would always come back with good results and a fun story. Being able to do so has really contributed to the joy I experienced during these years.

Next to all these work related things, I am also happy we could often find each other in many other things. For example our shared hatred for bureaucracy and shared love for Paris. Also, on conferences you showed us how to stay true to our Dutch nationality by introducing the concept of "economical drinking". All in all, I feel like you have seriously invested in me during these 4 years and I can genuinly say it has really had a positive impact on my life.

Of course there is also a big thank you to my second promotor, Erik. While you operated a lot at the sidelines, you did often show interest in the project and were always happy to talk about progress or new ideas. I always admired your straight forward "just do it" mentality. Just get started on a project in the most practical way possible and it will hopefully just sort itself out. You showed that you can apply this tactic to almost anything, whether it is running a lab, writing an article, or building a tiny house.

Everyone who has ever been part of the luminescence materials group knows that Johan deserves more credit than he can ever be given in an acknowledgement chapter of a dissertation. Johan, it is fair to say that this thesis would not have been possible without your years of hands on experience, great physical intuition, flawless storage of old "junk" and justified grumpy responses to our stupid ideas. Thank you for being an amazing technician and making it all happen.

Obviously I owe a great thank you to our collaborators, team Bern, the legendary crystal growers. Karl, in the years of working with you, I got to know you as one of the most friendly, gentle and honest persons I ever worked with. You trusted us with the decisions for what compounds we needed and supplied us with many more crystals than we could have hoped for. With every manuscript I wrote, it was obvious that you checked it with

the greatest care. Not all these manuscripts would be published as smoothly, for example the one time a reviewer suggested we "consult with someone who knows anything about crystal growth". Luckily you could laugh about that absurd situation as much as I did. With all the work you took out of our hands by providing us with the countless crystals you enabled us to generate results very efficiently. This meant that we never had to stress about the scientific output during my PhD and the entire project went as smooth as it could go.

And of course Daniel, the other half of team Bern. We have not spoken an awful lot in person, but it was very clear to me that you were working really hard in the background. I am happy we got to meet during our visit in Bern and I will never forget your genuine love for crystal growth. Please know that every single crystal you sent to Delft gave us the feeling of unwrapping a Christmas present.

To the people of the Luxium/Saint Gobain team: Vladimir, John and Peter. Thank you for being part of the project, the fun and often informal meetings, the scientific discussions and the late night dinners that John would by pure coincidence often skip most of. While these things might be considered part of usual business, it feels a lot more special when you have just started your research project and get to experience these things for the first time. I am grateful that I was allowed to be part of it.

I also still owe a thank you to Weronika. Technically speaking, you left the group before I started, but your contribution had already been made at that point. You introduced me to the concept of scintillators and laid the foundation my dissertation with the last 3 chapters of yours. I was happy to hear you stayed interested in the developments and took the effort to read my articles as they got published. Besides the shared interest for this very specific topic, I am also happy we shared some very memorable moments. Two true highlights were us flying upside down in an airplane, and running up a mountain at the SCINT conference in New Mexico after Johan specifically said "not too far and not too steep".

Then there are the many colleagues, fellow PhD students, and people who have already left the group by now. We will start with the eternal optimist and sunshine of the group, Jasper, who I shared the project with. Next to going to conferences together, our similar music taste resulted in endless scrolling through rateyourmusic lists and we took the time to go to concerts. I also specifically enjoyed the "let's just walk, it's only an hour" attitude we shared. We proved that sometimes a long nighttime walk through Paris can be faster than the hassle with public transport. Additionally, I also owe you a thank you for allowing me aid in consuming your seemingly limitless tea stash. Next up is Max. It was great fun working next to you in the office, especially since you managed to keep me off my work with countless hours of entertaining distraction. This included watching videos of finfluencers taking their wives out for dinner, beautiful kazoo music, and battling over the "Apollo colour" in way too many games of go. Thank you for often bringing colleagues together socially, either by organising Mario kart tournaments in 't Koepeltje or inviting everyone over for an evening of board games at your place. We may not forget the man of culture, Justin. The person who brings amazing things from the homeland, among which the famous coconut cheetos, and bags filled with the most delicious tea from the sun moon lake. Red tea, yes, for us uncultured Europeans. Thank you for giving us a literal taste of all the good stuff Taiwan has to offer. Jeffrey, the newest addition to

the group at the time of writing this, but perhaps also the biggest luminescence enthusiast. Thank you for saving me by taking over the job of organising the group meetings, you seem to enjoy it a lot more than I did! And lastly a thank you to the various other people who have been part of the group during the same time as me and have helped me out on several occasions, namely Maarten, Francesco, Giacomo and Vasya.

Our research group was also heavily supported by Trudy, the real expert in getting anything done within the administrative systems of the university. You are always one of the first people who any of us would meet when starting to work here for one simple reason: no one gets to enter the building without your permission! Also, every time we got stuck in the electronic jungle of excessive forms that would do nothing but spit out errors, you were the one to help us navigate through them. Thank you for all this help!

Then we have our neighbours, in order of appearance: Stefan, David, Jack, and Marc. You were the best assorted selection of people that one can have working down the hall. The long stops in your office, eating David's chocolate (there was so much!) and accompanied best April fools' joke ever, the sinister whiteboard humour, Jack's (dis)appearances, accurate Stefan impressions, hatred for vegemite, and nachos with the boys. I would not have wanted to miss any of these things.

I have been lucky enough to supervise countless student projects during my PhD. Many of you have expressed your gratitude for my supervision in a way I could tell was absolutely sincere. You have given me the feeling that, to some degree, I was able to provide you with supervision similar to what I have gotten from others myself. The idea that I have positively impacted your lives by sharing my small amount of experience and large amount of enthusiasm means a lot to me. Thank you all for your work and learning about luminescence together with me. In this category there must be two special mentions for helping me sort out the big stuff, those are for Nils and Twan. Thank you!

It makes me happy that I have been given the freedom to do some work outside of my project. Most notably this was the calcium oxide project with Bert. Thank you, Bert, for taking the time to share your expertise on many different topics, specifically synthesis and characterisation of phosphors. It was great to join forces and supervise students together with you. We would continuously theorise about how energy transfer in Eu^{3+} and Eu^{2+} co-doped CaO would go in the opposite direction of what is ordinarily observed. In the end we even managed to prove that our theories were correct!

I also want to thank the people who have had a much more indirect contribution. Such as the people from 't Koepeltje for sharing their (vast knowledge of) beers. And of course all of my friends, with a special mention for the people from the "actieve boktor". This oddly named group consists mostly of friends who I have known since secondary school or before. I find it very special that we have known each other for such a long time and are still such a tight group of friends. Thank you for the fun times and all the support everyone gives to each other.

Lastly, I want to thank my parents for their invaluable support from the sideline. It involved big things, such as helping me buy my first apartment during this period and all the help my father gave me during the renovation. But also the seemingly more simple things, such as the endless phone calls from my mother on sunday evenings. Both these things are excellent examples that show how involved you are as parents. I would not have been where I am now without all of this.

About the author

Casper van Aarle was born on 23 May 1994 in 's-Gravenhage, the Netherlands. He attended school at de Oase and subsequently secondary school (VWO) at Hofstad Lyceum, which conveniently were located next to each other. During this time, it was already clear that he had an interest for science and technology. This led to his choice of studyng applied physics at Delft University of Technology. He obtained his BSc degree after succesfully defending his thesis on energy and temperature dependent CsI:Tl scintillation decay in 2018 under supervision of W. Wolszczak. For obtaining his MSc degree, he specialised in a combination of solid state physics, radiation sciences and computational physics. He did an industrial internship on designing and modeling a Laue lens for radiation therapy at Cosine Measurement Systems. The work of his thesis was performed on the scintillation properties of Yb^{2+} and Sm^{2+}-doped $CsBa_2I_5$ under supervision of P. Dorenbos, the works of which formed a basis for the first chapter of this dissertation. After receiving his MSc degree cum laude, he continued the work on Sm^{2+}-doped scintillators in Delft, the results of which are presented in this dissertation.

List of Publications

1. **Casper van Aarle**, Karl W. Krämer, Pieter Dorenbos, "Lengthening of the Sm^{2+} $4f^5 5d \rightarrow 4f^6$ decay time through interplay with the $4f^6[^5D_0]$ level and its analogy to Eu^{2+} and Pr^{3+}", J. Lumin. 266 (2024) 120329.

2. **Casper van Aarle**, Nils Roturier, Daniel A. Biner, Karl W. Krämer, Pieter Dorenbos, "Light yield and thermal quenching of Ce^{3+} and Pr^{3+} co-doped $LaBr_3$: Sm^{2+} near-infrared scintillators", Opt. Mater. 145 (2023) 114375.

3. **Casper van Aarle**, Karl W. Krämer, Pieter Dorenbos, "Avoiding concentration quenching and self-absorption in Cs_4EuX_6 (X=Br,I) by Sm^{2+} doping", J. Mater. Chem. C 11 (2023) 2336.

4. **Casper van Aarle**, Karl W. Krämer, Pieter Dorenbos, "Characterisation of Sm^{2+}-doped $CsYbBr_3$, $CsYbI_3$ and $YbCl_2$ for near-infrared scintillator application", J. Lumin. 251 (2022) 119209.

5. David Girou, Eric Ford, Colin Wade, **Casper van Aarle**, Alexei Uliyanov, Lorraine Hanlon, John A Tomsick, Andreas Zoglauer, Maximilien J Collon, Marco W Beijersbergen, Nicolas M. Barrière, "Design and modeling of a Laue lens for radiation therapy with hard X-ray photons", Phys. Med. Biol. 66 (2021) 245007.

6. **Casper van Aarle**, Karl W. Krämer, Pieter Dorenbos, "The role of Yb^{2+} as a scintillation sensitiser in the near-infrared scintillator $CsBa_2I_5$:Sm^{2+}", J. Lumin. 238 (2021) 118257.